Atom-chip Gravimeter with Bose-Einstein Condensates

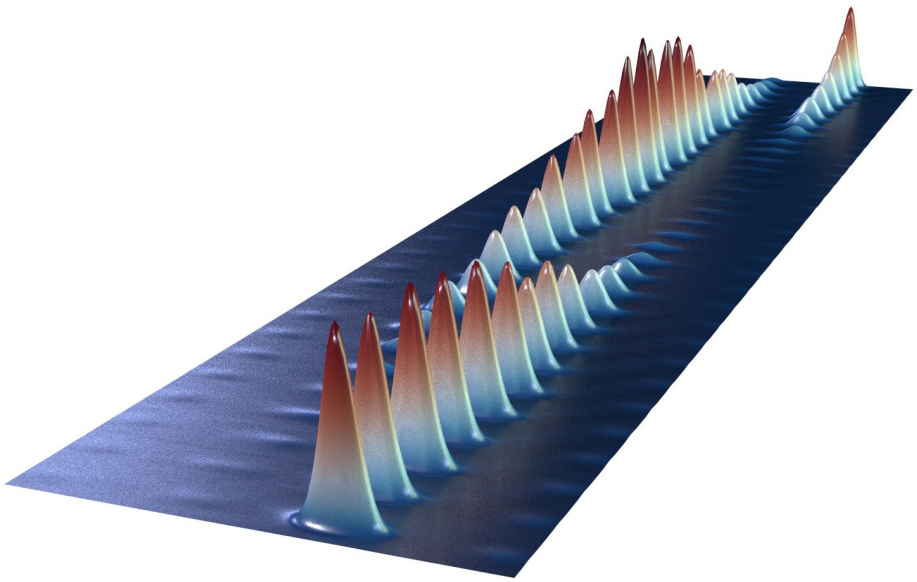

PhD thesis by Sven Abend, Hannover 2017

Leibniz Universität Hannover

The cover picture shows a series of density profiles taken from the output ports of a Mach-Zehnder atom interferometer with scanned laser phase $\Delta\phi$ between subsequent cycles (see page 66).

Atom-chip Gravimeter with Bose-Einstein Condensates

Von der QUEST-Leibniz-Forschungsschule der
Gottfried Wilhelm Leibniz Universität Hannover

zur Erlangung des Grades
Doktor der Naturwissenschaften
- Dr. rer. nat. -
genehmigte Dissertation von

Dipl.-Phys. Sven Abend

2017

Referent:
Prof. Dr. Ernst M. Rasel
Institut für Quantenoptik
Leibniz Universität Hannover

Korreferent:
apl. Prof. Dr. Carsten Klempt
Institut für Quantenoptik
Leibniz Universität Hannover

Korreferent:
Prof. Dr. Kai Bongs
School of Physics and Astronomy
University of Birmingham

Tag der Disputation:
10.08.2017

Kurzfassung: Atomchip Gravimeter mit Bose-Einstein Kondensaten

Die heutige Generation atomarer Inertialsensoren arbeitet typischerweise mit lasergekühlten Atomen, die aus einer optischen Melasse fallen gelassen oder gestartet werden. Die Expansion und Größe dieser Ensembles limitieren die Effizienz von Strahlteilern und die Analyse systematischer Unsicherheiten. Diese Limitierung kann durch die Verwendung von Ensembles mit einer Impulsverteilung, die deutlich kleiner als der Photonenimpuls ist, wie einem Bose-Einstein Kondensat (BEC), umgangen werden. Nachdem das BEC das Regime ballistischer Expansion erreicht hat, in dem die Wechselwirkungsenergie in kinetische Energie überführt wurde, kann die Expansionsrate eines BECs mit Delta-Kick Kollimation sogar weiter reduziert werden. Atomchip-Technologien ermöglichen hierbei die schnelle und robuste Generation von BECs sowie die Anwendung der Kollimation und ebnen den Weg für miniaturisierte atomare Sensoren.

Die Benutzung von BECs erlaubt die effiziente Bragg- oder Doppel-Bragg-Beugung. In dieser Arbeit werden dabei Effizienzen von über 95% erreicht, was eine wichtige Voraussetzung für die Interferometrie mit hohem Kontrast C ist. BECs erlauben es neue Methoden der kohärenten Manipulation zu entwickeln. Basierend auf einer Kombination aus Doppel-Bragg-Beugung und Bloch-Oszillationen wurde ein Startmechanismus mit mehr als 75% Effizienz in einem retroreflektiertem Laserstrahl realisiert. Die Neuerung dieser Methode ist, dass nur ein einzelner Laserstrahl nötig ist, der zudem als Strahlteiler genutzt wird und die Komplexität des Aufbaus nicht erhöht. Mit einem ähnlichen Schema wird ein skalierbarer symmetrischer Strahlteiler mit einem Impulstransfer von bis zu $1008\,\hbar k$ realisiert. Ein interferometrischer Kontrast kann mit einem Impulsübertrag von bis zu $208\,\hbar k$ beobachtet werden, was mehr als einer Verdopplung der größten Separation entspricht, die nach aktuellem Kenntnisstand bisher berichtet wurde.

Im Rahmen dieser Arbeit wurde das erste Atomchip Gravimeter mit Bose-Einstein Kondensaten realisiert, das in zwei Modi betrieben wird. Entweder wird das BEC schlicht fallen gelassen und die Interferometrie im Fall durchgeführt oder das BEC wird nach einer gewissen Fallzeit wieder nach oben beschleunigt, sodass sich die Interferometrie in einer Fontänen Geometrie über eine größere Zeit $2T$ erstreckt. Der Atomchip dient der Erzeugung des BECs, zur Zustandspräparation mit magnetischem Zustandstransfer, magnetischer Linse und Stern-Gerlach Ablenkung. Die Besonderheit des Aufbaus ist, dass der Laserstrahl, der das Mach-Zehnder Interferometer (MZI) mittels Bragg-Beugung aufspannt, vom Chip retroreflektiert wird. Der Chip dient somit als inertiale Referenz in einem äußerst kompakten Interferometer. Alle atomoptischen Operationen, die Interferometrie und die Detektion der Interferometerzustände können innerhalb eines Würfels von einem Zentimeter Kantenlänge erfolgen, was eine signifikante Verkleinerung ermöglicht.

Mit fallenden BECs löst das Gravimeter lokale Schwere mit $\Delta g/g = 1{,}3 \cdot 10^{-5}$ auf, limitiert durch seismisches Rauschen, das auf den Apparat einwirkt. Mit Bragg-Beugung erster Ordnung kann bei $2T = 10\,\mathrm{ms}$ eine intrinsische Sensitivität von $\Delta g/g = 3{,}2 \cdot 10^{-6}$ erreicht werden, was nahe dem berechneten Schrotrauschen für 10 000 Atome und einem Kontrast von $C = 0{,}75$ ist. Die Fontänengeometrie erlaubt, das MZI bei einem größeren Kontrast von $C = 0{,}8$ auf $2T = 50\,\mathrm{ms}$ zu verlängern und damit eine intrinsische Sensitivität von $\Delta g/g = 1{,}4 \cdot 10^{-7}$ zu erreichen. Ein wichtiger Baustein ist hierbei die Zustandspräparation durch magnetische Linse und die Reinigung magnetischer Unterzustände, um den Kontrast zu verbessern sowie das Detektionsrauschen zu verringern. Eine Betrachtung von systematischen Unsicherheiten im jetzigen Aufbau und ihre Projektion auf ein zukünftiges Gerät belegen, dass in Zukunft mit der Fontänengeometrie Genauigkeiten von unter einem µGal möglich sind.

Schlagwörter: Bose-Einstein Kondensate, Materiewelleninterferometrie, Gravimetrie

Abstract: Atom-chip Gravimeter with Bose-Einstein condensates

Today's generation of atomic inertial sensors typically operates with laser cooled atoms released or launched from an optical molasses. The velocity distribution and finite size of these sources limit the efficiency of employed beam splitters as well as the analysis of systematic uncertainties. These limits can be overcome by the use of ensembles with a momentum distribution well below the recoil of a photon, such as Bose-Einstein condensates (BEC). The momentum distribution of a BEC can even be narrowed down after reaching the regime of ballistic expansion, where all mean field energy is converted to kinetic energy, by the application of the delta-kick collimation technique. Atom-chip technologies offer the possibility to generate a BEC and perform delta-kick collimation in a fast and reliable away, paving the way for miniaturized atomic devices.

The use of BECs allows for Bragg and double Bragg diffraction at high efficiency. In this thesis, these can be driven with an efficiency of above 95% facilitating to perform interferometry with high contrast C. Furthermore, BECs allow to develop novel methods of coherent manipulation at high fidelity. Based on a combination of double Bragg diffraction and Bloch oscillations a relaunch procedure with more than 75% efficiency in a retro-reflected optical lattice has been implemented. The novelty of this method is, that it relies only on a single laser beam, which is also used for beam splitting and thus does not lead to an increased complexity of the setup. Additionally, with a similar scheme a symmetric scalable large momentum transfer beam splitter of up to $1008\,\hbar k$ is demonstrated. An interferometric contrast with up to a momentum separation inside the atom interferometer of $208\,\hbar k$ can be observed, which is to the best knowledge more than twice the largest momentum separation reported so far.

In this thesis, the first atom-chip gravimeter with Bose-Einstein condensates is realized, which operates in two different modes. The interferometry is either performed using dropped BECs directly after release, or the BECs are accelerated upwards after a certain time of free fall and the interferometry is performed like in a fountain, such that the time $2T$ in the interferometer can be extended. The atom chip is used for generating Bose-Einstein condensates and state preparation, including magnetic sub-state transfer, delta-kick collimation and Stern-Gerlach-type deflection. A special feature of this setup is that the light field, which forms the Mach-Zehnder interferometer (MZI) by Bragg diffraction, is reflected at the atom chip itself. In this way, the chip also serves as an inertial reference inside the vacuum chamber, which allows for the demonstration of a compact atom-chip gravimeter. All atom-optics operations, the interferometry and the detection of the output states of the atom interferometer are integrated into a volume of less than a cube of one centimeter side length marking a substantial downsizing.

In the drop mode, the gravimeter is capable of determining the local gravitational acceleration g with an uncertainty of $\Delta g/g = 1.3 \cdot 10^{-5}$ limited by seismic noise acting on the apparatus. With first-order Bragg diffraction and an interferometry time of $2T = 10\,\mathrm{ms}$ an intrinsic sensitivity of $\Delta g/g = 3.2 \cdot 10^{-6}$ is obtained which is close to the calculated shot-noise limit for 10 000 atoms at an interferometric contrast of $C = 0.75$. In the fountain mode, the MZI can be extended to an interferometry time of $2T = 50\,\mathrm{ms}$ at even larger contrast of $C = 0.8$ which reaches an intrinsic sensitivity $\Delta g/g = 1.4 \cdot 10^{-7}$. The state preparation comprising delta-kick collimation and Stern-Gerlach-type deflection has an important contribution to this achievement by improving the contrast and by reducing the detection noise. An estimation on systematic uncertainties for the current setup and their projection onto a future device proves that it is possible to reach sub-μGal accuracies with a fountain-type geometry in the future.

Keywords: Bose-Einstein condensates, matter wave interferometry, gravimetry

"I may be old, but I'm not obsolete."

— T-800

Acknowledgments - Danksagung

An erster Stelle gilt mein Dank meinem Doktorvater Ernst Rasel, der mir das Durchführen dieser Doktorarbeit überhaupt erst ermöglicht hat und der kontinuierlich Anregungen zum Experiment und zur Physik dahinter gegeben hat. Ich danke allen denjenigen, allen voran Wolfgang Ertmer, dem Sekretariat und der Werkstatt, die ganz wesentlich dafür sorgen, dass am Institut für Quantenoptik alles funktioniert. Mein Dank gebührt außerdem dem DLR, das die QUANTUS-Projekte seit mehr als einem Jahrzehnt finanziell fördert und intensiv begleitet. Ich möchte mich auch bei Carsten Klempt und Kai Bongs für die Übernahme der Gutachten zu meiner Dissertation und Klemens Hammerer für die Übernahme des Prüfungsvorsitzes bedanken.

In den vergangenen Jahren durfte ich mit einer unglaublich großen Zahl von Personen aus dem Institut für Quantenoptik aber auch von außerhalb zusammenarbeiten und von ihnen lernen. Das gilt ganz besonders für Christian Schubert, der mich schon seit meiner Zeit als Student betreut und dessen Ratschläge egal in welchem Bereich sehr wertvoll für meine Arbeit waren.

Begonnen hat meine experimentelle Arbeit am Institut bereits 2009 mit meiner Diplomarbeit am CASI Experiment. Dort habe ich neben Christian auch zusammen mit Thijs Wendrich, Michael Gilowski, Peter Berg und Gunnar Tackmann die erste Zeit meiner Doktorarbeit bestritten und so ziemlich alles gelernt, was man über Atominterferometrie überhaupt wissen kann.

Nach CASI kam für mich der große Schritt zu QUANTUS-1. Zusammen mit Martina Gebbe und Matthias Gersemann sind wir jetzt schon seit einigen Jahren das Team am Experiment. Die gemeinsame Arbeit macht immer sehr viel Spaß und es ist wirklich erstaunlich, was sich aus QUANTUS-1 alles herausholen lässt, das ganz sicher noch lange nicht zum alten Eisen gehört. Übernommen haben wir das Experiment Anfang 2014 von Hauke Müntinga und Holger Ahlers, die uns mit ihrer Erfahrung bis heute sehr helfen und oftmals auch retten können. Neben den Experimentatoren möchte mich bei der Theorie Gruppe um Naceur Gaaloul, allen voran bei Jan-Niclas Siemß, für ihre Hilfe bedanken, unsere Ergebnisse zu verstehen.

Ein wesentlicher Teil der Physik die im Rahmen dieser Arbeit erforscht wurde, insbesondere die Anwendung in der Gravimetrie, ist motiviert durch den Sonderforschungsbereich geo-Q. Es ist großartig zu dieser Forschung beitragen zu können und immer wieder mit den Kollegen aus dem IfE, dem AEI und dem ZARM intensiv über unsere Arbeit zu diskutieren. Am IQ ist das für mich primär das QG-1-Team, Jonas Matthias, Maral Sahelgozin, Waldemar Herr, Nina Grove, Hendrik Heine und Janina Molkenthin, aber auch darüber hinaus, allen voran Dennis Schlippert. Bei Dennis möchte ich mich zudem für seine Tex-Vorlage bedanken, Tikz rockt einfach!

Unseren Kollegen aus Ulm Wolfgang P. Schleich, Enno Giese und Alexander Friedrich danke ich für die hervorragenden Diskussionen zu unserem Experiment und für die Zusammenarbeit an unseren gemeinsamen Publikationen, insbesondere am PRL zum Chipgravimeter.

Zu guter Letzt möchte ich mich bei meiner Familie, meinen Freunden und ganz besonders bei Theresa, der wundervollsten Frau, die ich mir wünschen kann, für ihre Unterstützung bedanken.

Contents

Abbreviations or acronyms used in this thesis are listed here.

AOM - Acousto-optical modulator
ARP - Adiabatic rapid passage
AWG - Arbitrary waveform generator
a.u. - Arbitrary units
BEC - Bose-Einstein condensate
BO - Bloch oscillations
CASI - Cold Atom Sagnac Interferometer
CCD - Charge-coupled device
CODATA - Committee on Data for Science and Technology
CRC - Collaborative research center
DBD - Double Bragg diffraction
DDS - Direct digital synthesizer
DFB - Distributed feedback
DFG - Deutsche Forschungsgemeinschaft
DKC - Delta-kick cooling/collimation
DLR - Deutsche Luft- und Raumfahrtgesellschaft
ECDL - External cavity diode laser
EDFA - Erbium doped fiber amplifier
EEP - Einstein's equivalence principle
EOM - Electro-optic modulator
FPGA - Field-programmable gate array
FWHM - Full width at half maximum
geo-Q - Geodesy with Quantum sensors
IfE - Institut für Erdmessund
IQ - Institut für Quantenoptik
IPT - Ioffe-Pritchard trap
KAKTUS - Kompakte Atomchiptechnologie für den Einsatz unter Schwerelosigkeit
LIGO - Laser Interferometer Gravitational-Wave Observatory
LLR - Lunar-Laser-Ranging
LMT - Large momentum transfer
LUH - Leibniz Universität Hannover
MAIUS - Materiewellen-Interferometer unter Schwerelosigkeit
MTS - Modulation transfer spectroscopy
MOPA - Master-oscillator power-amplifier
MOT - Magneto-optical trap
MZI - Mach-Zehnder interferometer
PBS - Polarizing beam splitter
PCA - Principal component analysis
PDH - Pound-Drever-Hall
PSD - Power spectral density
QUANTUS - Quantensysteme unter Schwerelosigkeit
QG-I - Quantum-Gravimeter-I
RF - Radio frequency
SCI - Symmetrized composite-pulse interferometer
SHG - Second harmonic generation
SI - International System of Units
ToF - Time of flight/free fall
UFF - Universality of free fall
UHV - Ultra-high vacuum
VLBAI - Very long baseline atom interferometer
ZARM - Zentrum für angewandte Raumfahrtechnik

CHAPTER 1

A new generation of quantum sensors

Precision measurements tremendously contribute to our understanding of nature. Both fundamental theories - general relativity as well as quantum mechanics - were founded in the early 20th century and govern today's understanding in physics, each one at its own scale. General relativity [1] describes macroscopic and astronomical scales, whereas quantum mechanics [2, 3] leads to wave nature and quantized energies in microscopic systems. Today's most precise measurements are performed by devices using wave interference experiments. Outstanding examples of such devices are long baseline laser interferometers, as for instance the Laser Interferometer Gravitational Wave Observatory (LIGO), assembled and improved over decades due to large efforts of the gravitational wave community. In September 2015, these efforts ultimately led to the first direct observation of gravitational waves [4] emitted from a binary black hole merger [5]. Each of the two LIGO detectors simultaneously detected a swept differential length variation, the so called strain signal, from 35 to 250 Hz with a peak amplitude of $\Delta L/L = 1.0 \cdot 10^{-21}$. However, massive particles make ideal test samples for measurements of inertial quantities as space and time. Time today is defined in the International System of Units (SI) via the transition frequency between the two hyperfine groundstates of the Cesium atom at 9,191,631,770 Hz. Atomic clocks using optical transitions nowadays achieve fractional instabilities as low as $3 \cdot 10^{-18}$ [6]. Based on similar techniques, interfering matter-waves are used for measurements of inertial effects, making use of a fascinating role-reversal between atom and light. The schematic depicting of an atomic gravimeter in fig. 1.1 illustrates this principle, where pulsed laser light acts as a precise ruler to measure the position of atoms in free fall. Introduced more than two decades ago, the continuous progress allows these light-pulse atom interferometers to compete with conventional sensors on the forefront of the most precise measurement in various fields of applications.

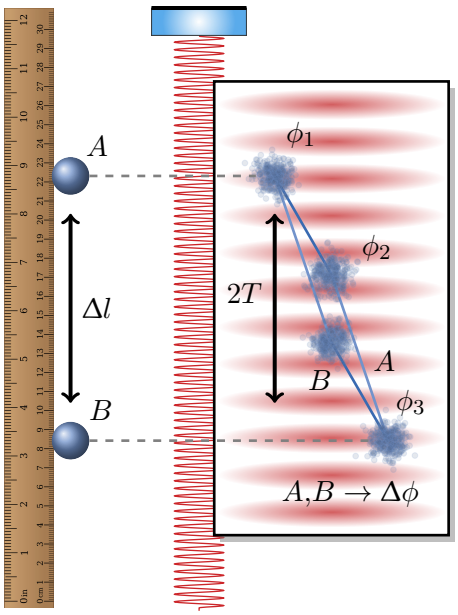

Fig. 1.1: Illustration of the principle how to sense inertial effects using atom interferometry. Laser light acts as a precise ruler to interferometrically read out atomic position in free fall.

1.1 Inertial sensing using cold atom interferometry

Based on the pioneering work done by M. Kasevich and S. Chu starting in 1991 [7, 8], light-pulse atom interferometry using laser cooled atoms has grown to a very successful tool for precise measurements. During the last decades ground breaking experiments have been performed in the fields of inertial sensing and testing fundamental physics. Inertial sensing covers the measurement of the local gravitational acceleration [9–12], rotations as the rotation of the Earth [13–17], as well as gravity gradiometry, by a differential read out of two spatially separated atom interferometers [18, 19]. The scope of testing fundamental physics with atom interferometry comprises on the one hand measurements of fundamental constants like Newton's gravitational constant G [20–23], or the fine-structure constant α [24–27]. A recent determination of α with a measurement of the photon-recoil energy by P. Cladé and colleagues even entered the CODATA definition, currently at a precision of $6.6 \cdot 10^{-10}$ [26], being close to the determination of the electron's magnetic moment [28]. On the other hand postulates are being tested underlying Einstein's principle of equivalence [29] as the universality of free fall (UFF) which is today of particular interest. A simple test of the UFF is to compare the measurement of local gravity with a classical gravimeter and an atomic gravimeter in parallel [9, 30]. More elaborate set-ups tend to use two different quantum objects, as two isotopes of a single atomic species or even two different atomic species, and to measure their free-fall rate within the same device [31–36]. These kind of experiments are expected to catch up to or even overcome today's best classical tests of the UFF using Lunar-Laser-Ranging [37] or torsion balance experiments [38] in the future. Additionally, tests with atoms can also contribute to models in particle physics by the search for unknown forces or dark energy [39–41]. Some more exotic experiments test foundations of quantum mechanics like a delayed-choice experiment [42] or create atomic Einstein-Podolski-Rosen pairs [43, 44].

Especially in the field of absolute gravimetry, atomic sensors compete with classical devices [45]. The established sensors used for geodesy [46] have to be distinguished in absolute gravimeters like the falling-corner cube gravimeters [47, 48] and relative gravimeters like a superconducting gravimeter [49–51], which have a changing bias over time. The current generation of state-of-the-art atomic gravimeters operate with Raman-type beam splitters and laser-cooled atoms, which are either dropped or launched in an optical molasses, a technique introduced in Cesium fountain clocks [52, 53]. Four laboratory grade examples of these gravimeters [12, 54–56] are listed in tab. 1.1, which in part reach inaccuracies in the low µGal regime. These type of devices got for the first time turned into commercial products, which currently measure to 10 µGal [57–59].

Table 1.1: Overview on the current generation cold atomic gravimeters. (* drift rate per year)

Gravimeter	Atomic species	Beam splitter	Release type	Pulse sep. T (ms)	Repetition rate (Hz)	Sensitivity (µGal/$\sqrt{\text{Hz}}$)	Accuracy (µGal)
HUB [55]	^{87}Rb	Raman	Fountain	260	0.7	9.6	3.9
Syrte [56]	^{87}Rb	Raman	Dropped	80	3	5.7	4.3
Wuhan [12]	^{87}Rb	Raman	Fountain	300	1	4.2	-
Onera [54]	^{87}Rb	Raman	Dropped	48	4	42	25
Muquans [58]	^{87}Rb	Raman	Dropped	40	2	50	< 10
AOSense [59]	only official information: 20 Hz repetition rate and autonomous operation for weeks						
FG-5X [47, 48]	falling corner cube gravimeter					15	2
SC [49–51]	superconducting relative gravimeter					< 0.1	$< \pm 5$/yr*

Bragg- and Raman-type interferometers

The coherent manipulation of matter waves is a central element in each matter wave interferometer [60]. Two widely spread methods are based on light-pulses driving Raman [7] and Bragg diffraction [61, 62]. The choice between them implies a few conceptual differences for an atom interferometer that measures inertial effects by the manipulation of external degrees of freedom [63]. Raman diffraction, where an atomic Λ-scheme is driven, requires phase-stable microwave-coupling between two hyperfine ground states of an Alkaline atom usually realized by two phase-locked lasers. Working with two different internal states has an advantageous behavior dealing with wide atomic velocity distributions, namely velocity filtering with blow-away pulses and state-selective detection [11, 64]. These state-labeling features are described in detail by C. Bordé [65]. Bragg diffraction, in contrast, involves only a single atomic ground state and is a pure momentum or recoil beam splitter which usually requires only a single laser system. But, due to the transition frequency in the RF-range, the detection needs to be spatially resolved and it requires a momentum distribution below recoil to distinguish different orders [11, 66].

An interesting aspect connected to the beam splitter, is the possibility to enlarge the momentum transfer during manipulation. Bragg diffraction is in particular noted for the experiments with large momentum transfer, either with direct higher orders [67], sequential transitions [68–70] or a combination with Bloch oscillations [71, 72]. In terms of scalable momentum transfer a Raman beam splitter is limited to transfer only two photons at each pulse due to the intrinsic state change. For specific applications this might be an actual drawback, nevertheless there are still options for large momentum transfer by pulse sequences [73, 74] or combined with Bloch oscillations [75, 76]. For both methods there is a symmetric version, which is not susceptible to laser phase changes [77–80], while Berg et al. [16] show a hybrid Raman-based topology.

Limitations of sensors using molasses cooled atoms by the example of CASI

Almost every state-of-the-art atomic sensor relies on ensembles of Alkali atoms, which are laser cooled and afterwards released or launched from an optical molasses. The Mach-Zehnder or sometimes also Ramsey-Bordé interferometers are routinely formed by the manipulation with

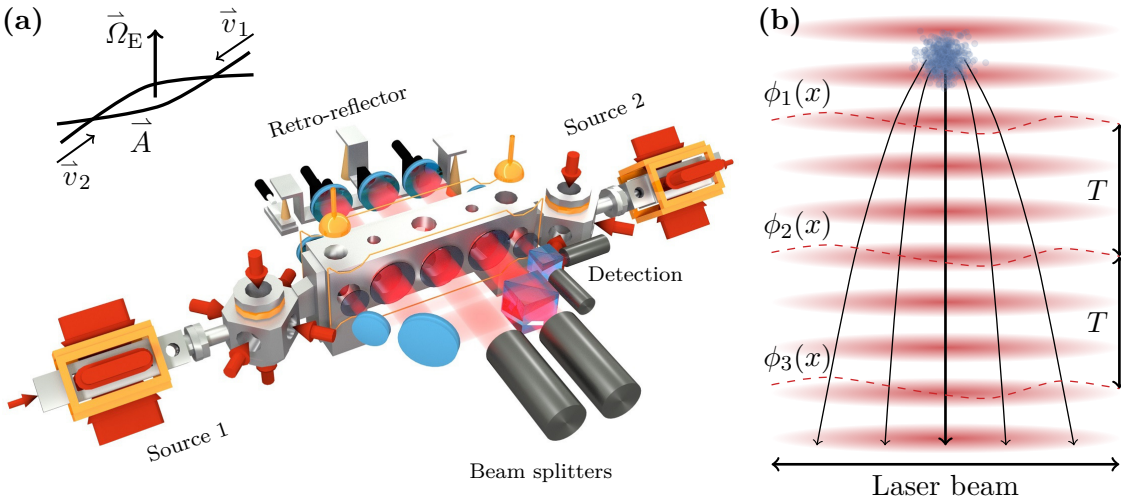

Figure 1.2: Illustration of the Cold Atom Sagnac Interferometer (CASI) experiment for the precise measurement of slow rotations **(a)**. A mayor limitation of the current generation of atom interferometers is arising from wave fronts inhomogeneities coupling to the ensembles' expansion **(b)**.

atom-light-interaction, using mostly pulsed Raman-type beam splitters [7, 8]. The Raman process is often exploited for velocity selection [11, 64], allowing to maintain interferometric contrast C. The contrast is a measure of which fraction of the total atom number can be manipulated by the beam splitter, e.g. contribute useful to the interferometric signal. Two prominent examples for these kind of measurements were recently performed at the Institut für Quantenoptik (IQ). The first one has performed the first dual-species quantum test of Einsteins equivalence principle by simultaneously dropping ensembles of Rubidium-87 and Potassium-39 [35]. Comparing the free-fall rates of both species leads to a proof of the UFF, at a published level of $(0.3 \pm 5.4) \cdot 10^{-7}$.

The second experiment at the IQ was determining the Earth's rotation by the Sagnac effect [81] with molasses cooled ensembles of Rubidium-87 launched from two sources onto opposing trajectories [16]. This Cold Atom Sagnac Interferometer (CASI) called experiment is schematically depicted in fig. 1.2(a). The sensitivity of this device to slow rotations reached $120\,(\mathrm{nrad/s})/\sqrt{\mathrm{Hz}}$ which is today among the best sensitivities reached with cold atomic gyroscopes and could recently only slightly be outperformed by the group of A. Landragin [17]. To reach this sensitivity in CASI a novel interferometer topology, named "symmetrized composite-pulse interferometer" (SCI), has been introduced using a special combination of Raman-type beam splitter pulses with alternating direction of momentum transfer [16]. In that way, attributes similar to double Diffraction [77, 78] are exploited without physically changing the assembly nor losing the ability to vary the output port populations via scanning the relative laser phase. A detailed description of the CASI experiment and an analysis on the noise sources or systematic uncertainties can be found in previous theses [82–85]. The dominant limitations of the experiment are the following:

- The **interferometric contrast** in the SCI can only be held at an acceptable level of $C = 0.19$ (reduced from $C = 0.36$ in a MZI) by exploiting the **velocity selectivity** of the Raman-process [11, 64] in combination with (one or) two **blow away** pulses. These pluses remove atoms and reduce the final detected atom number to some 10^5 atoms. The beam splitter efficiency itself is limited to below 50% after velocity selection, which prevents a useful application of larger momentum transfer beyond the $4\,\hbar k$ of the SCI.
- The **launch in a optical molasses** reaches a stability of a few 10^{-4} in 5 min which is a major source of uncertainty in the ensembles velocity [86]. The stability of the launch velocity is limited by the geometric alignment as well as the laser power stability [87]. Since the molasses launch relies on **spontaneous scattering** of photons rather than a coherent manipulations process, this method does **not pair with BECs** easily.
- Relative **tilts of the wave front** drastically reduces the interferometric contrast which can be regained by a complex alignment procedure presented in ref. [88]. Otherwise a phase gradient over the atomic ensemble averages out the interferometric signal completely due to the **non-spatially resolved detection** process. The uncertainty to align the relative wave fronts between subsequent Raman zones also limits the achievable accuracy [85].
- **Two independent source systems** are used to realize the counter-propagating interferometers and to subtract common noise between the two atomic ensembles in differential operation. Beside adding complexity to the experiment, the molasses launch as well as the detection of the ensembles are still independent. Due to the alignment errors and drifts [87] the **correlation is not as perfect** as expected for a single source.

The limitations of the CASI experiment motivate to have a look into condensed sources of atoms for the use in atom interferometry. The work presented in this thesis is to some degree inspired by these limitations and to find methods to overcome them using Bose-Einstein condensates.

1.2 Advantages of using Bose-Einstein condensates

A central question to be discussed in the frame of this thesis are possible advantages and the future perspective of using quantum degenerate atoms for light-pulse atom interferometry. Bose-Einstein condensation was predicted jointly by A. Einstein and S. N. Bose [89, 90] in 1924, but the experimental validation took till 1995 and was reported by three groups almost at the same time [91–93]. Interference experiments with Bose-Einstein condensates have been performed shortly after first observation, because of their fascinating coherence properties [94–96]. For light-pulse atom interferometry Bose-Einstein condensates were only recently used for inertial sensors [97]. In the past, one refrained from using them mainly because of two reservations:

- A **comparably low flux** of atoms is obtained, if the atom number N of a typical BECs and the time needed for its generation are contrasted with the flux obtained in an optical molasseses. After all, the generation of a BEC remains a rather **lossy and complex process**. The transfer of cold atomic clouds into optical or magnetic traps has a limited transfer efficiency and the evaporation itself relies on reducing atom numbers.
- A high atomic density in a Bose-Einstein condensate causes **atomic interactions** resulting in the so called **mean field shift**, a bias shift in the interferometer. Furthermore this potential energy converts to kinetic energy under free expansion and results in a **broadened velocity distribution** after a short time, even if the BEC was created extremely cold.

But, in return BECs offer several advantages and interesting perspectives:

- A **high fidelity** of employed **manipulation** methods, such as **Bragg diffraction or Bloch oscillations**, is possible with BECs, if the mean-field energy can be reduced. For a Mach-Zender interferometer this allows for a **contrast approaching unity** and in that way catching up in the atom number which contribute to the signal to velocity filtered sources. The possibility to drive **large momentum transfer** increasing the interferometer's scaling factor even promises to overcome the sensitivity of previous atom interferometers.
- The accurate determination of an inertial value needs a **precise knowledge and control** over the initial conditions of the test sample. In a gravimeter configuration the Coriolis effect and gravity gradients couple in via **initial velocity and position**. The influence of **wave front** distortion and curvature arising from expansion during free fall is greatly reduced due to the **small extend and slow expansion** of typical condensates. In fact, these bias shifts are the **major sources of systematic uncertainties** for gravimeters using molasses cooled atoms and can be sufficiently suppressed using colder atoms.
- A need for Bose-Einstein condensates lies in **accessing spatial features** of an atomic ensemble, because of their **unique point-like nature** [98]. Interferometry with point sources allows for a new method to deduce variables and to obtain more information in a single cycle over the **phase shear across an ensemble** [98–100]. A spatially resolved readout of the interferometer's output ports is always applied in the presented experiments and the spatial distribution is used for evaluation.
- The shot noise represents a limit to the sensitivity of an atom interferometer at a given atom number N. To overcome this limit without increasing N, BECs offer a **perspective towards squeezing**. There are remarkable examples for non-degenerate squeezed sources [101, 102], but a large fraction of methods to generate correlations [103–105] and demonstrate atom interferometers [106–109] rely on BECs. For **preserving non-classical correlations** during the interferometry a high efficiency in the manipulation is mandatory.

QUANTUS-1 as a testbed for atom interferometry with Bose-Einstein condensates

In the past, the increased complexity of the experiments and the additional effort to condense atoms has detained the interferometry community to use them for precision measurements. When technology and experiments advanced, this situation changed and the generation of a Bose-Einstein condensate is no longer an insuperable barrier. In this thesis, the QUANTUS-1 experiment is employed to have access to their reliable generation. The device routinely provides $1.5 \cdot 10^4$ condensed atoms of Rubidium-87 every 15 s [110] which to a large extent is used for MOT-loading. The evaporation itself only takes less than 1.5 s. Atom-chip technologies grant access to robust trapping and fast evaporation providing steep magnetic traps in vacuum close to the atoms and fast switching times. Pioneering atom-chip experiments generating ultracold atoms have been performed more than a decade in the past [111–113]. Today, atom-chip setups are robust and reliable tools for fast condensate generation [114–117] and even commercially available [118]. The current generation QUANTUS-2 generates 10^5 condensed atoms each second [117] competing with all-optical approaches [119–122]. Condensates up to several 10^6 atoms can be generated in macroscopic magnetic traps or dipole traps, but the condensation is fairly slow and takes up to minutes [99, 123, 124]. The atom chip in QUANTUS-1 shown on a photograph in fig. 1.3(a) not only allows to generate the condensates, moreover it provides control over the release conditions, and to perform a state preparation after release. This makes QUANTUS-1 an ideal testbed for interferometry with Bose-Einstein condensates [80, 98, 110].

The main argument always brought forward against the use of Bose-Einstein condensates in atom interferometry is that the occurrence of atomic interactions due to a large atomic density in the condensate causes effects like frequency shifts or phase diffusion [125–127]. There are two options to relax density dependent effects. The first and obvious way is the relaxation of mean field effects after a certain time of free expansion [97, 128, 129]. But an additional waiting time, especially for condensate temperatures in the low nanokelvin region, elongates the free-fall time and therefore the baseline needed for an experiment. However, the broadening of the momentum distribution due to the conversion of mean field energy can not be counteracted and might lead to substantial larger expansion rates and reduced beam splitter fidelities. Both drawbacks can be circumvented by the application of a technique often called delta-kick cooling or matter wave lensing [130–132]. Hereby, a position dependent force generated by a harmonic potential and applied after a given expansion period for appropriate time slows down the expansion of the atoms and ideally collimates it, analogous to a lens in optics. In that way a larger initial expansion for a short time leads to an adjustable cloud size tailored to the needed atomic density, while the final expansion during the experiment is rather small as illustrated in fig. 1.3(c). However, this effect is no “cooling”, in the sense that the phase space density is increased by this process, but rather a “collimation” of the atomic motion. Delta-kick collimation can be performed by optical potentials of a dipole trap [133] or as in the case of QUANTUS-1 the magnetic potential provided by the chip [98] which can be switched on and off in a very fast manner.

With the QUANTUS-1 apparatus previous experiments in the droptower in Bremen have been performed exploiting the point-like behavior of a delta-kick collimated Bose-Einstein condensate in free fall [98]. An asymmetric Mach-Zehnder interferometer is formed by Bragg diffraction, which can be seen as a giant double-slit experiment [134]. The delta-kick collimation allows to observe the condensates even after free-fall times beyond a second. The interferometer scheme and a density depiction of its output ports are displayed in fig. 1.3(b). Due to the asymmetry in the interferometer a phase gradient causes a fringe pattern to appear across the interferometer output ports, from which contrast and orientation can be extracted from a single experiment.

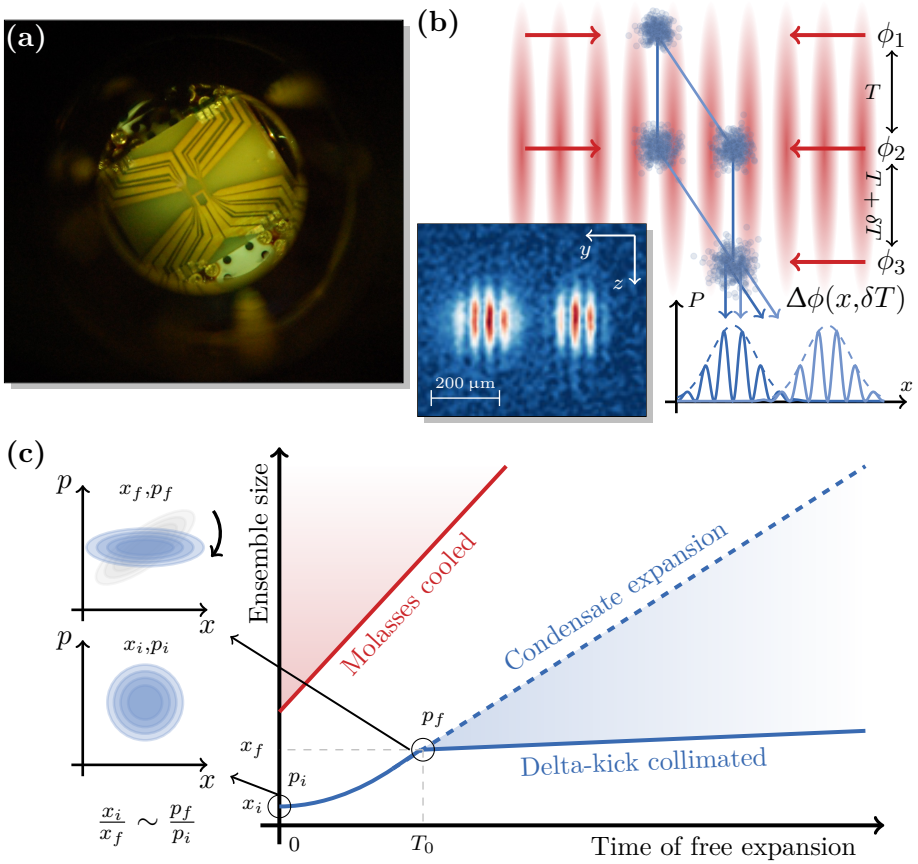

Figure 1.3: Previous work with Bose-Einstein condensates done at the QUANTUS-1 experiment. Photograph of the QUANTUS-1 atom chip inside the vacuum chamber **(a)**. An asymmetric Mach-Zehnder interferometer with a condensate in free fall simulates a giant double-slit experiment [98] **(b)**. A schematic illustration of delta-kick collimation, to slow down the atomic ensembles expansion **(c)**.

Towards compact absolute atomic gravimeters with Bose-Einstein condensates

Major work is ongoing to improve the current generation of atomic gravimeters in terms of accuracy but also miniaturization. The use of a Bose-Einstein condensate as a source for an atomic gravimeter is a promising approach for the future. Absolute gravimetry is a primary field of application suitable for atom interferometers as already the current generation of laboratory grade devices almost matches the needs of geodesists. The primary goal in terms of performance is to reach accuracies below 1 µGal in a modest integration time of around 100 s, because this is the region relevant for terrestrial geodetic Earth observation and would significantly outperform classical absolute gravimeters [135–137]. The accepted approach to overcome current systematic uncertainties and to reach this goal is the use of colder and smaller atomic ensembles due to their reduced susceptibility to wave front errors and residual initial motion [88, 138]. Another interesting topic is, to find solutions to shrink these sensors further down in size. In this respect, the use of Bose-Einstein condensates and atom chips provide a valuable contribution. Geodetic field applications rely on robustness and transportability, two strong arguments in favor of an atom-chip setup. Miniaturization and at the same time decreased complexity definitely open up other applications, as for example to locate resources or autonomous inertial navigation.

1.3 Scope and organization of this thesis

The presented work focuses on the investigation of novel methods for the coherent manipulation of Bose-Einstein condensates with laser light and the development of compact schemes for atom interferometry relying on an atom-chip-based source. For this purpose, the prototype of an atom-chip gravimeter is implemented in the QUANTUS-1 apparatus and a variety of atom interferometry experiments are performed with the setup using these novel methods. The results of these experiments are analyzed from a scientific perspective and the relevance for future experiments is highlighted. A diagram of the organization of this thesis is shown in fig. 1.4.

The key to miniaturize quantum gravimeters is to shorten the atom interferometer's baseline, i.e. the distance the atoms fall from their origin, by new methods and measurement schemes. A number of experiments already demonstrated compact measurement schemes, but up to now without ever exceeding the proof-of-principle status nor showing a complete miniaturization of all necessary steps in the device. Atom interferometry with magnetically trapped [139, 140] and guided [141] atoms has been demonstrated and successfully employed as magnetometers [108]. Optically guided atom interferometers measuring acceleration along the guiding axis [72, 142] combined Bragg beam splitters with Bloch oscillations to achieve faster scaling [143]. But, these were not yet employed as gravimeters. Atoms trapped in optical lattices, that target for measuring short range forces [144, 145] determined the Bloch frequency of the tilted lattice as a measure for gravity [146, 147]. An optical lattice as guide and beam splitter has been proposed [148] and the relaunch using Bloch oscillations has been used with a Ramsey-Bordé geometry [149, 150]. The disadvantage of the Ramsey-Bordé geometry is the scaling behavior proportional to T rather than T^2 which is similar to a suspension in a standing wave [151]. Up to now it is not sufficiently analyzed how the guiding or reflection process itself will disturb the measurement at high accuracies. Additional systematic uncertainties and a dephasing of the interferometric signal will arise from light shifts [138, 152], the interaction between guide and atoms as well as from scattering processes between atoms within the guide [145, 153–155]. As long as these effects can not successfully be overcome, interferometry with undisturbed free-falling condensates remains a more promising choice to reach the target of an uncertainty below 1 µGal.

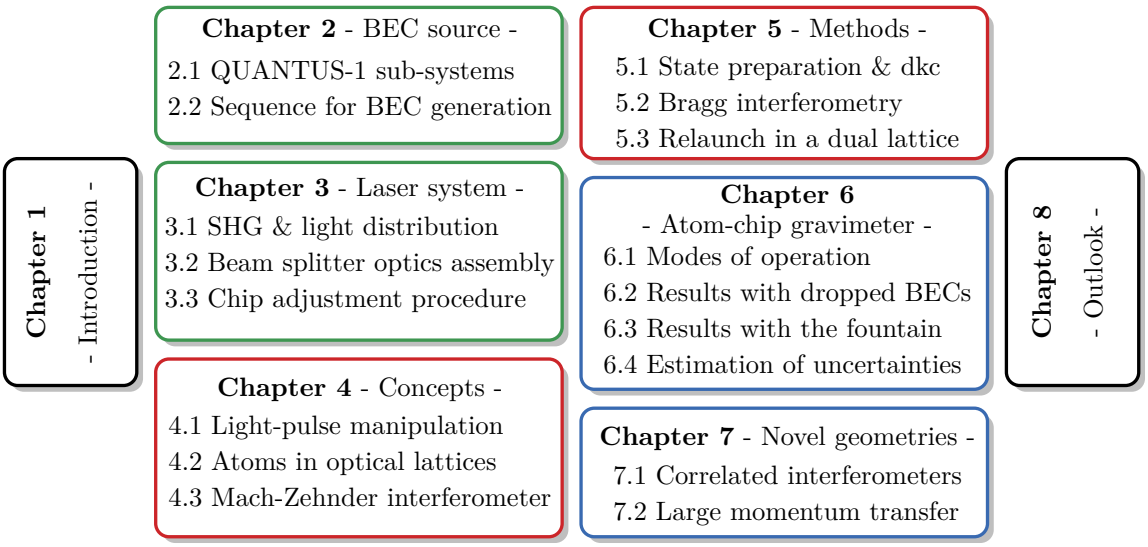

Figure 1.4: A diagram of the organization of this thesis. The main content is divided into experimental **realization** —, **concepts** and **methods** — and **interferometry** —.

Realizing the first atom-chip gravimeter and novel interferometer geometries

Within the scope of this thesis, a novel route to miniaturized quantum senors is opened and the prototype of an atom-chip gravimeter implemented in the QUANTUS-1 apparatus is demonstrated. The prototype relies on Bose-Einstein condensates generated by an atom chip as a source and Bragg diffraction as beam splitters, forming Mach-Zehnder interferometers. The specifics of this combination together with delta-kick collimation and spatial readout, both techniques well established at the QUANTUS-1 experiment, have been published in ref. [156] and are highlighted throughout this thesis. Due to the characteristics of the condensed sources of atoms which are used, especially in combination with delta-kick collimation, the Bragg and double Bragg diffraction realized in this thesis are driven with a high fidelity above 95%. Furthermore, the use of Bose-Einstein condensates allows to develop novel methods of coherent manipulation based on Bloch oscillations in a dual-lattice configuration combined with double Bragg diffraction.

A specialty of the implementation of the atom-chip gravimeter is that the light field for generating the interferometer is reflected at the atom-chip surface. In this way, the chip serves as inertial reference inside vacuum. Moreover, with the atom chip all atom-optics operations can be performed, including source generation, state preparation, the interferometry itself and the final detection of the interferometer output states in a cube of less than 1 cm side length. The atom-chip gravimeter is operated in two different modes. The interferometry in the first mode, which is kept on a basic level, is performed using Bose-Einstein condensates simply dropped from the magnetic trap generated by the atom chip. In addition, a fountain geometry is employed, which overcomes the limitations of using dropped Bose-Einstein condensates by the implementation of a relaunch. The relaunch redirects the trajectory of a condensate upwards after a certain time of initial free fall by a newly developed method based on a retro-reflected optical lattice. The interferometry in this mode is performed after the relaunch with atoms still under free fall and nearly undisturbed by the relaunch but on a parabolic trajectory. The novelty of this relaunch method is that it relies only on a single laser beam which is also used for generating the interferometer and thus does not increase the complexity of the setup. Given the fact that this setup employs a retro-reflective or dual-lattice configuration, the relaunch cannot be performed by a simple acceleration via Bloch oscillation but in combination with double Bragg diffraction. The current limitation of this method is given by a momentum broadening during the relaunch caused by the insufficient surface quality of the atom chip. The fountain mode in total provides a three times larger observation time compared to a single drop. The additional time is primarily used for extending the pulse separation time T inside the interferometer to increase its intrinsic sensitivity, but it also allows for additional state preparation steps beforehand, namely delta-kick collimation and magnetic state purification, to reduce systematic uncertainties and to improve the interferometric contrast. In a nutshell, with the fountain geometry an atomic gravimeter with enlarged scaling factor is demonstrated, while keeping the volume in which every atom-optics operation is performed as compact and close to the atom chip as possible.

Based on the experimental methods developed for the atom-chip gravimeter, several novel interferometer geometries are investigated in this thesis. The important addition is to include a horizontal dual lattice for driving double Bragg diffraction. This allows on the one hand configurations based on two correlated Mach-Zehnder interferometers. Both are fed by a single condensate, which is initially split such that the ports of the two interferometers move with a relative velocity either in horizontal or vertical direction. On the other hand, a novel symmetric scalable interferometer using large momentum transfer is developed with the combination of double Bragg diffraction and Bloch oscillations in a dual-lattice configuration.

This work in the framework of QUANTUS and geo-Q

Quantum technology is at present actively discussed in the European context [157, 158]. Atom interferometry with Bose-Einstein condensates used for inertial sensing on Earth as well as for fundamental science in space is a particular active field of research. The work presented in this thesis is embedded in the framework of two research collaborations - **QUANTUS and geo-Q**.

The research collaboration named **QUANTensysteme Unter Schwerelosigkeit** under the supervision of the Deutsche Luft und Raumfahrtgesellschaft (DLR) was founded in 2004 to perform research exploring degenerate quantum gases and atom interferometry under conditions of microgravity. The participating organizations in this collaboration are, beside the Institut für Quantenoptik in Hannover: the Zentrum für angewandte Raumfahrtechnik (ZARM) in Bremen, the Universität Ulm, the Technische Universität Darmstadt, the Humbolt Universität zu Berlin, the Gutenberg Universität Mainz and formerly the Universität Hamburg. The QUANTUS-1 apparatus was originally designed for being dropped at the 110 m high drop-tower located at the ZARM in Bremen and shown in fig. 1.5. It is the first generation apparatus realized within this collaboration and was dropped more than 400 times. Although none of the presented experiments in this thesis were actually performed in a microgravity environment, this work would have not been possible without all the former developments done within this collaboration and the different projects. The recent highlight of this research is the successful launch of the MAIUS-1 sounding rocket [159–161] in January 2017 achieving the first Bose-Einstein condensates in space [162].

Figure 1.5: The droptower at the ZARM in Bremen. The photograph shows the hole ZARM from the outside (left) as well as the inner basement (right). (pictures by H. Müntinga and H. Ahlers)

The collaborative research center **Relativistic Geodesy and Gravimetry with Quantum Sensors** (SFB 1128) [163] was started in 2014 between Hannover, Braunschweig and Bremen with the aim to perform research on the determination of the Earth's gravitational field and to monitor global and regional mass distribution. Within this center, novel sensors for quantum metrology and relativistic geodesy will be developed, as well as geodetic modeling will be advanced to interpret processes of global and regional change. The IQ is primarily taking part in these activities with the development of two next generation atomic gravimeters presented in chp. 8. Especially, the next generation mobile gravimeter QG-1 will profit greatly from the research on atom-chip-based quantum gravimetry with Bose-Einstein condensates presented in this thesis.

CHAPTER 2

Atom-chip-based source of ultracold atoms

The QUANTUS-1 experiment has been designed to study methods for the generation and manipulation of Bose-Einstein condensates during extended free fall in microgravity environments [110] and realized atom interferometry in the drop tower with at that time unrivaled pulse separation times [98]. The apparatus offers a compact and robust way to generate Bose-Einstein condensates as well as to employ delta-kick collimation with the use of the atom chip allowing for ultra-slow expansion rates corresponding to temperature equivalents of few nK [164, 165]. With these capabilities QUANTUS-1 serves as an ideal test-bed for atom interferometry, allowing e.g. to implement double Bragg diffraction as a novel symmetric beam splitter [80]. The photograph in fig. 2.1 shows the complete drop capsule as it was dropped in the drop tower more than 400 times.

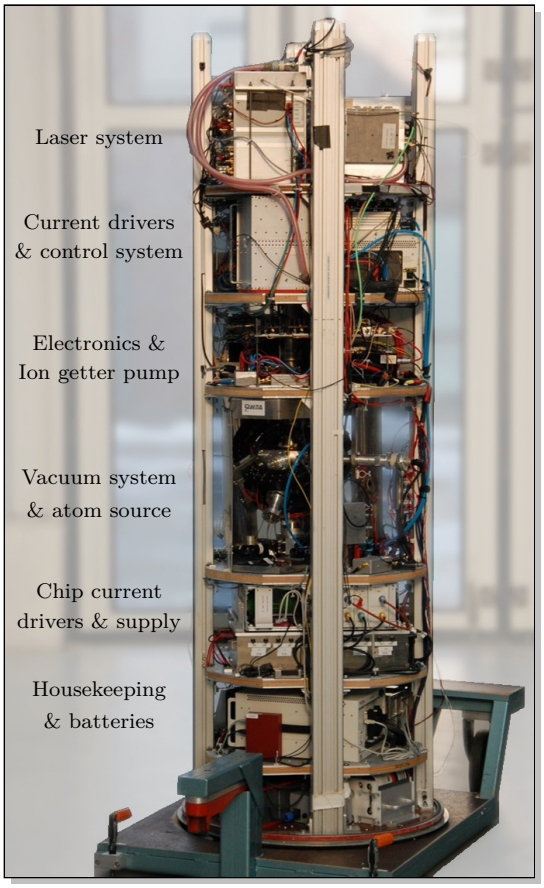

Fig. 2.1: Photograph of the QUANTUS-1 drop capsule with labeled section in front of the laboratory at ZARM. (picture by H. Müntinga)

In the course of this chapter there will be only a brief overview on the components (sec. 2.1) of the experiment and a recall of the sequence performed to generate Bose-Einstein condensates with the machine (sec. 2.2) presented, since this was described a few times already [164–166]. Introductions to the basics of trapping and cooling of neutral atoms can be found in literature [167] and the realization of Bose-Einstein condensation was described in great detail in refs. [168–170]. The QUANTUS-1 device has its strength in the satisfactory level of previously performed characterization and reliability of the setup. It allows to generate Bose-Einstein condensates of up to $1.5 \cdot 10^4$ ^{87}Rb atoms with a cycle time of roughly 15 s, mainly limited by slow loading of the magneto-optical trap (MOT) from background vapor. After release, the atom chip allows to apply delta-kick collimation and to prepare the atoms in a non-magnetic state (sec. 5.1).

2.1 Subsystems of the QUANTUS-1 experiment

The central element of the source system of the QUANTUS-1 experiment is clearly the atom chip used for the generation of Bose-Einstein condensates. This chip consists of planar wire structures down to 50 µm width to generate magnetic fields for trapping and cooling of atomic ensembles. This section focuses on special aspects of the QUANTUS-1 apparatus and gives a brief overview on the provided sub-systems needed to perform the experiments. A more detailed description on the devices and generation of Bose-Einstein condensates as well as on experiments previously performed in microgravity can be found in a number of previous theses [164–166]. Due to the design for the droptower operation, the QUANTUS-1 experiment offers some beneficial features:

- The whole device is by design **robust** against mechanical **shock** and **temperature** changes.
- Each component is to some extend **miniaturized** to fit into a single drop capsule.
- Each component was optimized regarding **low mass and power consumption**, since during droptower operation for a certain time the device needs to be powered by batteries.
- Every experimental step is **remote controllable** and read out via computer systems.

2.1.1 Vacuum system and atom chip

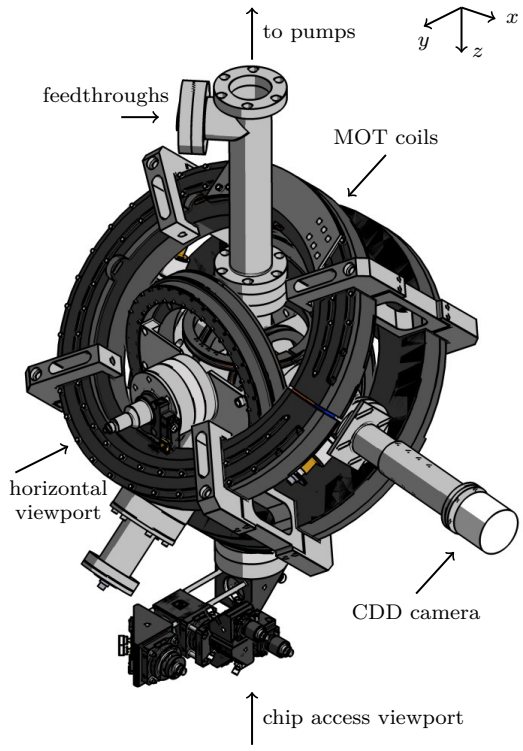

Fig. 2.2: The vacuum system is composed of commercial CF components and optical access is granted via anti-reflection coated viewports. The science chamber is a single cross with two additional 45° ports for retro-reflected MOT beams. Coil housings for the generation of MOT and bias magnetic fields are visible in black.

The ultra-high vacuum (UHV) system is made of non-magnetic stainless steel components based on copper seals (CF type). CF vacuum components are commercially available, robust against mechanical shock and grant a UHV-grade vacuum quality. The single science chamber in the center of the system consists of a cross with eight tubes which are closed by anti-reflection coated viewports. The atom chip is mounted on a copper mount and integrated from the upper tube of the cross. The pressure inside the vacuum is held below 10^{-11} mbar with an ion getter pump (PID25, MECA2000, 25 L/S) and a passive getter (SAES Getters) mounted in a section above the atom chip. The Rubidium is disposed from alkali metal dispensers (SEAS Getters) integrated in the lower tube and controlled by the amount of current fed through the wire shaped dispensers. This is a compromise between condensate lifetime of 3 s and loading rate of the MOT limiting the cycle time to 15 s. A CAD drawing of the chamber assembly is depicted in fig. 2.2 with the upper pump and valve section missing. Around the science chamber there are in total four pairs of coils mounted spaced in Helmholtz configuration. Only the biggest pair of them which is used for the MOT magnetic field is water-cooled because of its high power consumption and heat dissipation. The other three pairs are oriented pairwise orthogonal and used to generate magnetic bias fields during the experiment.

The functionality of an atom chip can be illustrated with a simple current carrying wire, the straight conductor which is mounted on a two-dimensional plane, the surface of the atom chip. For geometric reasons it is clear, that a trap for atoms can only be generated shifted away from surface with an offset field B_{bias}. The magnetic field B of a straight conducting wire carrying a current I and its derivatives B', B'' are at a distance z perpendicular to the surface

$$B(z) = \frac{\mu_0}{2\pi} \cdot \frac{I}{z} - B_{\text{bias}},\ B'(z) = \frac{\mu_0}{2\pi} \cdot \frac{I}{z^2} \text{ and } B''(z) = \frac{\mu_0}{2\pi} \cdot \frac{I}{z^3} \tag{2.1}$$

with an offset field B_{bias} and zero magnetic field line ($B(z_0) = 0$) at a distance

$$z_0 = \frac{\mu_0}{2\pi} \cdot \frac{I}{B_{\text{bias}}}. \tag{2.2}$$

This configuration alone provides two-dimensional trapping along the wire, that can be used as a wave guide. The offset field B_{bias} which is needed to shift the zero magnetic field line out of the wire, is in the case of the atom chip generated by one of the external coil pairs, aligned in the plane of the chip. The two other coil pairs K1 and K2 are aligned perpendicular to the first pair.

By bending a straight conductor in the two-dimensional plane of the atom chip three-dimensional trapping potentials are created, the most common are the U-type and the Z-type which are implemented on the atom chip displayed in fig. 2.3(a). The two bend wires to form the U-type cancel each other out and this type generates a three-dimensional quadrupole trap as needed for a MOT. The Z-type bending is used to generate a so called Ioffe-Pritchard-trap.

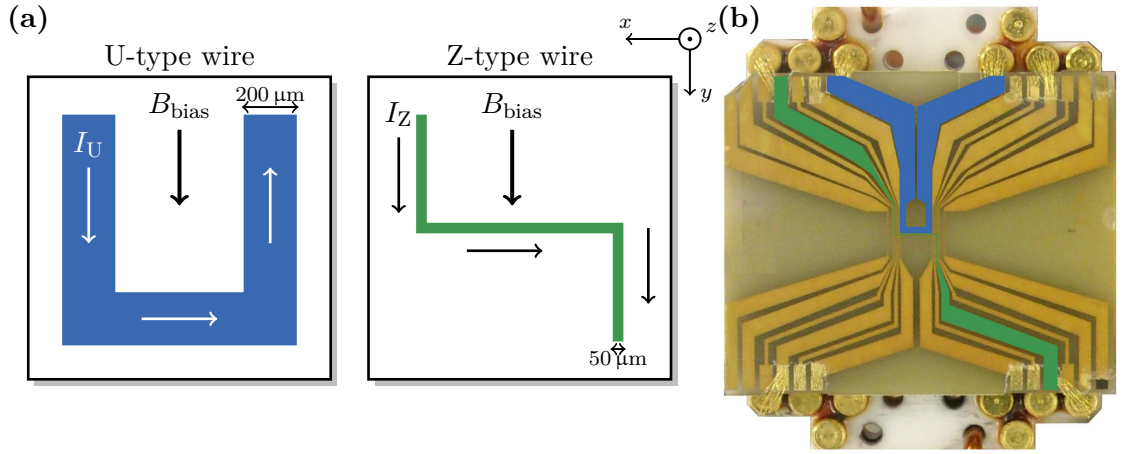

Figure 2.3: The magnetic field is generated by U- and Z-wires with an external offset field B_{bias} **(a)**. Surface of the atom chip in the QUANTUS-1 experiment with U- and Z-wire highlighted **(b)**.

The atom chip which is employed in the QUANTUS-1 experiment is displayed in fig. 2.3(b) with the U- and Z-wire highlighted on its surface. To dissipate the heat caused by the electric currents and to connect the structures on the chip to electrical feed-throughs on the vacuum chamber, it is mounted on a block of copper attached to a CF-flange. The speed to evaporate atoms in a magnetic trap highly depends on the trap frequencies in the generated potential, because these are anti-proportional to the time needed for rethermalization after cutting out the hottest fraction with an RF-knife. In the case of this atom chip, trapping frequencies of up to 8 kHz can be generated allowing to evaporate a cloud of atom in below 1.5 s to quantum degeneracy which is fast compared to magnetic traps relying on macroscopic coil.

2.1.2 Laser system, light distribution and stabilization

For trapping, cooling and basic manipulation of the atoms, distributed feedback (DFB) diode based laser systems are integrated into the drop capsule and are placed on its top level to enable access for alignment. These DFB laser diodes offer an acceptable linewidth of about 3 MHz but require no external resonator making them quite robust to mechanical stress on the experiment. The laser system is composed of four modules based on customized optics holders at 2 cm beam height, designed for high stability, while remaining adjustable. These modules are interconnected by polarization maintaining optical fibers (e.g. Suk PMC-850-5,1-NA13-3-APC-400-P), that are also used to interface the vacuum system. The complete laser system consists of two DFB diodes and two amplified DFB diode lasers described in refs. [166, 171]. All DFB laser diodes are of the same type Eagleyard, EYPDFB-0780-00080-1500-TOC03-0000. Figure 2.4(a) gives an overview on the laser frequencies used in the experiment and fig. 2.4(b) shows photographs of two exemplary laser modules. These laser modules are:

- A DFB **reference** laser diode is stabilized with a modulation transfer spectroscopy [172] 40 MHz below the $|5S_{1/2},F=3\rangle \rightarrow |5P_{3/2},F'=4\rangle$ transition of ^{85}Rb.
- The DFB **repumping** laser diode is of the same type and 10 mW of laser light behind the optical fiber is emitted resonant to the $|5S_{1/2},F=1\rangle \rightarrow |5P_{3/2},F'=2\rangle$ transition of ^{87}Rb.
- For laser **cooling** a larger power is needed, than is provided by a single DFB diode. For this purpose another DFB laser diode is amplified in a tapered amplifier (Eagleyard, EYP-TPL-0780-01000-3006-CMT03-0000) and about 125 mW coupled into an optical fiber. A beat offset lock stabilizes the cooling laser at the frequency $2-3\Gamma$ red-detuned to the $|5S_{1/2},F=2\rangle \rightarrow |5P_{3/2},F'=3\rangle$ transition of ^{87}Rb.
- The integrated laser used to drive first-order **Bragg or double Bragg diffraction** is a micro-integrated diode based Master-Oscillator Power-Amplifier (MOPA) build by the Ferdinand-Braun Institut für Höchstfrequenztechnik (FBH) and provides up to 150 mW of power behind an optical fiber output [173]. Its frequency is locked to the cooling laser with an offset of $\Delta = 0.5$ GHz by a beat measurement. The module to generate and distribute the beam splitting frequencies is described in detail in ref. [171].

Distribution of the laser light and frequency stabilization

The distribution module divides the light from the cooling and repumping laser onto fibers guided to the vacuum chamber and contains the frequency stabilization. The frequency of the cooling and repumping laser is stabilized to the reference laser by beat offset locking with fast photo diodes (Hamamatsu, G4176-03) according to the locking scheme in fig. 2.4(a). While the lock of the repumping laser is static in frequency during the experiment, the cooling laser can be dynamically detuned with a phase-frequency detector (Hittite Microwave Corporation, HMC440QS16G, $10-1200$ MHz) and a synthesizer (AA-Opto-Electronics, DDSPA, $10-350$ MHz). The shifting and switching of the cooling and repumping light is performed with acousto-optical modulators (AOM, Crystal Technology, 3080-125) driven by voltage-controlled oscillators. Remaining stray light is blocked by mechanical shutters in front of the fibers. Four fibers guide each $10-12$ mW of power for cooling and 0.8 mW of power for repumping to the science chamber. The outputs of the fibers are collimated to a diameter of $\oslash = 21$ mm. Two of the laser beams for the MOT are retro-reflected at the atom-chip surface with an angle of 45°. An additional fiber with few 100 µW of only cooling light which is individually controlled by an AOM is guided to the detection axis.

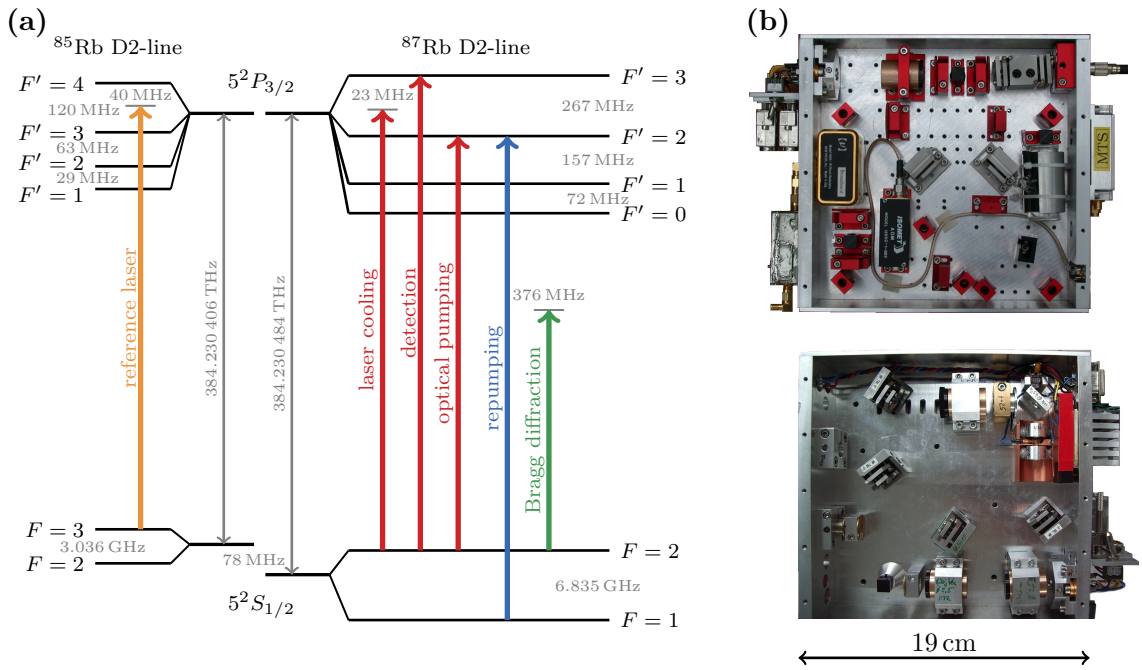

Figure 2.4: Scheme of laser wavelengths used in the QUANTUS-1 experiment **(a)**. Two of the laser modules **(b)** for the modulation transfer spectroscopy (top) and laser cooling (bottom).

2.1.3 Computer control, current drivers and detection

The computer control integrated into the drop capsule guaranties a mostly autonomous operation of the experiment. However at the start the laser system still needs to be manually switched on and the diode temperatures as well as currents are adjusted by hand.

- In total three **computer systems** are integrated into the drop capsule. These are two commercial LabView real time based PXI-systems (National Instruments, PXI-1000B) for multipurpose and a Linux based PC exclusively controlling a PulseBlasterDDS-II via USB. This DDS generates the frequencies and amplitudes to drive the AOMs for Bragg and double Bragg diffraction. The experimental sequence is timed by two PXI-cards (PXI-6259, PXI-6723) with digital trigger-lines, analog in- and outputs unchanged to ref. [166]. The communication between the integrated computers and three Windows computers in the laboratory is realized by Ethernet.
- The **laser locks** are controlled via analog outputs, while the supply electronics are self-built laboratory-grade electronics. Two additional PXI-cards are used to generate the **radio frequencies** for evaporation (PXI-5406) and magnetic sub-state transfer (PXI-5422). All **miscellaneous electronics** used to drive the AOMs or to control the laser locks as RF-switches, amplifiers and bias-tees are mostly components made by Mini Circuits.
- The **current drivers**, that drive the **chip structures** as well as the **bias coils** are of the type High Finesse, BCSP7. These drivers are powered by individual batteries (Hawker Energy, Cyclon Series) and stand out by a very low output noise figure. All other devices integrated in the drop tower are supplied by 28 V batteries on the lowest platform converted by DCDC-converters. In laboratory operation all batteries are constantly connected to power supplies and act as buffers to maintain low current noise.

Spatially resolved absorption detection

The imaging system as depicted in fig. 2.5 is oriented along the x-axis of the atom chip, so that absorption pictures of the condensates are taken in the $y-z$-plane. The circular polarized light beam is tuned to the $|F=2\rangle \rightarrow |F'=3\rangle$ transition of ^{87}Rb collimated with a telescope to a diameter of $\oslash = 20\,\mathrm{mm}$. Typically the laser beam as an intensity of $I_{\mathrm{det}} = 0.3 - 0.5\,\mathrm{mW/cm^2}$ corresponding to 0.2 of the saturation intensity I_{sat}. A 12 bit charge-coupled-device (CCD) camera of the type HAMAMATSU, C8484-15G† collects the transmitted light with an aspheric lens (LINOS G322307525, $f = 80\,\mathrm{mm}$) at the opposite side of the vacuum chamber. Absorption detection is a common method for the detection of dense atomic samples [169] and the atom number N is obtained by reconstructing the density distribution from the absorption profile

$$N = \frac{1}{\sigma}\int D(y,z)\,\mathrm{d}y\,\mathrm{d}z \text{ with } D(y,z) = \ln\left[\frac{I_{\mathrm{beam}} - I_{\mathrm{dark}}}{I_{\mathrm{atom}} - I_{\mathrm{dark}}}\right] = \int n(x,y,z)\,\mathrm{d}x, \tag{2.3}$$

with the interaction cross section $\sigma = \sigma_0/(1 + I_{\mathrm{det}}/I_{\mathrm{sat}} + 4\delta^4/\Gamma^2)$, derived from the resonant cross section σ_0 [174]. Herby, each detection sequence comprises an image I_{atom} of the condensate as well as an image I_{beam} of the background taken 130 ms later to subtract the detection beam profile. Once per day a dark image I_{dark} is taken to subtract additional noise from the camera.

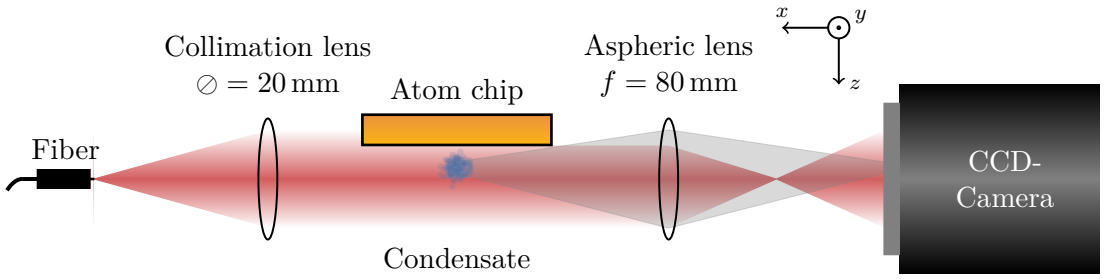

Figure 2.5: Setup of the spatially resolved absorption detection in QUANTUS-1.

The absorption detection is used to detect either a series of time of flight images to examine properties of the produced condensates, as size $\sigma_{z,y}$ and atom number N or to detect the output ports of the atom interferometer. On the one hand, the extraction of absolute atom numbers and sizes is always inflicted with an error due to the calibration of factors as the pixel-size, magnification and signal to density conversion. Those errors are typically on the few percent level. On the other hand, since the output ports $|p_0\rangle$ and $|p_n\rangle$ of the atom interferometer are recorded simultaneously, only the ability to extract a relative population P between two areas in a single picture is of importance. At a sum of $N = 10\,000$ atoms this difference needs to be measured to better than $1/\sqrt{N} = 1\%$ equivalent to a phase uncertainty of below $\sigma_{\Delta\phi} < 10\,\mathrm{mrad}$. Otherwise the detection noise would contribute to more than the quantum projection noise σ_{qpn} itself and would limit the interferometer readout. This simultaneous detection of both ports suppresses to a large extend common noise contributions and it is experimentally proven in sec. 6.2.1, that the detection does not limit the interferometer's performance in appropriate operation.

† Which did its duty righteously for a long, long period during this and every precedent thesis at the QUANTUS-1 experiment, but got replaced very recently by a GRASSHOPPER GS3-U3-15S5M-C. However, the optics remained unchanged and its performance is comparable, beside slightly different calibration factors.

2.2 Sequence for the generation of Bose-Einstein condensates

The principle of laser cooling of neutral atoms is following the pioneering experiments [175, 176] that has led to the discovery of the magneto-optical trap (MOT) [177–179]. A MOT is limited by the Doppler effect, until advanced methods have been introduced to reach sub-Doppler temperatures [180, 181] ultimately rewarded with the Nobel prize in 1998 [182, 183].

The sequence used to operate the mirror-MOT, to load the atoms into a Ioffe-Pritchard-trap (IPT) and to generate Bose-Einstein condensates by forced RF-evaporation in the QUANTUS-1 experiment has been well optimized during previous theses [165, 166] making it robust and reliable. A short overview as references containing details are presented in this section.

2.2.1 Magneto-optical cooling and magnetic trapping

In the QUANTUS-1 experiment a three dimensional MOT is used, that is loaded from ^{87}Rb background vapor provided by dispensers. Due to the close proximity of the atom chip two of the six MOT beams are retroreflected from the chip surface as depicted in fig. 2.6(a). In the first stage the magnetic quadrupole field is generated by a pair of macroscopic anti-Helmholtz coils. After typical loading times of 10 s seconds about $1.6 \cdot 10^7$ atoms are transferred into a second stage formed by the U-wire on the atom chip. The atom chip is able to generate steeper magnetic gradients, at the cost of a smaller trapping volume than the initial MOT state. With this second stage about $1 \cdot 10^7$ atoms are moved towards the chip and to the position of the magnetic trap. To optimize the transfer between the MOT stages, shift the trap centers and compensate for residual external gradients by using three pairs of offset coils according to fig. 2.6(b).

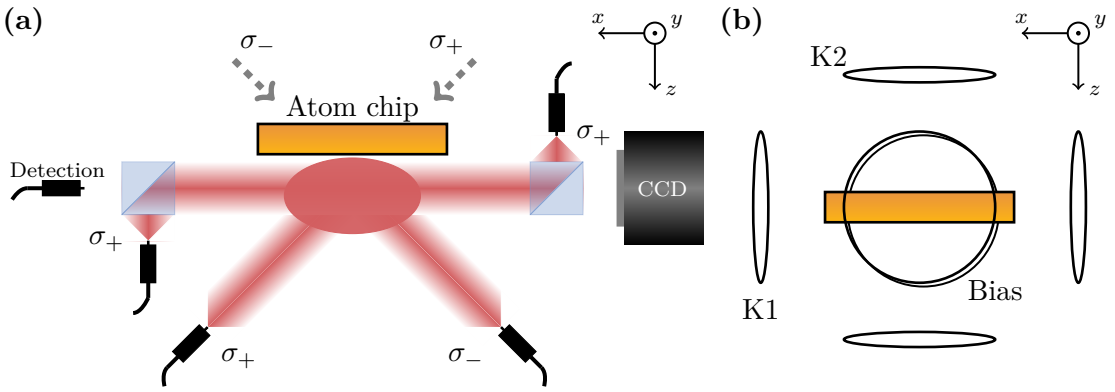

Figure 2.6: Schematic of mirror-MOT beams **(a)** and bias fields Bias, K1 and K2 **(b)**.

Reaching sub-Doppler temperatures with an optical molasses and optical pumping

The limit on laser cooling in a MOT is set by the statistic nature of photon scattering to $k_B T_{at} = \hbar\Gamma/2$ with line width Γ, which allows only temperatures as low as the Doppler temperature, which is 145.6 µK for ^{87}Rb. This temperature is too high to achieve an efficient loading into a magnetic trap, but it can be overcome by an optical molasses [182] at the end of the laser cooling stage. Hereby all magnetic fields are switched off, the cooling laser intensity is linearly reduced to about one-quarter and further red-detuned to $10\,\Gamma$ with no changes for the repumping laser. About $N \approx 7 \cdot 10^6$ atoms reach a final temperature of $T_{at} \approx 20\,\mu\text{K}$ at the end of the molasses.

Subsequent to the optical molasses the atoms should be loaded into the purely magnetic trap generated by the atom chip, in which the atoms will be evaporated [184]. To do so, it is favorable to first optically pump the atoms into the Zeeman sub-state with the highest magnetic

moment, in which the atoms experience the largest trapping potentials. This optical pumping is done by tuning the cooling laser resonant to the transition $|F = 2\rangle \rightarrow |F' = 2\rangle$ for 700 µs with only a single laser beam switched on to illuminate the atoms. A population trapping in the $|F = 2,m_\mathrm{F} = 2\rangle$ sub-state is now achieved by a circular polarization (σ_+) of the laser beam with respect to an 8 G quantization field in the y-direction.

Loading into a Ioffe-Pritchard trap for the evaporation

After the transfer into the $m_\mathrm{F} = 2$ sub-state is finished the atoms can be afterwards loaded into a magnetic trap. Since there is no light force anymore to confine the atoms, paramagnetic atoms are trapped due to the Stern-Gerlach force $\vec{F}_\mathrm{SG} = -g_\mathrm{F}\mu_\mathrm{B}m_\mathrm{F}\nabla|\vec{B}|$ with the Landé factor g_F pointing either towards the magnetic field minimum or maximum according to their m_F-state.

The most simple configuration for a magnetic trap, that provides a local field minimum is a quadrupole trap generated by a pair of anti-Helmholtz coils with axial symmetry in z-direction approximated by $B_x = xB'$, $B_y = yB'$ and $B_z = -2zB'$. To lift the zero field in the local minimum and avoid losses due to Majorana spin-flips, there are two commonly used methods, to add a repulsive (blue detuned) optical dipole potential [93], or a homogeneous magnetic field, that needs to be rotating in the plane perpendicular to the symmetric axis of the coils called a time-orbiting-average-potential (TOP) [91, 185]. Another magnetic field configuration is a so called Ioffe-Pritchard trap, named after Ioffe, who proposed this configuration first [186] and Pritchard, who adapted it to trap neutral atoms [187, 188]. In the axial symmetric case [169, 189], this magnetic field can be approximated by

$$\vec{B}(x,y,z) = B_0 \begin{pmatrix} 0 \\ 0 \\ 1 \end{pmatrix} + B' \begin{pmatrix} x \\ -y \\ 0 \end{pmatrix} + \frac{B''}{2} \begin{pmatrix} -xz \\ -yz \\ z^2 - \frac{1}{2}(x^2 + y^2) \end{pmatrix}. \tag{2.4}$$

This configuration can either be generated by a coil assembly [91, 93], or by an atom chip with a combination of a single current carrying wire and an external homogeneous offset field, as it is available in the QUANTUS-1 experiment. In both cases, the center of the chip's trapping potential may be approximated as an straightforwardly treatable harmonic potential

$$V(x,y,z) = \frac{m}{2}\left(\omega_x x^2 + \omega_y y^2 + \omega_z z^2\right), \tag{2.5}$$

with only two different trapping frequencies in axial ω_z and radial $\omega_\mathrm{rad} \equiv \omega_x = \omega_y$ direction, due to the axial symmetry. For the axial trapping frequency only the curvature B'' needs to be taken into account, while for the radial direction the ratio of the square of the gradient B' and the bottom B_0 of the trap scale its steepness

$$\begin{aligned} \omega_z &= \sqrt{\frac{\mu_\mathrm{B}g_\mathrm{F}m_\mathrm{F}}{m}} \cdot \sqrt{B''} \\ \omega_\mathrm{rad} &= \sqrt{\frac{\mu_\mathrm{B}g_\mathrm{F}m_\mathrm{F}}{m}} \cdot \sqrt{\frac{B'^2}{B_0} - \frac{B''}{2}}. \end{aligned} \tag{2.6}$$

In the experiment a cigar-shaped Ioffe-Pritchard-trap is loaded right after optical pumping by switching on the Z-wire current to $I_\mathrm{Z} = 2\,\mathrm{A}$ together with a bias field current of $I_\mathrm{bias} = 0.8\,\mathrm{A}$. An additional field by the K1 coil with a current $I_\mathrm{K1} = 1.6\,\mathrm{A}$ defines the magnetic field minimum B_0. About $N \approx 4{\cdot}10^6$ atoms are loaded into the trap without significant heating ready for evaporation.

2.2.2 Bose-Einstein condensation in a harmonic trap

The occurrence of the statistical phenomenon called Bose-Einstein condensation was predicted jointly by A. Einstein and S. N. Bose [89, 90], who showed that M. Planck's distribution law for electromagnetic radiation [190] could be derived purely from photon statistics rather than classical electrodynamics. The experimental validation took until 1995 and was reported by three groups almost at the same time in ref. [91–93]. A very brief review on the theoretical background of Bose-Einstein condensation based on ref. [170] will be presented here. The evaporation sequence to generate Bose-Einstein condensates and the different release traps used in the QUANTUS-1 experiment are summed up in this section. More detailed work on the characterization of these traps and the generated Bose-Einstein condensates can be found for instance in ref. [165].

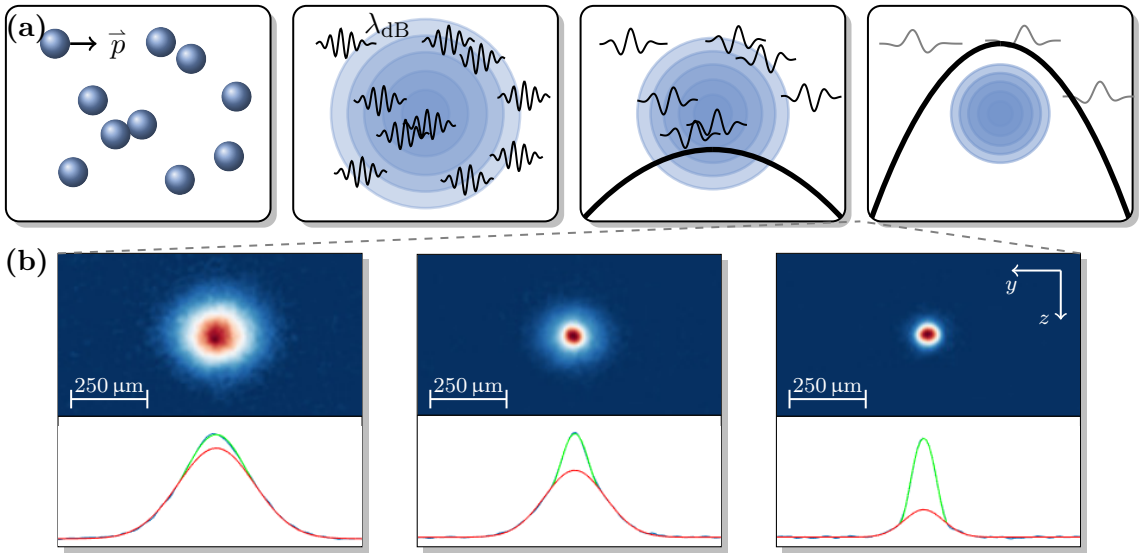

Figure 2.7: Illustration of the phase space density for increasing thermal de Broglie wavelength and increasing population of the ground state **(a)**. Formation of a Bose-Einstein condensate where the bimodal distribution is observable with increasing condensate fractions of 7%, 20% and 60% **(b)**.

The occurrence of Bose-Einstein condensation is a pure quantum effect relying on the concept of wave-particle duality. The wave nature of particles comes into play associated with the uncertainty in their thermal distribution, decreasing with the temperature T. The characteristic length scale at which quantum effects arise, is reached if the thermal de Broglie wavelength

$$\lambda_{\mathrm{bB}} = \sqrt{\frac{2\pi\hbar^2}{m k_{\mathrm{B}} T}} \tag{2.7}$$

in an ensemble of density n is of the same order as the mean distance $n^{1/3}$ between particles

$$\rho = n\lambda_{\mathrm{dB}}^3 = n\left(\frac{2\pi\hbar^2}{m k_{\mathrm{B}} T}\right)^{3/2} \geq 1 \text{ or } T \leq n^{2/3}\left(\frac{2\pi\hbar^2}{m k_{\mathrm{B}} T}\right) \text{ for Bosons.} \tag{2.8}$$

Under this condition, the atoms' wave functions spatially overlap until they reach condensation at a threshold density of $\rho \geq 2.613$. At this point, the system can be described by a single quantum mechanical state as illustrated in fig. 2.7(a,b). With continuing evaporation the temperature and fraction of thermal atoms is decreasing until a pure Bose-Einstein condensate is formed.

Only a few properties and expressions are necessary for the description of the phase transition at the threshold to condensation. The density of states, transition temperature and condensate fraction are derived for ideal Bose gases in a harmonic trap following ref. [170]. Ideal Bose gases have the property, that all particles are non-interacting as it is a good approximation for dilute thermal atoms like an optical molasses. Atomic interactions, which are neglected in the first place, are taken into account in the Gross-Pitaevskii equation and the Thomas-Fermi approximation.

Transition temperature and condensate fraction

For Bose-Einstein condensation, calculating the number of particles N_0 occupying the ground state of a harmonic trap is essential, since the ground state has the lowest possible energy ε_0 in the trap, which is needed to fulfill the condition in eq. 2.8. The occupation of states $N(\varepsilon)$ in a uniform non-interacting system with a temperature T is given by Bose-Einstein statistics

$$N(\varepsilon) = \frac{1}{e^{(\varepsilon-\mu)/k_\mathrm{B}T} - 1} \tag{2.9}$$

with an energy ε of a single particle and the chemical potential μ to add an additional particle to the distribution. The ground state energy ε_0 is thereby required to be larger than the chemical potential μ, since otherwise negative state occupation numbers would occur, that are naturally forbidden. The total atom number $N_\mathrm{tot} = \varepsilon \sum g(\varepsilon)$ can be understood as the sum over the density of states $g(\varepsilon)$ times this energy ε. For an infinite number of atoms the sum transforms into an integral over the density of states $\rho(\varepsilon)$ times their occupation $N(\varepsilon)$, where by hand the atoms in the ground state N_0 are separated from thermal ones

$$N_\mathrm{tot} = N_0 + N_\mathrm{therm} = N_0 + \int_0^\infty d\varepsilon\, N(\varepsilon)\rho(\varepsilon). \tag{2.10}$$

The density of states $\rho(\varepsilon)$ is now depending on the external potential V_ext the atoms are kept in. The magnetic trap generated by the atom chip can be approximated as a harmonic potential $V(x,y,z)_\mathrm{ext}$ around its minimum given by eq. 2.5. For non-interacting atoms the many-body Hamiltonian equals the sum over all Hamiltonians for individual atoms with eigenvalues

$$E_{(n_x,n_y,n_z)} = \left(n_x + \frac{1}{2}\right)\hbar\omega_x + \left(n_y + \frac{1}{2}\right)\hbar\omega_y + \left(n_z + \frac{1}{2}\right)\hbar\omega_z. \tag{2.11}$$

Hereby, the occupation numbers $n_{x,y,z}$ are all non-negative integers. The density of states $\rho(\varepsilon)$ in the considered harmonic potential V is calculated by deriving the number of states $G(\varepsilon)$ to

$$\rho(\varepsilon) = \frac{\mathrm{d}G(\varepsilon)}{\mathrm{d}\varepsilon} = \frac{\mathrm{d}}{\mathrm{d}\varepsilon}\left(\frac{1}{\hbar^3\omega_x\omega_y\omega_z}\int_0^\varepsilon \mathrm{d}\varepsilon_x \int_0^{\varepsilon-\varepsilon_x} \mathrm{d}\varepsilon_y \int_0^{\varepsilon-\varepsilon_x-\varepsilon_y} \mathrm{d}\varepsilon_z\right) = \frac{\varepsilon^3}{2\hbar^2\omega_x\omega_y\omega_z}. \tag{2.12}$$

With eq. 2.12 the fraction of thermal atoms N_therm from eq. 2.10 is calculated to

$$N_\mathrm{therm} = \frac{1}{2\hbar^3\omega_x\omega_y\omega_z}\int_0^\infty \mathrm{d}\varepsilon \frac{\varepsilon}{e^{(\varepsilon-\mu)/k_\mathrm{B}T_\mathrm{at}} - 1} = \zeta(3)\left(\frac{k_\mathrm{B}T}{\hbar\tilde{\omega}}\right), \tag{2.13}$$

with $\mu \approx 0$ close to the phase transition, the Riemann zeta-function ζ and the geometric mean of the trap frequencies $\tilde{\omega} = (\omega_x\omega_y\omega_z)^{1/3}$ [188]. Before the phase transition all atoms are still in excited states. Therefore, $N_\mathrm{tot} = N_\mathrm{therm}$ defines a critical temperature T_c at the phase transition

to condensation and the condensate fraction is given by

$$N_0 = N_{\mathrm{tot}}\left[1-\left(\frac{T}{T_c}\right)^3\right] \text{ with } kT_\mathrm{c} = \frac{\hbar\tilde{\omega}N^{1/3}}{|\zeta(3)|^{1/3}} \approx 0.94\cdot\hbar\tilde{\omega}N^{1/3}. \tag{2.14}$$

Gross-Pitaevskii equation and Thomas-Fermi approximation

So far, eq. 2.14 was derived for non-interacting gases. The inclusion of an interaction strength $g = \frac{4\pi\hbar^2}{m}a$ which depends on the scattering length a and the mass m leads to an atomic wave function that fulfills the time-dependent Gross-Pitaevskii equation

$$i\hbar\frac{d}{dt}\Phi(\vec{r},t) = \left[-\frac{\hbar^2}{2m}\Delta + V_{\mathrm{ext}}(\vec{r},t) + g|\Phi(\vec{r},t)|^2\right]\Phi(\vec{r},t). \tag{2.15}$$

The ground state of eq. 2.15 in a time-constant potential $V_{\mathrm{ext}}(\vec{r},t) \equiv V_{\mathrm{ext}}(\vec{r})$ is a pure condensate. The wave function can be separated into a position- and time-dependent part $\Phi(\vec{r},t) = \phi(\vec{r})e^{-i\mu t/\hbar}$ with a chemical potential μ leading to the time-independent Gross-Pitaevskii equation

$$\left[-\frac{\hbar^2}{2m}\Delta + V_{\mathrm{ext}}(\vec{r}) + g\left|\phi(\vec{r})\right|^2\right]\phi(\vec{r}) = \mu\phi(\vec{r}). \tag{2.16}$$

For vanishing interactions $g = 0$ eq. 2.16 is the original Schrödinger equation for single particles. The density distribution $n(\vec{r}) = \left|\phi(\vec{r})\right|^2$ is determined by the ratio between kinetic and interaction energy. In the limit of strong repulsive interaction ($a \gg 0$) or large densities the kinetic energy is negligibly small, which is expressed in the Thomas-Fermi approximation

$$n_{\mathrm{TF}} = \left|\Phi(\vec{r})\right|^2 = \max\left(\frac{\mu - V_{\mathrm{ext}}(\vec{r})}{g},0\right). \tag{2.17}$$

The density distribution expressed by eq. 2.17 is an inverted parabola with $n(0) = \mu/g$ and vanishing in every direction for $\mu \leq V_{\mathrm{ext}}(\vec{r})$, because it mirrors the shape of the potential. For the harmonic potential from eq. 2.5 and $N = \int \mathrm{d}\vec{r}\left|\phi(\vec{r})\right|^2$ the Thomas-Fermi radius [191, 192] is

$$R_i^{\mathrm{TF}} = \frac{1}{\omega_i}\sqrt{\frac{2\mu}{m}} = \left(\frac{15N\hbar^2 a}{m^2\omega_i^2}\right)^{\frac{1}{5}} \text{ with } \mu = \frac{\hbar\tilde{\omega}}{2}\left(15Na\sqrt{\frac{m\tilde{\omega}}{\hbar}}\right)^{\frac{2}{5}}. \tag{2.18}$$

This Thomas-Fermi radius is of different shape compared to the traditional Boltzmann distribution derived from the harmonic oscillator ground state a_i which is expressed by a Gaussian width

$$R_i^{\mathrm{BZ}} = a_i\sqrt{\frac{k_B T_{at}}{\hbar\omega_i}} \text{ with } a_i = \sqrt{\frac{\hbar}{m\omega_i}}. \tag{2.19}$$

Experimental sequence for Bose-Einstein condensation in QUANTUS-1

The evaporation of the clouds loaded into the Ioffe-Pritchard-trap is performed via forced RF-evaporation with an additional RF-field emitted from the Z-wire. Hereby, the frequency ν_{rf} of the RF-field is chosen to be resonant to the most energetic atoms in the trap driving spin changing transitions with $\Delta m_\mathrm{F} = 1$. Atoms ending up in a high-field seeking m_F-state are repelled from the potential minimum, the remaining distribution rethermalizes and the temperature decreases.

Due to this "cutting" of the most energetic atoms from the distribution this technique is referred to as RF-knife. The individual steps and frequency ramps are summed up in tab. 2.1. After a final evaporation ramp down to $\nu_{\mathrm{rf}} = 1.83\,\mathrm{MHz}$ close to the bottom of the trap condensation is reached after 1240 ms in total with a radial trapping frequency of $2\pi \cdot 2500\,\mathrm{Hz}$ of the cigar-shaped potential. The final atom number in the condensate is typically slightly larger than $N = 10\,000$ in 15 s atoms with a condensate fraction of 65%. Figure 2.7(b) shows the decreasing fraction of thermal atoms for further evaporation depending on the end frequencies of $\nu_{\mathrm{rf}} = 1.875\,\mathrm{MHz}$, 1.85 MHz and finally 1.83 MHz, corresponding to condensate fractions of 7%, 20% and 60%.

Table 2.1: Experimental sequence for the evaporation with an RF-knife.

	Δt (ms)	I_z (A)	I_{bias} (A)	I_{K1} (A)	ω_{rad} (Hz)	ν_{rf} (MHz)
z-trap 1	0	2	0.8	1.6	$2\pi \cdot 260$	-
z-trap 2	20	2	$0.8 \rightarrow 2.7$	1.6	$2\pi \cdot 1300$	-
evap. 1	290	2	$2.7 \rightarrow 6.5$	1.6	$2\pi \cdot 7600$	$40 \rightarrow 4$
	230	2	6.5	1.6	$2\pi \cdot 7600$	
	20	2	$6.5 \rightarrow 5.5$	1.6	$2\pi \cdot 5500$	
evap. 2	300	2	$5.5 \rightarrow 5$	1.6	-	$4 \rightarrow 2.3$
evap. 3	100	2	$5 \rightarrow 3.55$	1.6	$2\pi \cdot 2500$	$2.3 \rightarrow 1.99$
evap. 4	300	2		1.6		$1.99 \rightarrow 1.83$
condensate generation						
decomp.	152	$2 \rightarrow 1.2$	$3.55 \rightarrow 0.6$	1.6	$2\pi \cdot 130$	$1.83 \rightarrow 3$
h-trap	250	1.2	$0.6 \rightarrow I_{\mathrm{bias}}$	1.6	ω_{rad}	-
condensate release						

After the condensate generation ν_{rf} is ramped up again to repel residual thermal atoms while the trap is decompressed. Subsequent to the decompression the atoms are transferred into the final release trap, for which three different configurations can be chosen with different final bias currents I_{bias} and determined trap frequencies listed in tab. 2.2. As in ref. [165] the trap with $I_{\mathrm{bias}} = 0.36\,\mathrm{A}$ is called "shallow", the trap with $I_{\mathrm{bias}} = 0.6\,\mathrm{A}$ "steep" and, finally, the trap with $I_{\mathrm{bias}} = 1\,\mathrm{A}$ "lens", because in ref. [165] it was used for delta-kick collimation on ground.

From the release trap the condensate is released into free fall by switching the current from the Bias coil pair and the Z-wire ($I_{\mathrm{Z}} = I_{\mathrm{bias}} = 0$) off. The dynamics of the freely expanding Bose-Einstein condensate is thus not described anymore by the Thomas-Fermi approximation from eq. 2.17, because the mean field energy from the atomic interactions gets converted into kinetic energy until the expansion reaches a ballistic regime of only kinetic energy. In this case, the evolution of the wave function is usually described by the scaling law with three scaling parameters obtained by appropriate coordinate transformation described in refs. [191, 192].

Table 2.2: Different release trap configurations used in the experiment.

h-trap configuration	$\omega_x/2\pi$ (Hz)	$\omega_y/2\pi$ (Hz)	$\omega_z/2\pi$ (Hz)
shallow ($I_{\mathrm{bias}} = 0.36\,\mathrm{A}$)	17.8(1.1)	46.56(1.32)	31.29(31)
steep ($I_{\mathrm{bias}} = 0.6\,\mathrm{A}$)	17.6(9)	131.48(45)	126.9(4)
lens ($I_{\mathrm{bias}} = 1.0\,\mathrm{A}$)	48.9(5.3)	343.46(36)	343.88(38)

CHAPTER 3

Frequency-doubled high-power laser system

A frequency-doubled high-power laser system is assembled, which enables large momentum transfer and lattice manipulation of the atoms simultaneously in horizontal and vertical direction. While trapping, cooling and first-order Bragg diffraction is performed with diode-based laser systems fitting inside the drop capsule, there is an additional rack to host the high-power laser system, schematically depicted in fig. 3.1. Systems of this type advanced immensely during recent years and a variety of lasers, amplifiers but also components like modulators, switches and splitters are commercially available [193, 194], due to the fact, that their fundamental wavelength at 1560 nm is broadly used for telecommunication purpose. Our specific system utilizes a 10 W amplified fiber master laser system of type NKT BoostiK E15 that has an intrinsic wavelength stability of a few MHz and is tunable over roughly ±1 nm by temperature of the active fiber. One specialty of this particular laser system is an extremely narrow instantaneous linewidth specified to be smaller than 100 Hz and low output power fluctuations of below 100 dB at a noise frequency 0.7 MHz. The resonant doubling of the 1560 nm light takes place inside a Toptica SHG pro (sec. 3.1). Up to 5 W of doubled light at 780 nm are then distributed and guided to the experiment via polarization-maintaining single mode fibers (sec. 3.2). For gravimetry the atom chip itself is used as retro-reflector it needs to be alignment to gravity (sec. 3.3).

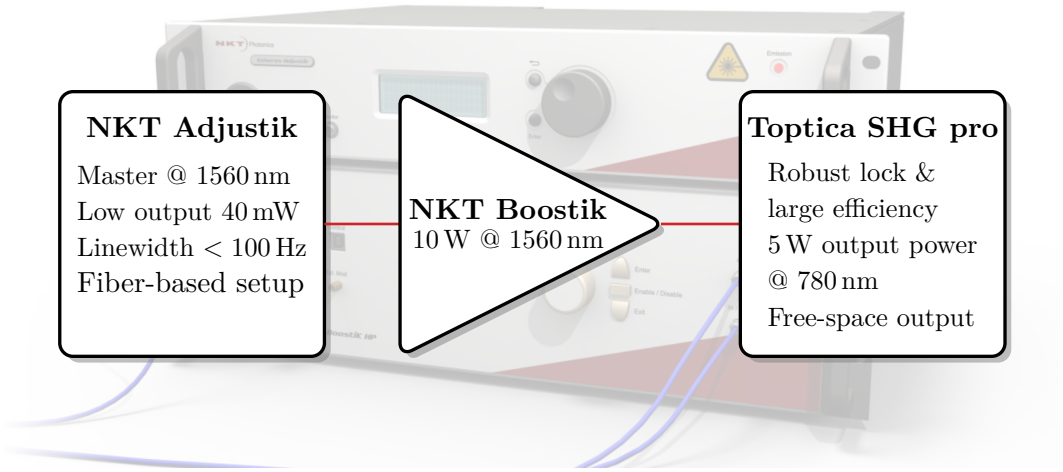

Figure 3.1: Schematic of the frequency-doubled high-power laser system used for higher-order (double) Bragg diffraction and the generation of optical lattices (image by NKT Photonics [195])

3.1 Frequency doubling and distribution module

Unlike other realizations of high-power laser systems based on frequency doubling [196, 197] which use a single pass through a periodically-poled Lithium Niobe (PPLN) crystal, here the frequency doubling takes place in a resonant bow-tie cavity of type TOPTICA SHG PRO. Due to power enhancement inside the cavity in combination with the non-linearity of the doubling process, this type of resonant doubling has the advantage of a comparably large conversion efficiency at lower pump power. A maximum output of 6 W at a pump power of 11 W is obtained [198], that results in a similar conversion efficiency compared to ref. [197] and twice the efficiency per power observed in ref. [196], but at lower absolute pumping powers. A limited pumping power is a constraint in the amplification of ultra narrow laser sources, since for linewidths below 1 kHz there is an enlarged Brillouin back scattering in fiber amplifiers which might destroy the amplifier [195]. The largest conversion efficiency per input power of $\eta \approx 1\,\frac{1}{W}$ is achieved by doubling in ridge waveguide crystals, but these are limited to the doubling of roughly one Watt [199].

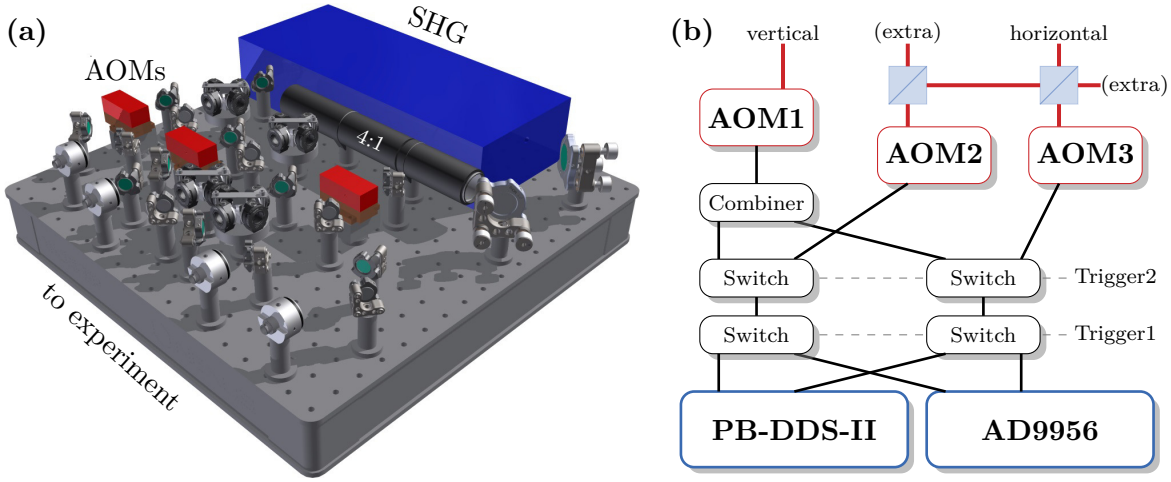

Figure 3.2: Resonant doubling stage and high-power distribution module at 780 nm. After the doubling stage the light is downsized by a 4:1 telescope and distributed into two paths **(a)**. A single AOM generates the frequencies for beam splitting in vertical direction. The frequencies for horizontal beam splitting are generated by two independent AOMs and overlapped before the fiber **(b)**.

For the doubling stage and the free-space distribution of the laser light at 780 nm a separate breadboard (THORLABS NEXUS) with a high stiffness and vibration damping capabilities is set up depicted in fig. 3.2(a). The breadboard is required since the cavity is susceptible to the incoupling of vibrational noise reducing the stability of the cavity lock. For a large enhancement factor of the power circulating inside the cavity, it is locked via a double-stage piezo lock using the Pound-Drever-Hall (PDH) method [200]. To generate the frequencies for the Bragg or lattice beams three acousto-optical modulators (AOM, AA OPTO ELECTRONIC MT80-A1.5-VIS) are used in total, two for the horizontal direction which are either overlapped or individually coupled into fibers (SUK PMC-850-5,1-NA13-3-APC-700-P) and guided to the experiment. The third AOM is driven by two mixed RF frequencies [201, 202] and is coupled into a fiber guided to the vertical direction. The RF sources are direct digital synthesizers (DDS) either for driving amplitude-shaped pulses at fixed frequency (PULSEBLASTERDDS-II) or a self-assembled device (ANALOG DEVICES AD9958) for driving amplitude and frequency ramps. The output signals of each dual-channel device is switched to drive the AOMs following fig. 3.2(b). Obtained Laser output powers and transfer functions to adjust the power are depicted in fig. 3.3(a,b).

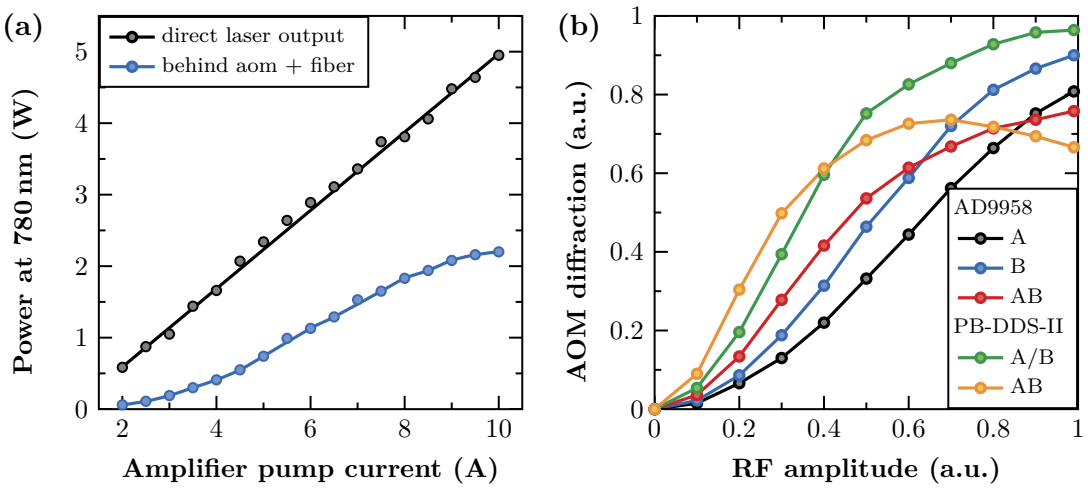

Figure 3.3: The total laser power is measured directly at the laser output and at the exit of a single-mode fiber, which is coupled with light diffracted by 80 MHz using an AOM in first order [198] **(a)**. Transfer functions of RF amplitude of the PulseBlasterDDS-II and AD9958 to the diffracted efficiency of the AOM **(b)**. The output channels are either fed each into individual AOMs or both channels are combined and fed into a single AOM with an offset of 500 kHz.

3.2 Horizontal and vertical beam-splitting optics assemblies

The beam splitting optics used in this work are assembled using Thorlabs mounts, which can easily be extended by the integration of commercial components. Three assemblies have been constructed for different purposes to perform interferometry either in a horizontal or a vertical axis, so either along gravity in z-direction or perpendicular to gravity in y-direction. The optics mount are attached via a custom made adapter directly to a CF vacuum window either from the lower viewport pointing towards the chip or a horizontal viewport on the axis perpendicular to the detection (see fig 2.2 for the definition of the coordinate system).

Vertical - parallel to gravity

Two versions of the gravimetry optics exist and are utilized for different purposes as shown in fig. 3.4 (a,b). Hereby, the first version was used in combination with the diode-based Bragg laser for low power beam splitting and employed for the determination of local gravity described in sec. 6.2 and ref. [171]. To have small wave-front aberrations the collimator uses a single lens (Thorlabs LA1608-B) mounted in a tube to a beam diameter of $\oslash = 7$ mm close to the free aperture the chamber allows for. The beam splitting light field is adjusted via a cornered mirror (Thorlabs BB1-E03, KCB1/M) in angle and an x-y mount (Thorlabs ST1XY-A/M) in position. The laser beams are reflected over a pentaprism (Edwards N-BK7 Vis) onto the atom chip. This guarantees a perfect 90° angle of the beam splitting telescope to the atom chip after alignment. A simple monitoring camera to observe and optimize MOT loading is mounted at a port of a polarizing beam splitter (Thorlabs CCM1-PBS252/M).

The second version of the optics mount is utilized for large momentum transfer beam splitting and lattice manipulation of the atoms together with the high power laser system presented here. Therefore the diameter $\oslash = 3.3$ mm of the beam is roughly a factor of two smaller. The single lens telescope is replaced by a pre-collimated fiber collimator (SuK 60FC-A18). Since the smaller beam has to be centered more precisely at the position of the atomic ensembles, the penta prism was replaced by a second mirror (Thorlabs BB05-E03, KCB05/M), to beam walk the

laser beam. At the second port of the polarizing beam splitter, the monitor camera is intended to be replaced by a pair of adjustable collimators with smaller beam diameter of $\oslash = 1\,\mathrm{mm}$ (SUK 60FC-A7,5). These are overlapped at a second polarizing beam splitter (QIOPTIQ G335592000) with a pair of half inch mirrors and provide the possibility to guide two independently polarized beam two the vacuum chamber for potential future use (see ref. [203] for reference).

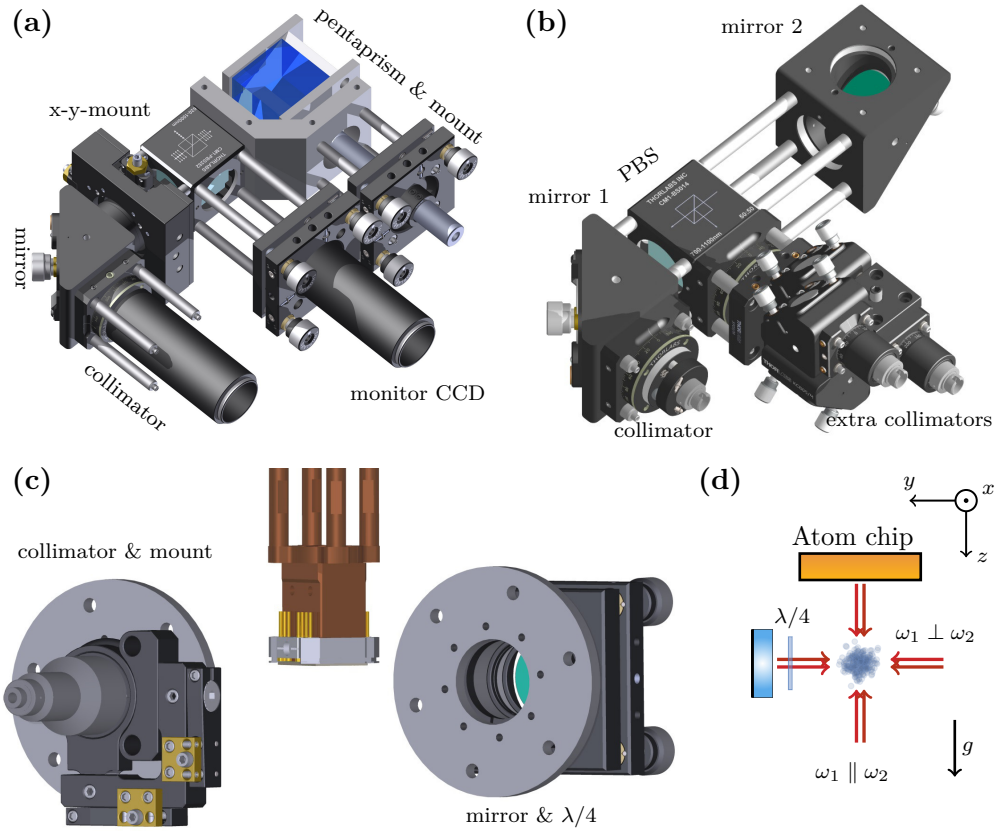

Figure 3.4: Low power **(a)** and high power version **(b)** of the optics module used for beam splitting in the vertical direction. Optics module used for beam splitting in horizontal direction **(c)**. Frequencies and polarizations in each direction with the coordinate system as detected with the CCD-camera **(d)**.

Horizontal - perpendicular to gravity

Additionally, light can be shined into the chamber at a viewport aligned on the horizontal axis along the y-direction, such that interferometer output ports can be detected by the camera. The main purpose of this horizontal axis is to perform interferometry with double Bragg diffraction as the work presented in sec. 7.2. Two light beams originating from different AOMs are overlapped in linear perpendicular polarization (lin⊥lin) before the fiber and retro reflected from a mirror (THORLABS BB1-E03, KC1-T/M) at the other end of the chamber, passing a $\lambda/4$-wave plate (THORLABS WPQ10M-780) twice. The optics are shown in fig. 3.4(c) with their to scale position relative to the atom chip. The diameter of the beam splitting light field is requested to be as large as possible, since the atoms fall through the light field due to gravity. On the other hand a large beam diameter reduces the peak light intensity. The current telescope (THORLABS F810APC-780) mounted in a Gimbal mount (THORLABS KC45D) has a collimated beam diameter of $\oslash = 7.5\,\mathrm{mm}$, which is a good compromise between size and available light intensity.

If the vertical beam center position is too close to the atom chip, diffraction at the edge of the chip occurs, causing amplitude as well as phase inhomogeneities which disturbs the manipulation of the atoms during interferometry. Thus, the telescope can be shifted with its mount in a range of approx. 1 cm along the z-direction to adjust the Gaussian shape relative to the atoms and its size reduced by an adjustable aperture (Thorlabs CP20S).

3.3 Adjustment procedure of atom chip and beam splitter

Due to the horizontal positioning of the atom chip inside the experimental chamber, the chip itself can be used as a retro-reflector for a beam splitting light field oriented along gravity. In that way, an astonishingly simple and compact setup is formed to measure gravity. Before a gravimeter can yet be implemented the adjustment of the atom chip as well as beam splitter relative to gravity has to be performed. Since the atom chip is not accessible for a direct alignment, the parallel orientation of the beam splitting light field along gravity can be only achieved by tilting the hole capsule. As reference access only the lower vacuum port used for the beam splitter is available. A method to tackle this adjustment procedure has been first described in a Bachelor thesis [204] and is schematically summed up in fig. 3.5. Instead of using the beam splitting optics described in sec. 3.2, a combination of a smaller pentaprism (CCM1-PS932/M) and a fiber

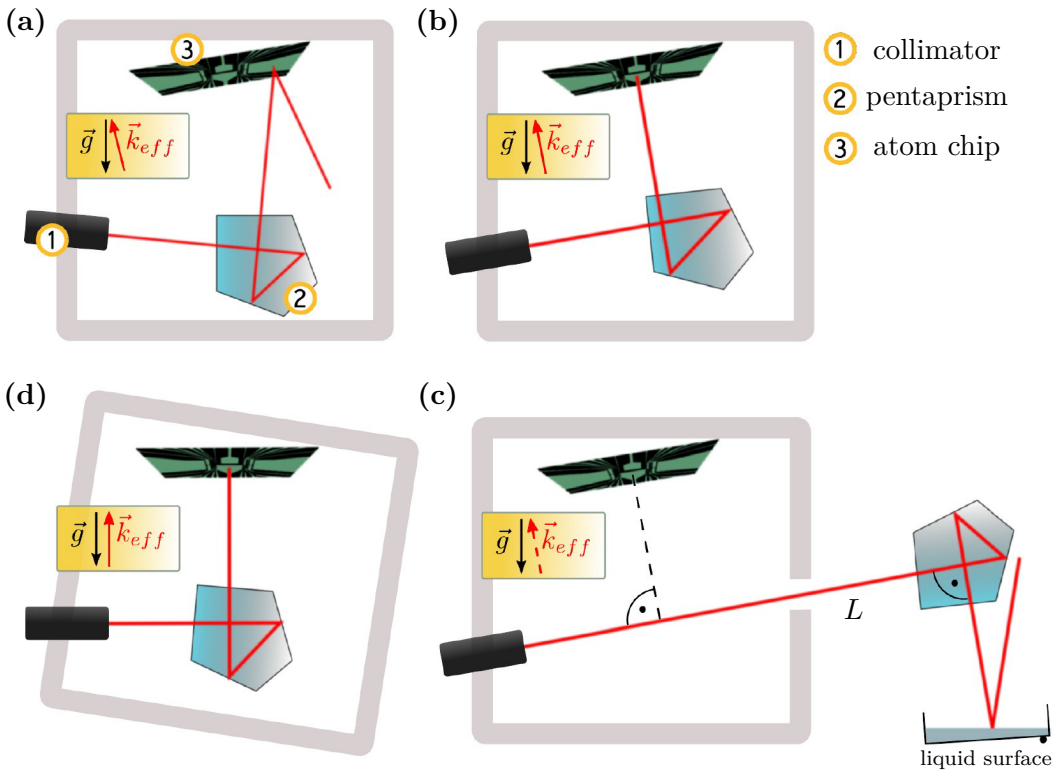

Figure 3.5: Adjustment procedure to align the atom chip perpendicular to gravity. With a collimator fixed to the drop capsule, a level beam is aligned perpendicular to gravity using a pentaprism **(a,b)**. In a second step the level beam is deflected via again a pentaprism, but now in an external position, on a liquid surface. Using the retro-reflection from the liquid surface as a reference, the capsule is leveled in two dimensions such, that the atom chip is aligned acting as an inertial reference perpendicular to gravity **(c,d)**. (This picture is a combined adaption from fig. 3.6 and fig. 3.8 in ref. [204].)

collimator with 1 mm beam diameter (SuK 60FC-A4,5) has proven to be the best choice for this adjustment. The pentaprism takes care, that the laser beam is always reflected by 90° and the smaller laser beam is less susceptible to apertures in the vacuum system and requires less laser power to work with. In a first alignment step the incoming level beam needs to be adjusted by beam walking with two mirrors (Thorlabs BB05-E03, KC05-T/M), in a way that the beam splitting light field is properly retro-reflected and therefore perpendicular to the atom chip.

The fiber collimator is now fixed to the drop capsule and acts as a substitute for the atom chip surface. By moving the pentaprism to an external position and with the retro-reflection from a liquid surface the whole capsule can now be leveled by two adjustable feet until the reflected beam is overlapped with the incoming one. This leveling needs to be performed iterative in two dimension until the capsule is fully aligned relative to gravity. Hereby, the distance L of the external position and the distance between level beam and atom chip define how sensitive the alignment can be performed. After this process, the beam splitting optics is reattached and the light field is retro-reflected, by coupling it back into the optical fiber to the optics distribution module. For the beam splitting optics itself a pentaprism is not mandatory and two mirrors for alignment can be used as well, since the orientation of the beam splitting telescope itself is no longer of importance, if the atom chip stays in place. The tilt of the capsule is long-term monitored with a commercial dual-axis tiltmeter (Variohm g-nsdog2-021) read out via USB.

Distortions on the atom-chip surface

After the alignment, the beam has a certain position where it is reflected from the atom-chip surface which is depicted in ref. 3.6 with the condensate ideally centered in the beam profile.

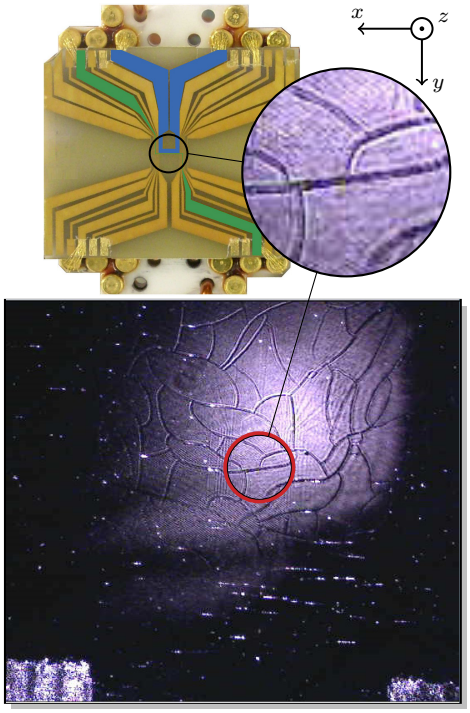

Fig. 3.6: Defects on the atom chip surface illuminated by laser light. The red circle indicates the position of the central atom-chip structures.

Due to its optical properties the atom chip is not an ideal reflector. The surface of the atom chip is made of a dielectric transfer coating which is specified to reach a surface quality of up to $\lambda/10$ [205]. Out of the box, this appears be of a quality on a level comparable to a standard mirror, but the surface is quite fragile. Figure 3.6 shows how the surface of the atom chip in the QUANTUS-1 experiment looks like in reality, when illuminated with laser light from lower viewport with large diameter. What is to be seen there, are clearly visible cracks in the surface. These cracks appeared after the bake-out procedure of the vacuum, even at comparably low temperatures. Also the underlying chip structures are illuminated, since the coating is thin and the overall reflectance is only in the order of 85%. For the magneto-optical trap, the quality of reflected beam is sufficient, but to realize undisturbed beam splitting with this surface quality will be more demanding. For this reason the employed transfer coating is not the ideal technique in terms of surface quality. Possible alternative techniques with which superior surfaces of really optical quality might be reached are discussed in sec. 8.3.

CHAPTER 4

Concepts for light-pulse atom interferometry

A fascinating insight in nature is granted by performing interference experiments with solid particles. While rather microscopic in size, atoms still show a classical and particle-like behavior in many aspects. From today's perspective it only requires fairly simple arrangements to observe other properties of massive objects, that can only be described taking into account their wave nature and once more reveal the duality between waves and particles. Quantitatively this is expressed by the de Broglie wavelength $\lambda_{dB} = h/p = h/(mv)$ [206] connecting the particles momentum p with Planck's constant h to a wavelength λ_{dB} that determines its wave properties. Experimentally, the wave nature has been demonstrated by various interference experiments for particles with increasing mass, starting from electrons over neutrons and atoms up to molecules [207–210]. Groundbreaking experiments with molecules and clusters with impressive sizes, orders of magnitudes beyond the mass of single atoms, have been performed over recent years, for example in the group of M. Arndt in Vienna [211, 212], and lead to tests of the macroscopic boundaries of quantum mechanics [213, 214]. Unlike photons from a monochromatic source, such as a laser with enormous coherence properties, thermal or laser cooled atomic and molecular ensembles are only well suited for performing white light or single particle interferometry, where the path length for both parts of the wave packet is equal or reasonable close to equality. This situation changes if one performs interference experiments with Bose-Einstein condensates which achieve coherence lengths of the order of a millimeter and enable the observation of spatial interference opening up new methods of deducing variables in a single experiment [98, 100].

In this chapter an overview of the theoretical concepts needed as a prerequisite for the later on performed atom interferometry experiments is given. A strong focus lies on methods to coherently manipulate atoms with laser light. Atom-light interaction is today a common and reliable technique to manipulate neutral atoms. While for instance Keith et al. [209] still used crystalline gratings to diffract atoms, Rasel et al. introduced gratings formed by light [215]. Today, rather than using stationary gratings, the application of light pulses is preferred instead [7, 8], since the interaction times and temporal pulse shapes are very well controllable parameters (sec. 4.1). Additionally, optical lattices offer another way to transfer a large amount of momentum to atoms by so called Bloch oscillations (sec. 4.2) which allow to efficiently manipulate atomic motion. With those beam splitters available, it is possible to apply a series of manipulations realizing an atom interferometer. Among the different possibilities to realize an interferometer, the Mach-Zehnder interferometer (MZI) which is a symmetric geometry and consists of three light pulses is a real workhorse in atom interferometry. It is in particular the favorite topology used for atomic gravimeters and its characteristics and features will be introduced (sec. 4.3).

4.1 Light-pulse manipulation

A key element to realize an atom interferometer is the employment of an adequate manipulation process able to split and recombine the atomic trajectories. The method of choice is hereby light-pulse manipulation. Especially since the development of lasers one has a very powerful technology at hand to control light fields being resonant to an atomic transition. A proper theoretical description of atom-light interaction based on quantum mechanics is to find the solution for the time-dependent Schrödinger equation. This is briefly done by introducing the Rabi model, which provides an easy way to understand these beam splitting processes (sec. 4.1.1). One way to experimentally perform light-pulse beam splitting is Bragg diffraction which has been used previously in various experiments (sec. 4.1.2). Bragg diffraction has advantages and differences compared to Raman diffraction which is spread especially in atom interferometry. A rather new extension of this technique is the so called double Bragg diffraction introduced theoretically in [79] which has very recently been realized in the QUANTUS-1 experiment [80]. Bragg diffraction is a powerful tool and at the same time pairs very well with Bose-Einstein condensates, since the velocity dispersion of the ensemble is of major relevance for the manipulation fidelity (sec. 4.1.3).

4.1.1 Rabi oscillations in a two-level system

A simple but extremely valuable method to describe the time evolution of an atomic wave function under the influence of a resonant electromagnetic field $\vec{E} = \vec{E}_0 \cos(\omega_{eg}\tau + \phi)$ with frequency $\omega_{\mathrm{eg}} = \omega_e - \omega_g$ are so called "Rabi oscillations". An idea of the Rabi formalism is presented in the following. Hereby, only two atomic states are taken into account, namely the ground state $|g\rangle$ and the excited state $|e\rangle$. These states are defined by their eigenenergies $E_{\mathrm{g}} = \hbar\omega_{\mathrm{g}}$ and $E_{\mathrm{e}} = \hbar\omega_{\mathrm{e}}$ respectively and do not necessarily have to reflect the internal energy structure of an atom. To determine these states' evolution after a given time τ one applies the following Hamiltonian

$$\hat{H} = \hat{H}_{\mathrm{pot}} + \hat{H}_{\mathrm{int}} = E_{\mathrm{e}} |e\rangle \langle e| + E_{\mathrm{g}} |g\rangle \langle g| - \vec{d} \cdot \vec{E}, \tag{4.1}$$

that is defined only by the potential energy and a coupling term between the atomic dipole moment $\vec{d} = |e|\vec{r}_e$ and the electromagnetic field $\vec{E}$ to the time dependent Schrödinger equation

$$-i\hbar \frac{\mathrm{d}}{\mathrm{d}t} |\Psi(\tau)\rangle = \hat{H} |\Psi(\tau)\rangle . \tag{4.2}$$

The solution of this eigenvalue problem is given by a wave function, which is the superposition of both states exclusively dependent on the duration of the interaction τ

$$|\Psi(\tau)\rangle = a_{\mathrm{g}}(\tau) |g\rangle + a_{\mathrm{e}}(\tau) |e\rangle , \tag{4.3}$$

with the probability amplitudes $a_{\mathrm{g}}(\tau)$ and $a_{\mathrm{e}}(\tau)$ to find the atom either in ground or excited state. Starting from the ground state, the atom will with a certain probability pick up an energy of $E_{\mathrm{eg}} = E_{\mathrm{e}} - E_{\mathrm{g}} = \hbar\omega_{\mathrm{eg}}$ to be transferred into the excited state and vice versa. The probability amplitudes for a light field, that is resonant to the transition frequency, are given by

$$|a_e(\tau)|^2 = P_{\mathrm{e}}(\tau) = \frac{1}{2}[1 - \cos(\Omega_{\mathrm{eg}}\tau)]. \tag{4.4}$$

The probability to find an atom still in the ground state is defined recursively by the relation $P_{\mathrm{e}}(\tau) + P_{\mathrm{g}}(\tau) = 1$. As a measure of coupling strength the Rabi frequency Ω_{eg} is introduced here:

$$\Omega_{\mathrm{eg}} \equiv \frac{\langle e|\,\vec{d}\cdot\vec{E}\,|g\rangle}{\hbar} = \frac{D\cdot E_0}{\hbar} = \sqrt{\frac{I[I_{\mathrm{sat}}]}{2}}\Gamma, \tag{4.5}$$

rewritten for the initially proposed two state assumption with an intensity of the light field $I[I_{\mathrm{sat}}]$ in terms of saturation intensity I_{sat} and a natural linewidth of the transition Γ. In the case of a non-resonant light field the effective Rabi frequency Ω_{eff} has to be taken into account, that is modified by the detuning $\delta = \omega_{\mathrm{eg}} - \omega_0$ of the light field relative to the transition frequency

$$\Omega_{\mathrm{eff}} \equiv \sqrt{|\Omega_{\mathrm{eg}}|^2 + \delta^2}. \tag{4.6}$$

This effective Rabi frequency always leads to a faster oscillation, but the amplitude of the oscillation is reduced by the ration between resonant and effective Rabi frequency. The new formula for the transition probability $P_{\mathrm{e}}(\tau,\delta)$ additionally depends on the detuning

$$P_{\mathrm{e}}(\tau,\delta) = \frac{1}{2}\left(\frac{\Omega_{\mathrm{eg}}}{\Omega_{\mathrm{eff}}}\right)^2 [1-\cos(\Omega_{\mathrm{eff}}\tau)]. \tag{4.7}$$

For a vanishing detuning δ this formula returns to its original form in eq. 4.4 and for a large detuning the oscillation vanishes completely. Fig. 4.1 shows Rabi oscillations for the resonant case or a small detuning $\delta/\Omega_{\mathrm{eg}}$. Two important points for atom interferometry are defined by their enclosed pulse area: "$\pi/2$"- and "π"-pulses. These points are given by the specific interaction times $\pi/(2\,\Omega_{\mathrm{eff}}) \equiv \tau_{\pi/2}$ and $\pi/(\Omega_{\mathrm{eff}}) \equiv \tau_{\pi}$ needed to achieve a probability of half respectively full times the amplitude for an atom to undergo a transition into the excited state. Due to their function in an interferometer these points are called "beam splitter"/"beam combiner" and "mirror" for atoms, like their counterparts in optics for light beams. In principle, this definition comprises everything required to realize an atom interferometer, but for a real experiment there are some useful extensions to this simple two state model, which is discussed in the following.

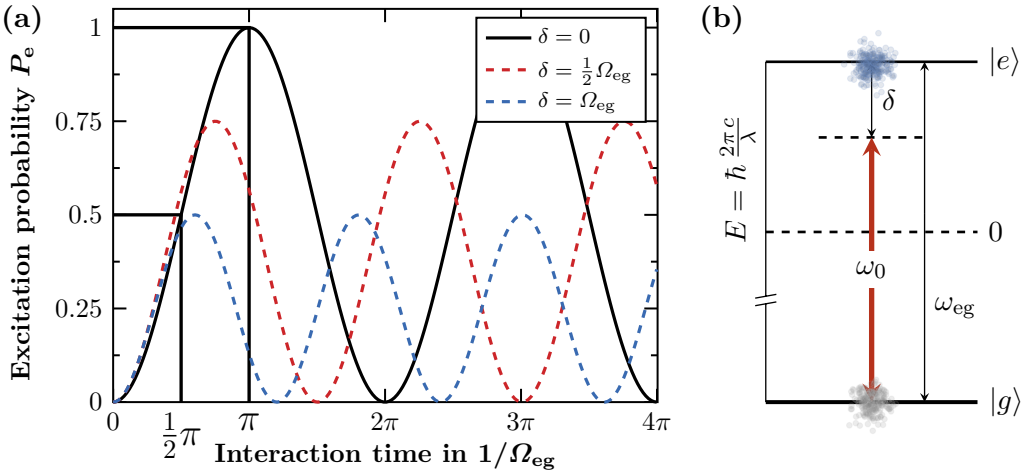

Figure 4.1: Rabi oscillations $P_{\mathrm{e}}(\tau)$ **(a)** in the two-level system **(b)** plotted for a resonantly driven light field (solid black line) and for two different detunings δ of $\frac{1}{2}\Omega_{\mathrm{eg}}$ and Ω_{eg} (red and blue dashed line) with reduced amplitudes and larger Rabi frequencies. The conditions for "$\pi/2$ pulse" and "π pulse" are marked in the resonant oscillation. These conditions lead to a superposition - called a "beam splitter" or "mixer" - or a total inversion of the population - named a "mirror".

Two-photon coupling: stimulated absorption and emission

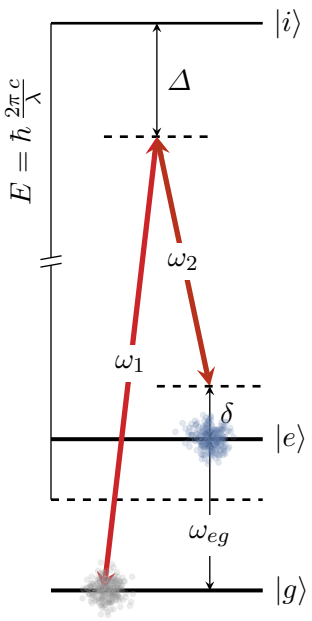

Fig. 4.2: Schematic depiction of the stimulated two-photon coupling between the states $|e\rangle$ and $|g\rangle$ via an intermediate level $|i\rangle$ by two light fields ω_1 and ω_2. Hereby Δ and δ denote the detuning to the intermediate state $|i\rangle$ respectively the detuning from the two-photon resonance $\omega_{\mathrm{eg}} = \omega_{12} - \delta \equiv |\omega_1 - \omega_2| - \delta$.

Rabi oscillations as described above can only be driven efficiently if the Rabi frequency Ω_{eff} is large compared to the lifetime τ of the ground and excited state. Otherwise, a short lived excited state will cause an immediate loss of atoms, which are no longer contributing to the oscillation. Transitions, where single photons couple two long lived states, might be available in clock transitions and there are recent proposals to utilize them for atom interferometry [216, 217]. Nevertheless, these transition are either complex to handle, since they are probed by ultra-stable lasers in optical clocks as for Ytterbium or Strontium [6, 218], or in the micro-wave range as for Rubidium or Cesium [52, 53]. The commonly used method is operating on an optical transition, that is not coupled by only one but rather two photons. The two photons are each non-resonant to a common atomic transition, but with a difference in frequency equal to the energy between ground and excited state $\omega_{12} \equiv |\omega_1 - \omega_2| = \omega_{\mathrm{eg}} + \delta$. For such a transition a third and intermediate state $|i\rangle$ is introduced according to fig. 4.2. The intermediate state can now be short lived itself, since it is only virtually populated, but rather enables decent coupling via simultaneous stimulated absorption and emission. The resulting two-photon Rabi frequency to drive the transition is a simple multiplication of both single photon Rabi frequencies 4.6 divided by two times the common detuning Δ to the intermediate state $|i\rangle$

$$\Omega_{12} \equiv \frac{\Omega_1^* \Omega_2}{2\Delta} = \frac{\Gamma\sqrt{I_1[I_{\mathrm{sat}}]I_2[I_{\mathrm{sat}}]}}{4\Delta[\Gamma]}. \tag{4.8}$$

Spontaneous decay rate

A fundamental loss mechanism occurring during this type of coherent manipulation is spontaneous emission, although it is suppressed by the fact that the two-photon transition is off-resonant by the detuning Δ relative to the intermediate state $|i\rangle$. The rate of residual spontaneous decay depends on the intensity of the light field I and the off-resonant detuning Δ and is given by

$$P_{\mathrm{sp}} = \frac{\Gamma}{2}\frac{I[I_{\mathrm{sat}}]}{(2\Delta[\Gamma])^2}, \tag{4.9}$$

expressed in terms of the natural linewidth Γ and saturation intensity I_{sat}. Comparing 4.8 and 4.9 it is easily seen, that to further suppress spontaneous emission while keeping the Rabi frequency constant, one needs to operate at higher detunings and laser intensities. So for sufficiently available laser power it is possible to drive a beam splitting process under almost loss-less conditions. The suppression of spontaneous emission is only limited by the available laser power and the use of high power laser systems is beneficial for high fidelity beam splitting. The high-power laser system used in the QUANTUS-1 experiment is presented in chp. 3.

One-photon AC-Stark shift

Apart from actively coupling a transition during a light-pulse manipulation, the sole presence of an off-resonant light field has still an influence on the atomic energy structure. This so called one-photon AC-Stark shift causes a shift of the eigenenergies of the undisturbed Hamiltonian resulting in a frequency shift, dependent on detuning Δ and Rabi frequency Ω of a light field [219]

$$\omega^{\mathrm{AC}} = \frac{\Omega^2}{4\,\Delta}\,. \tag{4.10}$$

To calculate this frequency shift all possible couplings of each present light field to an upper multiplet state have to be taken into account. For a two-photon light field consisting of frequencies ω_1 and ω_2 with a frequency difference ω_{12} the sum over all these couplings is

$$\omega_j^{\mathrm{AC}} = \sum_k \frac{\Omega_{k,1}^2}{4\,\omega_{k,1}} + \sum_k \frac{\Omega_{k,2}^2}{4\,\omega_{k,2}}\,. \tag{4.11}$$

with the respective detunings $\omega_{k,1}$ and $\omega_{k,2}$ to the multiplet state $|k\rangle$ with their respective Rabi frequencies weighted by the Clebsch-Gordon coefficients. In the case of a two-photon light field this results in an additional differential shift of the resonance frequency $\omega_{\mathrm{diff}}^{\mathrm{AC}} \equiv \omega_{\mathrm{e}}^{\mathrm{AC}} - \omega_{\mathrm{g}}^{\mathrm{AC}}$.

Momentum-state coupling: photon recoil and Doppler shift

A two-photon transition as displayed in fig. 4.2 is fully characterized by the transition frequency ω_{eg} as a measure of the energy difference between ground state $|g\rangle$ and exited state $|e\rangle$. Using an atom interferometer for inertial sensing requires to read out the external degrees of freedom, i.e. the atomic motion relative to a reference frame. The projection of the atomic motion to distinct momentum states comes into play, since during the interaction photons do not only transfer energy but as well momentum $\hbar\vec{k}$ to the atoms. Photon pairs transfer their largest momentum $\approx 2\hbar\vec{k}$ for counter-propagating light fields and the smallest ≈ 0 for co-propagating beams as depicted in fig. 4.3(a). In the general case of an n^{th}-order transition the total momentum transferred is the linear combination of n photon pairs scattered from two laser beams

$$n\vec{k}_{\mathrm{eff}} = n\left(\vec{k_{\mathrm{i},1}} - \vec{k_{\mathrm{i},2}}\right) \approx 2n\hbar\vec{k}. \tag{4.12}$$

Hereby the notion $\hbar|\vec{k}_{\mathrm{eff}}| = \hbar k_{\mathrm{eff}}$ is introduced to identify the effective momentum transferred during a two-photon process, not to be confused with the wave vector of single photons denoted by $\hbar|\vec{k}| = \hbar k$. The total momentum transfer $n\hbar k_{\mathrm{eff}} \approx 2n\hbar k$ in a two photon process driven by counter-propagating laser beams is always an integer number $2n$ of photon pairs and can be large, since it may include a large number of photons. Furthermore, the dispersion relation of a free particle is parabolic, in consequence any offset momentum $|\vec{p}| = p_0$ has to be taken into account. The offset $\vec{p}$ can intuitively be explained as the Doppler shift resulting from a motion of the atoms relative to the light fields and returns back to $\vec{p} = 0$ for atoms at rest.

The Rabi model is now employed to calculate the coupling between momentum states. To parametrize the atomic motion dependent on photon recoil and Doppler shift an initial state $|p_0\rangle$ and a n^{th}-order kicked state $|p_n\rangle$ are introduced representing the two momentum states

$$|p_0\rangle \equiv |\vec{p}\rangle \;\text{ and }\; |p_n\rangle \equiv |\vec{p} + \hbar\vec{k}_{\mathrm{eff}}\rangle\,, \tag{4.13}$$

with their respective eigenenergies in an electromagnetic field $\vec{E}$

$$E_{\vec{p}} = \frac{\vec{p}^2}{2m}, \quad E_{\vec{p}+\hbar\vec{k}_{\text{eff}}} = \frac{(\vec{p}+\hbar\vec{k}_{\text{eff}})^2}{2m} \text{ and } \vec{E}(\vec{x},t) = \vec{E}_0\cos(\omega t - \vec{k}_{\text{eff}}\cdot\vec{x}+\phi). \tag{4.14}$$

These give rise to a new Hamiltonian which is solved accordingly to eq. 4.1

$$\hat{H} = \frac{\vec{p}^2}{2m} + E_{\vec{p}+\hbar\vec{k}_{\text{eff}}} |\vec{p}+\hbar\vec{k}_{\text{eff}}\rangle\langle\vec{p}+\hbar\vec{k}_{\text{eff}}| + E_{\vec{p}}|\vec{p}\rangle\langle\vec{p}| - \vec{d}\cdot\vec{E}(\vec{x},t). \tag{4.15}$$

The solution of this system only provides two additional frequencies contributing to the resonance condition of the transition. The Rabi oscillation itself behaves exactly the same and an identical Rabi frequency applies as for the coupling of two internal states in eq. 4.8. The first of these additional terms is the recoil frequency ω_{r} of the two-photon light field, while the second one is the Doppler frequency ω_0 dependent on the initial momentum $\vec{p}$

$$\omega_{\text{r}} = \frac{\hbar\left|\vec{k}_{\text{eff}}\right|^2}{2m} \text{ and } \omega_0 = \frac{\vec{p}\cdot\vec{k}_{\text{eff}}}{m}. \tag{4.16}$$

This coupling in the atomic motion picture between the initial state $|p_0\rangle$ and kicked state $|p_n\rangle$ of an atom is completely independent from any internal energy structure $|a\rangle$ and $|b\rangle$

$$|a,p_0\rangle \equiv |a\rangle\otimes|p_0\rangle \text{ and } |b,p_n\rangle \equiv |b\rangle\otimes|p_n\rangle\,. \tag{4.17}$$

In eq. 4.17 the momentum states $|p_0\rangle$ and $|p_n\rangle$ can be decoupled from the internal energy structure $|a\rangle$ and $|b\rangle$ such that different types of diffraction are possible [65]. If the initial state $|a\rangle \equiv |g\rangle$ is an atomic ground state, the final state can be $|b\rangle \equiv |e\rangle$ or $|b\rangle \equiv |g\rangle$ depending if a state change is included or not as shown in fig. 4.3(b). A coupling including an internal state change is called "Raman"-type diffraction, while the one without is called "Bragg"-type diffraction.

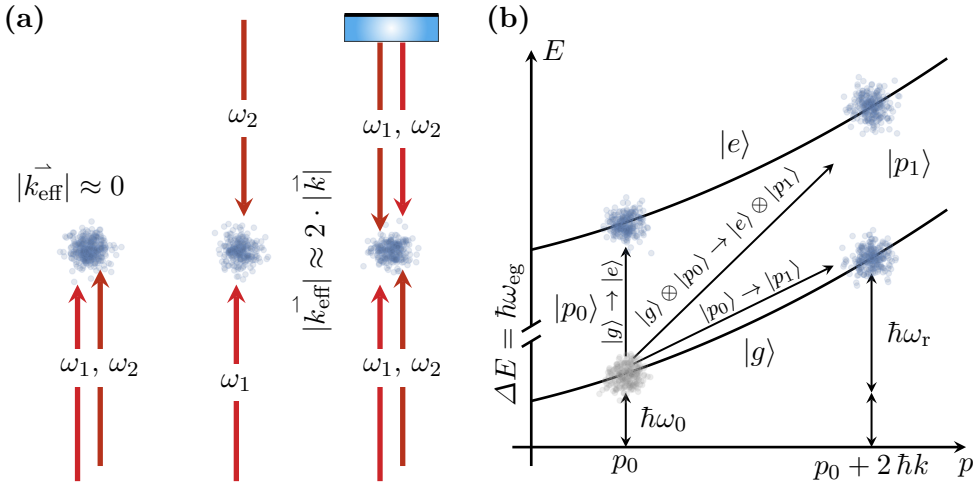

Figure 4.3: Definition of the effective wave vector k_{eff} for the coupling of momentum states depending on beam configuration and the use of a retro-reflection mirror **(a)**. As a result Doppler shift ω_0 and recoil frequency ω_{r} are introduced. Three possible couplings from a ground state $|g\rangle\otimes|p_0\rangle$ to a target state with and without $2\hbar k$ momentum transfer and/or internal state change $|g\rangle \to |e\rangle$ **(b)**.

4.1.2 Bragg and double Bragg diffraction

A method to realize a beam splitter for atoms is Bragg diffraction [220, 221], that is defined analog to the diffraction of electromagnetic radiation from a crystal [222, 223], where an atomic beam or ensemble is diffracted from a traveling light wave following the original Bragg condition

$$E_{\mathrm{kin}} = 4n \cdot \hbar\omega_{\mathrm{r}} = n \cdot \hbar(\omega_1 - \omega_2). \tag{4.18}$$

For the case of first-order diffraction with $n = 1$, this equation gives a very intuitive classical picture of what happens during the scattering process and the corresponding level scheme for the first-order transition is depicted in fig. 4.4. An atom scatters two photons from a traveling light wave if their beat frequency $\omega_1 - \omega_2$ matches the energy E_{kin} an atom has to absorb to proceed upwards on the kinetic energy parabola. Applying the last section's formalism for the two-photon transition, only photon recoil ω_{r} and Doppler shift ω_0 have to be taken into account, defining the transition frequency ω_n which drives the beam splitting process

$$\omega_n = 2n \cdot \omega_{\mathrm{r}} + \omega_0. \tag{4.19}$$

So the Bragg diffraction is a transition exclusively between momentum states $|p_0\rangle$ and $|p_1\rangle$ (or $|p_n\rangle$ in the case of larger momentum transfer) defined in eq. 4.13 and does not rely on any internal energy structure. Another result of the absence of internal state coupling is that, since the initial and target state are equal, it has a vanishing differential AC-Stark shift

$$\omega^{\mathrm{AC}}_{\mathrm{Bragg}} \equiv \omega^{\mathrm{AC}}_{\mathrm{a}} - \omega^{\mathrm{AC}}_{\mathrm{b}} \rightarrow \omega^{\mathrm{AC}}_{\mathrm{g}\rightarrow\mathrm{g}} = 0 + O^2. \tag{4.20}$$

Since the first observation of Bose-Einstein condensates, interference experiments have been performed where condensates are coherently manipulated with Bragg diffraction [61, 62]. The absence of internal state coupling makes Bragg diffraction comparably simple to realize and applicable to a variety of atomic species which do not provide a hyperfine splitting of their ground state [224, 225]. To drive Bragg diffraction with laser light, either a standing waves is used with atoms traveling under an angle [226, 227] or two different retro-reflected frequency components are used. Unlike Raman diffraction no pair of phase-locked lasers is required, because both frequencies to form the lattice can be derived from a single laser. The frequency difference from eq. 4.19 can be generated by acousto-optical modulators if the Doppler shift does not get too large during free fall or after launch.

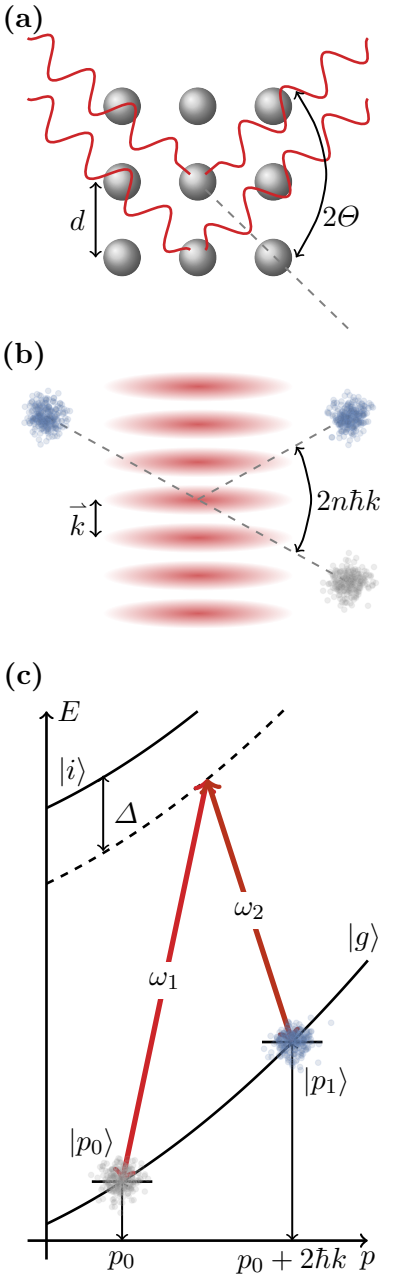

Fig. 4.4: Analogous to a crystalline grating for light **(a)**, atoms are diffracted from a traveling lattice following the Bragg condition **(b)**. The grating constant d in this role reversal between light and matter is replaced by the laser wave length λ. Coupling scheme for first-order Bragg diffraction between $|p_0\rangle$ and $|p_1\rangle$ **(c)**.

Double Bragg diffraction

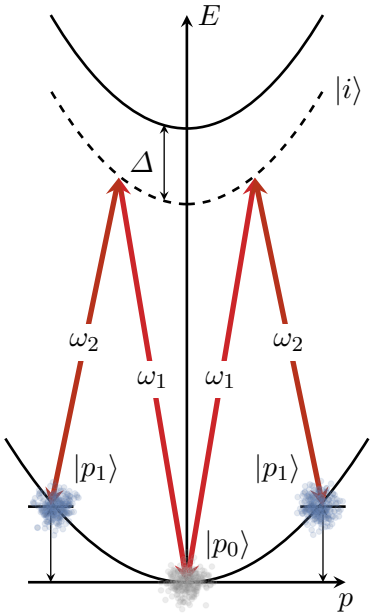

Fig. 4.5: Double Bragg diffraction level scheme driven by two retro-reflected light fields ω_1 and ω_2. Hereby, Δ denotes the detuning to the upper state and ω_r denotes the recoil frequency. The wave function of an atom is simultaneously diffracted in two directions by $\pm 2 \cdot \omega_r$ if the Doppler shift ω_0 vanishes.

A relevant extension on Bragg diffraction is occurring if a retro-reflected pair of laser beams interacts with atoms that are at rest with respect to the beams, such that the Doppler shift ω_0 vanishes. In such a case, the transitions with opposing effective wave vectors are degenerate in frequency and diffract the atoms' wave function in both directions at the same time. The relative momentum splitting between both arms in an interferometer is then increased to $4\hbar k$. The occurrence of this symmetric diffraction is called "double Bragg diffraction", according to the equivalent beam splitter introduced a couple of years ago for Raman transitions [77]. In order to not confuse the two diffraction techniques, the traditional Bragg diffraction can be referred to as "single or uni-directional Bragg diffraction", since only a single pair of laser beams drives the transition, while the other one is off resonant. The basic coupling scheme for first-order double Bragg diffraction is depicted in fig. 4.5. The transition frequency is given by the original Bragg condition in eq. 4.18 with recoil frequency ω_r. However, Rabi oscillations are more complicated, since more states have to be taken into account. The theoretical calculation of the Rabi oscillations has been described in ref. [79]. This kind of beam splitting has several new features for atom interferometry due to the intrinsic symmetry of the diffraction. Most prominently, the population of the output ports does no longer depend on the laser phase $\Delta\phi_{\text{Laser}}$, since both parts of the wave function get the same lasers phases imprinted during each pulse.

More detailed work on the experimental realization of using double Bragg diffraction for a quantum tiltmeter in the QUANTUS-1 experiment can be found in refs. [80, 228]. Double Bragg diffraction is an ideal beam splitting process for a microgravity environment, since there is initially no Doppler effect to lift the degeneracy between the two different beam pairs from retro-reflection. The straight forward way to realize double Bragg diffraction on ground is to implement a beam splitter, which is aligned perpendicular to gravity, such that the Doppler shift due to the free fall vanishes. The experimental challenge is then to align the beam splitter precisely perpendicular to gravity and handle each residual horizontal motion of the atoms to minimize the asymmetry between the diffraction to left and right. With a laser beam along gravity it is in general no longer possible to drive both arms of the symmetric beam splitter with just a pair of two retro-reflected frequencies. As the Doppler shift lifts the degeneracy of the transition during free fall, one beam pair would always be out of resonance with the atoms. Within this thesis, two applications of double Bragg diffraction are shown. The first application is to implement the mirror pulse for the relaunch sequence in sec. 5.3. The second application is to realize a symmetric scalable large momentum transfer beam splitter in combination with an optical lattice in horizontal direction. The possibility to combine double diffraction with an optical lattice has been proposed before [229], but has not been realized until now. This combination offers a beneficial scaling behavior which is investigated in sec. 7.2.

Higher-order diffraction and sequential transitions in the Bragg regime

The Bragg condition in eq. 4.18 does already include the case of scattering more than one photon pair at a time leading to the population of higher-order momentum states $|p_n\rangle$ since ideally every momentum state in between is not in resonance and should not be populated. A level scheme for higher-order transitions is given in fig. 4.6(a). The simultaneous scattering of n pairs of photons has been experimentally realized up to $n = 12$ resulting in a 24 $\hbar k$ large momentum transfer beam splitter [67]. Since the Doppler spacing between each individual Bragg order is only 30 kHz for ^{87}Rb, this leads to the case in which multiple orders can be populated.

Although the resonance frequency of the n$^{\text{th}}$-order Bragg transition is given by the original Bragg condition times the order n in eq. 4.18, the calculation of the transition probability requires further considerations beyond the simple two state assumption [230]. The ratio of laser power I or respective Rabi frequency Ω_{eff} used for driving the transition and the length of the interaction τ are of major importance. The ratio of these parameters defines if a clean oscillation into a single momentum state is possible or if multiple states are always populated, independently of the velocity distribution of the ensemble. These conditions are depicted in fig. 4.6(b), with clean oscillation only possible in the so called "Bragg regime". For the operation in the Bragg regime a generalized transition probability P_n in ref. [230] is given by

$$P_n(\tau) = \sin^2\left[\frac{\int_0^\tau \mathrm{d}\tau' \Omega_n(\tau')}{2}\right] \text{ with } \Omega_n(\tau) = \frac{[\Omega_{eg}(\tau)]^{2n}}{2^{2n-1}\Delta_1 \cdot \ldots \cdot \Delta_{2n-1}}, \tag{4.21}$$

with a new Rabi frequency Ω_n to drive the n^{th}-order transition which requires a quadratic increase in laser power I for a constant Rabi frequency. An approximate solution in ref. [230] shows conditions for a so-called "quasi Bragg regime" in which the probability to couple a single higher-order state is significantly higher as for all other orders via short and intense pulses.

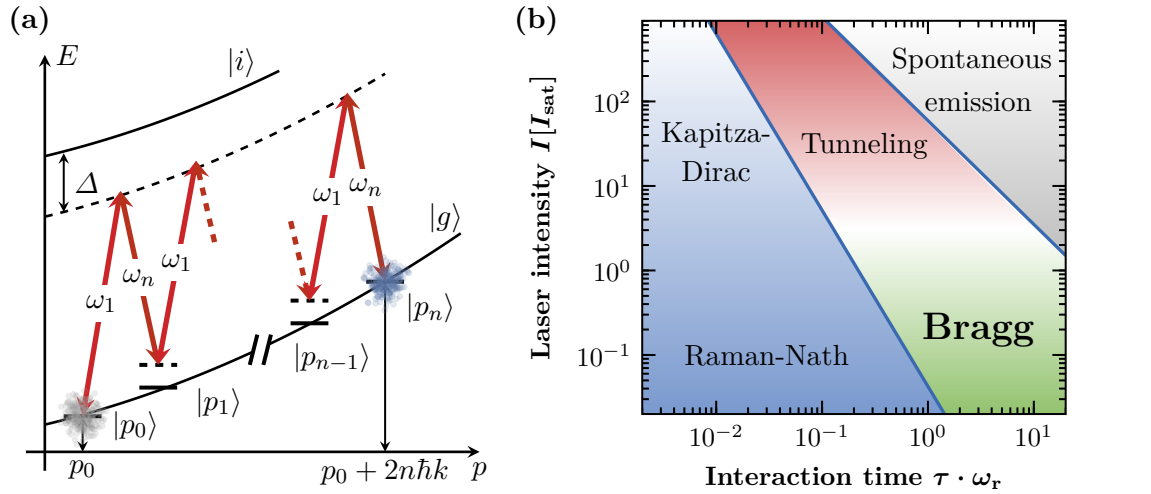

Figure 4.6: Level scheme of the n^{th}-order Bragg diffraction, in which a momentum of $2n\hbar\vec{k}$ is imprinted on the wave packet. The transition frequency is given by multiples of the recoil frequency $2n \cdot \omega_r$ **(a)**. The different diffraction regimes are defined depending on the interaction time τ times the recoil frequency ω_r and laser intensity I in terms of the saturation intensity I_{sat}. Only in the Bragg regime a single diffraction order can be purely populated. Coupling in all other regimes leads to significant losses into other orders or to spontaneous decaying processes **(b)**.

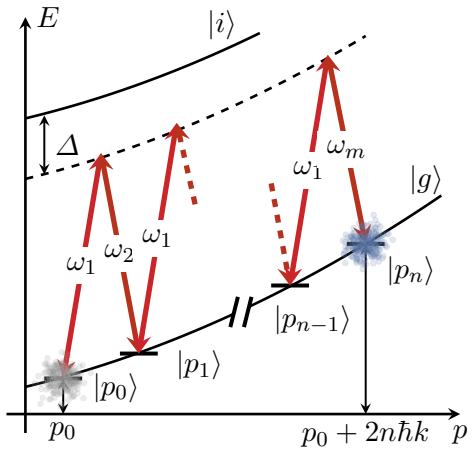

Fig. 4.7: Level scheme for driving sequential first-order transitions to circumvent the necessary increase in laser power. The resonance condition is equal to the Doppler shift obtained in a standing wave. In general, a transition from m to n is calculated according to eq. 4.22.

The necessary increase in laser power to directly drive higher-order Bragg diffraction can be circumvented if one uses sequential pulses. The same momentum transfer is achieved at the cost of a larger total time of the beam splitting process and a more complex waveform. The resonance condition to drive the m^{th} sequential transition with an n^{th}-order Bragg pulse and Doppler shift ω_0 is

$$\omega_{\text{m,n}} = (4m + 2n) \cdot \omega_{\text{r}} + \omega_0. \tag{4.22}$$

In principle, one is free to combine any number of sequential transitions m with any achievable Bragg-order n and obtain a transfer efficiency η_n^m. For example, a sequence with beam splitters transferring $6\,\hbar k$ each allowed for a total splitting of $102\,\hbar k$ [68] or a sequence of first order transitions allowed for $90\,\hbar k$ [70] in total. In our experiment Bragg pulses up to fourth-order can be driven with a reasonable high efficiency, while for even higher orders the transfer efficiency is drastically reduced.

4.1.3 Influence of a velocity distribution

So far, beam splitting is described solely using a single atom picture that is only valid for the case of a highly monochromatic atomic ensemble. Under this condition, for an available maximum laser power I at a given detuning Δ an interaction time τ can always be found, where the amplitude of the transition probability equals unity. The beam splitter efficiency is only limited by fraction of atoms lost due to spontaneous decay $P_{\text{sp}}\tau$ in this case. A finite temperature T and therefore a velocity spread σ_v along the atomic ensemble needs to be taken into account, even for Bose-Einstein condensates this situation may drastically change, as calculated in detail for higher-order Bragg diffraction in ref. [66]. In general, the influence of the velocity distribution is calculated taking into account a distribution of velocities across the ensemble in frequency space, which is for the calculations assumed to be the Gaussian distribution in one dimension

$$f_{1D}(v_x) = \frac{1}{\sqrt{2\pi}\sigma_v}\exp\left(-\frac{(v_x - v_0)^2}{2\sigma_v^2}\right) \text{ with } \sigma_v = \sqrt{\frac{k_{\text{B}}T}{m}}, \tag{4.23}$$

with an arbitrary offset velocity v_0. The Gaussian width σ_v in eq. 4.23 is defined by the ensemble's temperature T_{at}, the Boltzmann constant k_{B} and the single particle mass m. The three-dimensional distribution with $\vec{v}^2 = v_x^2 + v_y^2 + v_z^2$ and offset $\vec{v_0}$ for a uniform σ_v is then

$$f_{3D}(\vec{v}) = \frac{1}{(2\pi)^{3/2}\sigma_v^3}\exp\left(-\frac{(\vec{v} - \vec{v_0})^2}{2\sigma_v^2}\right). \tag{4.24}$$

The excitation probability P for a given velocity $\vec{v}$ takes into account the distribution in eq. 4.24 using the volume element d^3v as a probability for atoms with the velocity v in the distribution

$$P(\tau) = f_{3D}(\vec{v})\,\mathrm{d}^3v \cdot P(\vec{v},\tau) \propto \vec{v} \cdot \vec{k_{\text{eff}}} \equiv v_x'. \tag{4.25}$$

To calculate the total excitation probability as an integral over all velocities in the distribution, one needs to remember the fact, that in eq. 4.7 the detuning δ enters, which is calculated via the projection of the velocity $\vec{v}$ onto the wave vector $\vec{k}_{\text{eff}}$. The three-dimensional integral reduces to a one-dimensional integral over the new velocity v'_x aligned along $\vec{k}_{\text{eff}}$ where offsets $v'_0 = 0$ have been transformed away by central adjustment of the laser frequency

$$P_{1D}(\tau) = \int\int\int f_{3D}(\vec{v}) P(\vec{v},\tau)\,\mathrm{d}^3 v = \int f_{1D}(v'_x,\tau) P_1(v'_x,\tau)\,\mathrm{d}v. \tag{4.26}$$

However, not only the velocity spread σ_v has to be taken into account because an ensemble also has a finite size $\sigma_x = \sigma_y = \sigma_z$ and position $\vec{x}^2 = x^2 + y^2 + z^2$ in a Gaussian beam with a given diameter ω. The finite beam diameter causes a spatially dependent Rabi frequency $\Omega_0(\vec{x})$ due to the changing intensity $I(\vec{x})$ within the beam. For a collimated beam along the x-direction the excitation probability $P(\vec{x},\tau) \sim \vec{x} \cdot \vec{k}_{\text{eff}} \to P(y',z',\tau)$ only depends on the position y' and z' perpendicular to k_{eff}. Similar considerations as in eq. 4.25 lead to a two-dimensional equation

$$s_{2D}(y',z') = \frac{1}{2\pi\sigma_x^2} \exp\left(-\frac{y'^2 + z'^2}{2\sigma_x^2}\right), \tag{4.27}$$

with a Gaussian beam which is centered around the distribution such that $y'_0 = y'_z = 0$. From eq. 4.27 and eq. 4.26 the total transfer efficiency in three dimensions reads as

$$P_{3D}(\tau) = \int\int \mathrm{d}y'\,\mathrm{d}z' \int \mathrm{d}v'_x s_{2D} \cdot f_{1D} \cdot P(y',z',v'_x,\tau), \tag{4.28}$$

which for the previous assumptions is computed knowing only σ_v, σ_x, the beam diameter ω and the Rabi frequency Ω_0. Usually, the velocity distribution f_{1D} is constant in time if no external force is acting, but the spatial distribution s_{2D} is always a function of time, since the cloud spreads out with σ_v. Finding the three-dimensional probability $P(y',z',v'_x,\tau)$ is more complicated if these assumptions are not valid. For example, if the distributions are more complicated, the initial offsets are not vanishing, the beam is not homogeneous or not collimated properly.

Optimized pulse envelopes

The time evolution in section 4.1.1 was derived under certain conditions for the light field, namely that its intensity and frequency are constant during the entire interaction period. Nevertheless, to increase the efficiency of the beam splitting process under experimental conditions, it is advantageous to use different kinds of pulse envelopes. Starting from a simple square or box pulse that was assumed for the Rabi oscillation, the amplitude shape is of the form

$$A_{\text{box}}(t) = A_0 \text{ for } 0 < t < \tau = 1, \tag{4.29}$$

with a fixed amplitude A_0 and a pulse duration τ in arbitrary units. The instantaneous switching on at $t = 0$ and off at $t = 1$ leads to a sinc function as Fourier transform with a width

$$A_{\text{box}}(\omega) = \frac{A_0}{\sqrt{2\pi}} \text{sinc}\left(\frac{\omega}{2\pi}\right) \sim \frac{\sin(\omega)}{\omega} \text{ with } \omega = \frac{2\pi}{t}. \tag{4.30}$$

In contrast, a Gaussian pulse envelope retains its shape also in Fourier space. This is advantageous to optimize the overlap between the Gaussian velocity distribution of the atomic ensemble in eq. 4.23 and the frequency width of the pulse. Since a Gaussian wave form has per definition no

defined borders, there are slightly modified versions of this pulse shape discussed in literature [181, 231], that are from a technical point of view easier applicable and have similar characteristics. For the calculation we assume a pure Gaussian shape, that is cut off far beyond its pulse width. The intensity profile of a Gaussian pulse in time and frequency is defined as

$$A_\sigma(t) = A_0\, e^{-\frac{t^2}{2\sigma_\tau^2}} \text{ and } A_\sigma(\omega) = A_0\, e^{-\frac{\omega^2}{2\sigma_\omega^2}} \text{ with } \sigma_\omega = \frac{2\pi}{2\sqrt{2}\sigma_\tau} \tag{4.31}$$

where σ_τ is the temporal width of the Gaussian and σ_ω the corresponding frequency width. A Gaussian pulse is wider in frequency than the width of the central peak of the sinc function of a box pulse of the same length. But it requires $\sqrt{2\pi}$ larger amplitude to retain the same pulse area. In addition, it does not feature any sidebands, if the slope on the flanks are wide enough, which eliminates an overlap of the sidebands to higher-order momentum states. For Bragg diffraction it is therefore mandatory to use Gaussian pulses. Otherwise, even without other influences, about $\approx 10\%$ of the atoms would be lost into higher orders as illustrated in fig. 4.8(a). For Bragg spectroscopy [232] long box pulses are used instead to achieve a maximum in resolution $\delta\omega \sim \frac{1}{\tau}$.

A method to even increase the velocity acceptance of a beam splitter pulse is the use of adiabatic transfer via a chirped frequency. This technique was introduced for Bragg diffraction in ref. [69] with the use of eight fold inflated tanh-shaped pulsed, following the profile

$$A_{\tanh}(t) = A_0 \tanh(8t)\tanh[8(1-t)] \text{ with } 0 < t < 1. \tag{4.32}$$

The relative laser detuning δ is not fixed during the whole interaction time τ, but rather chirped from $-2\omega_\mathrm{r}$ to $2\omega_\mathrm{r}$, centered around the expected transition frequency. The Fourier width σ_ω is now broadened due to the frequency chirp. A velocity acceptance of roughly $0.7\,\hbar k$ was experimentally demonstrated with a waveform length of $\tau = 300\,\mu\mathrm{s}$ going far beyond anything achievable with other pulses of this length [69]. A comparison of all three pulse shapes is given in fig. 4.8(b). This technique is quite similar to Raman adiabatic passages, that can also be used to transfer momentum with enlarged velocity acceptance at high efficiency [74].

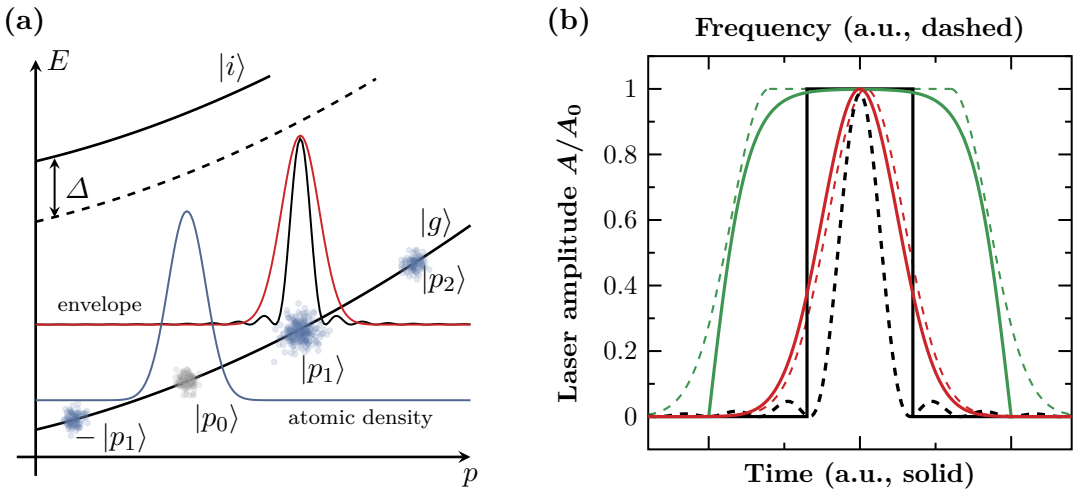

Figure 4.8: Insufficient overlap between atomic density profile and pulse shape in frequency space cause losses into other Bragg orders and reduced excitation probability **(a)**. Amplitude shape (solid) and Fourier transform (dashed) of box (—), Gaussian (—) and tanh (—) pulse envelopes **(b)**.

4.2 Atoms in optical lattices

The possibility to load cold atoms, and in particular Bose-Einstein condensates, into an optical lattice and manipulate them [233–235] offers by itself many interesting physical applications, a few of them listed in ref. [236–240]. For atom interferometry it is of special interest is to manipulate atomic motion by the transfer of a large number of photon momenta with high efficiency by so called Bloch oscillations [241] in an accelerated optical lattice, first experimentally found in 1996, simultaneously by the groups of C. Salomon [242, 243] and M. Raizen [244, 245]. Due to its nearly unlimited capability to manipulate the atomic motion, this technique is sometimes even called an atomic elevator. Instead of the direct absorption and emission of n pairs of photons as in light-pulse interaction, a different approach is used to describe the manipulation of atomic motion in an optical lattice. Based on the assumption of a simple spatially periodic optical potential V_0 with two frequency components a band structure is derived which describes the atomic states in the lattice equivalent to solid state physics (sec. 4.2.1). By introducing an acceleration a, i.e. a force, of the lattice by chirping one of the frequency components, the occurrence of Bloch oscillations is derived. With the accelerated lattice it is possible to sequentially transfer n photon pairs to the atoms with high efficiency (sec. 4.2.2). The calculation of the efficiency to drive Bloch oscillations is given by two main loss mechanism, dependent on the lattice parameters, namely spontaneous emission as derived in eq. 4.9 and losses due to inter-band transitions [246] calculated with the Landau-Zener formalism (sec. 4.2.3).

4.2.1 One dimensional optical potentials

To describe the manipulation of atoms in optical lattices, first the derivation of the dipole potential of a two-photon light field is performed analogous to ref. [247]. In the presence of a light field, the AC-Stark shift from eq. 4.10 leads to a shift of the Eigenvalues of the Hamiltonian $\hat{H}$ in a two-level system dependent on the common detuning Δ to an atomic transition as displayed in fig. 4.9(a). In general, the shift of the eigenenergy E_i of a state $|i\rangle$ due to a coupling $\hat{H}_{int}$ is derived with second-order perturbation theory for a large detuning $\Delta >> \Gamma$ of the light field to

$$\Delta E_i = \sum_{i \neq j} \frac{\left| \left\langle j | \hat{H}_{int} | i \right\rangle \right|^2}{E_i - E_j}. \tag{4.33}$$

For a two-level system with ground state $|g\rangle$, excited state $|e\rangle$ and a dipole interaction of form $\hat{H}_{int} = \vec{d} \cdot \vec{E}$ eq. 4.33 simplifies to

$$\Delta E_{\mathrm{g/e}} = \pm \frac{|\langle e| \vec{d} |g\rangle|^2}{\Delta} |\vec{E}|^2. \tag{4.34}$$

The energy shift is rewritten with the rotating-wave approximation for the dipole matrix element $|\langle e| \vec{d} |g\rangle|^2 = \frac{\Gamma \cdot 3\pi\varepsilon_0 \hbar c^3}{\omega^3}$ the electromagnetic field relation $I = \frac{1}{2}\varepsilon_0 c |E|^2$ as

$$\Delta E_{\mathrm{g/e}} = \pm \frac{2\pi c^2}{3\omega^3} \cdot \frac{\Gamma}{\Delta} I, \tag{4.35}$$

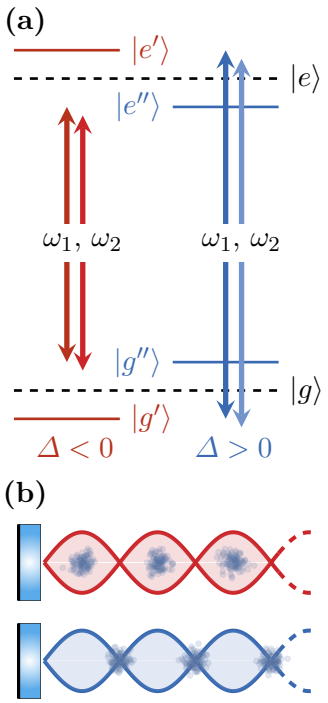

Fig. 4.9: Level shifting by the AC-Stark effect **(a)** and an optical lattice formed by retro-reflection from a mirror **(b)** with red or blue detuning Δ.

with the laser frequency ω, the laser intensity I and the detuning Δ. The energy shift of the ground state ΔE_g is equivalent to the dipole potential V_{dip} of a far detuned light field

$$V_{\mathrm{dip}} = \frac{\hbar\Omega^2}{4\Delta} \equiv \Delta E_{\mathrm{g}} = \frac{\hbar\Gamma}{8} \cdot \frac{I[I_{\mathrm{sat}}]}{\Delta[\Gamma]}, \tag{4.36}$$

in units of the saturation intensity I_{sat} and the natural linewidth Γ using eq. 4.5. If the dipole potential V_{dip} is spatially depended, a force acts on the atoms, as for example in an optical dipole trap [247]. This force on its own only indirectly interacts with the atomic dipole moment and does not drive any transition since the detuning Δ to any atomic resonance is rather large.

An optical lattice in one dimension can be obtained by retro-reflecting a light field from a mirror forming a standing wave as in fig. 4.9(b). The dipole potential of such a lattice is position dependent in forward direction $\vec{x}$ with the periodicity in units of the wave vector $|\vec{k}| = \frac{2\pi}{\lambda}$

$$V_{\mathrm{sw}}(\vec{x}) = V_0 \sin^2\left(\vec{k}\cdot\vec{x}\right) = 4 \cdot V_{\mathrm{dip}} \sin^2\left(\vec{k}\cdot\vec{x}\right) = \frac{1}{2}V_0\left[1-\cos\left(2\vec{k}\cdot\vec{x}\right)\right], \tag{4.37}$$

with an amplitude V_0 larger than V_{dip} by a factor of four arising from the quadratic scaling of the light field's intensity $I \propto |\vec{E}|^2$ during retro-reflection. The amplitude of the potential V_0 can be rewritten in units of the photon recoil energy $E_r = \frac{\hbar^2|\vec{k}|^2}{2m} = \hbar\omega_{\mathrm{r}}$ for simplicity

$$V_0[E_r] = 4 \cdot \frac{\hbar\Gamma}{8 \cdot E_r} \cdot \frac{I[I_{\mathrm{sat}}]}{\Delta[\Gamma]} = \frac{\Gamma}{2 \cdot \omega_{\mathrm{r}}} \cdot \frac{I[I_{\mathrm{sat}}]}{\Delta[\Gamma]}. \tag{4.38}$$

Band model in periodic optical potentials

To find the wave function of an atom inside an optical lattice of the form given in eq. 4.37, usually the assumption of an infinitely elongated potential $V(x)$ is made

$$V(x) = V(x+d), \tag{4.39}$$

with a periodicity d. The stationary Schrödinger equation with the Hamiltonian $\hat{H}$ used to describe an atom with mass m in a potential $V(x)$ following eq. 4.39 is in general given by

$$\hat{H}\,|\Psi_n\rangle = \left(\frac{p^2}{2m} + V(x)\right)|\Psi_n\rangle = E_n\,|\Psi_n\rangle\,. \tag{4.40}$$

Solutions of the stationary Schrödinger equation follows the Bloch theorem with the condition

$$\Psi_{n,q}(x) = \langle x|n,q\rangle = e^{iqx}u_{n,q}(x). \tag{4.41}$$

This means the atomic wave function is separable into a plane wave e^{iqx} with quasi momentum q and an amplitude $u_{n,q}(x)$ with the same periodicity as the original potential $V(x)$. A plane wave therefore is a solution to the Schrödinger equation

$$\hat{H}\,|u_{n,q}\rangle = \left(\frac{(p+\hbar q)^2}{2m} + V(x)\right)|u_{n,q}\rangle = E_n(q)\,|u_{n,q}\rangle \tag{4.42}$$

for the Hamiltonian in eq. 4.40 with the substitution $p \to p + \hbar q$ and gives rise to the eigenenergies $E_n(q)$. These Bloch states $|n,q\rangle$ and the eigenenergies $E_n(q)$ are periodic functions of the

quasi momentum q with periodicity $\frac{2\pi}{l}$. After the usual convention from solid state physics, q can be bound to the interval $]-\frac{\pi}{l}, +\frac{\pi}{l}]$, the so-called first Brillouin zone. A proper definition of the Brillouin zones can be found in a solid state text book, for example in ref. [248].

For the periodic potential of an optical lattice which is described in eq. 4.37, the limits to the first Brillouin zone are given by the wave vector $\vec{k}$ and are bound to the interval $]-\hbar\vec{k}, +\hbar\vec{k}]$. It is only natural to consider atomic ensembles with a momentum distribution much smaller than $\sigma_v << \hbar k$. A Bose-Einstein condensate fulfills this condition [234], as well as any distribution of cold atoms which are velocity filtered in one dimension [242, 243]. Figure 4.10 depicts the dispersion relation between the quasi momentum q and the eigenenergies $E_n(q)$ for increasing lattice depth V_0 in units of the recoil energy starting from $1\,E_r$ up to $100\,E_r$. For a vanishing potential, i.e. $V_0 = 0$ the dispersion relation is the kinetic energy E_{kin} of a free particle and $p = q$ its momentum. For a non-vanishing lattice, band gaps start to open which are increasing with the lattice depth V_0. If the lattice depth is already in the deep lattice regime (i.e. $V_0 > 10\,E_r$), the band curvature is flattening out starting from the lowest band until even a large number of bands remain flat and the band gap energy becomes equidistant. Since the lattice is stationary, an atom loaded into the fundamental band of the lattice at $q = 0$ remains at the potential minimum.

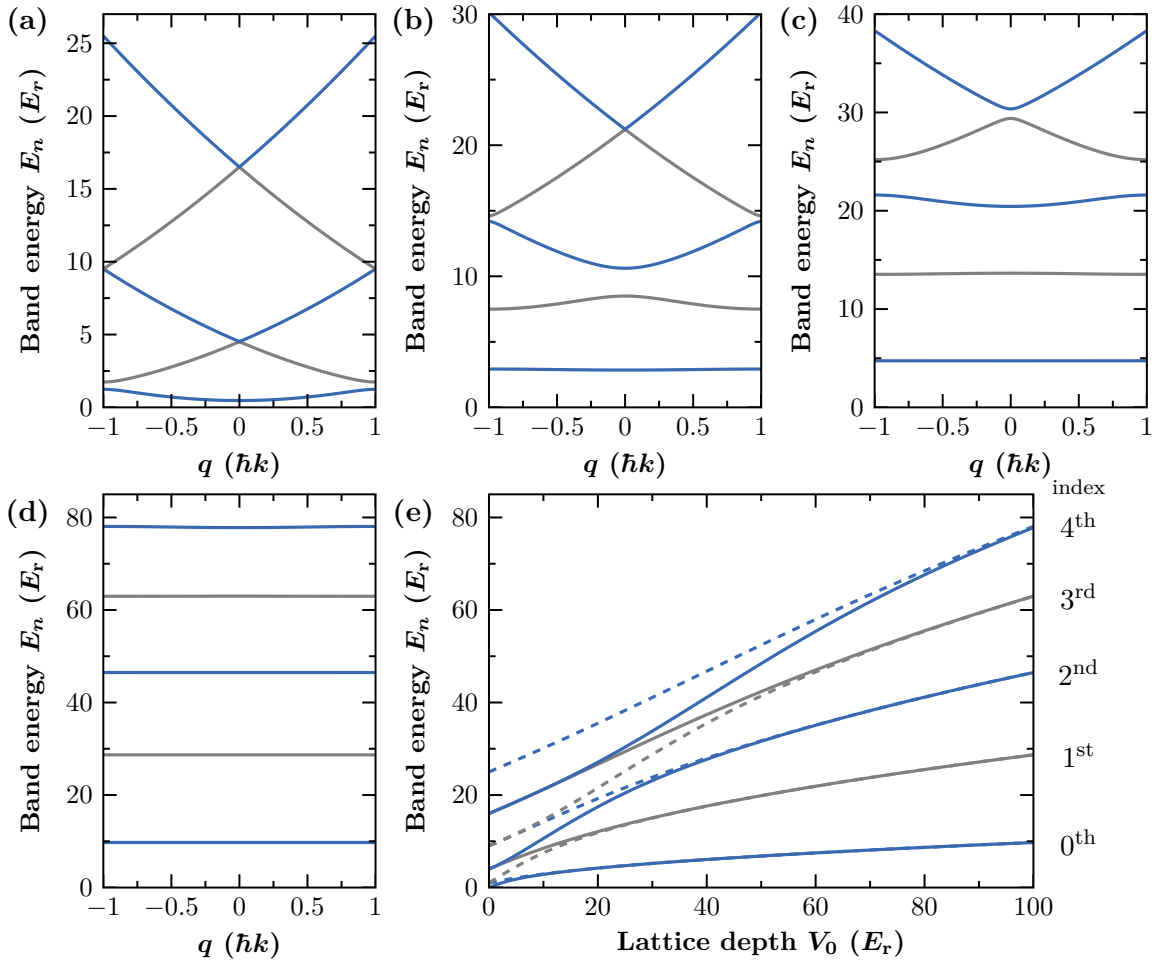

Figure 4.10: Band structure in the first Brillouin zone as a function of the quasi-momentum q for four different lattice depths $V = 1, 10, 25$ and $100\,E_r$ **(a,b,c,d)**. Band energy ΔE plotted as a function of the lattice depth V for $q = 0$ (— and —) and $q = \pm 1$ (- - - and - - -) **(e)**.

4.2.2 Coherent acceleration by Bloch oscillations

The Bloch states $|n,q\rangle$ are stationary solutions for wave functions of an atom inside an optical lattice. Dynamics only enter if an additional force F is introduced, which can be either an external force, like gravity, or an acceleration of the lattice itself. If a spatially uniform force $F = ma$ acts on an atom in an optical lattice, it is no longer stationary [242] and the Bloch states $|n,q\rangle$ are no longer eigenstates of the new Hamiltonian solving the Schrödinger equation

$$\hat{H}\,|\Psi_n\rangle = \left(\frac{p^2}{2m} + V(x) - Fx\right)|\Psi_n\rangle\,. \tag{4.43}$$

Nevertheless, the form of the eigenstates in eq. 4.42 can be maintained

$$\Psi_{n,q(\tau)}(x) = \langle x|n,\tau\rangle\, e^{iq(\tau)x} u(x,\tau) \tag{4.44}$$

with a time dependent quasi momentum $q(\tau) = q(0) + \frac{F\tau}{\hbar}$ and the wave function $u(x,\tau)$ with

$$i\hbar\frac{d}{d\tau}\,|u_{n,q}(\tau)\rangle = \hat{H}_{q(\tau)}\,|u(\tau)\rangle \tag{4.45}$$

which solves eq. 4.43. To avoid inter-band transitions, which will be treated later on, the force F at a given lattice depth V_0 is chosen small enough, such that the adiabatic assumption

$$\left|\left\langle u_{n,q}\left|\frac{\mathrm{d}}{\mathrm{d}\tau}\right|u_{n',q}\right\rangle\right| << \frac{E_n(q) - E_{n'}(q)}{\hbar} \text{ with } (n \neq n') \tag{4.46}$$

is valid. Under the adiabatic assumption the new eigenstates $|u(\tau)\rangle$ are equal to the original stationary Bloch states $|n,q(\tau)\rangle$ with a time dependent quasi momentum with oscillating phase

$$|u(\tau)\rangle = e^{-i\left[\int_0^\tau \frac{E_n(q(t))}{\hbar}\,\mathrm{d}t\right]}\,|n,q(\tau)\rangle\,. \tag{4.47}$$

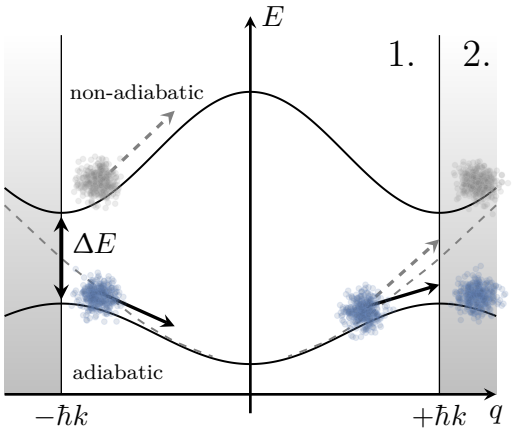

Fig. 4.11: Bloch oscillation in the first Brillouin zone caused by a force F acting on the atoms. If the force is weak enough to avoid inter-band transitions, the atoms undergo an adiabatic acceleration crossing the Brillouin zone.

In momentum space this oscillation causes an acceleration. Because the quasi momentum q changes with a uniform rate v_n, the wave function $\Psi_{n,q(\tau)}(x)$ has a periodicity of the Bloch period $\tau_{Bloch} = \frac{\hbar}{|F|a}$. This Bloch period equals a shift in quasi-momentum of $\frac{2\pi}{l}$, which is a complete crossing of the first Brillouin zone. The expectation value of the velocity v_n of an atom in a Bloch state $|n,q(\tau)\rangle$ is

$$\langle v_n(q(\tau))\rangle = \frac{1}{\hbar}\frac{\mathrm{d}}{\mathrm{d}q(\tau)}E_n(q(\tau)), \tag{4.48}$$

therefore the eigenenergies $E_n(q(\tau))$ are a function of $q(\tau)$. Because the quasi momentum q is swept linearly in time τ, the atomic velocity v_n along the lattice is an oscillating function and the temporal average vanishes $\langle v_n(q(\tau))\rangle = 0$. This oscillation is called the Bloch oscillation and its representation in the first Brillouin zone is depicted in fig. 4.11.

The quasi momentum q in the lowest band of the lattice can be adiabatically projected onto the momentum states $|p_n\rangle$ of a free particle with a difference of $2\,\hbar k$ between subsequent momentum states and a Doppler shift ω_0. This projection has to fulfill the adiabatic criterion

$$\left|\left\langle 1,q\left|\frac{\mathrm{d}}{\mathrm{d}\tau}\hat{H}\right|0,q\right\rangle\right| << \frac{E_1(q)-E_0(q)}{\hbar} \rightarrow \frac{\mathrm{d}}{\mathrm{d}\tau}V_0 << 16\sqrt{2}\frac{E_\mathrm{r}}{\hbar}V_0[E_\mathrm{r}]^{3/2}, \tag{4.49}$$

that the change in the potential $\frac{\mathrm{d}}{\mathrm{d}\tau}V_0$ has to be much slower than the energy difference between the bands to avoid inter-band transitions. In the experiment atoms are coherently accelerated with Bloch oscillations in the fundamental band by a linear chirp α of the laser frequency difference $\delta\omega$ of a two-photon light field. The accelerated lattice generated by this chirp is very well controllable and allows to efficiently couple momentum states $|p_0\rangle \rightarrow |p_n\rangle$ by transferring stepwise $2\,\hbar k$ to the atoms as depicted in fig. 4.12. Initial and target frequency of the chirp can be calculated using the conventions for sequential two-photon transitions in eq. 4.22.

The acceleration a caused by an optical lattice is given by the laser wavelength λ and the change rate, i.e. the chirp α, of the relative laser frequency $\delta\omega$

$$a \equiv \frac{\lambda}{4\pi}\left|\frac{\mathrm{d}}{\mathrm{d}\tau}\delta\omega(\tau)\right| = \frac{\lambda}{4\pi}\alpha. \tag{4.50}$$

If the atoms are initially loaded into a co-moving lattice at $\delta\omega(0)=\omega_0$, the chirp in time τ_acc is given by the recoil frequency ω_r and photon pairs n which should be scattered during the acceleration

$$\delta\omega(\tau_\mathrm{acc}) = \omega_0 + \tau_\mathrm{acc}\left|\frac{\mathrm{d}}{\mathrm{d}\tau}\delta\omega(\tau)\right| = \omega_0 + 4n\cdot\omega_\mathrm{r}. \tag{4.51}$$

Photon pairs are scattered from the light field in steps of the Bloch period $\tau_{Bloch} = \frac{2\,\hbar k}{ma}$ and each step transfers $2\,\hbar k$ of momentum to the atoms.

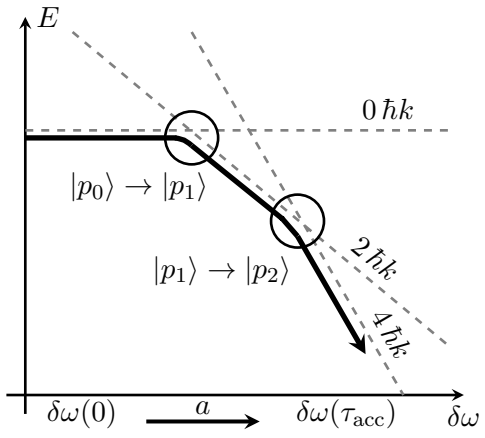

Fig. 4.12: Scheme of Bloch oscillations in the momentum-state picture as adiabatic transfer of $2\,\hbar k$ between two momentum states [243].

Spatial localization and Wannier-Stark states

The band model description so far considers a wave function of the atoms which is completely delocalized along the lattice. In general, this description is incomplete, but the Bloch states $|n,q(\tau)\rangle$ can be used to describe (quasi-)stationary states for the localization of the atomic wave function in several lattice sites [144, 249, 250]. In a non-accelerated lattice, the energy of all states is degenerate in each lattice site. Only in the case of a non-vanishing acceleration $a \neq 0$, the degeneracy is lifted and is more conveniently described by so called Wannier-Stark states [251, 252] whose detailed mathematical description can be found in ref. [253, 254].

Figure. 4.13 shows the spatial distribution of the wave function $|\langle z|W_\mathrm{m}\rangle|^2$ for a non-accelerated lattice aligned along gravity with two different depths $V_0 = 3\,E_r$ and $V_0 = 10\,E_r$ following the example given in ref. [255]. In the case of the deeper lattice already strong localization occurs, while for shallow lattices a spread over many lattice sites is still present. This spread would allow atoms to tunnel between neighboring lattice sites with distinct probability after a certain holding time and are lost. To avoid tunneling effects between different lattice sites it is advisable to operate in the deep lattice regime ($V_0 > 10\,E_r$), where also inter-band transitions are suppressed.

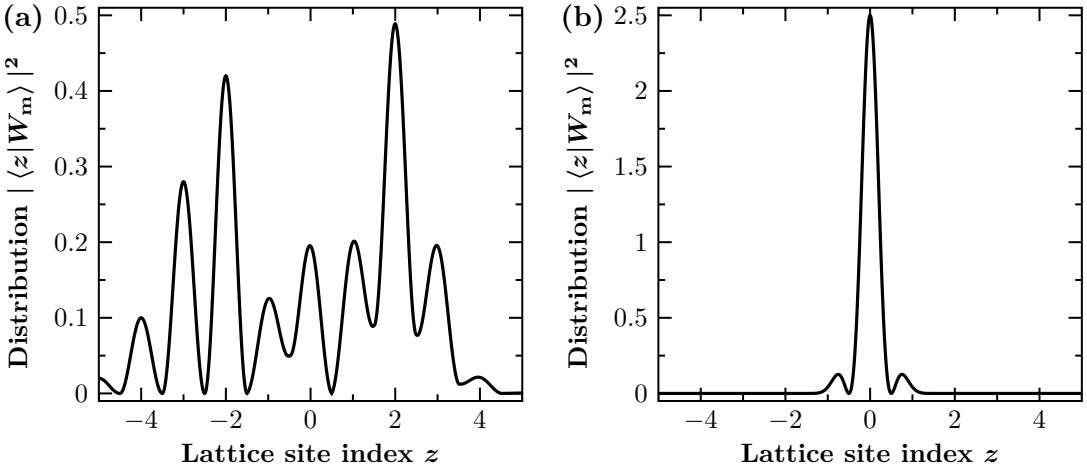

Figure 4.13: Spatial localization obtained from Wannier-Stark states for a non-accelerated lattice aligned along gravity with two different depths $V_0 = 3\,E_r$ **(a)** and $V_0 = 10\,E_r$ **(b)** following ref. [255]. For the deeper lattice the wave function is already strongly localized in a single lattice site.

4.2.3 Landau-Zener formalism

To get an estimate on the efficiency to drive Bloch oscillations and to transfer momentum, two main loss mechanisms have to be considered. The first one is spontaneous emission calculated according to eq. 4.9 where the time used for the acceleration τ_{acc} is of the order of several milliseconds. Although the detuning Δ is large, there is an appreciable fraction of atoms lost due to spontaneous scattering. The surviving fraction of atoms after the acceleration time τ_{acc} is

$$\eta_{\mathrm{sp}} = 1 - (P_{\mathrm{sp}}\tau_{\mathrm{acc}})\,. \tag{4.52}$$

The second loss mechanism arises due to insufficiently suppressed inter-band transitions, because the lattice is not infinitely deep and the transfer should happen as fast as possible. For the assumption of a lattice generated with just two counter-propagating frequency components with difference $\delta\omega$, the chirp $\alpha = \frac{4\pi}{\lambda}a$ of the lattice which is needed to transfer n pairs of photons during the time τ_{acc} has to follow the adiabatic criterion

$$\left|\frac{\mathrm{d}}{\mathrm{d}\tau}\delta\omega\right| = n\omega_{\mathrm{r}}/\tau_{\mathrm{acc}} \equiv \alpha << \Omega_{\mathrm{bg}}^2. \tag{4.53}$$

To calculate the efficiency of the momentum transfer depending on the properties of the light field, the Landau-Zener formalism [246] is used. The formalism gives rise to a simple formula, that calculates the surviving fraction of atoms for a given acceleration and band gap energy Ω_{bg}

$$\eta_{\mathrm{LZ}} = \left[1 - e^{-\frac{\pi}{2}\frac{\Omega_{\mathrm{bg}}^2}{\alpha}}\right]^n. \tag{4.54}$$

The power to the number of transitions n occurs because an inter-band transition may occur at each crossing of the Brillouin zone, i.e. whenever a photon pair is scattered. The total surviving fraction of atoms after the acceleration is given by the product of both fractions $\eta_{\mathrm{tot}} = \eta_{\mathrm{LZ}}\eta_{\mathrm{sp}}$ from eq. 4.52 and eq. 4.54. For shallow lattices often the effective two-photon Rabi frequency $\Omega_{\mathrm{eg}} = \frac{V_0[E_r]\cdot\omega_{\mathrm{r}}}{2}$ is used instead of the band gap Ω_{bg} which spares to solve eq. 4.42 to find the band

structure. For lattice depths larger than $V_0 > 10\,E_r$ using Ω_{eg} underestimates the Landau-Zener losses when the slope of band gap energy starts to decrease. Figure 4.14(a,b) shows two different ways to parametrize the Landau-Zener losses depending on the lattice depth V_0. Either, only two photons are transferred in different times τ_{acc}, where spontaneous emission is still insignificant, or the time is left constant to $\tau_{\mathrm{acc}} = 1\,\mathrm{ms}$ while the photon transfer n is increased.

In ref. [229, 256] the simple formula from eq. 4.54 is extended to the treatment of a superposition of two different momentum states by introducing an off-resonant transition in an excited band. A similar behavior is expected if multiple lattices have to be taken into account during the acceleration of atoms in a single momentum state. This happens for example, if the two-photon light field is not purely generated by just two opposing laser beams but is rather generated by two frequency components which are retro-reflected from a mirror surface. In this dual-lattice configuration there are two moving lattices with opposing chirp rate, distinguishable by the Doppler shift ω_0. Figure 4.14(c) displays the influence due to this off-resonant transition for the transfer of two photon momenta in different acceleration times τ_{acc} and fig. 4.14(d) shows the decrease of this effect with increasing band index of the off-resonant band.

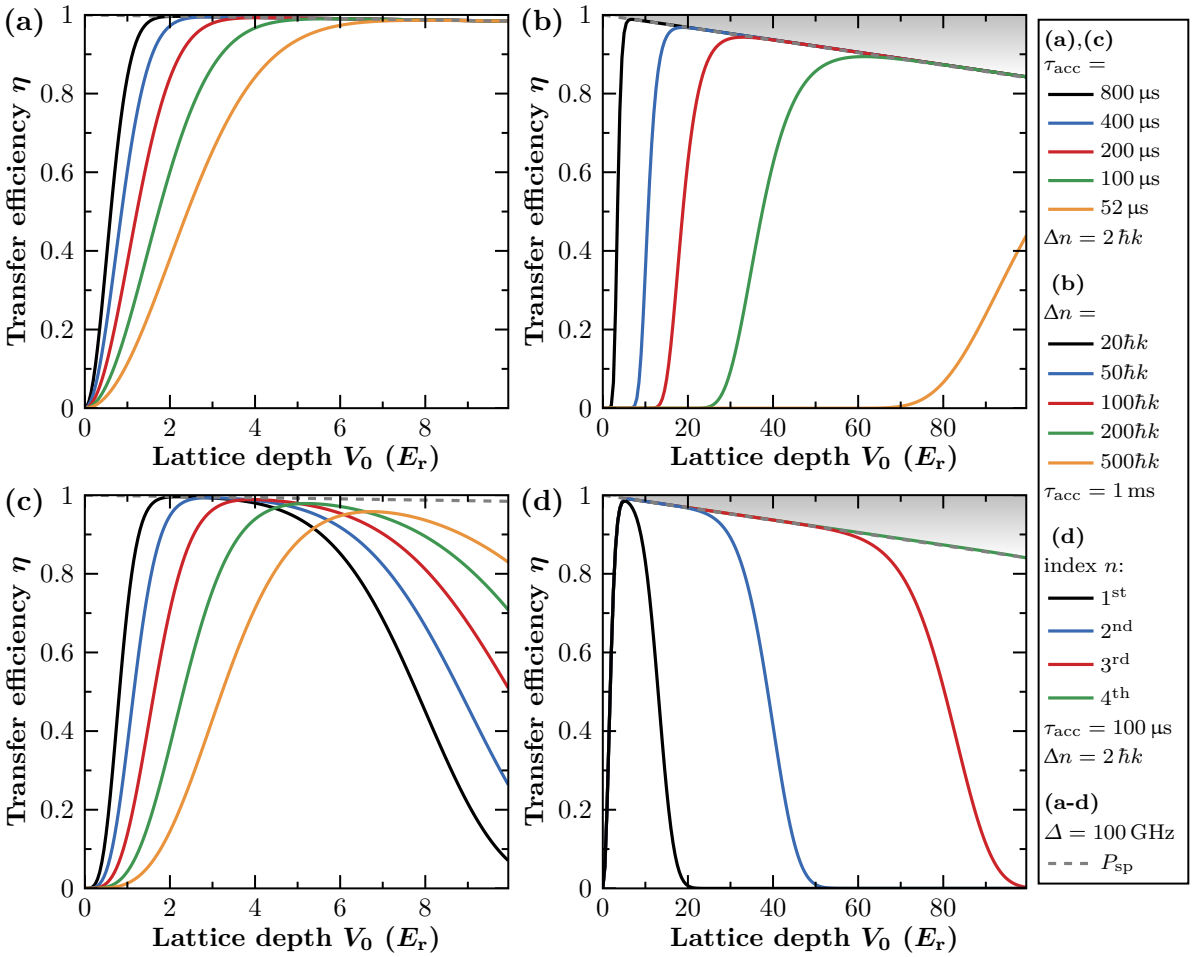

Figure 4.14: Landau-Zener losses for a single lattice parametrized by acceleration time τ_{acc} **(a)** or number of transferred photons n **(b)**. Influence of a parasitic lattice or a superposition of 0 and $2\,\hbar k$ parametrized by acceleration time τ_{acc} **(c)** which decays with increasing band index n **(d)**.

4.3 Mach-Zehnder interferometer

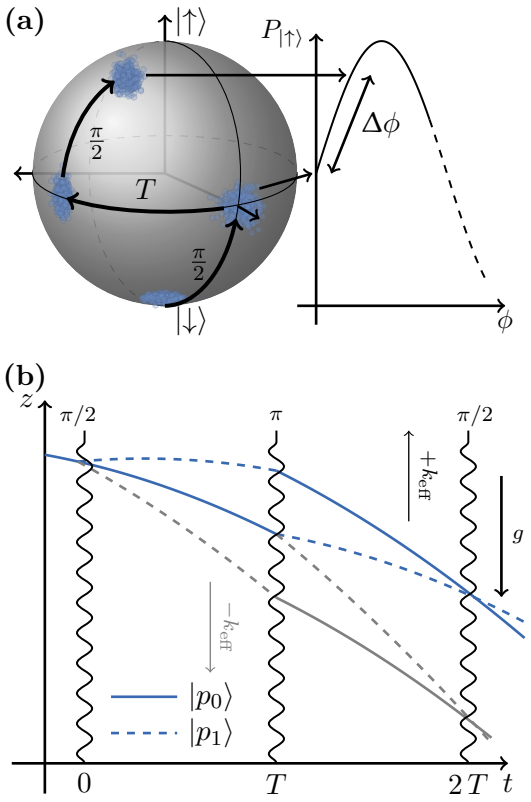

Fig. 4.15: Illustration of the Ramsey experiment in spin representation on the Bloch sphere **(a).** Space-time diagram of a Mach-Zehnder interferometer realized by a three pulse sequence **(b)** consisting of an initial $\frac{\pi}{2}$-pulse to split the atomic wave function, a π-pulse to mirror the imprinted momentum and a final $\frac{\pi}{2}$-pulse to project the probability amplitudes of the wave function onto classical populations.

All basic principles to operate an atom interferometer can be understood in an analogous way as the famous Ramsey experiment of separated oscillatory fields [257]. In this experiment a two-level atom is interacting with pulses of electromagnetic radiation at two different instants. The time T between the two interactions is called pulse separation, or free evolution time, because here the system evolves freely. The population of the two states in the superposition may evolve with a different frequency as the electromagnetic field and accumulates a phase $\Delta\phi$ with respect to the driving electromagnetic radiation. The Ramsey experiment is illustrated with the spin precession representation on the Bloch sphere depicted in fig. 4.15(a).

The pulse separation time T in a Ramsey experiment causes a separation of both wave packets over time if momentum is transferred during the interaction. Such a separation leads to a decay of the oscillation amplitude until the interference completely vanishes and, hence, sets a limit on the time T. The time T can be extended by inversion of the motional state inside the atom interferometer and form a topology which is closed in momentum space. The straight forward way to achieve such a topology is the application of additional interferometer pulses which perfectly preserve the coherence of the interference. Appropriately chosen, the wave packets always have a perfect final overlap independent of the time spend in the interferometer.

A prominent example of a closed interferometer topology is the Mach-Zehnder-type geometry, or short the Mach-Zehnder interferometer (MZI). This topology is defined analogue to its optical equivalent with three different interactions, where the wave function is split up, redirected and then recombined in the end. In the Rabi formalism from sec. 4.1.1, the sequence reads as $\frac{\pi}{2}-\pi-\frac{\pi}{2}$, with two equally long pulse separation times T. Quantum mechanically, the sequence consists of an initial $\frac{\pi}{2}$-pulse to split the atomic wave function and create a superposition of two different momentum states $|p_0\rangle$ and $|p_1\rangle$. A π-pulse reverses these momentum states after a time T to achieve a final overlap of the trajectories after $2T$, when a final $\frac{\pi}{2}$-pulse projects the wave function onto classical populations. In fig. 4.15(b) the space-time diagram of a Mach-Zehnder interferometer is depicted with the atomic trajectories (bend under the influence of gravity g) for a wave vector $\pm k_{\mathrm{eff}}$ directed upwards and downwards. Different to the first realization of a Raman-type light-pulse interferometer by M. Kasevich and S. Chu published in 1991 in ref. [7] there is no intrinsic internal state change connected to the topology. The following sections contain the output phase derivation and the noise assessment of the Mach-Zehnder interferometer.

4.3.1 Sensitivity to inertial forces

The theoretical work to demonstrate that Mach-Zehnder interferometers of the geometry described above are sensitive to different quantities of inertia has been performed prominently by C. Bordé at the end of the 1990's and can be read in detail in refs. [258–260]. In general, the output phase $\Delta\phi$ of an atom interferometer [261] is expressed by three different contributions

$$\Delta\phi = \Delta\phi_{\mathrm{Laser}} + \Delta\phi_{\mathrm{Path}} + \Delta\phi_{\mathrm{Split}}. \tag{4.55}$$

A separation phase $\Delta\phi_{\mathrm{Split}}$ is entering due do insufficient overlap of the wave packets at the outputs ports and vanishes if the interferometer closes perfectly. The second contribution is the imprinted laser phase during the pulses including single- and two-photon light shifts

$$\Delta\phi_{\mathrm{Laser}} = \phi_1 - 2\phi_2 + \phi_3 + \Delta\phi^{\mathrm{AC}} + \Delta\phi^{\mathrm{2ph}}. \tag{4.56}$$

The last pulse imprinting ϕ_3 is usually used to modulate the interferometer signal on purpose with a phase jump, otherwise all phases cancel out. Light shifts may lead to an offset shift which is in first order dependent on the difference in phase imprinted during the first and last pulse

$$\Delta\phi^{\mathrm{AC}} = \frac{\omega_3^{\mathrm{AC}}}{\Omega_{\mathrm{eff}}} - \frac{\omega_1^{\mathrm{AC}}}{\Omega_{\mathrm{eff}}} \text{ and } \Delta\phi^{\mathrm{2ph}} = \phi_3^{\mathrm{2ph}} - \phi_1^{\mathrm{2ph}}. \tag{4.57}$$

Different to Raman diffraction, where the intensity ratio of the two frequency components is properly adjusted [85, 262], the AC-Stark shift is intrinsically suppressed in Bragg diffraction. The contribution of the two-photon light shift is calculated in sec. 6.4.1 according to ref. [152].

The third term $\Delta\phi_{\mathrm{Path}}$ describes the phase arising from the propagation of the atoms during the interrogation with the action S_{cl} integrated along the Lagrangian L of the classical trajectories $x(t)$

$$S_{\mathrm{cl}} = \oint_0^{2T} L[x(t),\dot{x}(t)]\,\mathrm{d}t. \tag{4.58}$$

The phase shift due to inertial effects can be described by using only the laser phase ϕ_{Laser}, since separation and propagation phase nearly cancel. The two leading-order contributions to the sum in eq. 4.55 are the gravitational acceleration

$$\Delta\phi_{\mathrm{Grav}} = \vec{k}_{\mathrm{eff}} \cdot \vec{g} T^2 \tag{4.59}$$

and the Sagnac effect due to the rotating Earth

$$\Delta\phi_{\mathrm{Rot}} = 2\vec{k}_{\mathrm{eff}} \cdot (\vec{\Omega}_{\mathrm{E}} \times \vec{v}) T^2. \tag{4.60}$$

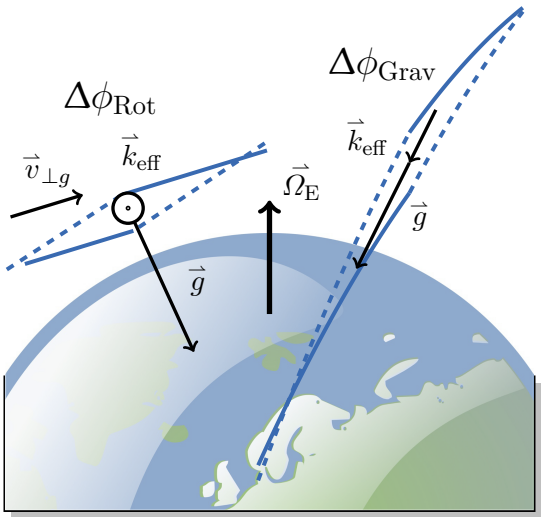

Fig. 4.16: A Mach-Zehnder interferometer on ground can be tailored to be sensitive to gravity or the rotation of the Earth depending on the projection of $\vec{v}$ and $\vec{k}_{\mathrm{eff}}$ to $\vec{g}$ and $\vec{\Omega}_{\mathrm{E}}$.

Figure 4.16 illustrates how to tailor an atom interferometer to maximize the sensitivity to gravity or the rotation of the Earth depending on projection of the atomic velocity $\vec{v}$ and the beam splitter orientation $\vec{k}_{\mathrm{eff}}$ to gravity. A more generalized formalism to express higher-order phase shifts by a Taylor expansion has been described in ref. [263] and the next term has recently been observed [264].

4.3.2 Sensitivity function formalism

With the help of the sensitivity function formalism, that was derived in detail in ref. [265], the influence of several noise contributions onto an atom interferometer can be calculated. The response of the interferometer output $\delta P(t,\delta\phi)$ to an infinitesimal change in phase $\delta\phi$ due to some external influence can be expressed with a weighting function defined by

$$g(t) \equiv 2 \lim_{\delta\phi\to 0} \frac{\delta P(t,\delta\phi)}{\delta\phi} \text{ and } G(\omega) \equiv \frac{H(\omega)}{\omega}. \tag{4.61}$$

The weighting function $g(t)$ is introduced together with a transfer function $H(\omega)$ which is derived from its Fourier transform $G(\omega)$. For a Mach-Zehnder interferometer with a pulse separation time T and all equal pulse times τ, the weighting function is defined piecewise as

$$g_{\mathrm{MZI}}(t) = \begin{cases} -\sin(\Omega_{\mathrm{eff}}\, t) & : 0 < t \le \tau \\ -1 & : \tau < t \le T + \tau \\ +\sin\left(2 \cdot \Omega_{\mathrm{eff}}\,(t - T - \frac{3}{2}\tau)\right) & : T + \tau < t \le T + 2\,\tau \\ +1 & : T + 2\,\tau < t \le 2\,T + 2\,\tau \\ +\sin(\Omega_{\mathrm{eff}}\,(t - 2\,T - \tau)) & : 2\,T + 2\,\tau < t \le 2\,T + 3\,\tau \\ 0 & : \text{at all other times.} \end{cases} \tag{4.62}$$

If a disturbance acts on the atoms during the interrogation, this will cause a phase shift. An integration over all disturbances caused by any time dependent frequency change $\omega(t)$ determines the bias phase shift and the phase noise density $S_\phi(\omega)$ observed at the output ports

$$\Delta\phi = \int_{-\infty}^{\infty} g(t)\,\omega(t)\,\mathrm{d}t \text{ and } (\sigma_{\Delta\phi})^2 = \int_{-\infty}^{\infty} |H(\omega)|^2 S_\phi(\omega)\,\mathrm{d}\omega. \tag{4.63}$$

Fig. 4.17(a) visualizes the weighting function g_{MZI} of a Mach-Zehnder interferometer consisting of two subsequent Ramsey experiments with inverted phase. The shape of the curve exhibits the response of the atom interferometer to noise sources in time. For example, frequency noise of the beam splitter laser cancels out due to the inversion of the phase shift with the π-pulse. The transfer function $H_{\mathrm{a}}(\omega) = \frac{k_{\mathrm{eff}}}{\omega^2} H(\omega)$ displayed in fig. 4.17(b) shows the response to accelerations.

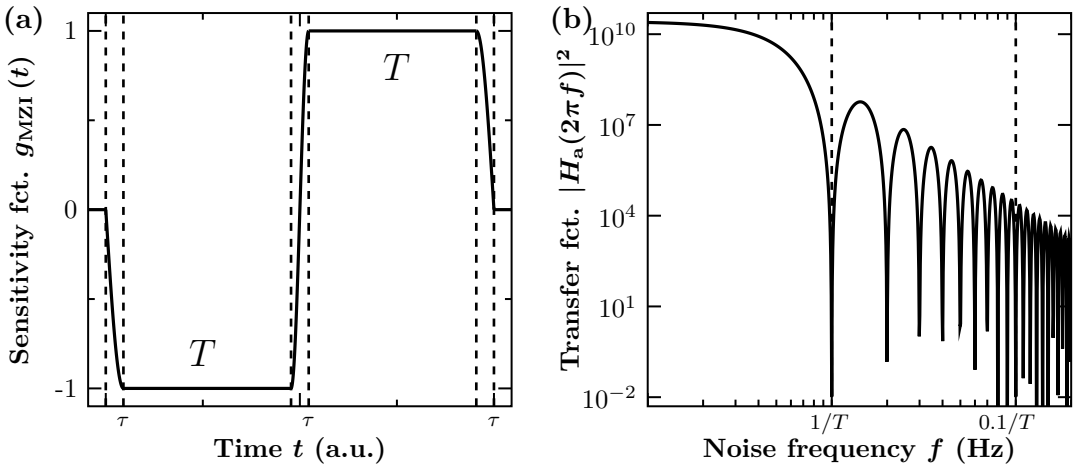

Figure 4.17: The sensitivity function g_{MZI} of a MZI **(a)** and its transfer function to accelerations **(b)**.

4.3.3 Output phase evaluation

In the experiment, the pulse separation time T denotes the time in between two subsequent waveforms of a beam splitter pulse as schematically depicted in fig. 4.18(a). If the duration of these waveforms τ is not negligible short compared to T, a recalculation of the interferometric phase $\Delta\phi_{\mathrm{Grav}}$ has to be performed [265–268]. To adapt this recalculation for Gaussian-shaped pulses, the pulse separation T is denoted by $T' = T + (\tau - \sqrt{2\pi}\sigma_\tau)/2$ and treat the beam splitter pulses as box-shaped pulses of length $\tau' = \sqrt{2\pi}\sigma_\tau$ for equally long π- and $\frac{\pi}{2}$-pulses. It is easy to understand, that the influence of this recalculation gets smaller for larger T, since the duration of the waveforms does not change and gets negligible in the limit of $T >> \tau$. With these denotions, the recalculation for ideal $\frac{\pi}{2}$-pulses is according to literature [265–268] a simple Taylor expansion in orders of $\frac{\tau'}{T'}$, which is cut off here after the first order correction for an ideal $\frac{\pi}{2}$-pulse

$$\Delta\phi_{\mathrm{Grav}} = g \cdot k_{\mathrm{eff}} T'^2 \left[1 + \left(1 + \frac{2}{\pi}\right)\frac{\tau'}{T'} + ...\right]. \tag{4.64}$$

The laser phase $\Delta\phi_{\mathrm{Laser}}$ accumulated in an atom interferometer does not only depend on the relative laser phase at each beam splitter pulse $\phi_{1,2,3}$, but also on the method used to adjust the relative laser frequency $\Delta\nu(t)$ over time. During free fall the resonance frequency ω_{eg} of the transition changes with the Doppler effect, that was derived in eq. 4.16. This effect needs to be accounted for by changing the detuning $\Delta\nu(t)$ after a certain free-fall time ToF. The appropriate value for the chirp to stay on resonance is estimated via

$$\Delta\nu(t) = \frac{\delta\omega(t)}{2\pi} \approx \left(\frac{2\pi g \cdot \mathrm{ToF}}{\omega_{\mathrm{r}}} - 1\right)\frac{\omega_0}{2\pi} \tag{4.65}$$

with ω_0 denoting the Doppler frequency and ω_{r} the recoil frequency of the beam splitting transition. Experimentally, this detuning has to be more precisely adapted to any non-vanishing initial velocity along the beam splitting direction determined by Bragg spectroscopy, since already a wrong detuning of the order of one or two kilohertz leads to a reduced excitation probability. Two possible solutions to implement this frequency change in the experiment yield the same interferometric output phase $\Delta\phi_{\mathrm{Laser}}$ are depicted in fig. 4.18(b). The relative laser detuning $\Delta\nu(t)$ can either be chirped continuously over the whole interrogation time with a rate $2\pi\alpha = \frac{\mathrm{d}\Delta\nu}{\mathrm{d}t}$ or stepped right in the middle between two subsequent pulses by $2\pi\alpha T$. Using frequency steps has the disadvantage, that the frequency is constant during the interaction time τ,

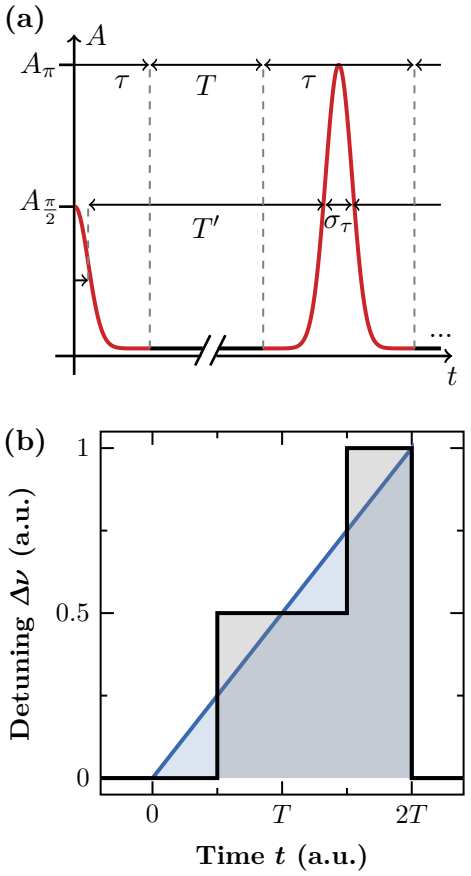

Fig. 4.18: Scheme for the phase shift recalculation **(a)**. To remain resonant, the laser detuning $\Delta\nu(t)$ can be either chirped at a constant rate over the whole interrogation period or two frequency steps are applied in the middle of both halves of the interrogation period **(b)**.

while the atoms are still falling. This might lead to a reduced excitation of longer pulses probability due to off-resonant driving as well as to a bias phase shift if the step is not applied appropriately. Frequency steps are easier to realize for most RF sources and for typical short pulses the reduction in efficiency is small due to their rather wide Fourier width.

Chirping the laser frequency is not only used to remain at the resonance. Moreover, the chirp rate defines the acceleration $a = 2\pi\alpha/k_{\text{eff}}$ of the wave fronts of the Bragg lattice during free fall. The adjustment of $2\pi\alpha$ can be used to modulate the interferometer output $\Delta\phi$ following

$$\Delta\phi(\alpha,T) = (k_{\text{eff}} \cdot g - 2\pi\alpha)T^2. \tag{4.66}$$

This chirp rate measurement is commonly used to realize an atomic gravimeter, since eq. 4.66 relates the output of the atom interferometer $P(\Delta\phi)$, which depends on the gravitational acceleration, to the two parameters T and α that can experimentally be controlled very well. To extract g, all that is needed is to evaluate the output phase of the atom interferometer with one parameter fixed, while the other one is varied. Figure 4.19 shows the output of an atom interferometer depending on the pulse separation time T for three different values of $\frac{2\pi\alpha}{k_{\text{eff}}} = 0, \frac{3}{4}\,g$ and g. The closer α is to the gravitational acceleration g in this picture, the slower the oscillation chirp gets until for $\frac{2\pi\alpha}{k_{\text{eff}}} = g$ the oscillation vanishes completely. In favor of a simpler picture of this principle the fact is neglected that, if the chirp rate α is too different from the free-fall rate g, the excitation vanishes due to the Doppler shift. In a real experiment the chirp rate only differs from the gravitational acceleration by less than one percent.

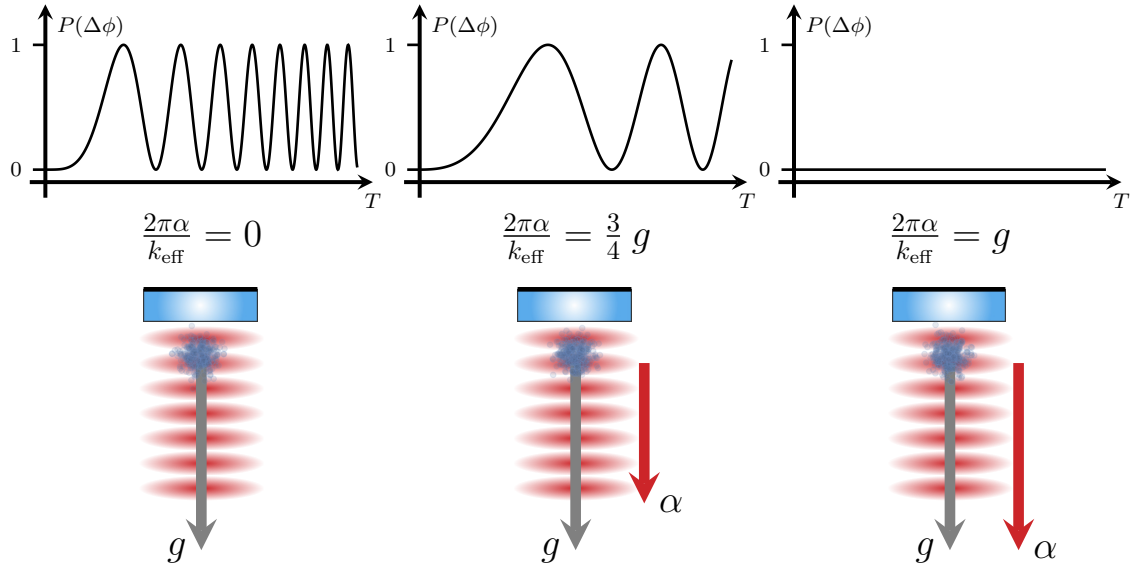

Figure 4.19: Chirp rate measurement in an atomic gravimeter to extract the local gravitational acceleration g. The output of an atom interferometer $P(\Delta\phi)$ is evaluated for different chirp rates α of the laser frequency and respective lattice wave front accelerations $\frac{2\pi\alpha}{k_{\text{eff}}} = 0, \frac{3}{4}\,g$ and g. For increasing pulse separation time T a chirped sinusoidal oscillation is obtained whose chirp rate is decreasing with increasing α and finally vanishes for $\frac{2\pi\alpha}{k_{\text{eff}}} = g$. (This picture is an adaption from fig. 2.4 in ref. [262].)

CHAPTER 5

Implementation of the experimental methods

The atom-chip gravimeter is implemented in the QUANTUS-1 apparatus using the setup illustrated in fig. 5.1. All atom-optics operations are performed in a cube of less than one centimeter side length below the atom chip. In a nutshell, each experimental sequence consists of three parts illustrated in fig. 5.2(a). These parts are: I. the preparation, II. the interferometry and III. the detection. The baseline on which Bose-Einstein condensates can be detected on the CCD detector is roughly 7 mm below the atom chip. If a condensate leaves this region it is in consequence not detectable anymore. Simply letting the atoms drop after release grants a free-fall time of roughly 34 ms on this baseline. The short time makes it challenging to realize a complete gravimeter sequence and prevents having a large interferometry time $2T$ and the application of delta-kick collimation. But, delta-kick collimation is an important corner-stone to tackle systematic uncertainties arising from mean-field interactions as well as the collimation allows to counteract the momentum broadening via mean-field energy conversion. For this reason it is important to find a way to extend the free-fall time without increasing the baseline. In the atom-chip gravimeter this challenge is faced by the integration of a relaunch, which extends the total free-fall time after release to a magnitude of 100 ms.

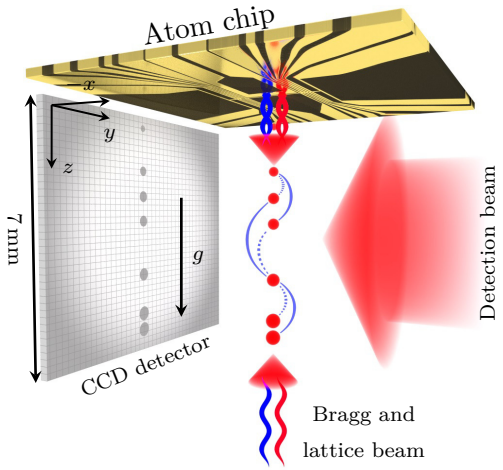

Fig. 5.1: Illustration of the atom-chip gravimeter realized in this thesis. All necessary atom-optics operations are realized by the atom-chip, including condensation, magnetic transfer and delta-kick collimation. The atom chip itself also acts as a retro-reflector in vacuum for the beam splitter and forms a reference for gravity.

The first part after the release of the atoms is always used for the preparation of the condensate (sec. 5.1). The preparation already includes the conditions the atoms are released from their magnetic trap. Because of the defects on the chip surface, the atoms have to be released at a spot at which later on undisturbed diffraction is observed. Such a spot is found by a shift of the condensate's position in the final magnetic trap transversally to the detection axis with an offset magnetic field. Hereby, the differentiation between the three different trap configurations summarized in tab. 2.2 has to be made, because the amplitude of this shift decreases with the steepness of the trap. In the next step, the parameters for delta-kick collimation have to be

adapted to this shift. The interferometry is performed in the non-magnetic state $m_F = 0$ to eliminate the linear Zeeman effect after the transfer via an adiabatic rapid passage.

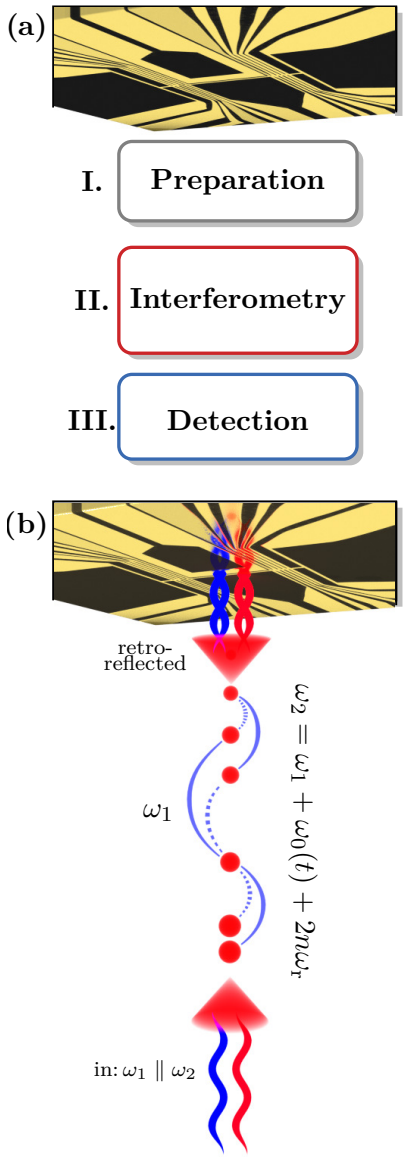

Fig. 5.2: In a nutshell, each experimental sequence consists of three parts: I. the preparation, II. the interferometry and III. the detection **(a)**. Frequencies to drive Bragg diffraction or Bloch oscillations via retro-reflection from the chip **(b)**.

The second part in the sequence is the interferometry which relies on light-pulse manipulation (sec. 5.2). The light field to manipulate the atoms is generated by retro-reflection off the chip. The occurring frequencies in the retro-reflected configuration are depicted in fig. 5.2(b). A single light field from a fiber consisting of two frequency components ω_1, ω_2 with linear parallel polarizations (lin$\parallel$lin) is shined onto the atom chip. This light field serves two purposes for the atom-chip gravimeter: Bragg diffraction used for beam splitting and Bloch oscillations used during the relaunch. The interferometer topology employed for measuring gravity is a Mach-Zehnder interferometer as introduced in sec. 4.3 formed by Bragg diffraction. The possibility to drive higher-order Bragg diffraction depends elementary on the available laser power and the momentum distribution of the atoms [66]. First-order Bragg diffraction is comparatively undemanding and can be realized with the diode based MOPA and the low power gravimeter optics, which are introduced in sec. 3.2 and used entirely in ref. [171]. With a beam diameter of $\oslash = 7\,\mathrm{mm}$, a detuning of $\Delta = 500\,\mathrm{MHz}$ and an available laser power of a few 10 mW, the first-order Bragg diffraction of a condensate without delta-kick collimation can be driven at efficiencies above 90%. However, for higher-order Bragg diffraction the high-power laser system introduced in chp. 3 provides sufficient laser power to even increase the efficiency for first-order diffraction and the interferometric contrast to unity. With a much larger detuning of $\Delta = 100\,\mathrm{GHz}$ the fraction of atoms lost due to spontaneous emission is suppressed in lattice operation. The last part in the sequence is the absorption detection, which mainly consists of a waiting time to separate the output states of the atom interferometer after the recombination pulse. After the output ports are sufficiently separated an absorption image is taken with the CCD detector, from which the normalized populations of the output states $|p_0\rangle$ and $|p_n\rangle$ are extracted.

To extend the free-fall time, a novel relaunch procedure is introduced in this thesis which is based on a combination of Bloch oscillations and double Bragg diffraction but still requires only a single light field (sec. 5.3). The optimized efficiency of this relaunch is 75%. It is integrated in the sequence in a way, that the preparation always takes place before the relaunch, which allows for delta-kick collimation. The interferometry as well as the detection takes place after the relaunch, which allows to extend the interferometry time $2T$ by a factor of five. Due to the insufficient surface quality of the atom chip a momentum broadening is observed which is the main limitation of the relaunch. But the expansion rates are still eligible to perform interferometry.

5.1 Preparation prior to interferometry

The QUANTUS-1 apparatus facilitates a Bose-Einstein condensate of up to $1.5 \cdot 10^4$ ^{87}Rb atoms every 15 s, with the sequence presented in sec. 2.2.2. The initial position and velocity of the condensates play an important role in an inertial measurement for which its release from the final trap needs to be characterized (sec. 5.1.1). A residual horizontal velocity induces a bias shift due to the coupling to the rotation of the Earth [138] and wave front curvatures [88], which are the major sources of systematic uncertainties in current devices. Considerations regarding these systematic uncertainties arising from an initial horizontal or vertical velocity are elaborated in sec. 6.4.1. Two additional preparation steps are performed after the condensate has been released to target for the intended systematic uncertainties. The first preparation step is delta-kick collimation, to further reduce the ensembles expansion. Based on previous work on ground, the delta-kick collimation protocol was adjusted to the new release conditions (sec. 5.1.2). Since the evaporation and delta-kick collimation takes place in a magnetic trap, the atoms need to be transferred to a non-magnetic sub-state for interferometry via an adiabatic rapid passage with a chirped radio frequency field (sec. 5.1.3).

5.1.1 Controlled release of the condensate from the trap

For the atom-chip gravimeter it is essential to find a position on the chip where the beam splitting can be applied (see also ref. [171]). For the release trap in QUANTUS-1, three different configurations are used, summarized in tab. 2.2. While the trap with $I_{\text{bias}} = 0.36\,\text{A}$ provides the smallest expansion rate after release, the traps with $I_{\text{bias}} = 0.6\,\text{A}$ and $I_{\text{bias}} = 1\,\text{A}$ are used for experiments with delta-kick collimation, to enable faster expansion before the collimation pulse (see sec. 5.1.2). With the offset field in the final magnetic trap generated by one of the offset-coil pairs K2 the atoms can be shifted in a controlled way to a position along the y-direction before they are released. Figure 5.3 shows this offset shifting dependent on I_{K2} ranging from -5 to $+5\,\text{A}$ for the three different trap depths I_{bias}. The shallowest one with a bias magnetic field of $I_{\text{bias}} = 0.36\,\text{A}$ is used for all the experiments presented later on, where no delta-kick collimation is performed. This trap is also the shallowest trap, which can be realized in QUANTUS-1 on ground and therefore grants the condensates with the smallest initial expansion rate and size. The amplitude of the shift is noticeably reduced with increasing trap depth, because of the

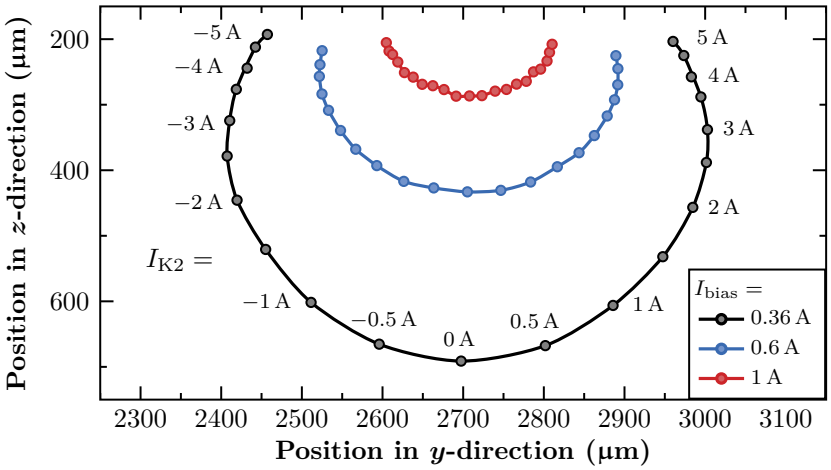

Figure 5.3: An offset current I_{K2} induces a shift of the condensates' position in y- and z-direction before release. Residual motion is compensated via adjusting the holding time τ_{trap} in this trap.

decreasing distance to the chip. While in the shallowest trap with $I_{\mathrm{bias}} = 0.36\,\mathrm{A}$ the amplitude of the shift in y-direction is in the order of 600 µm, in the steeper trap with $I_{\mathrm{bias}} = 0.6\,\mathrm{A}$ the amplitude decreases to 370 µm and even further to 210 µm in the steepest trap with $I_{\mathrm{bias}} = 1\,\mathrm{A}$. For the trap with $I_{\mathrm{bias}} = 0.36\,\mathrm{A}$ the amplitude is even limited by the rotation around the center, so only a shift between -2.5 and $+2.5\,\mathrm{A}$ leads to a significantly increasing shifting in y-direction. Depending on the holding time τ_{trap} oscillation measurements in the final trap are performed [164]. For the trap with $I_{\mathrm{bias}} = 0.36\,\mathrm{A}$ the frequency and amplitude of these oscillations are summarized in fig. 5.4(a,b). The offset velocity of the oscillations determined by Bragg spectroscopy and back-calculated from the expected Doppler detuning after a given time of flight is depicted in fig. 5.4(c). These figures reveal, that the position shift induces a change in the trapping frequencies and depths as well as an offset velocity which is compensated by the dipole oscillations with an adjusted holding time τ_{trap} if a value for $I_{\mathrm{K2}} \neq 0$ is chosen.

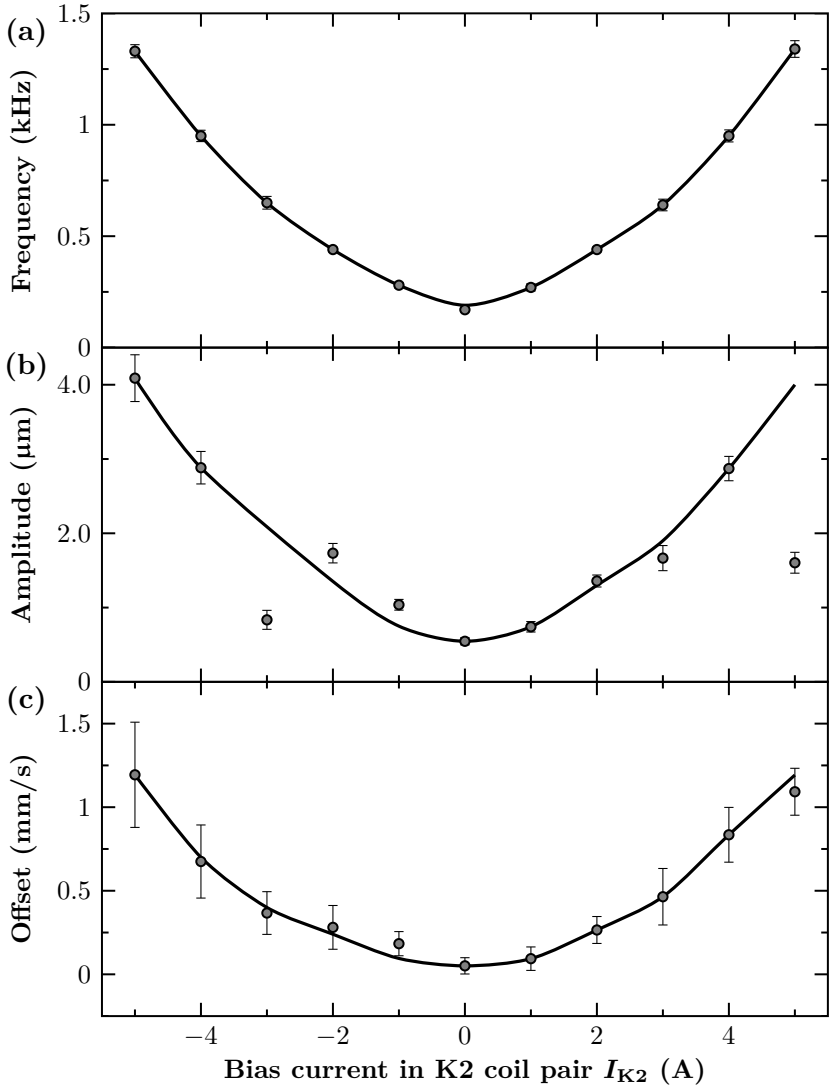

Figure 5.4: Frequency **(a)** and amplitude **(b)** of the oscillations in the shallow trap with $I_{\mathrm{bias}} = 0.36\,\mathrm{A}$ are determined from time of flight measurements while the offset velocity **(c)** is determined from Bragg spectroscopy, each dependent on the position shift in y-direction with I_{K2}.

Initial shift to avoid wave front distortions

The atom chip does not have a perfect reflective surface as to be seen in fig. 3.6. A surface of high optical quality is crucial for the application of light pulses and optical lattices, which might get distorted, if the wave front quality is insufficient at the position of the condensates. Figure 5.6 shows density plots of a condensate coherently split by a Bragg process perpendicular to the chip while scanning I_{K2} from -1 to $+1$ A which controls the release position of the condensate in y-direction. These density plot shows an inhomogeneity across the condensate which is presumingly caused by an intensity inhomogeneity of the retro-reflected laser beam. This inhomogeneity corresponds to a crack in the coating above the central position of the Z-wire in fig. 3.6. The diffraction pattern of a crack causes inhomogeneities even if the condensate is not directly above it. Figure 5.5 shows the same data as fig. 5.4 but with a color code which indicates where undisturbed diffraction is possible. Hereby, the center of the defect is slightly asymmetric around the zero of the current at $I_{K2} = 0$ A into the direction of positive currents.

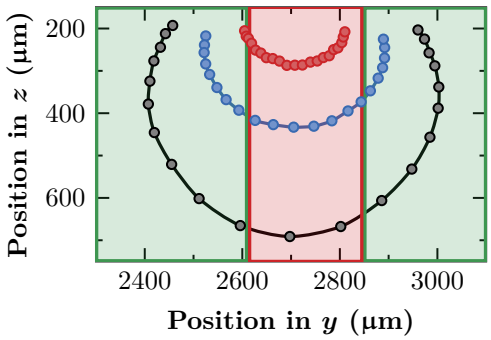

Fig. 5.5: Application of a beam splitter pulse on a BEC released in the red area (—) between the two green regions (—) does not allow to perform undisturbed interferometry. Only two shallower traps allow to shift BECs away from the defect above the center of the atom chip.

Experimentally it is determined in fig. 5.6, that offset shifts in the order of $I_{K2} > \pm 0.8$ A result in a non-disturbed Bragg diffraction for the shallowest trap with $I_{bias} = 0.36$ A, which is used in all following experiments with dropped Bose-Einstein condensates. To be on the save side, for the atom-chip gravimeter a current of $I_{K2} = -1$ A is used which is well in the green region. A larger shift away from the inhomogeneity is less susceptible to possible misalignments of the atom chip and residual horizontal velocities. The holding times for dipole oscillations in the release trap which give rise to the initial position and velocity as well as the magnetic lensing parameters have to adapted to the offset shift. Therefore, for the application of the magnetic lens the solution to avoid the defect is not so obvious, because for steeper traps a larger offset current needs be applied to have the same displacement. As indicated by the red area, there is no solution for the steepest trap with $I_{bias} = 1.0$ A to achieve undisturbed diffraction. In consequence to combine delta-kick collimation with a laser beam along gravity only the trap with $I_{bias} = 0.6$ A can be chosen, because there a shift into the green region is possible.

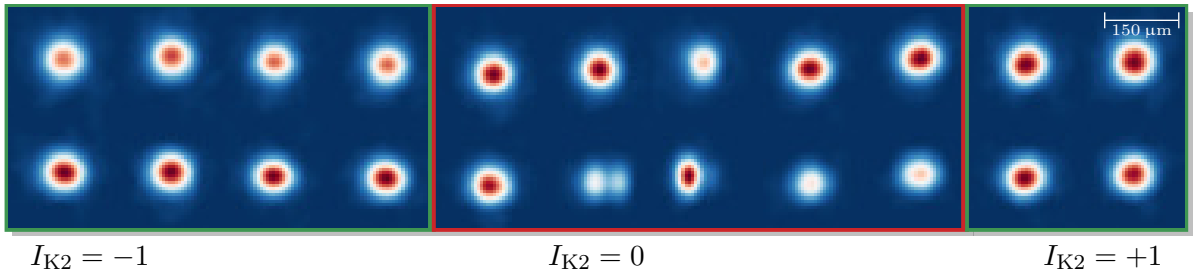

Figure 5.6: Defects during the application of a beam splitting pulse dependent on the offset shift in y-direction current I_{K2} in the shallowest release trap with $I_{bias} = 0.36$ A. The green area (—) indicates undistorted wave fronts, while the red area (—) indicates shifts too close to the defect.

5.1.2 Momentum collimation by a magnetic lens

After the release of the condensate from the magnetic trap, it starts to expand freely and falls away from the chip due to the gravitational acceleration. During the first milliseconds after release most of the mean field energy is converted into kinetic energy. The time depends on the atomic density of the condensate and hence on the steepness of the trap the atoms are released from. An exemplary evolution of the velocity width σ_v taken after increasing expansion time ToF after release of the condensate from the shallowest trap with $I_{\mathrm{bias}} = 0.36\,\mathrm{A}$ is depicted in fig 5.7. The momentum width evolution in this figure during the mean field conversion time is resolved with Bragg spectroscopy, since this method gives an in-situ value for the expansion rate at each measurement. Final expansion rates in the ballistic regime can be more precisely evaluated with a time of flight measurement if sufficient time of flight is available. After a free-expansion time of ToF $> 10\,\mathrm{ms}$ for the trap with $I_{\mathrm{bias}} = 0.36\,\mathrm{A}$ the momentum width of the cloud stays almost constant and reaches a final expansion rate of $\sigma_v \approx 750\,\mu\mathrm{m/s} \equiv 0.125\,\hbar k$. In the case of the steeper traps with $I_{\mathrm{bias}} = 0.6\,\mathrm{A}$ and $1\,\mathrm{A}$ the mean field conversion happens faster and only consumes 1-2 ms, but the final expansion rates of $\sigma_v \approx 1.6\,\mathrm{mm/s} \equiv 0.3\,\hbar k$ and even $\sigma_v \approx 2.6\,\mathrm{mm/s} \equiv 0.45\,\hbar k$ are significantly higher. These cases are not depicted in the figure, since momentum width changes during the first millisecond after release are difficult to resolve.

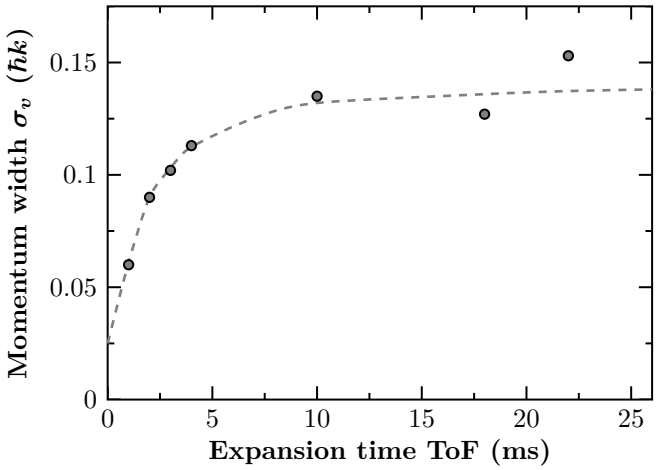

Figure 5.7: Mean field conversion after release from the shallow trap with $I_{\mathrm{bias}} = 0.36\,\mathrm{A}$.

Even an atomic source that is initially condensed has a finite velocity spread that leads to a significant increase of the cloud size after expansion and may reduce the performance of the atom interferometer due to increased detection noise or enlarged contributions to systematic uncertainties. The condensate released from the shallowest trap with $I_{\mathrm{bias}} = 0.36\,\mathrm{A}$ expands reasonably slow enough to perform experiments with short free-fall times and its momentum width of $0.125\,\hbar k$ is small enough to reach high Bragg diffraction efficiencies (see sec. 4.1.2). For an atom number of $N = 10\,000$ the mean-field conversion in a time of $t_{\mathrm{exp}} > 10\,\mathrm{ms}$ is acceptable. However, in general this statement is not true especially for a larger densities of the condensate.

Delta-kick collimation with the harmonic chip trap

Delta-kick collimation by a magnetic lens [269] is most of all motivated by reaching long expansion times. Recent demonstration show expansion rates equivalent to temperatures of nK in 3D [98] in the drop tower with QUANTUS-1 or even pK in 2D [133] in a 10 m-fountain. These momentum widths are smaller than the one of the coldest reported condensates [270]. Delta-kick collimation

in the QUANTUS-1 experiment in the drop tower but also on ground has been intensively studied during former theses and the results are presented in refs. [164, 165].

The idea behind delta-kick collimation is, that in momentum space the expansion of a released ensemble is a projection of the oscillation in the final release trap. So there is a point T_0 in time after release when all atoms come to rest with respect to the potential. A position-dependent force $F(x)$ at this time generated by a short pulse of length τ_{dkc} (e.g. a delta kick)

$$F(x) \cdot \tau_{\mathrm{dkc}} = -\frac{V_{\mathrm{dkc}}}{\delta x} \cdot \tau_{\mathrm{dkc}} = -m\omega_{\mathrm{dkc}}^2 x \cdot \tau_{\mathrm{dkc}} \tag{5.1}$$

with an appropriately matched harmonic potential ω_{dkc} slows the atoms down at each position x. The strength of a delta kick is defined by $S = 1/T_0 = \omega_{\mathrm{dkc}}^2 \cdot \tau_{\mathrm{dkc}}$ which is an analogue to the power P of an optical lens. Delta-kick collimation can be illustrated by a tilt of the ellipse in phase space arising due to shearing during expansion in space x on the momentum axis p depicted in fig. 5.8. After the tilt the ensemble is expanding with a smaller rate as initially.

The harmonic potential ω_{dkc} for an ideal collimation pulse with an error in momentum collimation δp depending on the mismatches of the parameters has to fulfill the condition

$$T_0 \cdot \tau_{\mathrm{dkc}} = \frac{1}{\omega_{\mathrm{dkc}}^2} \text{ and } \delta p = p_i \delta(\omega_{\mathrm{dkc}}^2 \tau_{\mathrm{dkc}} T_0) < p_f = x_i p_i / x_f. \tag{5.2}$$

The collimation error δp, which would cause the ensemble to expand with a higher rate as limited by the optimal lensing p_f, is expressed by the errors in the corresponding parameter

$$\frac{\delta(\omega_{\mathrm{dkc}}^2)}{\omega_{\mathrm{dkc}}} + \frac{\delta\tau_{\mathrm{dkc}}}{\tau_{\mathrm{dkc}}} + \frac{\delta T_0}{T_0} < \frac{x_i}{x_f} \sim \frac{p_f}{p_i} \tag{5.3}$$

which is acceptable if it is smaller than the limit set by initial x_i and final radius x_f or the ratio between initial p_i and final momentum p_f. For a divergence after the collimation as small as possible a size x_f can be achieved by enlarging the time T_0. On ground the waiting time and the other errors are not only limited by technical means, but also by the free-fall away from the chip which reduces the trap frequencies of the potential and limits T_0 to $\leq 6\,\mathrm{ms}$. For the shallow trap after this time the expansion is not even in the ballistic regime, so a release trap with faster initial expansion is required to increase x_f prior to collimation. Another cause of errors are the anharmonicities of the generated potential causing deformations for too large condensates.

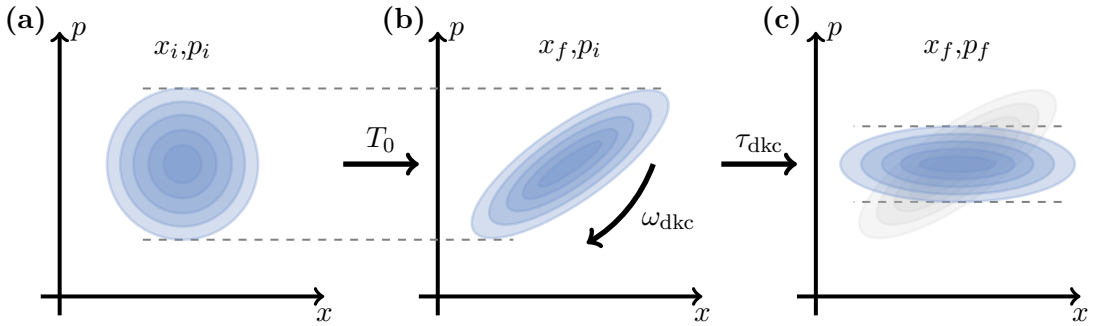

Figure 5.8: Principle of delta-kick collimation in phase space. An ensemble after release has an initial distribution in momentum and space **(a)**. After some time the cloud has expanded in space causing an ellipse **(b)** which is tilted on the momentum axis with a collimating pulse **(c)**.

Optimized delta-kick collimation protocol for the displaced trap

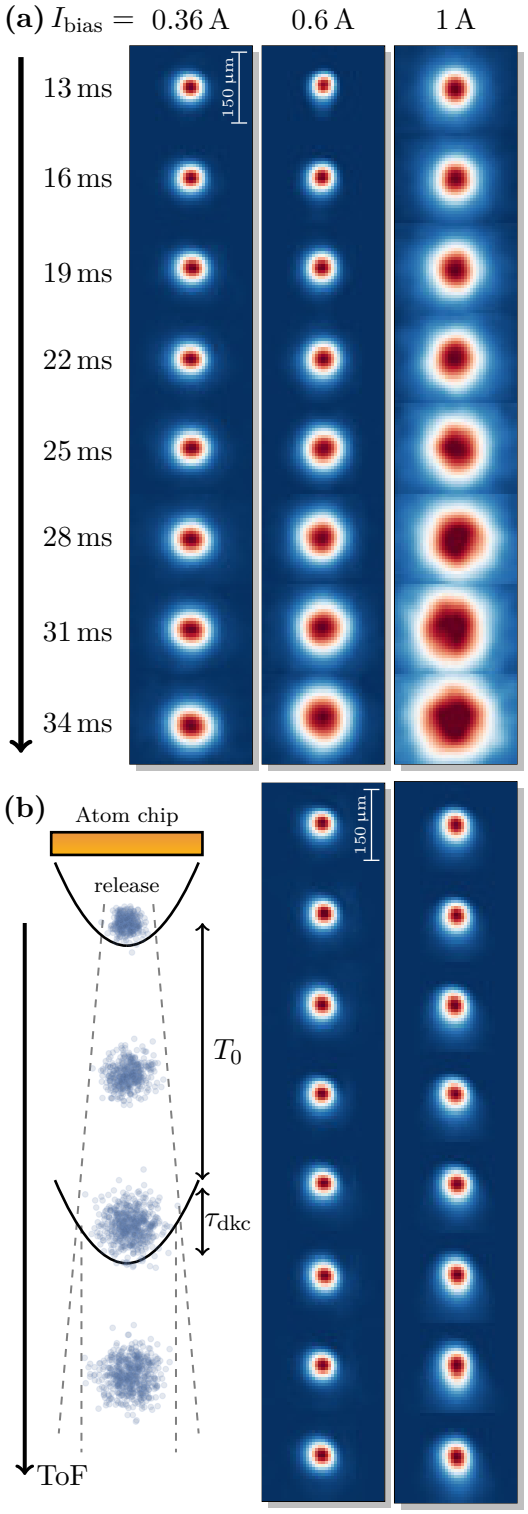

Fig. 5.9: Density plots for released condensates **(a)**. Scheme for delta-kick collimation **(b)**.

Figure 5.9(a) shows density plots for the expansion of condensates released from the magnetic traps with $I_{\mathrm{bias}} = 0.36\,\mathrm{A}$ (left), 0.6 A (middle) and 1 A (right) taken for expansion times between 13 and 34 ms which is close to the end of the detection region. In these density plots the increase in expansion rate from 750 µm/s over 1.6 mm/s up to 2.6 mm/s is clearly observable. The best result for delta-kick collimation in previous thesis [164, 165] has been achieved for the lens release trap with $I_{\mathrm{bias}} = 1\,\mathrm{A}$ but with no initial shift, e.g. with $I_{\mathrm{K2}} = 0$. This configuration is unsuitable for the operation with a laser beam retro-reflected from the atom chip according to fig. 5.5 and for this application different parameters need to be used.

The protocol used for delta-kick collimation starting with the release of the condensate from the atom chip is depicted in fig. 5.9(b). After release the atoms start to speed up due to gravity and expand with a rate according to the release trap. After a short expansion time the lensing pulse is applied which slows down the expansion and ideally imprints no velocity kick to the atoms. For the new sequence, only the release trap configuration and the parameters of the lensing pulse need to be adapted to the required shift of $> 200\,\mu\mathrm{m}$. This new configuration uses a steep release trap with $I_{\mathrm{bias}} = 0.6\,\mathrm{A}$ and a shift with maximum displacement for $I_{\mathrm{K2}} = -3\,\mathrm{A}$. The collimation pulse is applied after an expansion time of $\tau_{\mathrm{exp}} = 6\,\mathrm{ms}$ for $\tau_{\mathrm{dkc}} = 280\,\mu\mathrm{s}$ with a current in the Z-wire of $I_{\mathrm{Z}} = 2\,\mathrm{A}$, offset fields of $I_{\mathrm{K2}} = -7\,\mathrm{A}$ and $I_{\mathrm{K1}} = 1.6\,\mathrm{A}$ adjusted to the new position of the ensemble after the free fall during τ_{exp}.

The density plots in fig. 5.9(b) show the expansion of delta-kick collimated condensates released from the displaced steep trap with $I_{\mathrm{bias}} = 0.6\,\mathrm{A}$ (left) compared to the the original lens trap with $I_{\mathrm{bias}} = 1\,\mathrm{A}$ (right) with no significant visible anharmonicities. The estimated expansion rate from the same ToF between 13 and 34 ms is 150 µm/s. This expansion rate is comparable to the previous result. Thus, the ensembles are due to the shallower trap $\approx 30\%$ smaller after the same expansion time, which is uncritical at the current atomic density.

5.1.3 Transfer to the non-magnetic state

The generation of a Bose-Einstein condensate by an atom chip relies on the magnetic trapability of the atoms in the potential generated by the atom chip. After release, the condensate can be prepared in the most favorable state which has the lowest uncertainty. Because this preparation step is so essential for every inertial measurement the magnetic state transfer has to be always included in the interferometry sequence. Consequently, in each sequence used in the experiment at least the magnetic transfer has to be dedicated to the preparation. This is different to the delta-kick collimation where in the case of small observation times it is still arguable whether it needs to be performed.

In the case of ^{87}Rb, coming from the magnetic state $m_\mathrm{F} = 2$ which has the highest trapping potential inside a magnetic trap the atoms for an inertial measurement need to be transferred to the magnetically insensitive $m_\mathrm{F} = 0$-state. This preparation step is crucial for the atoms before being employed in an interferometer, since the $m_\mathrm{F} = 0$-state is the most robust against magnetic stray fields during free fall. The linear Zeeman effect in all magnetic sensitive states with $m_\mathrm{F} \neq 0$ during the atom interferometer would lead to a bias phase shift which is roughly in the same order as the gravitational acceleration. These states are hence highly unsuitable for any kind of inertially sensitive measurements. However, even in the $m_\mathrm{F} = 0$-state the quadratic Zeeman shift remains and causes a significant systematic uncertainty damped by the magnetic shielding around the vacuum system.

For the transfer from the magnetic state $m_\mathrm{F} = 2$ into the non-magnetic state $m_\mathrm{F} = 0$ a radio frequency field is emitted from the atom chip, that couples different magnetic states as depicted in

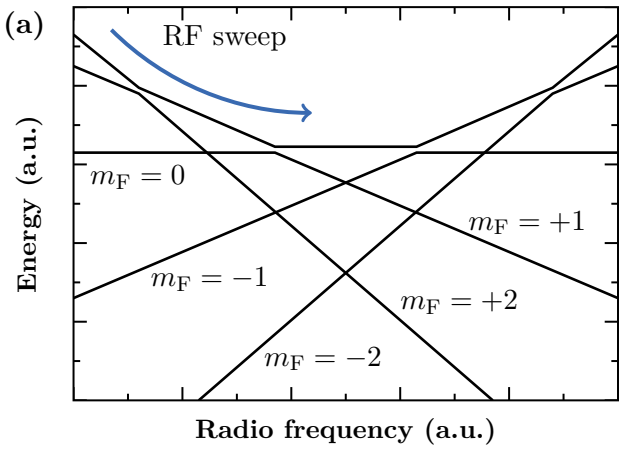

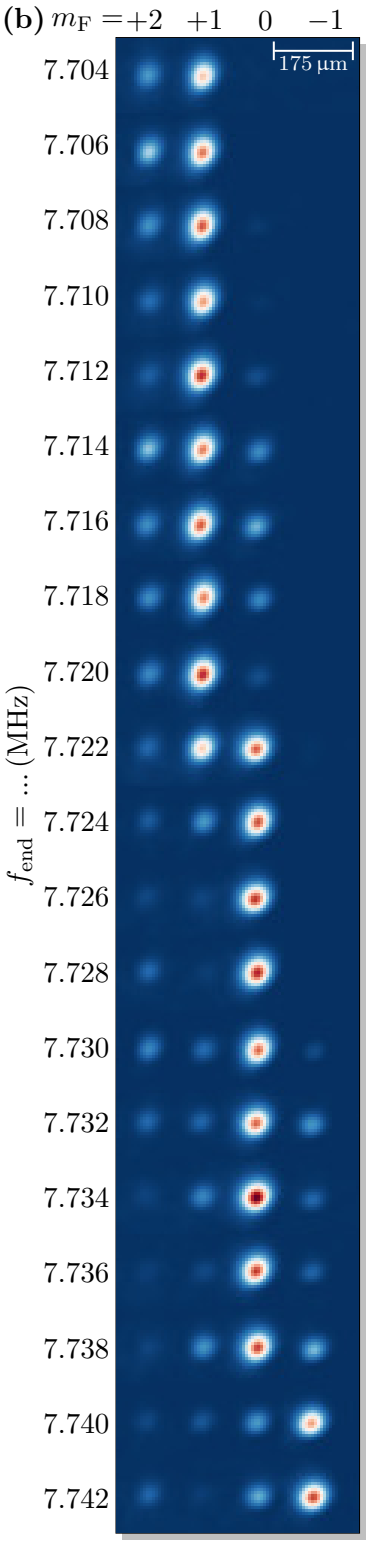

Figure 5.10: Coupling scheme of the adiabatic rapid passage used for magnetic sub-state transfer **(a)**. A scan of the end frequency of the adiabatic rapid passage determines the final sub-state **(b)**.

fig. 5.10(a). Instead of π-pulses with fixed radio frequency, an adiabatic transfer via a swept radio frequency is used to enhance the transfer efficiency. Figure 5.10(b) shows density plots which are rotated by $-85°$ for vertical alignment of the states. The state transfer is depicted with a chirp starting from an initial frequency of $f_{\mathrm{start}} = 7.7\,\mathrm{MHz}$ dependent on the end frequency f_{end} of the adiabatic rapid passage (arp). To lift the degeneracy of the magnetic states first a homogeneous bias field of a few Gauss is ramped up to its final value within 4 ms. Afterwards the frequency chirp itself consumes 5.2 ms and, finally, the bias field is linearly ramped down again for 1 ms leading to a total time of the sequence of $\tau_{\mathrm{arp}} = 10.2\,\mathrm{ms}$. The largest obtained transfer efficiency into the sub-state $m_{\mathrm{F}} = 0$ is in the order of roughly 95% for an end frequency of $f_{\mathrm{end}} = 7.727\,\mathrm{MHz}$ at a bias field of 10.5 G. The distinction of the magnetic sub-states in fig. 5.10(b) is realized by Stern-Gerlach-type deflection generated by the MOT coils in anti-Helmholtz configuration and letting the atoms accelerate for $\tau_{\mathrm{SG}} \geq 20\,\mathrm{ms}$. For more details on the implementation and characterization of the adiabatic rapid passage in QUANTUS-1 see refs. [164, 165].

State purification with Stern-Gerlach-type deflection

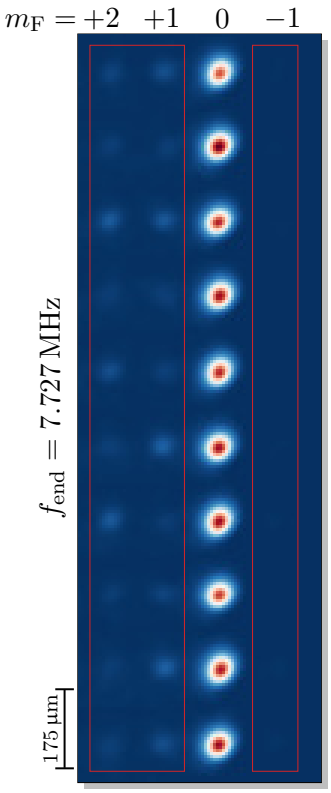

Fig. 5.11: Residual atoms in $m_{\mathrm{F}} \neq 0$ sub-states cause loss of contrast due to dephasing. The density plots show, that even in the case of an optimized end frequency of the adiabatic rapid passage approx. 5% of the atoms remain in other sub-states and are pushed away by Stern-Gerlach-type deflection.

Even though the efficiency of the magnetic state transfer is enlarged by the adiabatic rapid passage, still approx. 5% of the atoms remain in states with $m_{\mathrm{F}} \neq 0$. Figure 5.11 shows density plots again rotated by $-85°$ for ten subsequent cycles with an adiabatic rapid passage adjusted to the largest transfer efficiency at a fixed end frequency of $f_{\mathrm{end}} = 7.727\,\mathrm{MHz}$. The fluctuations of the transferred fraction to the $m_{\mathrm{F}} = 0$-state between the cycles are in the order of a few percent of the total atom number. These fluctuations may arise from power fluctuations of the radio frequency but also from temporal fluctuations of the magnetic environment. If Stern-Gerlach-type deflection is not applied in an experiment after the adiabatic rapid passage the magnetic states can not be distinguished by the detection system since they are spatially overlapping. The non-transferred atoms will cause a slight loss of contrast up to 10%, since they can in the worst case destructively interfere. Additionally, a fluctuating transfer efficiency will cause noise as well as possibly bias shifts.

These effects can be completely suppressed by a subsequent Stern-Gerlach-type deflection which pushes away remaining atoms in states with $m_{\mathrm{F}} \neq 0$ and removes them from the area where the interferometer output ports are evaluated. This only causes a slightly enlarged fluctuating atom number, which is normalized during the detection process. Stern-Gerlach-type deflection can be performed in two different ways in the experiment. With the MOT coils a nicely homogeneous field is generated which performs sufficiently but it requires a significantly large amount of time of $\tau_{\mathrm{SG}} \geq 20\,\mathrm{ms}$ to separate the states properly, which cannot be used for other operations. Alternatively, the Z-wire of the atom chip can be used for Stern-Gerlach-type deflection. Because the generated field is stronger but due to the changing distance during free fall not as homogeneous, a proper separation is reached after a shorter time of $\tau_{\mathrm{SG}} = 7\,\mathrm{ms}$ at a current of $I = 2\,\mathrm{A}$.

5.2 High-fidelity interferometry using Bragg diffraction

Light-pulse manipulation with high fidelity η is the feature, that makes Bose-Einstein condensates interesting for atom interferometry. Even the fastest available sources of Bose-Einstein condensates [117] suffer from a lower flux compared to thermal sources fed by a simple molasses. To a large extent the lower flux can be compensated by a significantly larger excitation probability during the light-pulse manipulation and the application of larger momentum transfer. For a simple Mach-Zehnder interferometer consisting of a three pulse sequence only, the contrast scales with the third power of the beam splitter fidelity $C \sim \eta^3$ as a rule of thumb. Interferometers using molasses cooled atoms commonly apply a velocity filter using a Doppler-selective Raman transition [64] selecting a distribution of atoms with reduced atom number but a momentum width smaller than the recoil velocity. Even in this case, the obtained interferometric contrast usually stays below $C < 0.5$, i.e. only half of the atoms contribute to the interferometric signal. For Bragg diffraction with spatial detection the momentum width of the employed source plays an even more crucial role than for Raman diffraction with fluorescence detection [66].

5.2.1 Higher-order Bragg diffraction

The condensates used for the Bragg diffraction are released from the shallow trap and prepared in the non-magnetic sub-state $m_\mathrm{F} = 0$. Working with delta-kick collimated condensates would especially for higher orders yield larger efficiencies compared to this source. The Bragg diffraction pulses are applied approx. 15 ms after the condensate is released from the trap. At this time atoms in the thermal background are still present and even at the time of the detection a significant amount of thermal atoms is observed. Due to their wider velocity spread these atoms are more likely to be diffracted into spurious orders, so orders which are not intentionally populated during the diffraction process, or not to be diffracted at all. Not only the velocity sensitivity due to the spread of the atomic momentum is observed in the experiment, but also due to the free fall of the atoms during the pulse. Figure 5.12 shows density plots of diffracted condensates with Bragg orders up to the fifth transferring $10\,\hbar k$ with a Gaussian pulse width of $\sigma_\tau = 12.5\,\mu\mathrm{s}$. The laser powers and detunings are in each case optimized to have the maximum transition efficiency equal to a π-pulse in an atom interferometer. The fifth-order transition suffers already from a drastically reduced excitation efficiency, because although the laser power is not yet limited, the optimal pulse length is required to be significantly longer, as in detail calculated in ref. [66].

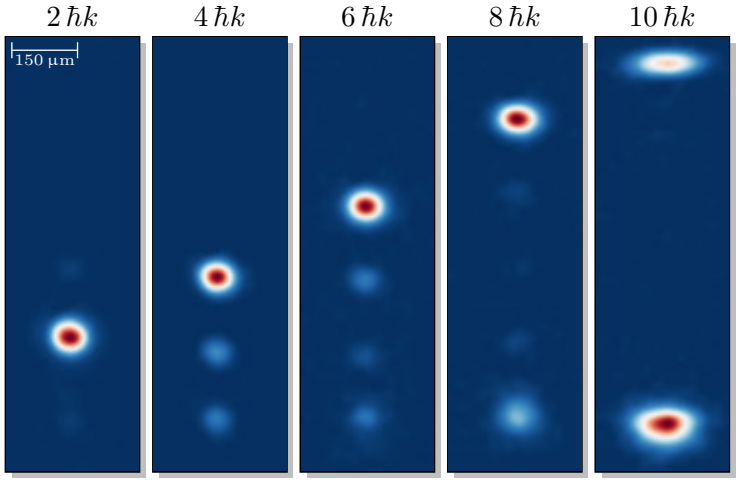

Figure 5.12: Density plots for higher-order Bragg diffraction.

The basic properties to adjust an n$^{\text{th}}$-order Bragg diffraction pulse of length σ_τ are the laser power P and the detuning $\Delta\nu$ of the laser. Scans of these parameters with the other parameter set to maximum diffraction efficiency for pulse times of $\sigma_\tau = 12.5\,\mu s$, $17.5\,\mu s$ and $25\,\mu s$ are shown in fig. 5.13(a,b). These values are chosen, because for longer pulses the frequency could no longer be held constant over the complete pulse length, but the free fall must be compensated to remain sufficiently resonant. The amplitude of both frequency components in the two-photon light field is adjusted equally for simplicity, disregarding the reflectivity of the atom chip. Adjusting the laser power P instead of the pulse length σ_τ as implied from the Rabi oscillations has the advantage, that the velocity selectivity of π- and $\frac{\pi}{2}$-pulse do not differ. Furthermore, the transfer function in eq. 4.62 stays identical if the same pulse length is chosen during each experiment. For larger order n the relative amplitude needs to be increased, but the total efficiency slightly decreases. With increasing pulse length σ_τ the frequency scans get narrower such that in total the shortest pulses in any case yield the best efficiencies. Broader peaks in frequency and slow oscillations in amplitude also have the advantage, that the diffraction is less susceptible to fluctuations and drifts in the laser power or initial motion. This especially makes the first-order Bragg diffraction attractive for a stable and low-noise operation of an atom interferometer.

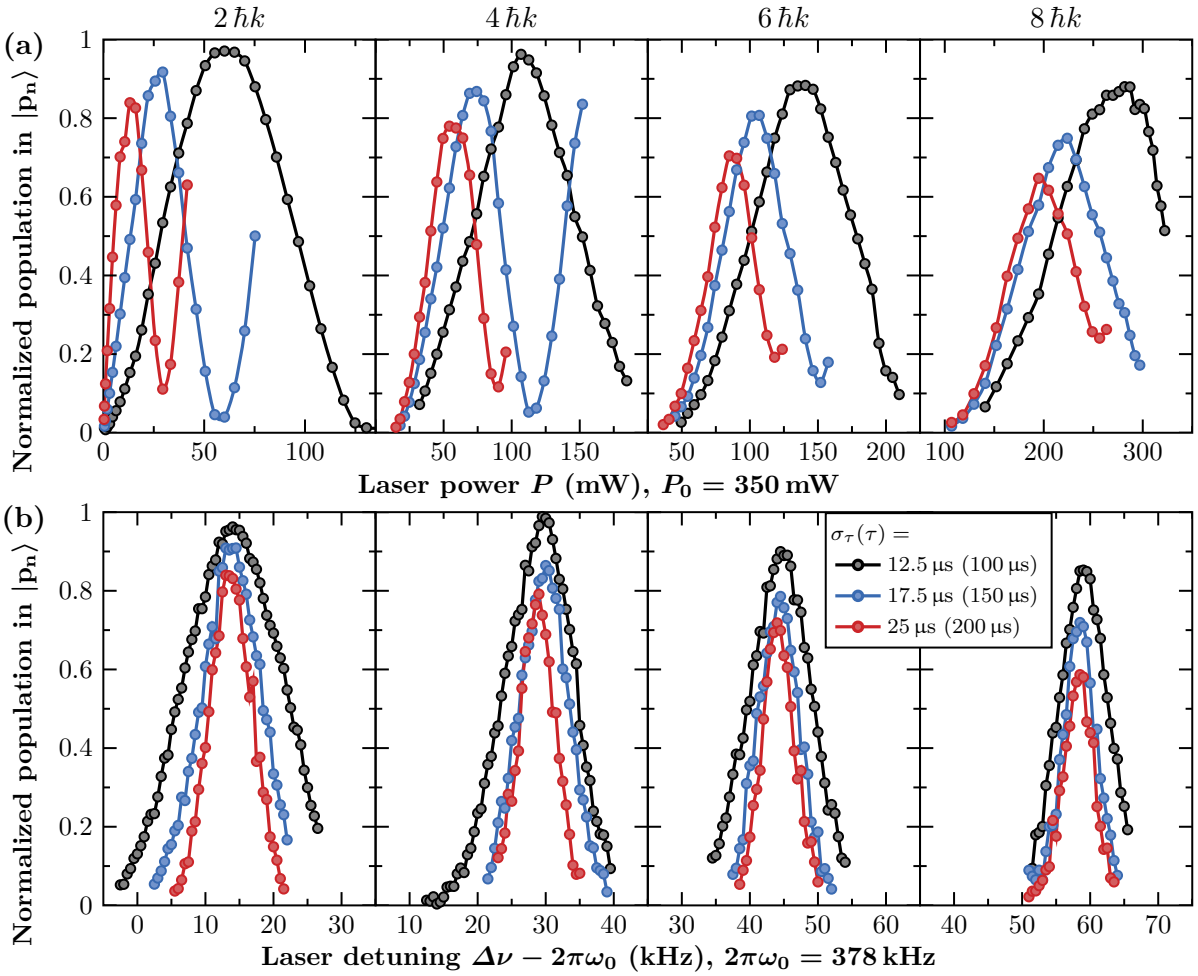

Figure 5.13: Scans of the relative amplitude **(a)** and laser detuning **(b)** for up to fourth-order Bragg diffraction ($n = 1 - 4$) with three pulse lengths $\sigma_\tau = 12.5\,\mu s$ (—), $17.5\,\mu s$ (—) and $25\,\mu s$ (—).

Disturbances due to the dual-lattice configuration

An important point to discuss is the occurrence of standing waves when simply retro-reflecting the two frequency components of the light fields with parallel linear polarizations (lin||lin). Since the atom chip in the QUANTUS-1 experiment has no $\frac{\lambda}{4}$-wave-plate coating the parallel linear polarizations is necessary to drive Bragg diffraction. in this specific configuration, the incoming and retro-reflected light fields can beat with each other and amplitude modulation occurs. The amplitude modulation causes the diffracted population to oscillate with the phase $\Delta\phi_{\text{Laser}}$ visible in the density plots in fig. 5.14(a). In this figure a first-order Bragg pulse with duration $\tau = 150\,\mu\text{s}$ and, respectively, $\sigma_\tau = 17.5\,\mu\text{s}$ is applied in vertical direction right after the release of the condensate, when the Doppler shift is still the smallest. With only a minimal resonance detuning to drive a Bragg transition of $\delta = 15\,\text{kHz}$ the amplitude modulation frequency is in the same order as the length of the beam splitting pulse itself $1/15\,\text{kHz} = 67\,\mu\text{s}$, which gives rise to the maximum effect. In this example double Bragg diffraction occurs as well, since both beam pairs are still at resonance with the slow motion of the atoms. The plot in fig. 5.14(b) shows an oscillatory behavior of the transition probability depending on the laser phase $\Delta\phi_{\text{Laser}}$. An asymmetry between upwards and downwards diffracted atoms is visible, that comes from the fact, that the atoms are in free fall during the beam splitting pulse. This causes a velocity of roughly 1 mm/s and explains the asymmetry. To sufficiently suppress this effect, the Doppler shift needs to be increased to a detuning in the order of $\delta_{\text{min}} > 100\,\text{kHz}$.

In general, this effect can be suppressed to a large extend by the use of perpendicular linear polarizations (lin⊥lin) of the incoming frequency components in the beam splitting light field. In combination with the $\frac{\lambda}{4}$-wave-plate in front of the retro-reflection mirror, which is passed twice by the laser beam, each incoming frequency component and its corresponding reflected component, have orthogonal polarizations. Therefore no standing wave would form, except for imperfections of the fiber and polarization optics as well as misalignment of the $\frac{\lambda}{4}$-wave-plate.

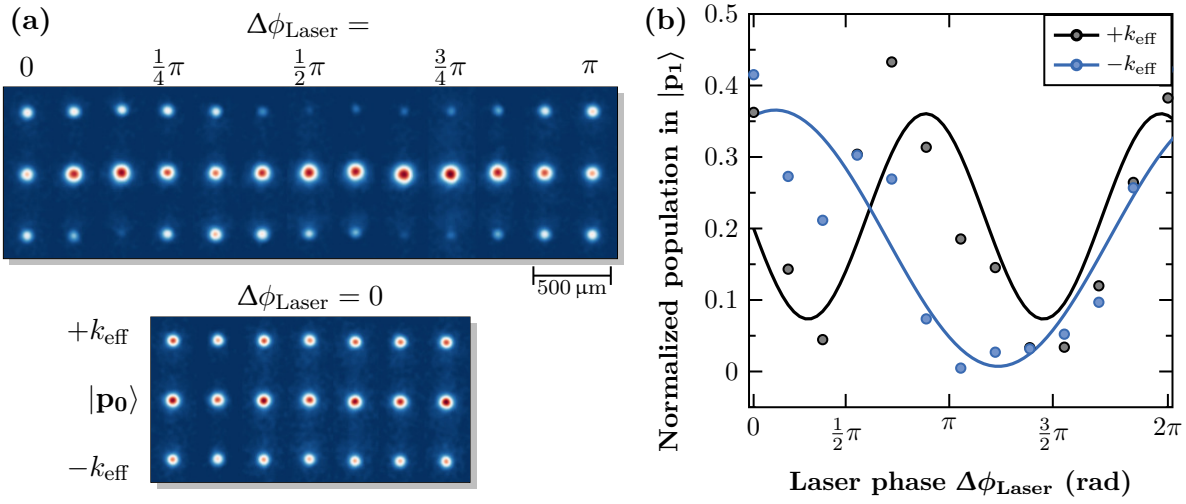

Figure 5.14: Density plots of the diffraction efficiency modulation by standing waves in the retro-reflected beam splitting light field for changing and fixed laser phase $\Delta\phi_{\text{Laser}}$ **(a)**. Directly after release a Bragg beam splitting pulse is applied in vertical direction. Since the detuning is small double diffraction occurs. The from the density plots extracted beam splitting efficiency shows oscillatory behavior depending on the relative phase $\Delta\phi$ and the direction of the momentum transfer **(b)**.

5.2.2 Mach-Zehnder fringes

Three Bragg pulses of the same order n applied in a $\frac{\pi}{2}-\pi-\frac{\pi}{2}$-configuration and a scan of the laser phase ϕ_3 of the last pulse between subsequent cycles gives rise to the characteristic fringe pattern of the Mach-Zehnder interferometer. With vanishing pulse separation $T = 0$ the sensitivity to inertial effects is still reasonably low and the obtained population at the output ports is directly proportional to the laser phase $\Delta\phi_{\text{Laser}}$. Figure 5.15(a) shows density plots of closed interferometers formed by different Bragg orders with a laser phase on the interval $\Delta\phi_{\text{Laser}} = 0$ to π and fig. 5.15(b) the extracted populations. From this fringe scan an essential property to describe the performance of an atom interferometer is obtained with the interferometric contrast

$$C = \frac{A}{P_0} \leq \frac{P_{\max} - P_{\min}}{P_{\max} + P_{\min}}, \tag{5.4}$$

defined by the amplitude A of the sinusoidal signal divided by its mean P_0 with an upper bound given by the maximum and the minimum of the signal. Two main observations can be made from the figure. First, the density plots show a significant fraction of atoms lost to spurious orders. Second, the signal between the two output ports of interest $|p_0\rangle$ and $|p_n\rangle$ which is plotted in fig. 5.15(a) is close to unity for the first and second order, but starts to decrease by 25% for the third order and even by 50% for the fourth order. This reduction results from a decrease in diffraction efficiency to $\eta = 0.9 \rightarrow C \sim 0.9^3 \approx 0.7$ for third-order diffraction or even to $\eta = 0.8 \rightarrow C \sim 0.8^3 \approx 0.5$ for fourth-order diffraction. This decrease makes the fourth order at the moment inapplicable for interferometry, while for third order a gain in sensitivity of 2.25 compared to first order and still 1.125 compared to second order is expected. The obtained efficiencies and especially the atoms in spurious ports are limited by thermal background atoms due to the condensate fraction of 65%, which could be eliminated with an improved preparation and a detection after longer free-fall times where hotter atoms have spread out. Even though there is no significant sensitivity to inertial effects due to the small scaling factor, the fringe scan provides useful an estimation about the intrinsic sensitivity of the atom interferometer.

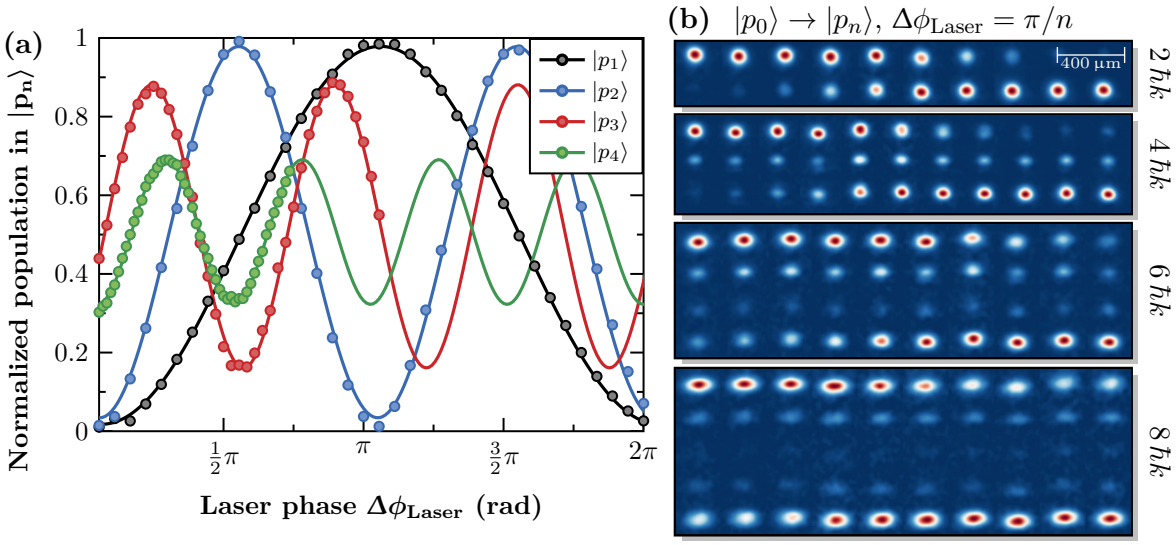

Figure 5.15: Mach-Zehnder fringes for an adjusted laser phase on the interval from $\Delta\phi_{\text{Laser}} = 0$ to π with up to fourth-order Bragg diffraction. The density plots show for each order a complete change in population **(b)** requiring a phase shift inversely proportional to the order n.

Output port separation with spurious ports

Spatially resolved imaging offers the great advantage, that the two output ports of an atom interferometer can be synchronously detected in a single picture, therefore suppressing a large amount of common mode noise arising from the properties of the detection light beam, e.g. power and frequency fluctuations. Thus the read out of the relative output port population ideally only depends on the difference in atom number counted at two different spots on the CCD detector. It is mandatory, that these two spots have to be appropriately separated at a given waiting time after the final pulse of the interferometer. This waiting time is requested to be as short as possible, because it reduces the time $2T$ available for interferometry.

The separation happens due to the relative velocity $v_{\mathrm{sep}} = 2n \cdot v_r = n \cdot 2\,\hbar k/m$ between the two interferometer states $|p_0\rangle$ and $|p_n\rangle$ at the output ports of the atom interferometer. Hereby, the relative velocity only scales with the momentum $2n\,\hbar k$ imprinted during recombination pulse, independently of enlarged momentum transfer by Bloch oscillations or sequential transitions inside the interferometer. A problem connected to higher-order diffraction is the occurrence of spurious ports if the efficiency of the pulse is limited [11]. As a rule of thumb, the contrast C is not decreased by overlapping ports, if the time for separation τ_{sep} is larger than

$$\tau_{\mathrm{sep}} > \frac{\sigma_z}{2 \cdot v_r} = \frac{\sigma_0 + \sigma_v \cdot \mathrm{ToF}}{2 \cdot v_r} \tag{5.5}$$

with σ_{z} being the size of the atomic ensemble along the beam splitter in z-direction after a time of flight ToF independent of the order n. The size σ_z at the detection depends on the initial size σ_0 and the expansion rate σ_v. From eq. 5.5 it is apparent, that the size σ_z of the ensembles at the output ports is the main limitation for τ_{sep}, which is another strong motivation for the use of ultra-slow expanding - e.g. delta-kick collimated condensates. The detection process may be carried out after a shorter time τ_{sep}/n for larger $n > 1$, if spurious ports are not significantly populated. Of course, there is no separation possible at all, if the expansion rate σ_v is larger than the recoil for the highest possible order $2n \cdot v_r$ even if spurious ports are accepted to overlap.

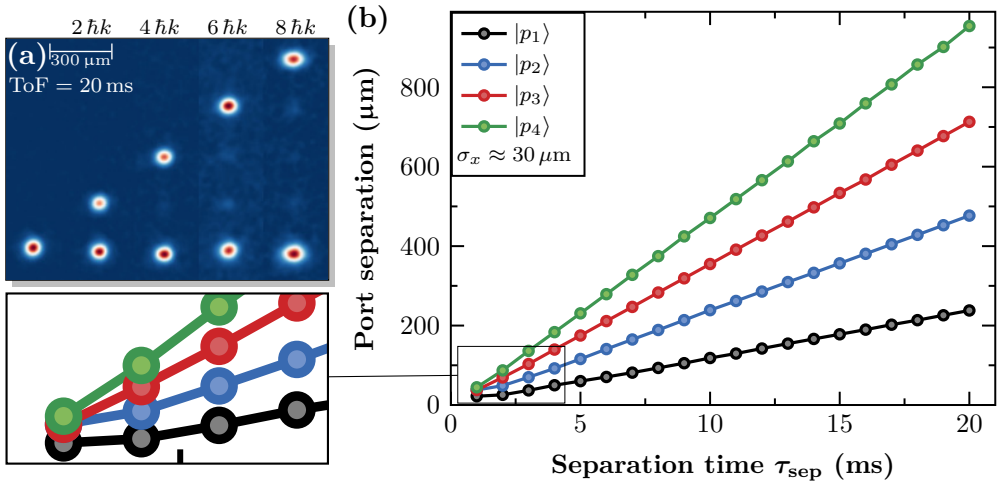

Figure 5.16: The scaling of the differential velocity by higher order can only be useful, if the beam splitting is of high enough fidelity such, that spurious ports do not overlay the outputs of the atom interferometer **(a)**. Separation of the output ports for different orders n of the Bragg beam splitting process depending on the final separation time τ_{sep}. For each cloud size σ_z an optimal separation time can be determined to establish a maximum interferometric contrast C **(b)**.

5.3 Relaunch of atoms in a retro-reflected optical lattice

Within this section a simple but effective method is developed to coherently relaunch atoms in free fall by the transfer of a large number of photon momenta in an optical lattice. The method presented here differs from previous work, which either relies on two crossed beams reflected from a mirror surface [271], two opposing beams [150], velocity selection from a molasses [11, 149, 225] or on the transfer of only few photons from a standing wave [151, 272]. For the first time, an efficient sequence relaunching atoms is realized in a retro-reflected optical lattice, as they are commonly used for atomic sensors. The novelty and at the same time the challenge of this method is, that for the experiment only a single vertical beam axis with two co-propagating linearly polarized laser frequencies is used, which form in total four lattices: two moving lattices with opposite velocity and two additional ones at rest. The relaunch procedure is performed in three subsequent steps to surpass the zero crossing of the moving lattices' velocity:

- **A lattice deceleration sequence:** First, the sequence starts with loading the atoms adiabatically into an optical lattice. In the lattice Bloch oscillations are performed for deceleration until the atomic motion is almost stopped. In the end the atoms are adiabatically unloaded from the lattice with only a few $\hbar k/m$ of residual velocity.
- **A momentum inversion pulse:** Second, after a certain small waiting time to carefully match the resonance condition to the velocity of the atoms a higher order double Bragg diffraction pulse is applied that inverts the momentum.
- **A lattice acceleration sequence:** Finally, a second lattice acceleration sequence is applied, which precisely speeds up the atomic ensemble to launch them on a parabolic trajectory used for atom interferometry with adjustable apex close to the atom-chip surface.

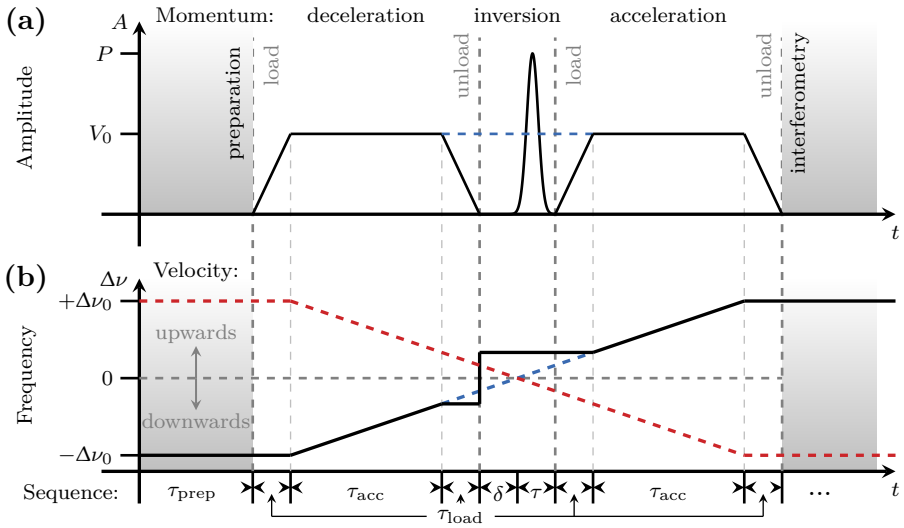

Figure 5.17: Amplitude **(a)** and frequency **(b)** modulation of the lattice during the relaunch sequence (——) compared to a single lattice acceleration (- - -). The relaunch sequence surpasses the zero velocity crossing of the dual lattice (- - -) by a double Bragg pulse inverting the momentum.

The amplitude and frequency modulation scheme of the dual-lattice light used to perform the relaunch sequence is depicted in fig. 5.17. Compared to a single-lattice acceleration this scheme is rather complex. The necessity of this procedure is given, because the additional lattices from

retro-reflection are shifted out of resonance only by the Doppler effect of the falling atoms. This effect does not allow to accelerate the lattices in a way, that the motion of the atomic ensemble crosses the zero momentum state without loosing a major fraction of atoms. The occurrence of these losses can be understood by the fact, that at the zero momentum state, e.g. where the atoms are at rest, the two moving optical lattices are both in resonance with the atoms - one attempting to move the atoms upwards, but the other one to move them downwards. This would already reduce the fraction of atoms that are launched upwards to about one-half of the original atom number, by a double Bragg diffraction like behavior. Moreover, close to a vanishing velocity of the atoms, non-adiabatic transitions arise due to parasitic acceleration in the non-resonant lattice. These transitions remove atoms from the upward moving lattice and further reduce the launched atom number to about one-quarter. Instead, a combination of Bloch oscillations in an optical lattice together with higher-order Bragg diffraction is used to prevent those losses. Most of the momentum is hereby transferred via Bloch oscillations with high efficiency close to unity to stop and launch the atoms. Since only a smaller fraction of momentum needs to be transferred by a single Bragg pulse, this sequence maintains an overall decent launch efficiency.

The method presented here provides a novel tool to implement into atomic quantum sensors extending the free-fall time without increasing their complexity. This is a crucial point for the construction of compact and very accurate inertial sensors, since our new method has some advantages over the previously used approaches. Foremost, there is no need for more than a single laser beam axis, this reduces immensely the need for additional optical access, laser power and alignment. Second, the lattice launch and thus the fountain parabola is perfectly aligned with the beam splitter. A parameter optimization for driving the Bloch oscillations in the vertical lattice (sec. 5.3.1) as well as for the momentum inversion pulse (sec. 5.3.2) of the developed relaunch procedure is performed and compared to a single lattice acceleration. The only current limitation of the relaunch is at the moment a momentum broadening perpendicular to the lattice axis due to the insufficient surface quality of the atom chip (sec. 5.3.3).

5.3.1 Coherent acceleration by Bloch oscillations

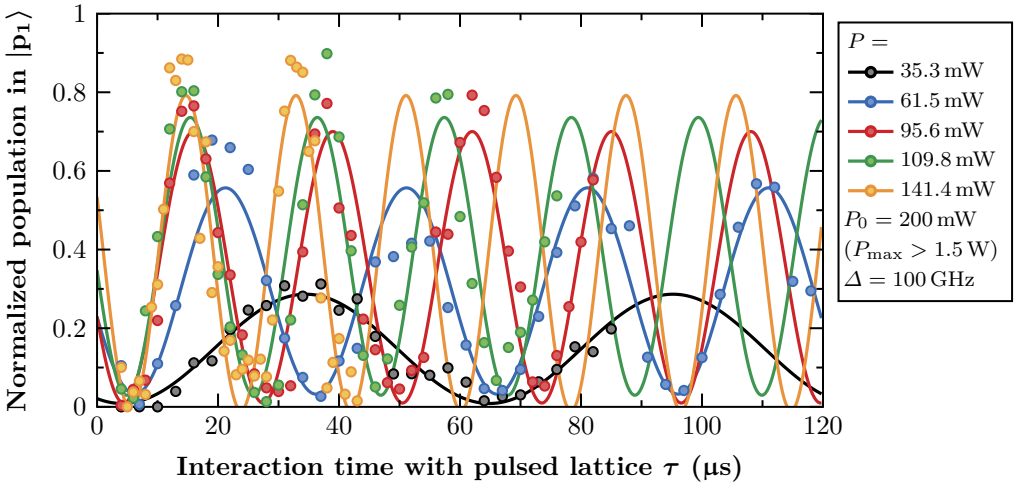

Figure 5.18: Oscillations between the fundamental and second Bloch-band induced by a pulsed lattice. By applying short pulses in the Kapitza-Dirac regime the depth of the optical lattice V_0 in units of the recoil energy E_r can be determined experimentally. The oscillation's period T is extracted from the sinusoidal fits and the lattice depth is calculated by the band gap relation.

The experimental results driving Bloch oscillations are presented in the following. In particular, the parameters for the relaunch will be investigated as well as the experimental limits of the acceleration. These limits provide useful information to make a prediction onto future experiments, that feature much larger baselines and use a larger amount of transferred photons.

Lattice depths calibration by inter-band Rabi oscillations

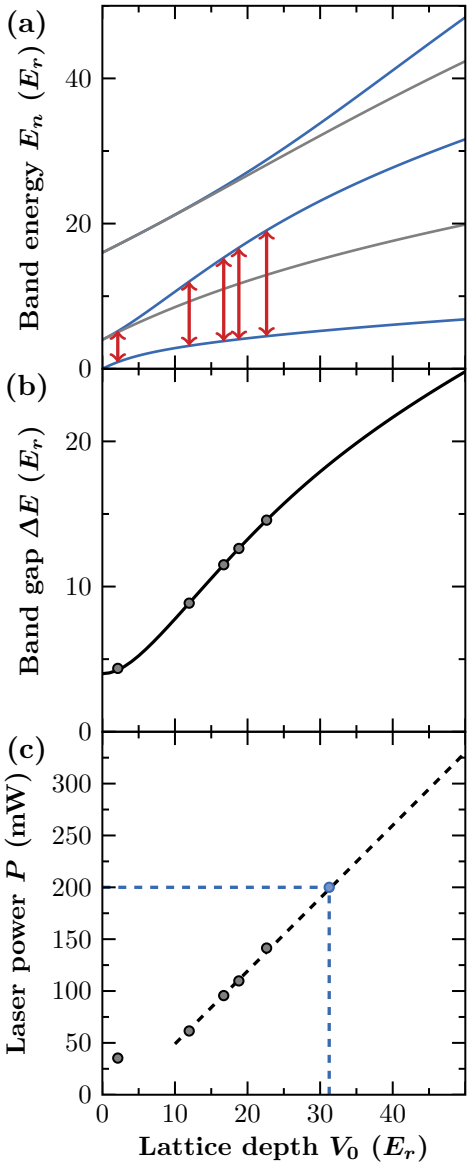

Fig. 5.19: For each band gap energy the corresponding lattice depth V_0 in E_r can be calculated **(a)** and from this the lattice depths for the measured oscillations determined **(b)**. Data points on a straight line (- - -) represent a linear dependence on the laser power **(c)**.

Following sec. 4.2, the lattice depth V_0 is the relevant parameter to characterize an optical lattice. For a quantitative analysis of the experiment the depth should be measured depending on the adjusted laster power P in the fiber. The common method to characterize the lattice depth is to measure the Rabi frequency between the fundamental and second exited band with a short non-adiabatic pulse in the Kapitza-Dirac regime, known from sec. 4.1.2. This method is more accurate than a calculation of the lattice depths from the laser parameters I and σ itself given by eq. 4.38, since losses of laser power on in-vacuum optics and imbalances do not need to be known. Fig. 5.18 shows this oscillation for different RF amplitudes, e.g. adjusted laser powers.

The lattice depth V_0 in E_r can be directly calculated from this oscillation, since the period T of the oscillation is connected to the band gap Energy $\Delta E = E_2 - E_0$ between the fundamental and the second excited band by the relation

$$T = \frac{2\pi\hbar}{\Delta E(V_0)}. \tag{5.6}$$

With the band structure calculation performed in sec. 4.2.1, this band gap energy ΔE can be related to the depth of the optical lattice [234, 273] displayed in fig. 5.19(a) and the lattice depths can be obtained from the measurement in fig. 5.19(b). The measured oscillations are above $10\,E_\mathrm{r}$ in reasonable agreement to a linear dependence on the laser intensity for larger RF and therefore laser powers, according to fig. 5.19(c). From this plot corresponding laser powers can be calculated backwards with eq. 4.38 and a beam diameter of $\oslash = 3.3\,\mathrm{mm}$. These calculated laser powers, which would correspond to the measured lattice depth, are actually a factor of two lower than the measured fiber output power. This means, that large losses of 50% occur on the optics. The reflectivity of the atom chip was characterized to about $R = 0.85$ at an incident beam angle of 0°. The remaining fraction of 35% are therefore lost at the optical components,

especially the polarizing beam splitter, that cleans the polarization, and the vacuum window, which has no ideal anti-reflective coating. The calibration can be performed for laser powers up to 150 mW, as for larger values the signal gets too weak to measure Rabi oscillations. It is expected that for these larger values the lattice depth scale further, as the theory predicts. According to this calibration measurements the largest achievable lattice depth with the current laser-power attribution of approximately $P_0 = 200\,\mathrm{mW}$ (compared to in total $P_{\max} > 1.5\,\mathrm{W}$ available laser power) is around $30\,E_\mathrm{r}$. This is already in the deep lattice regime and beyond the assumptions for the simple Landau-Zener relations, discussed in sec. 4.2.2. At these lattice depths, the band gap energy ΔE already scales below linearly with increasing laser power, as visible in fig. 5.19(a,b). Operating far beyond the linearity of the Landau-Zener regime is anyway undesirable, since the fraction of spontaneous losses is enlarged.

Adiabatic loading into and unloading from the lattice

Efficient transport can only be achieved in the fundamental band of a lattice. Instantaneous or non-adiabatic switching of the lattice leads to population of several higher-order bands. Similarly, higher-order momentum states are created, if the lattice is abruptly, i.e. in a non-adiabatic way, is switched off. Therefore, the atoms are initially loaded into and in the end released adiabatically from a co-moving lattice. This is realized by ramping the amplitude of the lattice linearly up and down, respectively, starting with a fixed detuning of the Doppler shift $\Delta\nu(0) = \omega_0$. The co-movement of the lattice is reached by slightly chirping the detuning with the atoms' free-fall rate of $\Delta\nu(t) \approx t \cdot 25\,\mathrm{MHz/s}$. This slight chirp is not critical for fast loading, but when the loading takes long enough, Bloch-oscillation would already occur due to the free-fall rate.

The adiabatic loading behavior for different lattice depths V_0 is displayed in fig. 5.20 for the following procedure: The atoms are loaded with linear ramps of durations $\tau_\mathrm{load} < 200\,\mu\mathrm{s}$ into the lattice, then held for $\tau_\mathrm{acc} = 1\,\mathrm{ms}$ without transferring momentum and finally unloaded from the lattice with the same time for simplicity. For lattice depths smaller $V_0 < 20\,E_r$ an adiabatic loading time of $\tau_\mathrm{load} = 100\,\mu\mathrm{s}$ is sufficient to load a large fraction η of atoms into the lattice. For larger values this time should be increased to 200 µs. The saturation efficiency in the figure reduces due to spontaneous emission during the holding time.

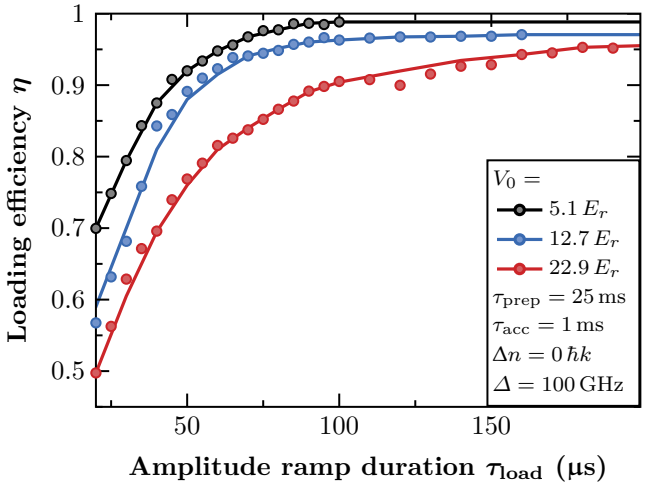

Figure 5.20: Adiabatic loading and unloading of atoms into a co-moving optical lattice with varying change in the duration of amplitude ramp τ_load. The laser detuning is fixed at $\Delta = 100\,\mathrm{GHz}$ and the holding time in between loading and unloading is constant $\tau_\mathrm{acc} = 1\,\mathrm{ms}$. The frequency detuning $\Delta\nu(t) \approx t{\cdot}25\,\mathrm{MHz/s}$ of the lattice compensates gravity such that no momentum is transferred.

Landau-Zener losses and resonant tunneling

After the atoms have been loaded into a co-moving lattice at $\Delta\nu(0)$ Bloch oscillations are performed by chirping the relative laser frequency to a fixed end-frequency $\Delta\nu = \Delta\nu(\tau_{\mathrm{acc}}) - \Delta\nu(0)$. Depending on the sign of the chirp rate $\pm\Delta\nu$ the atoms are further accelerated along the free-fall direction (frequency is increasing) or slowed down (frequency is decreasing) with respect to their free fall determined by $\Delta\nu(0) = \omega_0$. As described theoretically in sec. 4.2.3, the acceleration of the lattice $a = \frac{\Delta\nu}{\tau_{\mathrm{acc}}}$ cannot be arbitrarily large, since this would induce Landau-Zener losses by non-adiabatic transitions into higher order bands, given by eq. 4.54. In the experiment, the influence of Landau-Zener losses are studied to optimize the transfer efficiency η with a frequency ramp which has a fixed overall detuning range $\Delta\nu = 2n\nu_{\mathrm{r}}$, e.g. a fixed momentum transfer $\Delta n = n\,\hbar k$ is achieved to decelerate or accelerate the atoms, while the duration τ_{acc} in which this detuning is swept is varied and/or the lattice depth V_0 is increased.

Figure 5.21(a) shows the dependence of the transfer efficiency η for varying acceleration time τ_{acc} for different lattice depths ranging from $V_0 = 5.1\,E_{\mathrm{r}}$ to $15.1\,E_{\mathrm{r}}$. The curves show a similar behavior to fig. 4.14 as expected for a reduction of Landau-Zener losses at smaller acceleration. Moreover, a second loss mechanism is clearly visible, due to the so called "resonant tunneling" between lattice sites which is expressed by distinct dips in the Landau-Zener curves. A dip occurs, when atoms have a high probability to tunnel between two neighboring lattice sites. As schematically depicted in fig. 5.21(b), this process happens in an accelerated lattice, if the energy level of an atom in one lattice site is close to an exited energy level of a neighboring lattice site [249] and has been previously experimentally observed [274]. An atom which has tunneled to an excited level in another lattice site is not efficiently accelerated anymore and are lost. The occurrence of these resonances is in well agreement with the theoretical prediction [275] and the dips get smaller with increasing lattice depth V_0, where the tunneling probability gets suppressed. For durations of the acceleration above $\tau_{\mathrm{acc}} > 1.5\,\mathrm{ms}$ resonant tunneling completely vanishes and the transfer efficiencies approach the limit set by spontaneous emission.

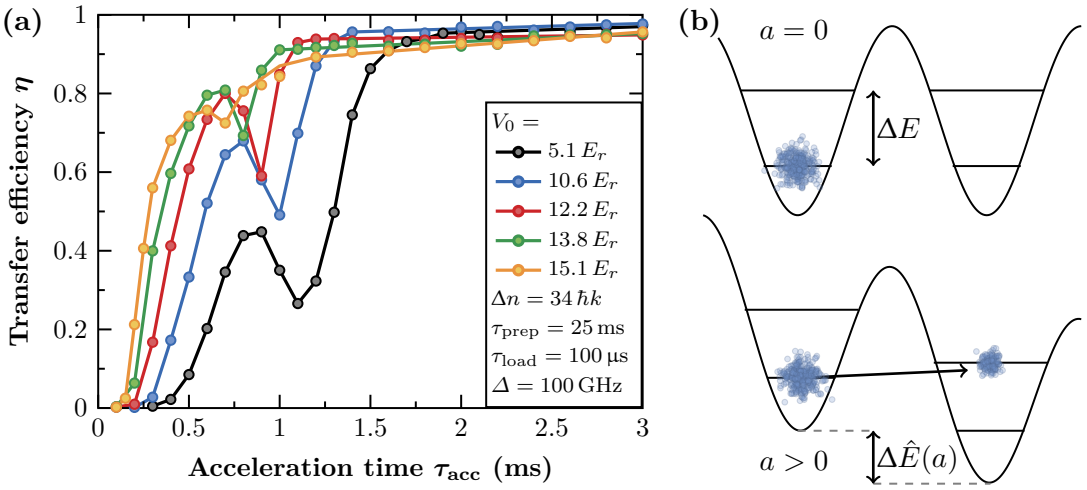

Figure 5.21: Resonant tunneling observed for different lattice depths V_0. For specific acceleration times τ_{acc} a sudden drop in transfer efficiency η is observed. These drops vanish with increasing lattice depth and at an acceleration time $\tau_{\mathrm{acc}} > 1.5\,\mathrm{ms}$ the maximal transfer efficiency is observed **(a)**. Schematic depiction of neighboring lattices sites of an accelerated lattice. Resonant tunneling between these sites occurs if the energy levels get close to each other. The atoms, which undergo tunneling, are lost during further acceleration, since they are now in exited energy levels **(b)**.

Spontaneous emission suppression by a large laser detuning

The absolute frequency of the laser system and therefore the detuning Δ to the D_2 line of ^{87}Rb has a major influence on the lattice depth V_0 in eq. 4.38 and the rate of spontaneous emission P_{sp} in eq. 4.9. The spontaneous emission rate decreases quadratically with the detuning and the lattice depth only decreases linearly, while both depend linearly on the laser power. Therefore, it is possible to reduce the fraction spontaneously scattered atoms $P_{\mathrm{sp}}\tau_{\mathrm{acc}}$ with larger detunings Δ and compensate the decrease lattice depth V_0 with larger laser powers P. The suppression of spontaneous emission for optical lattices is more crucial than for Bragg pulses since the acceleration times are one or two orders of magnitude larger as the pulses and the fraction of lost atoms may increase drastically. For Bragg pulses typically a detuning below 1 Ghz may be chosen, but for a lattice this increases to several tens of GHz. In the case of a dual lattice it is not possible to profit from a blue detuning as for a single lattice where the atoms are trapped at the nodes of the lattice (see fig. 4.9) which reduces the spontaneous emission rate [271].

In order to verify the dependence of spontaneous emission of the dual lattice the detuning Δ of the light field with respect to the D_2 line is varied with the following sequence: After a free-fall time of $\tau_{\mathrm{prep}} = 25\,\mathrm{ms}$, the atoms are (un-)loaded within $\tau_{\mathrm{load}} = 100\,\mu\mathrm{s}$ and $\Delta n = 34\,\hbar k$ are transferred to them within $\tau_{\mathrm{acc}} = 1\,\mathrm{ms}$. For a changing detuning Δ, the laser power P is adjusted to obtain maximal transfer efficiency, so ideally the lattice depth $V_0 \sim \frac{P}{\Delta}$ is held constant. In principle, the thermal tuning range of the fiber master laser (for reference see chp. 3) to adjust the laser frequency allows for approx. 130 GHz either red- or blue-detuned to the D_2 line of ^{87}Rb. Since there is no observable difference the measurement is only performed for blue-detuning. Figure 5.22 shows, that over the complete tuning range of the laser frequency the transfer efficiency can be held constantly over 90%, with a peak around 60-110 GHz of $\eta = 0.94$ or $\eta/\hbar k = 0.9982$ and the ratio between detuning Δ and optimal laser power P is also almost constant. This means, the transfer efficiency is so far not limited by the available laser power. For the following experiments the laser system is operated at the higher end of the frequency tuning range at a detuning of $\Delta = 100\,\mathrm{GHz}$ blue to the D_2 line which leaves a fraction of spontaneously scattered atoms of around 1-2 percent for every 1 ms of acceleration time τ_{acc}.

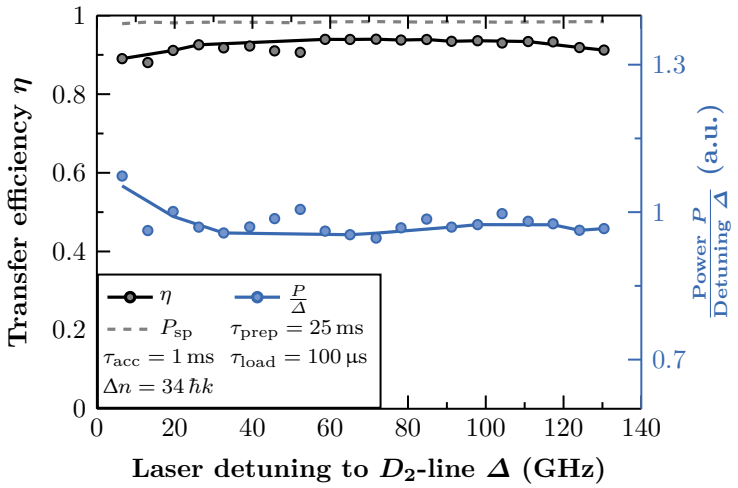

Figure 5.22: Dependence of the achievable transfer efficiency η on the laser detuning Δ (——) for the transfer of $\Delta n = 34\,\hbar k$ in $\tau_{\mathrm{acc}} = 1\,\mathrm{ms}$. At these small acceleration times the total spontaneous emission is still small (- - -). The ratio between required laser power P to compensate the larger detuning Δ (——) is reasonably constant over the complete tuning range of the laser system.

Large momentum transfer in fixed time

In the case of the atom-chip gravimeter a transfer of between 30 and 50 $\hbar k$ by Bloch oscillations is used for both the deceleration and acceleration sequence. The 7 mm small baseline of free fall in the experiment limits the waiting time τ_{prep} anyway to $\sqrt{2 \cdot 7\,\mathrm{mm}/g} \approx 34\,\mathrm{ms}$ and this transfer can be achieved within $1 - 2\,\mathrm{ms}$ avoiding Landau-Zener losses. Figure 5.23 shows the transfer efficiencies η for the transfer of different momenta Δn within a fixed acceleration period of only $\tau_{\mathrm{acc}} = 1\,\mathrm{ms}$ depending on the lattice depth V_0. The lines are computed from the Landau-Zener formula in eq. 4.54 and the spontaneous emission in eq. 4.9, which fits almost perfectly for $\Delta n = 20\,\hbar k$, but is scaled to the maximum measured transfer efficiency η for all other Δn. For the data points with $\Delta n = 50\,\hbar k$ and $100\,\hbar k$ residual resonant tunneling is visible, which was not taken into account in the curves. In principle, the amount of momenta which can be transferred by Bloch oscillations in a given time is not fundamentally limited but purely technical. A limitation that cannot easily be beaten is the spontaneous emission P_{sp}. Spontaneous emission effectively reduces the launched fraction of atoms η, since laser detuning Δ and power P cannot be endlessly enlarged. For the chosen laser detuning of $\Delta = 100\,\mathrm{GHz}$ even at the largest lattice depth of $V_0 = 23\,E_{\mathrm{r}}$, the fraction of spontaneous emission still stays at the few percent level.

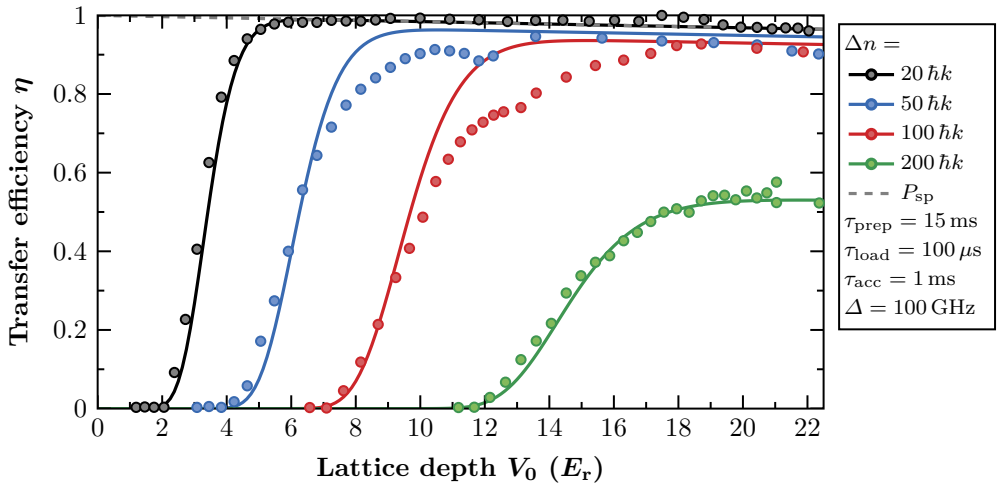

Figure 5.23: Landau-Zener losses for a transfer of different momenta Δn in a given time of $\tau_{\mathrm{acc}} = 1\,\mathrm{ms}$ depending on the lattice depth V_0. Up to $\Delta n = 100\,\hbar k$ the remaining fraction of atoms in the target momentum state can be held above $\eta > 0.9$. The lines are calculations of Landau-Zener losses and spontaneous emission normalized to the measured maximum transfer efficiency.

Δn	η	$\eta_{\mathrm{LZ}}/\hbar k$	η_{sp}
20	0.993	0.99**99**	0.992
50	0.946	0.99**94**	0.980
100	0.927	0.99**95**	0.972
200	0.542	0.99**71**	0.968

Table 5.1: Maximum total and relative transfer efficiencies η and $\eta/\hbar k$ for different transferred momenta Δn extracted from the curves in fig. 5.23.

The results of the graph are summarized in tab. 5.1 together with the relative Landau-Zener efficiencies $\eta_{\mathrm{LZ}}/\hbar k$ and the surviving fraction η_{sp} of atoms which are not spontaneously scattered. Up to an acceleration of $100\,\hbar k/\mathrm{ms}$ the relative transfer efficiencies can be held at a level of $\eta_{\mathrm{LZ}}/\hbar k > 0.999$. For larger accelerations the relative transfer efficiency starts to decrease, due to an insufficient adiabaticity of the process. As seen for $200\,\hbar k/\mathrm{ms}$ this decrease of efficiency drastically reduces the remaining fraction of accelerated atoms. For $\Delta n = 20\,\hbar k$ the process is fully limited by spontaneous emission, within the error of the measurement. This performance would allow to transfer $1\,000\,\hbar k$ in at minimum $\tau_{\mathrm{acc}} = 10\,\mathrm{ms}$ with a remaining 50% fraction of accelerated atoms.

5.3.2 Momentum inversion using double Bragg diffraction

With Bloch oscillations it is possible to slow the atoms down after free fall with high efficiency. But it is not possible to entirely stop them or to even invert their momentum and accelerate them upwards again without loosing a major fraction of atoms. The closer the velocity of the atoms to zero is, where both lattices have the same frequency, the larger losses occur to different momentum states. Figure 5.24(b) shows density plots of these losses then the atoms are slowed down with Bloch oscillations and the deceleration crosses the $0\,\hbar k$ momentum state. The losses can be understood due to standing waves close to the zero momentum state, already discussed in sec. 5.2 and the influence of the dual-lattice configuration, which will be discussed in more detail in sec. 7.2. The deceleration leads to a final atomic momentum state as an approximate multiple n of $-2\,\hbar k$, referenced to atoms at rest. According to fig. 5.24(a) the losses start to increase beyond $-8\,\hbar k$, at which the unloading is still nearly undisturbed. It is supposed, that these losses are symmetric around the zero momentum, therefore the preferred momentum state to begin the second acceleration sequence with would be $+8\,\hbar k$. The deceleration for the atom-chip gravimeter should be chosen such, that the atoms are unloaded from the lattice with as small as possible residual velocity but before non-adiabatic losses occur.

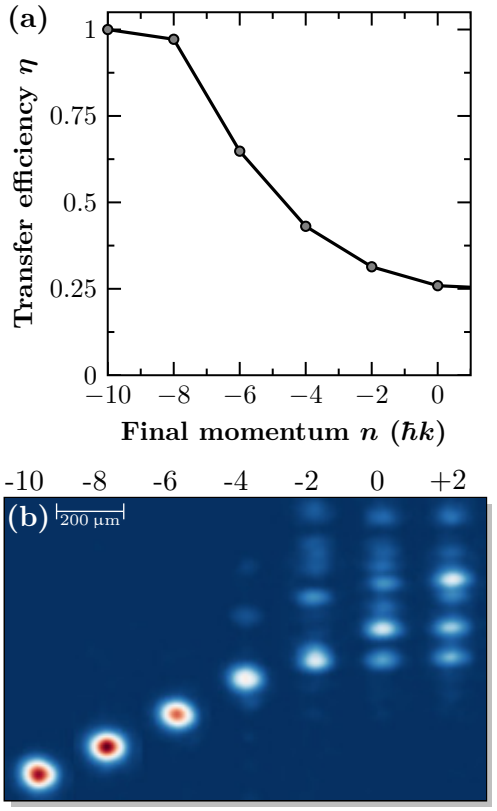

Fig. 5.24: Non-adiabatic losses dependent on the residual momentum after the deceleration by Bloch oscillations **(a)** and respective density plots crossing the $0\,\hbar k$ momentum state, where the atoms are resonant to both lattices **(b)**.

Optimized double Bragg pulse to invert the momentum

After the deceleration by Bloch oscillations the momentum is inverted with a higher-order double Bragg diffraction pulse. Using a single higher-order pulse has the advantage, that the relative laser frequency $\Delta\nu$ is fixed during the interaction and at no time the frequency of both lattices is the same. The total momentum to bypass with this pulse is $16\,\hbar k$, which is equivalent to fourth-order double Bragg diffraction. To drive this high order demands large laser powers and low fluctuations as well as a narrow velocity distribution and low fluctuations of the initial motion of the ensemble (see sec. 5.2). Using sequential transitions as in eq. 4.22 is not an option, since the described losses occur there as well. To increase the transfer efficiency, rather than using a resonance frequency of $\Delta\nu = 2n \cdot \omega_\mathrm{r}$ with $n = 8$ for single or $n = 4$ for double Bragg diffraction, instead a frequency of $\Delta\nu = 10 \cdot \omega_\mathrm{r} = 75.5\,\mathrm{kHz}$ is chosen for the pulse, which is detuned by $2\,\omega_\mathrm{r}$ to the traditional fourth-order double Bragg resonance as depicted in fig. 5.25. While the conventional fourth-order double Bragg resonance couples $0\,\hbar k \rightarrow \pm 8\,\hbar k$, the detuned resonance couples $\mp 8\,\hbar k \rightarrow \pm 8\,\hbar k$ and hence directly inverts the momentum of the incoming atoms. This process is possible because higher-order double Bragg diffraction has a much richer structure than conventional couplings due to the four frequency components.

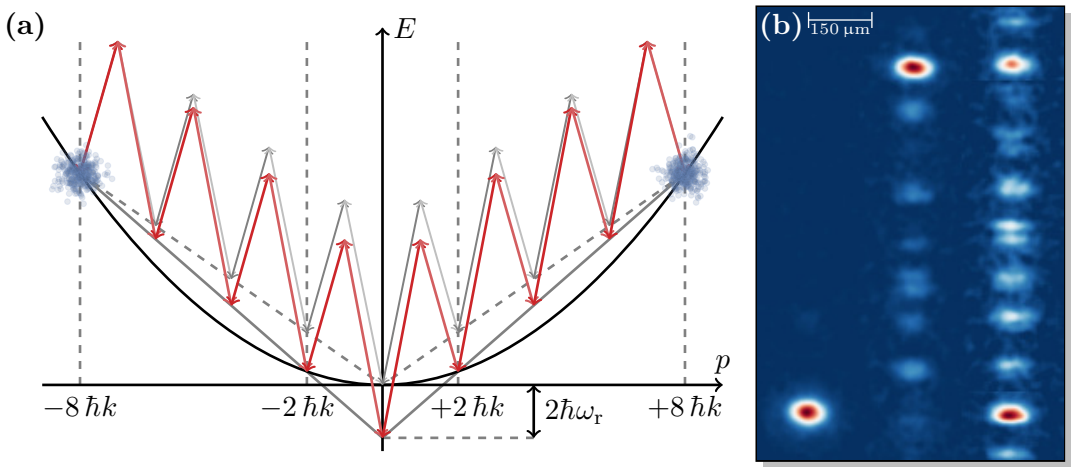

Figure 5.25: The resonance condition **(a)** of the momentum inversion pulse (—) is detuned $2\,\omega_\mathrm{r}$ from the fourth-order double Bragg transition (—) and suppresses losses into the $0\,\hbar k$ momentum state via a violation of energy conservation. Density plots **(b)** of the momentum inversion with a $16\,\hbar k$ double Bragg diffraction pulse (middle), compared to the atoms after the deceleration (left) and a simple sweep through resonance with Bloch oscillations (right). The optimized transfer efficiency of the inversion pulse is with $\eta = 80$-83% at the same level as in [67].

The main advantage of using this resonance lies in the detuning with respect to the energy of the zero momentum state and suppresses its population. An exemplary density plot for such a double Bragg pulse with a waveform length of $\tau = 100\,\mu\mathrm{s}$ and width of $\sigma = 12.5\,\mu\mathrm{s}$ is shown in fig. 5.25(b) at an efficiency of roughly $\eta \sim 0.8$ for a condensate without and even slightly larger $\eta \sim 0.83$ with delta-kick collimation (middle) compared to a sweep through the zero momentum state by Bloch oscillations only (right). This efficiency for a transfer of $16\,\hbar k$ is comparable to ref. [67]. The efficiency per transferred photon is $\eta/\hbar k = 0.987$, while for a fourth-order double Bragg diffraction pulse it is measured to $\eta/\hbar k = 0.915$ which in total only leads to $\eta \sim 0.25$.

Velocity match and width of the resonance

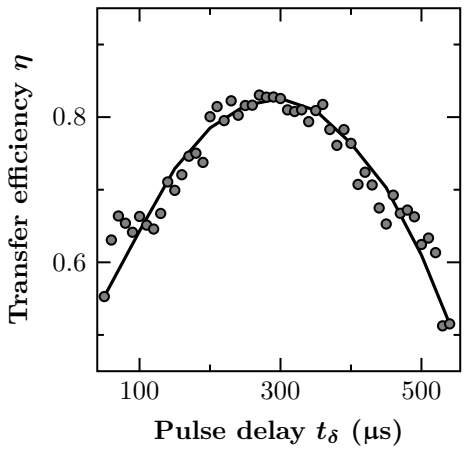

Fig. 5.26: The transfer efficiency η for a $16\,\hbar k$ double Bragg pulse as a function of the delay t_δ after deceleration before the pulse is applied.

Since the atoms are falling due to gravity the Doppler effect needs to be compensated. For single Bragg diffraction, the Doppler shift is simply added to the relative laser frequency $\Delta\nu$ following eq. 4.19. For double Bragg diffraction, it is not possible to change the relative laser frequency to a different value as $\Delta\nu = 75.5\,\mathrm{kHz}$, because the Doppler shift changes its sign dependent on the direction of momentum transfer. Hence, the symmetry of the process is mandatory to invert the momentum and both pairs of laser beams need to be in resonance at once. Here, the Doppler shift can be precisely adjusted by the timing of the pulse. To make sure that an arbitrary Doppler shift can be matched to the transition frequency, the lattice deceleration sequence is not stopped exactly at the $-8\,\hbar k$ momentum state, but in between $-8\,\hbar k$

and $-7\,\hbar k$ to continuously adjust the mismatch of the transition by a small pulse delay t_δ. This gives rise to a detuning of $\delta = 4 - 5\,\mathrm{kHz}$ to the resonance condition and a range to optimize the delay within a few 100 µs of free fall. The delay is then adjusted in steps of 10 µs, corresponding each to an additional Doppler detuning of 250 Hz, to optimize the resonance condition for the pulse and thereby its diffraction efficiency as seen in fig. 5.26. The efficiency of the pulse is limited due to the finite momentum width of the condensate and the peak of the resonance is reasonably flat for $1 - 2\,\mathrm{kHz}$, which is quite resistant to jitter in laser power.

Comparison of the relaunch with and without the momentum inversion pulse

Figure 5.27 shows stepwise density plots of a complete relaunch sequence, to compare the new composed relaunch sequence (a) to a single lattice acceleration (b). After an initial free-fall time of $\tau_{\mathrm{prep}} = 25\,\mathrm{ms}$, a Doppler shift of 625 kHz occurs which requires a transfer of $34\,\hbar k$ to reach the $-8\,\hbar k$, where the momentum is inverted by the double Bragg pulse. Since the number of density plots in (a) and (b) is equal, the total transferred momentum is $76\,\hbar k$ for 38 steps during the single lattice acceleration, and respectively $90\,\hbar k$ for the composed sequence, since a $2\,\hbar k$ step is substituted by a $16\,\hbar k$ double Bragg pulse. Note, that each density plot is normalized individually, so only the relative atom number in each momentum state, which are separated with a time of flight of 10 ms, is indicated but not between subsequents density plots. The suppression of losses into other momentum states due to the double Bragg pulse is clearly visible. That way, the fraction of launched atoms is greatly enhanced from 25% to 75% which would be even slightly more for delta-kick collimated condensates. This efficiency results mostly from the limited efficiency of the double Bragg pulse with only a small additional amount of spontaneously scattered atoms during the Bloch oscillations. Since the losses due to the double Bragg pulse occur only once, the increase of the momentum transfer only depends on the Bloch oscillations, which allows to coherently relaunch atoms in meter sized fountains with this new method.

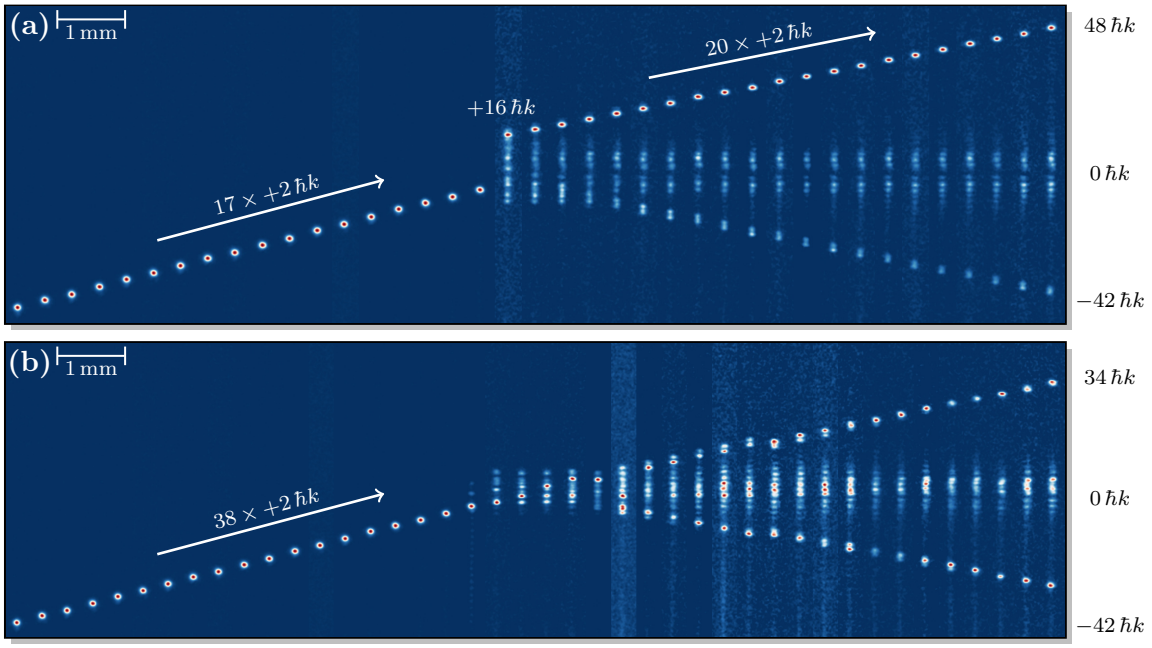

Figure 5.27: Comparison between composed relaunch with a double Bragg pulse **(a)** or a single lattice acceleration **(b)**. In total the transferred fraction of atoms for the single lattice acceleration is around 25%, while this fraction increases to more than 75% for the composed sequence.

5.3.3 Free expansion of the relaunched ensemble

In the frame of this study the effect of the relaunch on the velocity distribution of the ensemble is investigated. A time series of density plots for two fountain parabolas relaunched after more than $\tau_{\mathrm{prep}} > 30\,\mathrm{ms}$ is depicted in fig. 5.28 for condensates with (a) and without (b) delta-kick collimation. Already these density plots clearly reveal an inhomogeneous momentum broadening caused by the relaunch. The reason for this broadening is attributed to the insufficient surface quality of the atom chip. Anyway, the relaunch is still suitable to perform interferometry with, because even after almost 100 ms of free fall and without delta-kick collimation the clouds are still reasonably compact and detectable. In order to confirm the suspicion, that the atom chip causes the broadening, the expansion is studied in detail. Three different implementations of the relaunch will be employed in the fountain mode of the atom-chip gravimeter. Condensates without delta-kick collimation are relaunched either after $\tau_{\mathrm{prep}} = 25\,\mathrm{ms}$ or $\tau_{\mathrm{prep}} = 31.2\,\mathrm{ms}$ and the collimated condensates are relaunched after the longest time of $\tau_{\mathrm{prep}} = 33.2\,\mathrm{ms}$. Figure. 5.29 shows the expansions curves for all implementations and for comparison the initial expansion rates for the condensate with and without delta-kick collimation are included. The linear fitted expansion rates and their relative ratio Δp are listed in tab. 5.2.

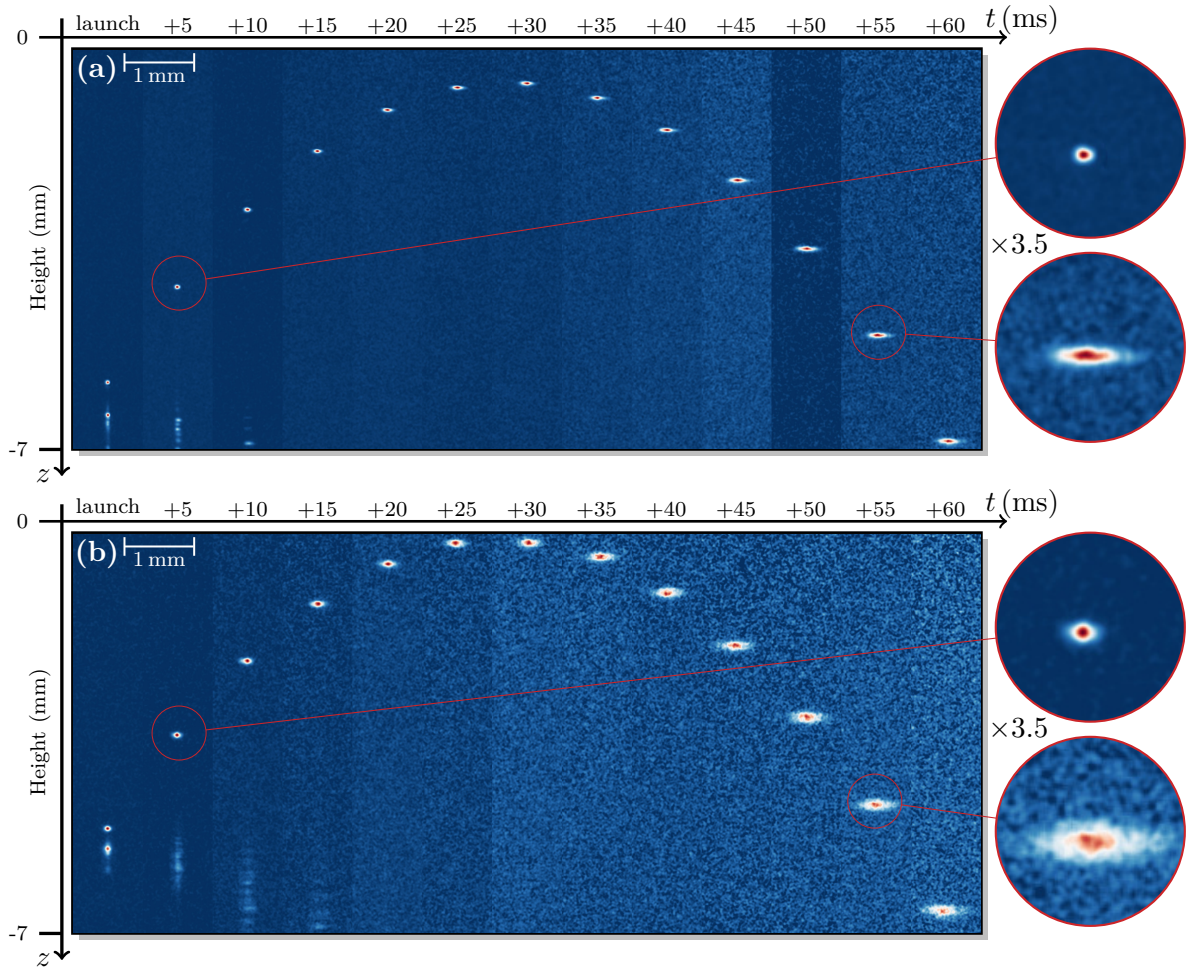

Figure 5.28: Fountain parabola for Bose-Einstein condensates with **(a)** and without **(b)** delta-kick collimation relaunched after a waiting time $\tau_{\mathrm{prep}} > 30\,\mathrm{ms}$. The step size between each plot is 5 ms and the expansion is anisotropic. At the beginning the losses during the relaunch are still observable.

The relaunch has only marginal effect on the expansion rate in z-direction (vertical) shown in fig. 5.29(b). The double Bragg pulse which inverts the momentum even acts as a slight velocity and spatial filter for the uncollimated condensates [11, 64]. The expansion for the collimated ensemble deviates from the linear fit for expansion times larger than 80 ms because due to the large extend in y-direction also σ_z appears to be larger. In y-direction (horizontal) a broadening Δp is clearly visible in fig. 5.29(a). The lager relative broadening for the delta-kick collimated condensate is caused by the reduced distance to the defect during the launch, because the initial shift in the steeper trap prior to the kick is smaller, than for the swallow trap without delta-kick collimation (see sec. 5.1.1). Although, the relative broadening $\Delta p \approx 9$ is the largest for the collimated ensemble, the net expansion of 1.5 mm/s is still smaller than for the uncollimated condensates and even the largest expansion of 3.1 mm/s is still below the recoil velocity ($< v_{\mathrm{rec}} = 5.5$mm/s). This momentum broadening is the current limitation of the relaunch, since it causes larger expansion rates v_y and sizes σ_y of the condensate as given by the initial expansion or even the delta-kick collimation.

Relaunch τ_{prep} (ms)		Before µm/s	After µm/s	Δp
w/o DKC	y	648	3110	4.8
after 25 ms	z	610	519	0.9
w/o DKC	y	487	1913	3.9
after 31.2 ms	z	610	497	0.8
with DKC	y	165	1467	8.9
after 33.2 ms	z	131	148	1.1

Table 5.2: Summary of the expansion rates in horizontal and vertical direction after relaunch for condensates with and without delta-kick collimation obtained after waiting times τ_{prep}.

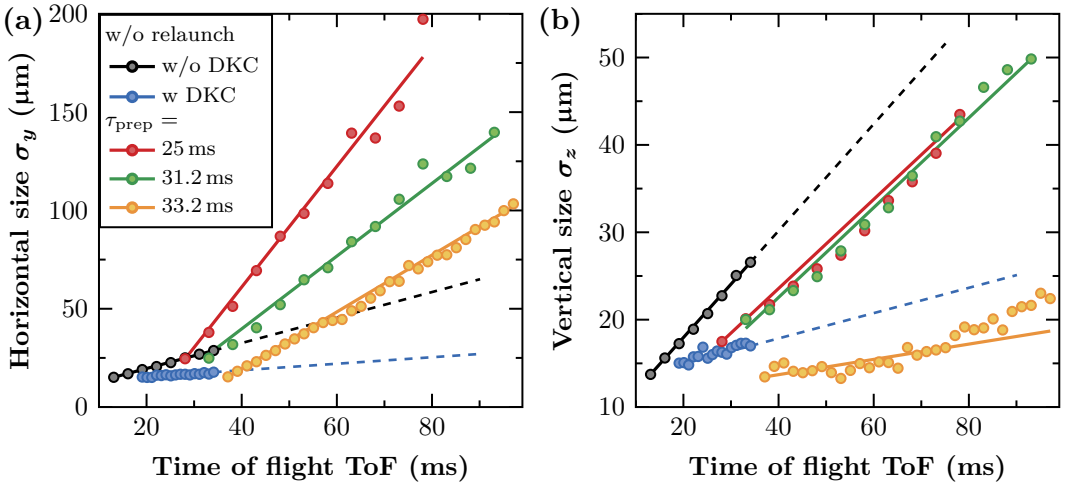

Figure 5.29: Expansion rates of the launched ensembles for different cases in horizontal **(a)** and vertical **(b)** direction. The relaunch is applied after 25 ms (—) or 31.2 ms (—) for Bose-Einstein condensates released from the shallow trap without delta-kick collimation (—) and after 33.2 ms (—) for condensates released from the steeper trap with delta-kick collimation (—).

Analysis of the horizontal momentum broadening

Three different effects can possibly cause a momentum broadening during the relaunch: heating due to spontaneous scattering of photons, interactions due to the high density of a Bose-Einstein condensate or a broadening due the potential of the lattice in combination with the surface quality of the atom chip. A broadening caused by heating due to spontaneous scattering of photons like in an optical molasses [276] can be directly ruled out by the observation of the anisotropy of

the measured expansion, because the spontaneous decay is not a directed process. Additionally, spontaneous scattering would heat up the ensemble to the recoil velocity. Concerning atomic interactions it is known, that the high atomic density of a Bose-Einstein condensate can cause heating in an optical lattice [235, 277–279]. From the literature these effects would be expected to cause a heating in the direction along the lattice, so in z-direction, because the confinement perpendicular to the lattice in a collimated beam is rather negligible.

Double Bragg diffraction can be used as a tool to position-dependently analyze the surface quality of the atom chip, by kicking the atoms horizontally prior to the relaunch to have a larger distance to the defect. The problem connected to double Bragg diffraction at this point is, that the atoms cannot be simply displaced but rather keep the lateral velocity and the atom number is reduced by two. Figure 5.30 shows the time of flight measurements (a) and extracted expansion rates (b) for different initial shifts realized with a varying number of double Bragg pulses for delta-kick collimated condensates. The plots show, that in fact the momentum broadening can be lowered with a shift far below the largest expansion rate observed at the central position, but still not as low as without the relaunch. However, to acceptability implement this in the experiment the optical setup needs to be changed.

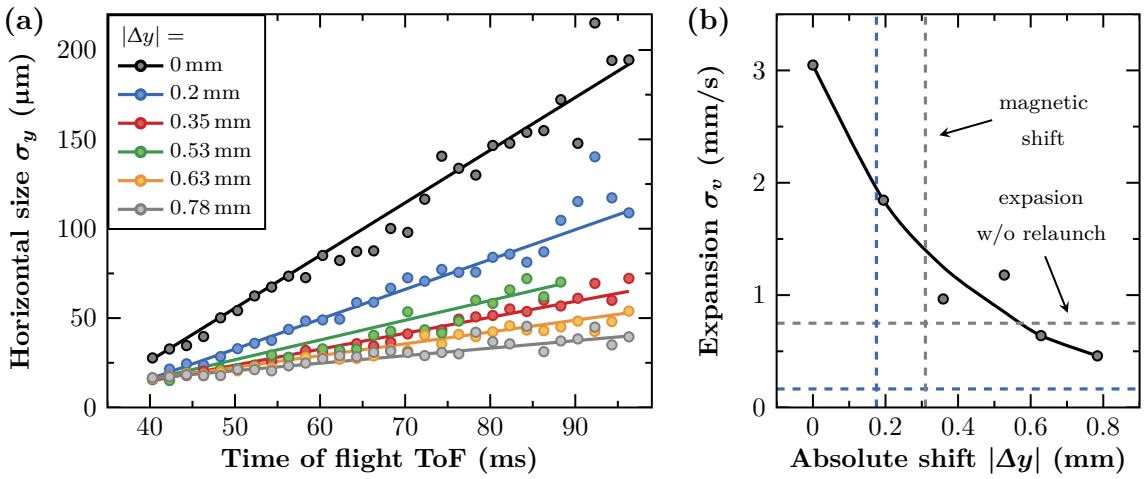

Figure 5.30: Dependence of the horizontal expansion on the initial shift which is realized with a variable number of light pulses **(a)**. The extracted expansion rates are compared to the expansion without relaunch and the maximum shift in the magnetic trap **(b)** for condensates released from the shallow trap (- - -) and condensates released from the steeper trap with delta-kick collimation(- - -).

CHAPTER 6

Atom-chip gravimeter

Gravimetry with atomic quantum sensors based on laser-cooled atoms has a more than two decades long history [8, 9, 12] and can today reach very high accuracies competitive to falling corner cube gravimeters [30]. Compact gravimeters using Bose-Einstein condensates have been demonstrated only recently [97, 156]. Due to their small extent and expansion, condensates which are delta-kick collimated have attracted attention for large scale devices on ground [99] and in space missions [280]. In the light of these experiments systematic uncertainties specific to Bose-Einstein condensates have been analyzed [281, 282] and novel techniques have been introduced, which are not applicable to laser-cooled atoms [100]. These achievements will allow sensors relying on Bose-Einstein condensates to target sub-μGal accuracies in the near future and to overcome current limitations set by laser cooled atoms [12, 54–56]. The use of a chip-based source for such a sensor, utilizing the atom chip for all preparation steps and itself as a retro-reflector is a novelty in the presented work. Although this experiment is currently at the status of proof-of-principle, this result represents an important pathway to the application of an atom-chip gravimeter for precision measurements, that are of importance in e.g. the field of geodesy. In particular these results demonstrate the complete functionality and methods of atom-chip-based gravity measurements, that will be needed for the future gravimeter QG-I (see 8.1). The results shown in this chapter represent the first realization of a quantum gravimeter with an atom-chip device and a selection of these results have been published in ref. [156].

In the course of this chapter, the various experimental results with the two different implementations of a prototype atom-chip gravimeter are discussed (sec. 6.1). The first implementation uses dropped Bose-Einstein condensates for interferometry and demonstrates the methods to evaluate the sensitivity to the gravitational acceleration (sec. 6.2), which is completely limited by statistical noise from vibrations. The precision of the experiment can be improved by eight hours of integration down to $\Delta g/g = 1.3 \cdot 10^{-5}$, demonstrating the long term stability. To demonstrate high sensitivities in the atom-chip gravimeter a fountain is implemented (sec. 6.3) which allows for an enlarged pulse separation time of up to $T = 25\,\mathrm{ms}$ and reaches an intrinsic sensitivity of up to $\Delta g/g = 1.4 \cdot 10^{-7}$ at a contrast of $C = 0.8$. At these high sensitivities the performance of the Mach-Zehnder interferometer is evaluated using purely statistical methods. The use of a PCA-based evaluation allows to overcome a loss of contrast which is caused by dephasing due to curved wave fronts for third-order Bragg diffraction and a regain of contrast from $C = 0.35$ to 0.72 is observed. Finally, estimations on systematic uncertainties are performed to find possible mitigation strategies (sec. 6.4.1). These mitigation strategies are the key for future experiments, which are by design build for gravimetry, to reach sub-μGal accuracies in the near future.

6.1 Operation of the atom-chip gravimeter in two modes

The atom-chip gravimeter is implemented with a Mach-Zehnder interferometer in two different modes: with dropped Bose-Einstein condensates (sec. 6.1.1) and with a fountain using the relaunch technique (sec. 6.1.2). While the drop mode is in the first place very simple to realize, it is shown, that the fountain mode can reach high intrinsic sensitivities and allows to integrate delta-kick collimation into the sequence. For these reasons, the fountain mode is superior with respect to the drop mode and the necessary step towards a precision measurement with such a scheme in the future. In this section, the sequences of both modes are described in detail with the parameters investigated during the implementation of the experimental methods in chp. 5.

Comparison between the different atomic sources

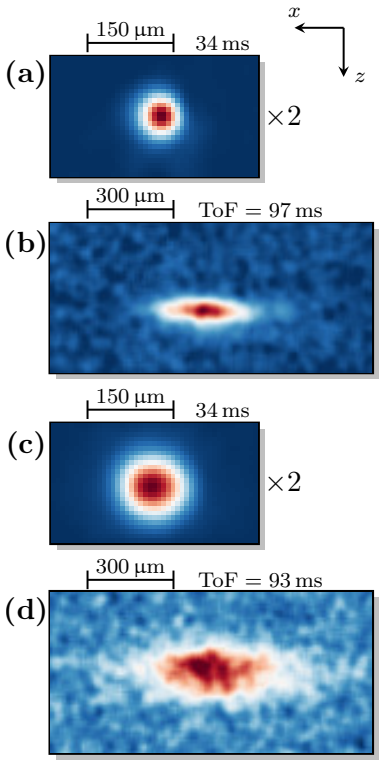

Fig. 6.1: Density plots of atomic clouds for delta-kick collimated ensembles and BECs after 34 ms of expansion **(a,c)** as well as after relaunch with extended time ToF = 93/97 ms **(b,d)**. The plots with smaller ToF are magnified by two in size.

Two different source configurations for the generation of a Bose-Einstein condensate can be used in the atom-chip gravimeter. In the first configuration, Bose-Einstein condensates are employed which are released from the shallow trap with the shift of $I_{\mathrm{K2}} = -1\,\mathrm{A}$ introduced in sec. 5.1.1. With trapping frequencies of $f_{(\mathrm{x,y,z})} = (18, 46, 31)\,\mathrm{Hz}$ an expansion rate along the beam splitting axis of $\sigma_v = 750\,\mu\mathrm{m/s} \equiv 0.125\,\hbar k$ is measured which corresponds to an effective temperature in the direction of the beam splitter of about 5-10 nK. This configuration is the perfect choice for experiments with dropped condensates when the time of flight is constrained by the end of the detection region to ToF = 34 ms where the clouds are still reasonably small without delta-kick collimation. In the second configuration, delta-kick collimated condensates are used following the protocol developed in sec. 5.1.2. Prior to the kick, the condensates are generated in a steep trap with frequencies $f_{(\mathrm{x,y,z})} = (18, 131, 127)\,\mathrm{Hz}$ at initially higher expansion rates of $\sigma_v = 1.6\,\mathrm{mm/s} \equiv 0.3\,\hbar k$. Delta-kick collimation is applied by switching on this release trap again after expansion for $\tau_{\mathrm{exp}} = 6\,\mathrm{ms}$ for $\tau_{\mathrm{dkc}} = 280\,\mu\mathrm{s}$ to collimate and further reduce the expansion of the atomic ensemble below 1 nK to $150\,\mu\mathrm{m/s} \equiv 0.025\,\hbar k$. While it is not possible to use the second configuration with delta-kick collimation in the drop mode of the gravimeter, in the fountain mode both sources can be employed and the influence of the momentum width on the Bragg efficiencies can be studied. A lower momentum width is especially for higher-order Bragg diffraction beneficial. Figure 6.1 compares the sizes of both of these sources after a free-fall time of ToF = 34 ms, which is the limit of the drop mode and for ToF > 90 ms which is only achievable in the fountain mode. In this figure the density plots for the smaller free-fall times (a,c) are magnified by a factor of two. These reveal, that the difference between the two source configurations in only short free-fall time is not drastically. There is a difference in size, but both ensembles are still compact and dense. For larger free-fall times of ToF > 90 ms this situation changes and a condensate without delta-kick collimation appears rather dilute and less dense. A reduced final cloud sizes at the output ports also leads to smaller final separation times τ_{sep} and more time for interferometry.

6.1.1 Gravimeter using dropped Bose-Einstein condensates

The sequence of the atom-chip gravimeter with dropped atoms is kept simple and only integrates the most essential steps, in order to achieve a sufficient pulse separation time, which determines the sensitivity of the Mach-Zehnder interferometer. This sequence is depicted in a space-time diagram in fig. 6.2 which contains the timings after release of the condensate from the trap and the corresponding heights in the detection region. It consists of only three steps: I. the atomic state preparation via an adiabatic rapid passage, which consumes the total preparation time $\tau_{\mathrm{arp}} = 10.2\,\mathrm{ms}$, II. the Mach-Zehnder interferometer formed by three first-order Bragg pulses with pulse separation times between $T = 1 - 5\,\mathrm{ms}$ and III. the spatial output port detection.

The Mach-Zehnder interferometer can in principle be performed with momentum transfer either in upward or downward direction to characterize systematic effects which are dependent on the recoil of the beam splitter [18, 138]. However, since these effects are at the moment expected to be negligible (see sec. 6.4.1) only the upward diffraction is used instead of an interleaved operation between both upward and downward direction, which is called a “k-flip” measurement. The time $\tau_{\mathrm{sep}} \geq 13\,\mathrm{ms}$ for separating the output ports guarantees a clean separation after a total time of flight of $\mathrm{ToF} = 34\,\mathrm{ms}$. A clean separation of the output ports maximizes the achievable

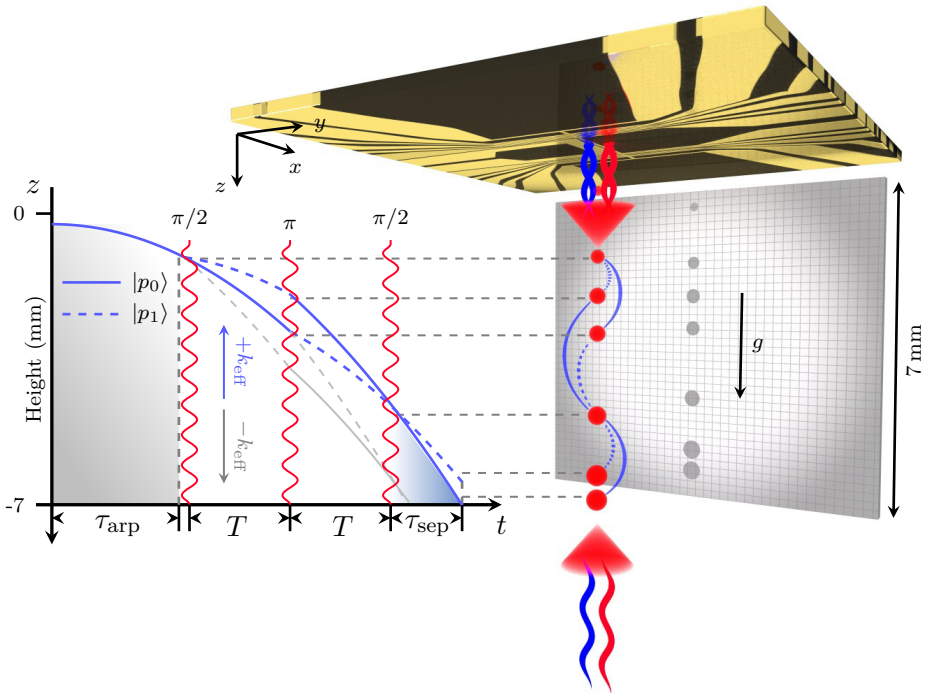

Figure 6.2: The experimental realization of the atom-chip gravimeter using dropped atoms, operates with condensates released from the shallow trap with frequencies of $(46, 31, 18)\,\mathrm{Hz}$ and expansion rates of $\sigma_v = 750\,\mu\mathrm{m/s} \equiv 0.125\,\hbar k$. The sequence employed for the determination of gravity consists of three segments: the atomic state preparation via an adiabatic rapid passage (▭), which consumes the total preparation time $\tau_{\mathrm{arp}} = 10.2\,\mathrm{ms}$, the Mach-Zehnder interferometer with pulse separation times ranging from $T = 1 - 5\,\mathrm{ms}$ and the spatial output port detection after a fixed time of flight $\mathrm{ToF} = 34\,\mathrm{ms}$. Constraining the pulse separation to $T \leq 5\,\mathrm{ms}$ leaves the output ports sufficient time $\tau_{\mathrm{sep}} > 13\,\mathrm{ms}$ to separate (▭). The MZI can be performed with momentum transfer either in upward (▭) or downward (▭) direction to characterize systematic effects [18, 138].

interferometric contrast C and directly influences the intrinsic sensitivity of the Mach-Zehnder interferometer. Adding up τ_{arp}, τ_{sep} and T makes it plausible, that a more complex preparation or larger pulse separation times is not possible in this small detection volume.

First-order Bragg diffraction with a Gaussian-shaped pulse envelope of an overall duration of $\tau = 200\ \mu\mathrm{s}$ corresponding to a Gaussian width of $\sigma_\tau = \frac{\tau}{8} = 25\,\mu\mathrm{s}$ is employed to realize the Mach-Zehnder interferometer. The pulse's Fourier width of $\sigma_\nu = 0.3\,\hbar k$ is sufficiently wide even for the $\sigma_v = 0.125\,\hbar k$ momentum width of the condensate without delta-kick collimation. The diffraction efficiency is in the order of $\eta_{1\mathrm{st}} = 0.95$, which is limited by spurious thermal background atoms and spontaneous emission, but is close to the limit predicted by the theory [66]. The pulse amplitude is adjusted to either drive a π- or $\frac{\pi}{2}$-pulse according to the measurements performed in sec. 5.2 at a constant pulse duration σ_τ for all pulses. At each pulse, the Doppler shift ω_0 during free fall is accounted for by adapting the relative laser frequency $\Delta\nu$. The phase shift at the output ports of the Mach-Zehnder interferometer $\Delta\phi$ is calculated as in sec. 4.3.1.

6.1.2 Fountain gravimeter with extended free-fall time

The space-time diagram of the fountain geometry is schematically depicted in fig. 6.3. Additionally, Stern-Gerlach-type deflection is performed subsequent to the adiabatic rapid passage by a magnetic field pulse using the Z-wire with a duration of $\tau_{\mathrm{SG}} = 7\,\mathrm{ms}$. Thereby, remaining atoms in magnetic sensitive states are removed to enhance the contrast. The maximum value of τ_{prep} is limited to 34 ms given by the end of the detection region at 7 mm below the chip. The relaunch process itself follows the optimization investigated in sec. 5.3 and has in the sequence

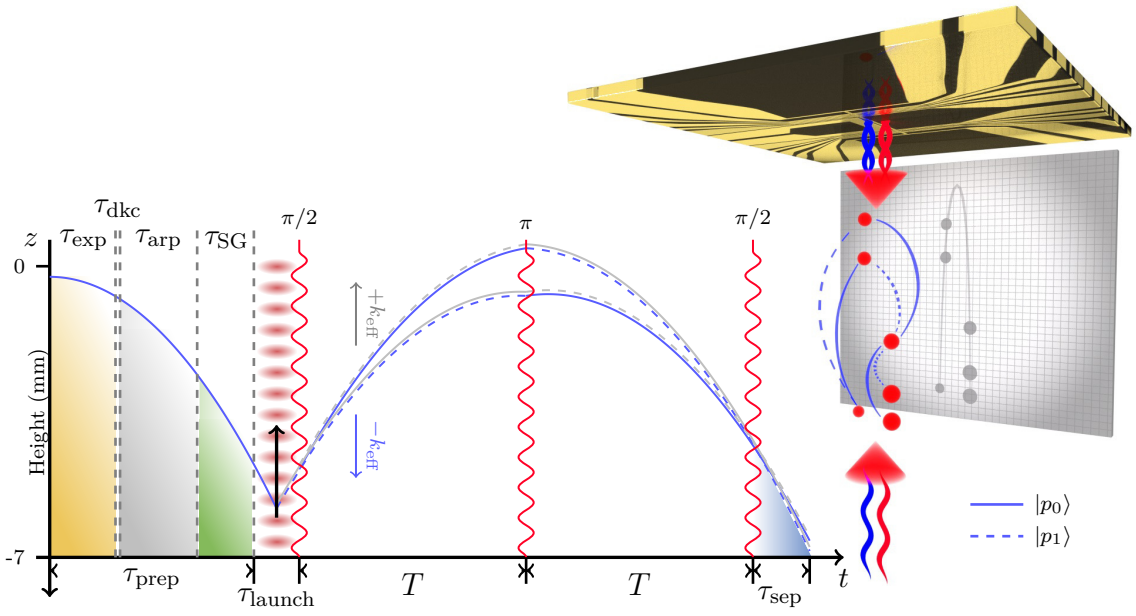

Figure 6.3: Experimental sequence of the fountain geometry with extended free-fall time of up to ToF $\approx 100\,\mathrm{ms}$. The preparation of the atomic ensemble is performed in τ_{prep} before the relaunch. Due to the elongated free-fall time it also allows for DKC (■) to reduce the expansion rate, as well the ARP (■) and Stern-Gerlach-type deflection (■) to remove remaining atoms in magnetic sensitive states. The relaunch in the retro-reflected optical lattice (■) itself is realized as introduced in sec. 5.3. The Mach-Zehnder interferometer (■,■) features up to third-order Bragg diffraction, pulse separation times up to $T = 25\,\mathrm{ms}$ and a detection after a separation time of $\tau_{\mathrm{sep}} \geq 10\,\mathrm{ms}$ (■).

an overall duration of $\tau_{\mathrm{launch}} = 2.9\,\mathrm{ms}$. With a relaunch realized after the largest waiting time of $\tau_{\mathrm{prep}} = 33.2\,\mathrm{ms}$ the total time of flight after initial release of the atoms is greatly enlarged to $\mathrm{ToF} = 97.6\,\mathrm{ms}$. The actual interferometer is operated after the atoms have been launched on the fountain trajectory. The final waiting time after a $\mathrm{ToF} > 90\,\mathrm{ms}$ to separate the output ports can be reduced from $\tau_{\mathrm{sep}} \geq 20\,\mathrm{ms}$ to $\geq 10\,\mathrm{ms}$ if delta-kick collimation is used. The remaining time $2T = \mathrm{ToF} - \tau_{\mathrm{prep}} - \tau_{\mathrm{launch}} - \tau_{\mathrm{sep}} < 51\,\mathrm{ms}$ can be entirely used for the interferometry, which allows for a pulse separation time as large as $T = 25\,\mathrm{ms}$.

Implementation of higher-order Bragg diffraction

State-of-the-art Raman-type gravimeters routinely operate with pulse separation times of 70 ms [56] or more [12, 55]. To further increase the scaling factor, not only first-order but also higher-order Bragg diffraction can be implemented in the Mach-Zehnder interferometer. At the current status of the experiment third-order Bragg diffraction can be performed with an efficiency of above 90%. With future improvements, already fourth-order Bragg diffraction would permit to compensate a decrease of a factor of two in the pulse separation time T.

To allow for higher-order Bragg diffraction, the beam splitter pulses use Gaussian-shaped envelopes with shorter waveform lengths of $\tau = 100\,\mu\mathrm{s}$ and Gaussian widths of $\sigma_\tau = 12.5\,\mu\mathrm{s}$ but at larger laser powers P. The first $\frac{\pi}{2}$-pulse of the Mach-Zehnder interferometer follows with a short delay of one millisecond after the relaunch to maximize the time usable for interrogation. The timing of the Mach-Zehnder interferometer needs to be asymmetrically around the apex of the fountain, to avoid π-pulses at the apex. In this case, both lattices are in resonance and losses due to double Bragg diffraction and standing waves would disturb the π-pulse, as discussed in sec 5.2. In consequence, the Doppler detuning of the π-pulse should not be smaller than $\delta > 100\,\mathrm{kHz}$ or correspondingly the time difference to the apex of $7 - 8\,\mathrm{ms}$. Respectively, the separation time of the outputs in the end is always larger than $\tau_{\mathrm{sep}} > 14\,\mathrm{ms}$.

However, larger momentum transfer slightly reduces the free-fall time, because depending on the direction of momentum transfer $\pm k_{\mathrm{eff}}$ the atoms are either kicked towards the atom chip, or downwards such that they leave the detection region faster. By choosing the momentum transfer of the second and final lattice acceleration in the relaunch sequence according to the direction of the beam splitter's momentum transfer, the height of the parabola can be maximized and in consequence the pulse separation time T can be held constant, independently of $\pm k_{\mathrm{eff}}$ as depicted in fig. 6.3. In both cases for larger momentum separation the point of detection and in consequence the free-fall time ToF of the atoms are slightly reduced by $\mathrm{ToF} = 3 \cdot \tau_{\mathrm{prep}} - n \cdot v_{\mathrm{r}}/g$.

6.2 Results using dropped Bose-Einstein condensates

In this section the results for the determination of local gravity with an atom-chip gravimeter using dropped Bose-Einstein condensate are presented. Some more experimental details can be found in a previous master thesis [171]. The Mach-Zehnder interferometer with a pulse separation time of $T = 5\,\mathrm{ms}$ achieved the determination of local gravity with a precision of $\Delta g/g = 1.3 \cdot 10^{-5}$ at a contrast of $C = 0.75$ after roughly eight hours of integration, purely limited by vibrational background noise. However, the phase read-out of the Mach-Zehnder interferometer is operated very close to the shot-noise limit for $N = 10^4$ atoms, that would allow to determine gravity with an intrinsic sensitivity of $\Delta g/g = 3.2 \cdot 10^{-6}$ per experimental cycle. First, some requirements and characterizations have to be fulfilled. The performance of the employed Mach-Zehnder interferometer is analyzed, taking into account the limits set by shot noise, as well as technical noise on the phase read out in the setup (sec. 6.2.1). Afterwards, the results for the determination of local gravity (sec. 6.2.2) and its stability (sec. 6.2.3) are presented.

6.2.1 Intrinsic performance evaluation

The intrinsic sensitivity of an interferometer includes only noise sources which are intrinsic to the atom interferometer itself. These sources are arising from the beam splitter due to fluctuations of the laser intensity or the imprinted phase, the detection as well as the quantum projection noise. In consequence, the intrinsic sensitivity is determined in the absence of any noise sources which are included in the measured signal, as vibrations. The intrinsic performance evaluation gives rise to important key parameters of the atom-chip gravimeter, as the interferometric contrast C and the stability of the output phase $\sigma_{\Delta\phi}$ throughout integration. The stability of the beam splitting process is of major importance, since a changing Bragg diffraction efficiency can not easily be distinguished from a phase change due to a variation in the signal. In the end, this discussion gives an insight into the limitations of the presented atom-chip gravimeter.

Contrast extraction from the fringe scan

An important lever on the experiment's sensitivity is the interferometric contrast C, because it directly scales to the sensitivity of a measurement for a given interferometer output signal. The interferometric contrast is defined by the amplitude A of a laser phase scan, the so called "fringe", divided by its mean P_0 and normalized between zero and one. A Mach-Zehnder interferometer where all three pulses are applied subsequently to each other and the pulse separation time T is vanishing, operates in a regime where technical noise contributions dominate, because the sensitivity to inertial noise is very small. Figure 6.4 shows a fringe scan of a Mach-Zehnder

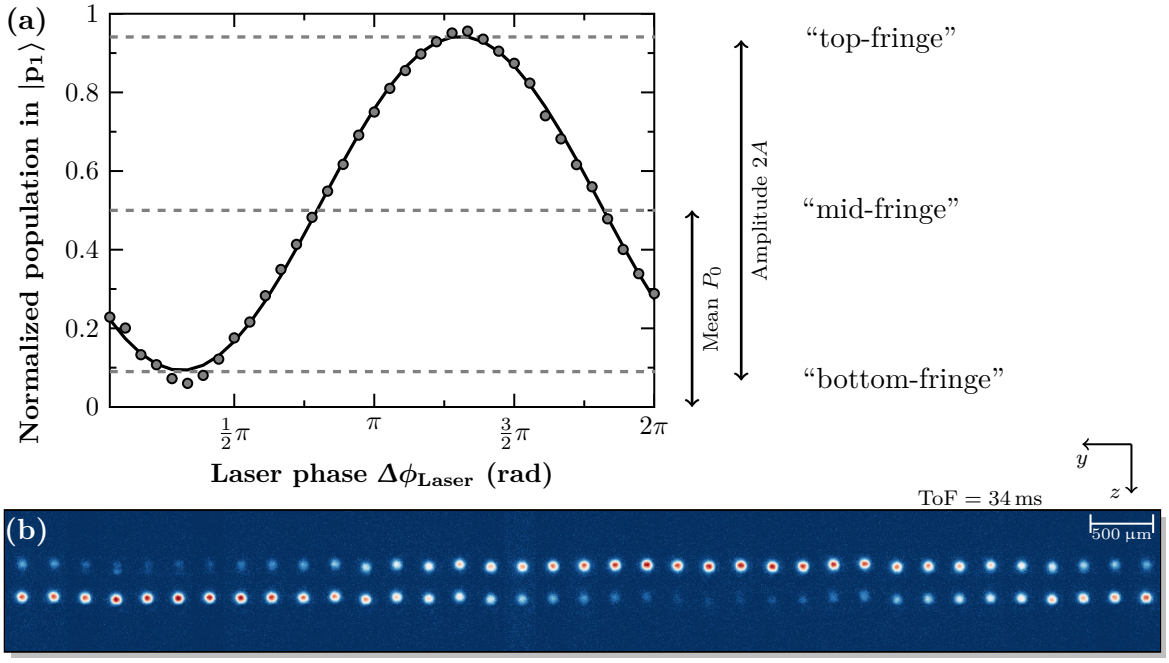

Figure 6.4: The interferometer's contrast C and the read out noise of the measurement is determined by a phase scan **(a)**. The pulse separation time is chosen to be only $T = 0$ to obtain only low inertial sensitivity. The interferometric contrast is calculated to $C = 0.84$. The phase noise is in the order of 15 to 20 mrad depending on the port's population. Top- and bottom-fringe positions suffer from a larger relative contribution of detection noise due to the lower atom number in one of the output ports. The density plot **(b)** shows the raw image series used for the evaluation.

interferometer with $T = 0$ and changing laser phase $\Delta\phi$ from which the contrast is determine to

$$C = \frac{A}{P_0} = \frac{0.425}{0.515} = 0.84, \tag{6.1}$$

that is in well agreement to the diffraction efficiency $\eta_{1\text{st}}^3 = 0.95^3 = 0.84$ multiplied three times. The sensitivity of the interferometer to phase changes is determined by the slope of the sinusoidal signal. Figure 6.4 defines the point of equally distributed output ports (the so called "mid-fringe"), where the slope is maximal and the points of maximal imbalanced population (the so called "top- and bottom-fringe"), where the slope is zero. As a result the sensitivity of a fringe scan with equal steps in phase is reduced by a factor of $\sqrt{2}$ compared to a mid-fringe measurement. If vanishing inertial sensitivity is supposed, the standard deviation of the fringe fit directly gives a first estimate on the intrinsic noise. This deviation is determined between 15 to 20 mrad dependent on the population of the ports, with the smallest deviation at mid-fringe position.

Stability of beam splitter and phase readout

The performance gain in resolution of a measured value throughout integration for a given time t can be inferred from the so called Allan deviation [283] defined by

$$\sigma_{\text{adev}}(t) = \sqrt{\sigma^2(t)} = \sqrt{\frac{1}{2}\langle (x' - x)^2 \rangle}, \tag{6.2}$$

for two subsequent measurements x and x'. The maximum number of samples or the longest time to integrate over in the Allan deviation, is one-third of the amount of taken data points, because some statistical independence between the intervals is required.

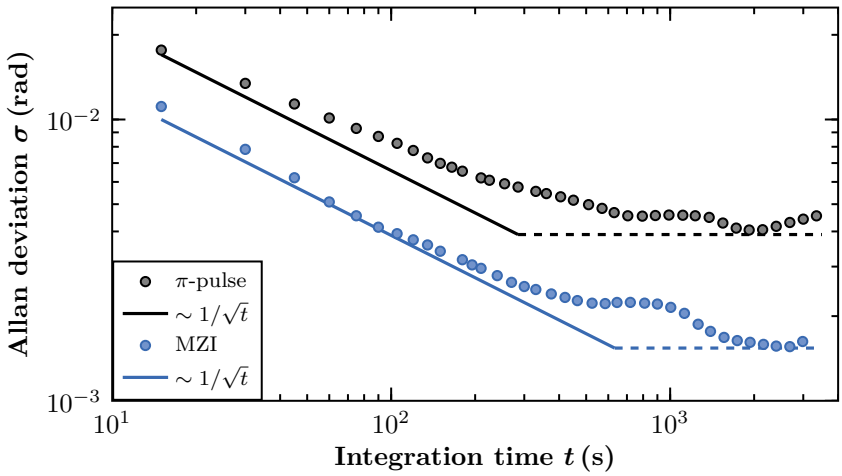

Figure 6.5: Integration behavior for the diffraction efficiency of a π-pulse (——) and the phase read out of a Mach-Zehnder sequence with $T = 0$ (——) over roughly one hour of integration time t. The starting value of the Allan deviation σ represents the noise per measurement and it is lower at mid-fringe position than for a single π-pulse ($\sigma_{\Delta\phi} = 11.5 \pm 1$ mrad compared to $\sigma_\pi = 17.5 \pm 1$ mrad).

Figure 6.5 shows the Allan deviation of the stability an hour of the diffraction efficiency for a single π-pulse as well as a Mach-Zehnder interferometer with $T = 0$ and a laser phase adjusted to the mid-fringe position measured for roughly. The first value in the Allan deviation is called the "short-term noise" of the measurement. It turns out, that the phase noise of the output of the Mach-Zehnder interferometer $\sigma_{\Delta\phi} = 11.5 \pm 1$ mrad at mid-fringe position is lower than the

noise $\sigma_\pi = 17.5 \pm 1\,\text{mrad}$ of a single π-pulse, as expected from the fringe scan. The lowest values in the Allan deviation are reached for the Mach-Zehnder interferometer with $\sigma_{\Delta\phi} = 1.5 \pm 1\,\text{mrad}$ after $t = 3\,000\,\text{s}$ of integration and for the π-pulse with $\sigma_{\Delta\phi} = 3.9 \pm 1\,\text{mrad}$ after $t = 2\,000\,\text{s}$. Thus, the detection noise for largely unequal population is higher, than for equal populations, because the clouds have a much lower density for atom numbers close to zero.

Contrast reduction due to atoms in magnetic sensitive states

Two typical mechanisms that contribute to a loss of contrast are dephasing and incoherent loss of atoms. An in-coherent loss of atoms is caused by a number of technical effects, like the limited beam splitter efficiency and spontaneous emission [64]. In contrast, dephasing occurs when atoms still close an interferometer, but with position dependent output phases across the ensemble [88]. Normally, these dephasing processes scale with the pulse separation time T. The contrast for non-vanishing pulse separation times $T = 1$ ms to $T = 5\,\text{ms}$ reduces according to tab. 6.1 from $C = 0.84$ to 0.75. This reduction of contrast can be according to sec. 5.1.3 mainly attributed to dephasing of atoms in different m_F states. While most of the atoms are prepared in the $m_\text{F} = 0$ state, approx. 5% of the atoms remain in magnetic sensitive states after the sub-state transfer. These atoms are still coherent and close interferometers, whose phases are due to magnetic stray fields depending on T more or less off-phase and can therefore in the worst case reduce the contrast by approx. 0.1. The measured drop of contrast for atoms in $m_\text{F} = 0$ state is in agreement to this. This behavior is proven by a Mach-Zehnder interferometer performed with atoms in the $m_\text{F} = -2$ state, where no decreasing contrast with increasing T is observed.

Summary of shot-noise limits and intrinsic sensitivity

T (ms)	C	$\Delta g/g$
0	0.84	-
1	0.82	$5.8 \cdot 10^{-5}$
2	0.78	$1.8 \cdot 10^{-5}$
3	0.77	$8.3 \cdot 10^{-6}$
4	0.76	$4.8 \cdot 10^{-6}$
5	0.75	$3.2 \cdot 10^{-6}$
Source	Noise estimate	
σ_qpn	11.9 mrad	
$\sigma_{\Delta\phi}$	(11.5 ± 1) mrad	
σ_π	(17.5 ± 1) mrad	

Table 6.1: Intrinsic sensitivity for pulse separation times of $T = 1-5\,\text{ms}$, their respective contrasts C, with an atom number of $N = 10\,000$ and a first-order Bragg diffraction.

A lower bound on the experiments sensitivity is given by the quantum projection noise σ_qpn, or short shot-noise. This limit is a direct consequence of the statistical nature of quantum mechanics. The arising noise contribution to the atom interferometer is computed taking only into account the detected atom number $N = 10\,000$ at a given contrast of $C = 0.84$

$$\sigma_\text{qpn} = \frac{1}{C\sqrt{N}} \geq 11.9\,\text{mrad}. \tag{6.3}$$

The shot-noise σ_qpn represents the minimal phase difference or resolution detectable on a fringe scan. This contribution is in agreement to the phase readout noise, determined from the Allan deviation in fig. 6.5. So within the uncertainty of this measurement, the experiment is operated at the shot noise limit or in the worst case close by. The intrinsic sensitivity limit on the gravity measurement is estimated by

$$\Delta g/g = \sigma_{qpn} \cdot \sigma_g = \frac{1}{C\sqrt{N} g k_\text{eff} T^2}, \tag{6.4}$$

with the interferometric contrast C for each T and σ_g the response or scaling factor of the interferometer to changes in g. The values for intrinsic noise limits in the experiment computed from eq. 6.4 for separation times ranging from $T = 1$ ms to $T = 5$ ms are depicted in tab. 6.1.

6.2.2 Determination of local gravity

In this section the methods to determine gravity with the atom-chip gravimeter are be investigated. Testing of the prototype for gravity measurements is challenged by the setup, which was originally built for different purposes, and the unsuited environment at the drop tower.

There are two commonly used techniques, how gravity can be read out from an atom interferometric measurement. In order to determine the local gravitational acceleration from the output phase $\Delta\phi$ of an atom interferometer in eq. 4.59, there are two free parameters to vary, namely the pulse separation time T and the chirp rate α of the relative laser frequency. The wave front acceleration $a = 2\pi\alpha/k_{\text{eff}}$ extracted from the chirp rate α can be compared to a independently determined reference value for gravity g_{ref} or a detailed error analysis can be performed. These two different methods of the determination of gravity will be demonstrated experimentally. They both make use of the fact, that if the chirp rate α of the light field is matched to the free-fall rate of the atoms the phase shift at the output ports vanishes

$$\Delta\phi(\alpha,T) = (k_{\text{eff}} \cdot g - 2\pi\alpha)T^2 \equiv 0 \text{ for } \alpha = k_{\text{eff}} \cdot g/2\pi. \tag{6.5}$$

Due to the efforts waged in the German gravity network, the Bundesamt für Kartographie und Geodäsie (BKG) [284] is able to provide an independently determined reference value for the gravitational acceleration g_{ref}. It is composed of several reference points within Germany, which are then interpolated with a well tested model to provide a closed gravity system.

Table 6.2 lists causes for gravity variations and their respective magnitudes. The model's precision is computed to the limit of the temporal variation arising from tides and thus can not include local variations as the building itself or other heavy masses around the experiment. The given reference value at the position of the ZARM and an approximate ground floor height of 1.76 m above normalized water level is

$$g_{\text{ref}} \pm \Delta g_{\text{ref}} = (9.81327 \pm 0.00002)\,\frac{\text{m}}{\text{s}^2}. \tag{6.6}$$

Local gravity is defined as the sum of the gravitational and the centrifugal acceleration at a given latitude, which is the cause of the global scale variation. The centrifugal contribution in our experiment can be calculated with a latitude at reference position in Bremen of $\zeta_{\text{ref}} = 53.1°$ to

$$a_{\text{cen}} = R_{\text{E}}(\Omega_{\text{E}}\cos\zeta_{\text{ref}})^2 = 1.28 \cdot 10^{-2}\,\frac{\text{m}}{\text{s}^2} \tag{6.7}$$

and is always included in the gravity measurements.

Large scale variations $\Delta g/g$	
Centrifugal force	10^{-3}
Regional scale	10^{-6}
Tidal effect	10^{-7}
Local mass variations $\Delta g/g$	
Buildings	10^{-8}
Trains, people	10^{-9}
Geological effects $\Delta g/g$	
Tectonics	10^{-9}
Vulcanology	10^{-9}
Atmospheric effects $\Delta g/g$	
Pressure	$3 \cdot 10^{-9}$/mbar
Free air	$3 \cdot 10^{-9}$/cm

Table 6.2: Gravity variations.

Vibrational noise measured with classical sensors

The intrinsic sensitivities estimated in tab. 6.1 would allow for seeing regional scale variations and tidal effects through integration. A major problem performing gravity measurements which prevents to reach a determination at the intrinsic sensitivities is arising from vibrational noise. The phase changes due to vibrations are misinterpreted as changes in the measured signal and can not be distinguished from the gravitational acceleration itself. The noise $\sigma_{\Delta\phi}$ measured at the output of an interferometer with different T is summed up in tab. 6.3. Vibrations are the

dominant limitation for the experiment, since the capsule is non-isolated against the floor. The vibrations due to the ground motion inside the ZARM with the machines to operate the drop tower, are three orders of magnitude larger than the current intrinsic sensitivities. But also active elements within the drop capsule contribute to this noise which are not sufficiently damped, like the water cooling of the MOT coils and fans from electronic devices.

T (ms)	$\sigma_{\Delta\Phi}$ (mrad)
1	665
2	1127
3	1632
4	1920
5	2158
Device	Noise ($\frac{\mathrm{m}}{\mathrm{s}^2}/\sqrt{\mathrm{Hz}}$)
IMU	$1.3 \cdot 10^{-2}$
Guralp	$1.2 \cdot 10^{-2}$

Table 6.3: Vibration noise measured by the atom interferometer depending on the pulse separation time T and the comparison of two classical sensors.

The vibrational noise at the apparatus can be measured using classical seismic sensors before atoms are used for experiments. Two different sensors have been incorporated quantifying the noise level of the drop capsule. The first one is a six-axis inertial measurement unit of type iIMU-FCR-E-03, that was mounted on top of the drop capsule and was used for previous experiments with double Bragg diffraction as well as in the drop tower. The second one is a frequently used three axis seismometer of the type Guralp CMG-40T [285], that is mounted on a platform rigidly attached to the mounting structure of the drop capsule at the height of the vacuum system. The noise measured by these sensors in fig. 6.6(a) is at a level of $\sigma_{\mathrm{vib}} = 1.3 \cdot 10^{-2}\,\frac{\mathrm{m}}{\mathrm{s}^2}/\sqrt{\mathrm{Hz}}$, that is roughly a factor of four above the IMUs specified noise floor of $300\,\mu g/\sqrt{\mathrm{Hz}}$ and in agreement to the value determined by the Guralp CMG-40T. In order to suppress vibrations, one can either shield the device or correct for the noise. The power spectral density measured with the Guralp CMG-40T at our platform is depicted in fig. 6.6(b) compared to an exemplary one on a minus-K passive isolation platform taken at the IQ. A vibration isolation sufficiently suppresses noise frequencies above 1 Hz and for example a noise value of $\sigma_{\mathrm{vib}} = 6 \cdot 10^{-6}\,\frac{\mathrm{m}}{\mathrm{s}^2}/\sqrt{\mathrm{Hz}}$ has previously been reached at the IQ [85]. Alternatively, a correlation of the two can be used to subtract vibrations from the measured signal [286]. In QUANTUS-1, due to the relatively large distance between classical device and atom chip - the inertial reference point - it will be challenging to establish decent correlation between them. A more detailed investigation will be left to future work.

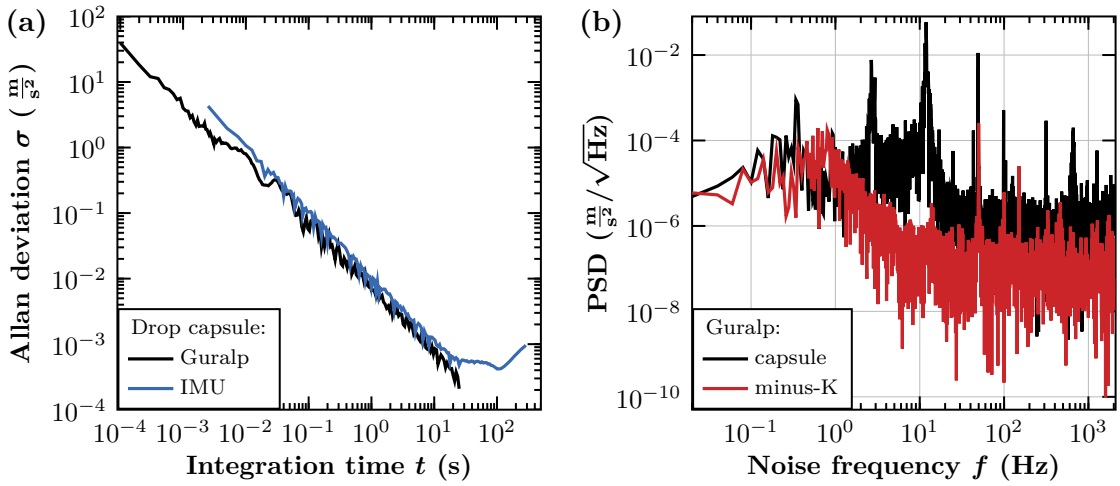

Figure 6.6: Allan deviation **(a)** of the vibrational noise at the experiment's platform measured with a Guralp CMG-40T (—) and a iIMU-FCR-E-03 (—) as well as the power spectral density **(b)** of the Guralp compared to the one taken with the same device on a Minus-K (—) platform.

Scanning the pulse separation time

The first method to determine gravity directly follows the example in fig. 4.19 and obtains a chirped fringe pattern by increasing the pulse separation time T subsequently in between each measurement. This chirped fringe pattern looks similar to the signal obtained by a falling corner cube gravimeter [30, 48, 287]. The major difference between these two lies in the fact, that in the case of an atom interferometer a number of experimental cycles are needed to obtain a single fringe pattern. This has the downside, that the atom interferometer is not operated at fixed sensitivity for all data points. In contrast the test mass in the falling corner cube gravimeter is interrogated continuously by the laser, generating a complete fringe pattern each experimental cycle. To ensure a non-vanishing phase shift at the output ports a slightly off resonant chirp rate of $\alpha_0 = 25.632\,\mathrm{MHz/s}$ is chosen which would correspond to a gravitational acceleration of $g_{\alpha_0} = 10\ \frac{\mathrm{m}}{\mathrm{s}^2}$. The scanned parameter ranges from $T_{\min} = 150\,\mu\mathrm{s}$ to $T_{\max} = 3.75\,\mathrm{ms}$ and the resulting fringe pattern is displayed in fig. 6.7. For larger pulse separation times the phase noise gets too large for the fit function and a further averaging the data points would be required.

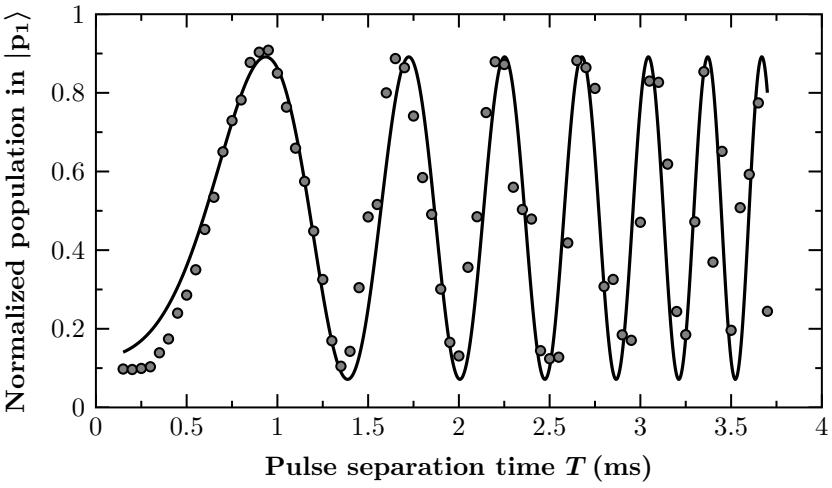

Figure 6.7: Determination of local gravity via a scan of the pulse separation time from $T_{\min} = 150\,\mu\mathrm{s}$ to $T_{\max} = 3.75\,\mathrm{ms}$ and for a given chirp rate $\alpha_0 = 25.632\,\mathrm{MHz/s}$. The black line is given by the fit routine from which a value for local gravity of $g \pm \Delta g = (9.8141 \pm 0.0019)\ \frac{\mathrm{m}}{\mathrm{s}^2}$ is determined.

To extract a gravity value from the chirp fringe the fit function $f(T)$ with two parameters amplitude A and offset B fits the phase ϕ_{offset} to the data set:

$$f(T) = \frac{1}{2}[B - A \cdot cos(2\pi(\alpha - \alpha_0)T^2 - \phi_{\mathrm{offset}})]. \tag{6.8}$$

The chirp rate α found in eq. 6.8 and its fitting error correspond to the measured gravitational acceleration that can be determined with eq. 6.5 to a value of

$$g \pm \Delta g = (9.8141 \pm 0.0019)\,\frac{\mathrm{m}}{\mathrm{s}^2}. \tag{6.9}$$

This measured value is in good agreement to the reference value g_{ref} within its precision. The difference between mean and reference value of $g - g_{\mathrm{ref}} = 8.5 \cdot 10^{-5}$ is actually significantly lower than the fitting error of $\Delta g/g = 1.9 \cdot 10^{-4}$ which is an indicator for purely statistical measured noise and the result would improve by integration. The effect of the finite pulse length is neglected here, because the correction would be below the precision of the measurement.

Central fringe determination

The second method to determine gravity is to vary the chirp rate α of the relative detuning $\Delta\nu(t)$ between the beam splitting light fields during the interferometer while leaving T and the scaling factor constant. The fringe pattern has a common minimum, that is independent of T if systematic bias shifts are negligible. To identify this so called "central fringe" a calibration measurement for different pulse separation times T is performed as displayed in fig. 6.8. Hereby, the effect of the finite pulse times is corrected for in the phase, to identify the correct fringe.

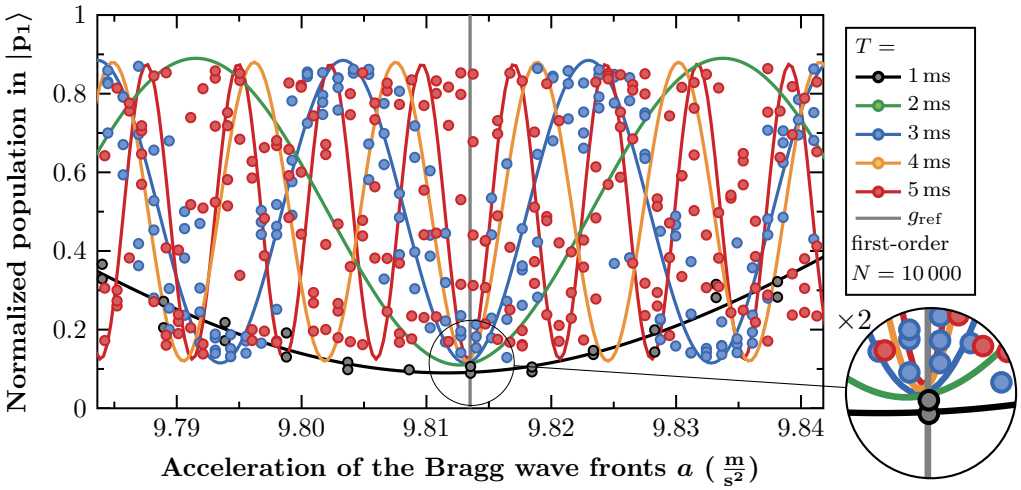

Figure 6.8: Central fringe determination for three different pulse separation times $T = 1 - 5\,\text{ms}$. Note, that the data points for $T = 2$ and $4\,\text{ms}$ are not depicted to enhance the readability. Due to vibrational background, which increases with T, additional $2-3$ data sets were taken for $T = 3-5\,\text{ms}$ to perform fringe fitting with already averaged values and to read out the central fringe position. This limits the determination of local gravity to $\Delta g/g = 5 \cdot 10^{-5}$. For scaling factors beyond $T = 5\,\text{ms}$, the vibrational noise exceeds π and a determination of a central fringe is no longer possible.

T (ms)	$g \pm \Delta g$ ($\frac{m}{s^2}$)
1	9.8102 ± 0.0012
2	9.8123 ± 0.0011
3	9.8133 ± 0.0005
4	9.8134 ± 0.0006
5	9.8137 ± 0.0006

Table 6.4: Gravity values determined from a central fringe measurement for pulse separation times $T = 1 - 5\,\text{ms}$.

With increasing T the scaling factor for gravity increases as well and therefore the number of minima within a certain interval. Measurements with smaller scaling factor give rise to a rough estimate of the correct center position, while larger scaling factors achieve higher intrinsic sensitivities. Once the central fringe is identified, one has the possibility to only operate at highest sensitivity and track this central fringe only, if the signal is not changing more than one fringe spacing. The values for local gravity and their respective uncertainties obtained for five different T are displayed in tab. 6.4. The data points for $T = 2\,\text{ms}$ and $T = 4\,\text{ms}$ are not displayed in fig. 6.8 to enhance the readability of the graph but their scatter is in between the remaining data sets. The vibrational noise which increases with T according to tab. 6.3 causes an ambiguity of the phase and additional data sets were taken for $T = 3 - 5\,\text{ms}$ to average over several data points prior to performing the fringe fitting. This results in a non-decreasing evaluation error. Once the vibrational noise has become the dominant contribution the error in evaluation is not decreasing without further integration. For even larger pulse separation times the phase noise exceeds 2π and the information on which fringe the data point was taken is lost. In this regime, the fringe fit method can not be performed at all, without further information.

6.2.3 Stability of the gravity measurement

To improve the resolution of the determined gravity value through integration the stability of the experiment is exploited. The Mach-Zehnder interferometer is operated with a pulse separation time of $T = 5\,\mathrm{ms}$ and first-order Bragg diffraction to perform consecutive measurements around the central fringe. The chirp rates are determined from the central fringe measurement in fig. 6.8 but the variation of the chirp rate is only performed on an interval of 2π around the minimum. Since each experimental cycle takes approx. $T_{\mathrm{cyc}} = 15\,\mathrm{s}$, it requires roughly 8 hours to obtain $n = 80$ data sets of 21 data points for each fringe fit. The fringe fit method was necessary due to a large vibrational noise, that requires averaging to read out a single value for g. Alternatively, it would be possible to take the difference of two data points, taken at the mid-fringe position left or right of the central minimum, which always have maximum sensitivity [286]. Due to missing pictures and laser instability, two data sets have a deviation of more than five standard deviations $5\sigma_{\mathrm{std}}$ and are ignored in the evaluation. The time series is depicted in fig. 6.9(a) together with its corresponding Allan deviation (b).

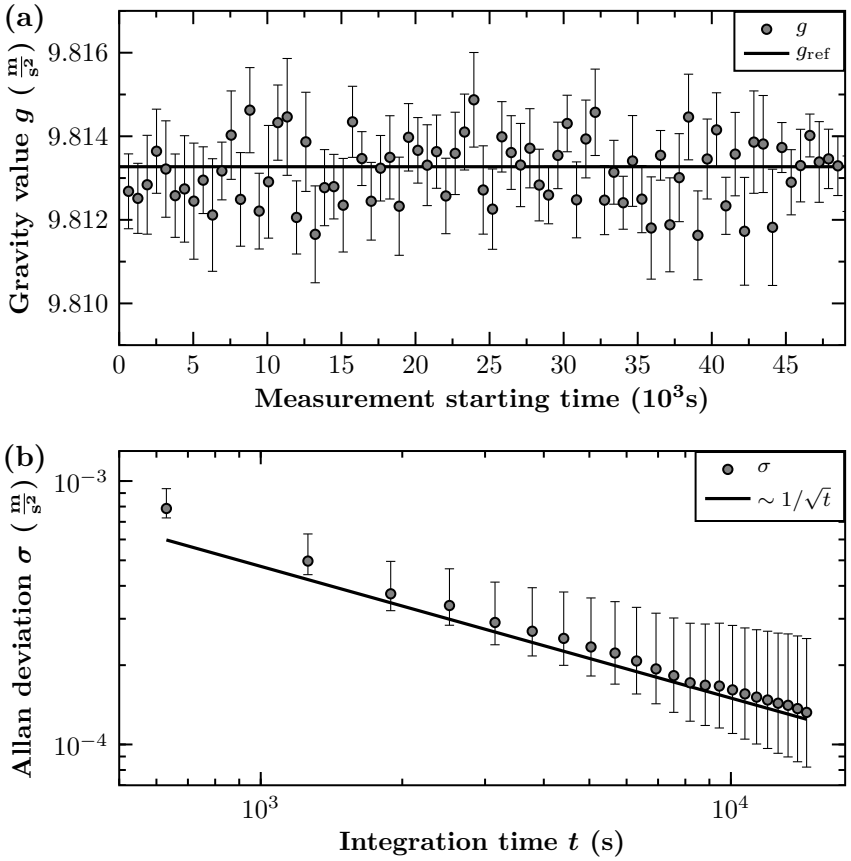

Figure 6.9: Consecutive determinations of local gravity **(a)** and corresponding Allan deviation **(b)**. After obtaining the central fringe a pulse separation time $T = 5\,\mathrm{ms}$ is used for consecutive measurements and data points in an interval of π around the central minimum were taken. The obtained g values scatter around the reference value g_{ref} (——). The error bars in the time series are given by the error of the fringe fitting routine. Within roughly eight hours the uncertainty in the determination of local gravity can be integrated down to $\Delta g/g = 1.3 \cdot 10^{-5}$, close to a $\sim 1/\sqrt{t}$ (——) behavior. The error bars in the Allan deviation indicate a confidence interval of one standard deviation.

The error bars for the data points obtained during the gravity determination are computed from one standard deviation σ_{std} of the fringe fit routine. Not all of these error bars are overlapping with the reference value r_{ref}. This indicates, that the error bars are either underestimated or that there is a non-Gaussian noise involved in the measurement. The power spectral density $S(f)$ of the points is depicted in fig. 6.10 and allows to estimate the noise figure as a representation for the shape of the noise depending on the noise frequency f. Figure 6.10 reveals a functional relation to the noise frequency f of the form $S(f) \sim f^{-0.84}$ which is between the expected relation for white noise ($S(f) \sim f^{-1}$) and flicker noise ($S(f) \sim f^{0}$) [288]. This identification is thus not fully reliable due to the small amount of available data points.

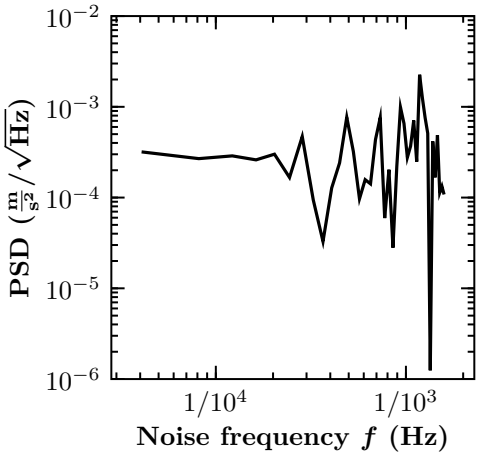

Fig. 6.10: The power spectral density for the data points obtained during the gravity determination show deviations from Gaussian noise due to insufficient statistics or non-Gaussian contributions and reveals a functional relation to the noise frequency f of the form $S(f) \approx f^{-0.84}$.

The error bars of the Allan deviation which are depicted in fig. 6.9 are computed for Chi-squared statistics at a confidence interval of one standard deviation σ_{std} and the assumption of approximately white noise. Nevertheless, for flicker noise the error bars would have only a non-visible difference to the ones depicted. The integration during the first $10^3\,\mathrm{s}$ is slightly faster than $\sim 1/\sqrt{t}$ but hits the expected integrations behavior for the later data points. The Allan deviation shows a first oscillation at $t = 5 \cdot 10^3\,\mathrm{s}$ with a rather small amplitude but an overall integration behavior reasonable close to $\sim 1/\sqrt{t}$. This is a strong indicator, that the noise obtained in the data series is in fact closer to white noise than estimated in fig. 6.10. Such a behavior is in agreement to the conclusion, that the interferometer is limited as expected by statistical noise as vibrations. The residual oscillations may occur due to temperature changes in the laboratory.

The smallest deviation in 6.9 is obtained for the last point $\sigma_{\mathrm{dev}} = 1.3 \cdot 10^{-4}\,\frac{\mathrm{m}}{\mathrm{s}^2}$ after $t = 14\,500\,\mathrm{s}$. Using the mean value from all data points, the local gravity value is determined to

$$g \pm \Delta g = (9.81316 \pm 0.00013)\,\frac{\mathrm{m}}{\mathrm{s}^2} \tag{6.10}$$

which is still in agreement with the reference value g_{ref}. The uncertainty is roughly a factor of five smaller compared to single central fringe determination. A short term sensitivity of

$$\Delta g/g = 6 \cdot 10^{-5} \text{ or } (\Delta g/g)/\sqrt{\mathrm{Hz}} = 1.5 \cdot 10^{-3} \tag{6.11}$$

is extracted from the first point in the Allan deviation and is in reasonable agreement to the noise determined by the seismic sensors at the drop capsule. The integration still shows a $\sim 1/\sqrt{\tau}$ behavior at the cut-off of the Allan deviation without visible drift or flicker floor. Consequently, longer integration times τ are in principle possible, because the uncertainty in gravity is still magnitudes above the limit set by the integration behavior of the phase readout, investigated in sec. 6.2.1, which would allow us to resolve tidal variations on the $\Delta g/g = 10^{-7}$ level. On an hour timescale these variations would prevent further integration without taking into account corrections from geodetic models. Nevertheless, taking data for more than eight hours is challenging at the current status of the experiment.

6.3 Results using the fountain geometry

In this section the results with the fountain geometry are presented for which the total time of free-fall can be as large as ToF = 100 ms, hence, the pulse separation time inside the interferometer can be stretched up to $T = 25$ ms. The measurements are performed either with Bose-Einstein condensates released from the shallow trap, or delta-kick collimated condensates together with Stern-Gerlach-type deflection. In that way, the influence of state preparation and expansion rates on the performance can be assessed to find the optimal configuration and to infer intrinsic sensitivities for the fountain geometry (sec. 6.3.1). In particular, the quality and curvature of the wave fronts are crucial since the atom-chip surface is used as a retro-reflector for the beam splitter. To access these spatial features and to discuss the influence of phase gradients across the output ports on the interferometric contrast a principal component analysis is used (sec. 6.3.2).

6.3.1 Fluctuation dependent performance evaluation

The performance evaluation of the Mach-Zehnder interferometer for the atom-chip fountain gravimeter is no longer possible with the common fringe fit method or via an Allan deviation, because the background vibration level for pulse separation times larger than $T > 5$ ms leads to a complete loss of visible fringe pattern [72]. This means even if the laser phase $\Delta\phi_{\mathrm{Laser}}$ and the chirp rate α are held constant between subsequent measurements the output phase scatters over multiple 2π-intervals as illustrated in fig. 6.11(a). As a consequence, at these high levels of sensitivity the readout of a gravity value is impossible without having further information about the vibrations during the interferometry, i.e. without seismic correlation. Nevertheless, the beam splitting still has high fidelity and oscillations between the output ports can clearly be observed. Using the simple peak to valley or standard deviation calculation though over- or underestimates the contrast and does not yield a useful noise analysis for the output signals.

Evaluation of a histogram distribution

The alternative method to solve the problem of distinguishing between useful contrast C and technical noise $\sigma_{\Delta\phi} = \sigma_P/C$ is a histogram analysis revealing contrast of an interferometer without relying on fringe visibility [289]. The output signals of a data set are split into equidistant intervals in normalized population P and the number of data points within each interval is counted. The resulting histogram shows a characteristic double peak structure reflecting the sinusoidal dependence of the interference signal. This structure results from the simple noise model, that the probability to find an output state with a normalized population at top or bottom of a sinusoidal fringe pattern is larger than at the mid position for a completely random signal. This method requires sufficient statistics over several hundred experimental cycles with stable signal. The contrast $C = A/P_0$ is extracted from a fit of the distribution according to fig. 6.11(b), given by the amplitude A of the signal divided by its mean P_0. As input for the fitting routine a kernel density estimation (KDE) of the data points is used, rather than using the histogram itself*. In a KDE each data point is weighted with a Gaussian function of a fixed width of $\sigma_{\mathrm{kde}} = 0.01$. All Gaussian functions are then added and the signal normalized such that in the end a continuous distribution properly reflects the density of data points without neglecting information. For the width σ_{kde} it is only of importance to choose a value smaller than the expected technical noise. The histogram yield only insufficient information to be fitted for small number of bins n_{bin} and would lead to a larger uncertainty in the extracted parameters.

∗ This evaluation yields a slightly better intrinsic sensitivity compared to the value published in ref. [156].

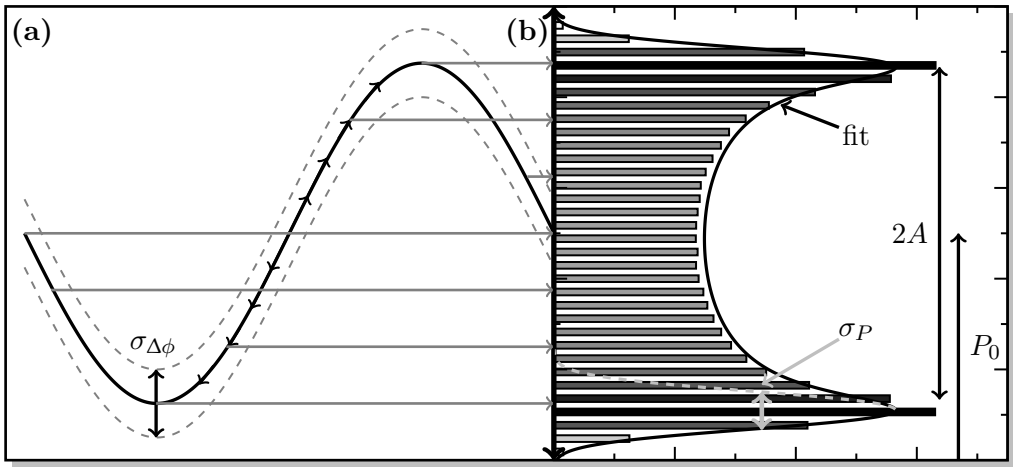

Figure 6.11: Vibrational noise completely washes out a sinusoidal signal and only fluctuations are left to be measured in the relative population between the two output ports **(a)**. The histogram distribution gives rise to a characteristic double peak structure from which the contrast $C = A/P_0$ can be extracted, given by the amplitude A of the sinusoidal signal divided by its mean P_0 **(b)**.

Results without delta-kick collimation and first-order Bragg diffraction

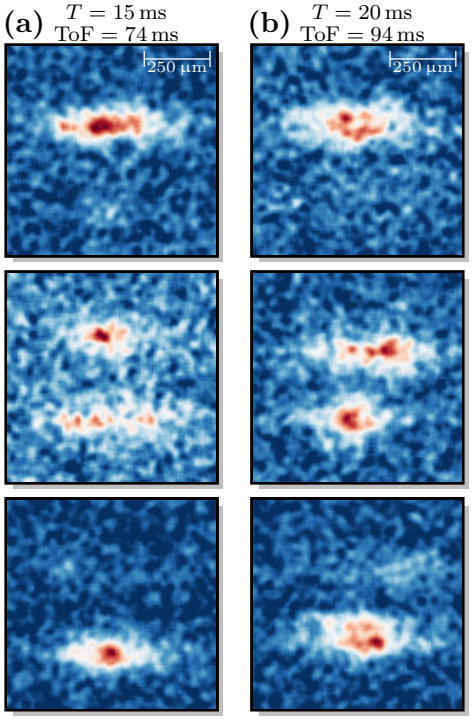

Fig. 6.12: Density plots of the output ports for BECs and MZIs with $T = 15\,\mathrm{ms}$ **(a)** and $T = 20\,\mathrm{ms}$ **(b)**. The population changes from top over equally distributed to bottom.

The evaluation of the histogram distribution using Bose-Einstein condensates without delta-kick collimation is performed for data sets of roughly eight hundred measurements. The output signals as depicted in fig. 6.13 are obtained for two different pulse separation times $T = 15\,\mathrm{ms}$ and $T = 20\,\mathrm{ms}$ in both cases with first-order Bragg diffraction, which assures the largest achievable interferometric contrast C. From the corresponding fits to the density distribution a contrast of $C = 0.78$ for the Mach-Zehnder interferometer with $T = 15\,\mathrm{ms}$ rand a slightly lower contrast of $C = 0.76$ for $T = 20\,\mathrm{ms}$ is obtained in fig. 6.13. In this case, the contrast is at the same level as observed for the experiments with dropped atoms in sec. 6.2.1 and depends mainly on the employed preparation. The contrast reduction does not result from insufficient diffraction efficiency, since for first-order diffraction the efficiencies are extremely close to unity. The observed contrast reduction is still due to the effect, that there are atoms remaining in magnetic sensitive states as measured for $T \leq 5\,\mathrm{ms}$ in sec. 6.2.1.

Larger cloud sizes are observed, due to the dispersion effect during the launch in combination with longer time of flights, that have been measured in

sec. 5.3.3. To visualize this, there are three exemplary density plots of output port signals for the fountain geometry depicted in fig. 6.12, each with $T = 15\,\mathrm{ms}$ (a) and $T = 20\,\mathrm{ms}$ (b) for maximal imbalanced population as well as almost balanced number population. Most importantly to see is, that the clouds for $T = 20\,\mathrm{ms}$ are larger in beam splitter direction due to longer times of flight (94 ms compared to 74 ms) as measured in sec. 5.3.3. Nevertheless, the interferometer ports are still separable after a sufficient separation of $\tau_{\mathrm{sep}} > 20\,\mathrm{ms}$. Since the fit integrates transversally over the beam splitter direction, the larger size leads already to slightly decreased contrast in the case of $T = 20\,\mathrm{ms}$. Enlarging the pulse separation time beyond 20 ms is not possible, because the ports would not separate any more. Already in this case, the increase in pulse separation time from $T = 5\,\mathrm{ms}$ to $T = 20\,\mathrm{ms}$ gives rise to a 16-fold increase in the scaling factor.

To finally get an estimate on the improvements of the intrinsic sensitivities by the larger pulse separation times, the technical noise $\sigma_{\Delta\phi}$ is taken into account. The width of the peaks for $T = 15\,\mathrm{ms}$ gives rise to a noise of $\sigma_{\Delta\phi} = 49\,\mathrm{mrad}$ which is significantly larger compared to a calculated shot noise of $\sigma_{\mathrm{qpn}} = 16\,\mathrm{mrad}$ for a smaller contrast $C = 0.76$ and atom number $N = 7\,500$ and leads to an intrinsic sensitivity of $\Delta g/g = 13.8 \cdot 10^{-7}$. The measured technical noise is enlarged due to the lower density of the ensembles at the output ports of the interferometer which leads to increased detection noise. In the case of $T = 20\,\mathrm{ms}$ the measured technical noise of $\sigma_{\Delta\phi} = 37\,\mathrm{mrad}$ is slightly lower, because the atom number of $N = 8\,000$ is higher due to a better optimized launch, and leads to an intrinsic sensitivity of $\Delta g/g = 5.9 \cdot 10^{-7}$.

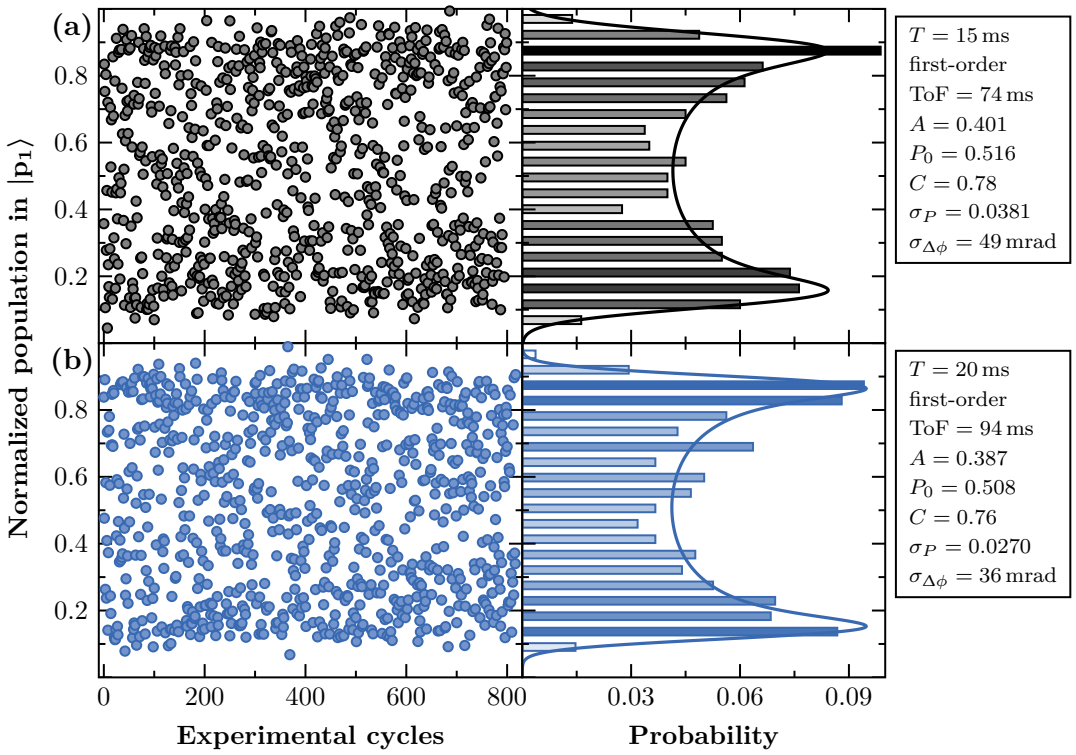

Figure 6.13: Output signal of the fountain geometry using Bose-Einstein condensates for pulse separation times of $T = 15\,\mathrm{ms}$ (**a** (——)) and $T = 20\,\mathrm{ms}$ (**b** (——)). The Mach-Zehnder interferometers are performed with first-order Bragg diffraction over 800 measurements. A contrast of $C = 0.78$ for the interferometer with $T = 15\,\mathrm{ms}$ respectively of $C = 0.76$ for $T = 20\,\mathrm{ms}$ is obtained from the histogram distribution. The estimated noise level is increased compared to dropped atoms.

Results without delta-kick collimation and third-order Bragg diffraction

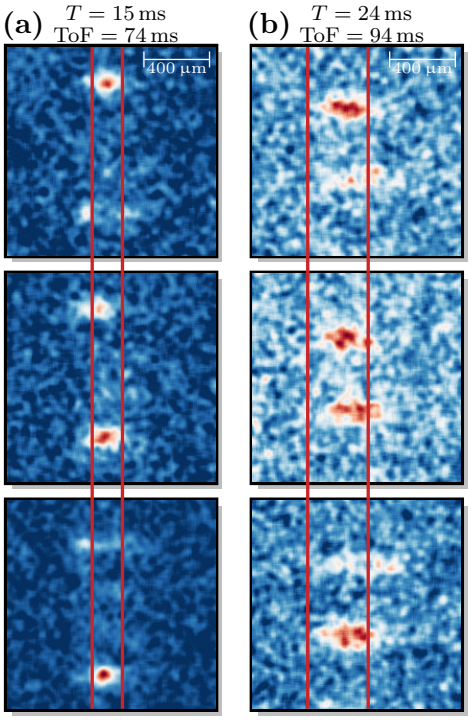

Fig. 6.14: Density plots of the output ports for interferometers with third-order Bragg diffraction with $T = 15\,\mathrm{ms}$ **(a)** and $T = 24\,\mathrm{ms}$ **(b)**. The red lines (—) indicate the individual crop marks for the evaluation with an aperture.

To study the influence of higher-order beam splitters, two Mach-Zehnder interferometers with third-order Bragg diffraction are implemented in the fountain geometry and their outputs evaluated using the same statistical analysis. The first employs $T = 15\,\mathrm{ms}$, which leaves enough time to separate spurious ports, while a second one increases the pulse separation to $T = 24\,\mathrm{ms}$, with spurious ports still overlapping, due to the sizes of the clouds. The theoretically achievable contrast is given by the beam splitter efficiencies in sec. 5.2 and expected to be 5-10% smaller as for first-order. Already from the raw-data in fig. 6.15(a,b) a drastic reduction of contrast is visible and the analysis reveals a contrast of $C = 0.33$ for $T = 15\,\mathrm{ms}$ and $C = 0.18$ for $T = 24\,\mathrm{ms}$. Compared to the fountain gravimeters with first-order beam splitters, this loss of contrast compensates the gain in scaling factor, thus the sensitivity can not be increased. The observed contrast is not in agreement to the measured beam splitter efficiencies taken from sec. 5.2, which can only explain a decrease of roughly $5 - 10\%$. The density plots in fig. 6.14 reveal, that the additional loss of contrast has its origin in a phase gradient over the atomic cloud, that results in different parts of the ensemble oscillating with different phases, thus washing out the contrast [88]. The origin of these gradients is identified to arise from the wave front defects of the light field driving Bragg diffraction due to the atom-chip surface shown in sec. 3.3 and sec. 5.3.3. These phase gradients get amplified by higher-order beam splitters as reported in ref. [67] with respect to the experiments with first-order diffraction.

A straight forward approach to overcome loss of contrast due to the phase gradients and to improve the technical noise of the measurement, is to manually constrain the initially used fitting routine to a smaller part of the output ports. By this, parts in the ports can be identified, that oscillate with the same phase and therefore give larger contrast. This procedure simulates an aperture in the detection beam, as it would be applied for thermal atoms [88, 226]. Hereby, only regions of the image are taken for the evaluation, that are aligned in vertical direction reflecting a horizontal phase gradient. Fig. 6.15(c) shows the histograms for $T = 15\,\mathrm{ms}$ and $T = 24\,\mathrm{ms}$, which were evaluated with the aperture chosen according to fig. 6.14, compared to the original plots using no aperture for third- as well as first-order beam splitter. The contrast improves for $T = 15\,\mathrm{ms}$ to $C = 0.66$ and for $T = 24\,\mathrm{ms}$ to $C = 0.42$. This is in both cases an improvement by a factor of almost three. The improved contrast is below the values for first-order Bragg diffraction, because a residual phase gradient of the wave front remains in the evaluated region.

In the case of $T = 15\,\mathrm{ms}$ the extracted phase noise is exactly as large as for first-order beam splitters and the calculated intrinsic sensitivity of $\Delta g/g = 4.6 \cdot 10^{-7}$ is improved by the expected factor of three. In the case of $T = 24\,\mathrm{ms}$ an additional contrast reduction in increased technical

noise due to overlapping spurious ports is observed, because these can not be separated properly at the increased pulse separation time. As a result, an intrinsic sensitivity of $\Delta g/g = 2.9 \cdot 10^{-7}$ is achieved, which still represents an improvement compared to the measurement with first-order Bragg diffraction and $T = 24\,\mathrm{ms}$. The increased technical or shot noise compromises the gain in contrast by this method, because the detected atom number is reduced to $N = 5\,000$ atoms due to the cut. In total, the sensitivity of the atom interferometer can still be enhanced, because mainly regions with a phase shift of π are left out in the evaluation and the relative gain in contrast is larger, than the loss in atom number.

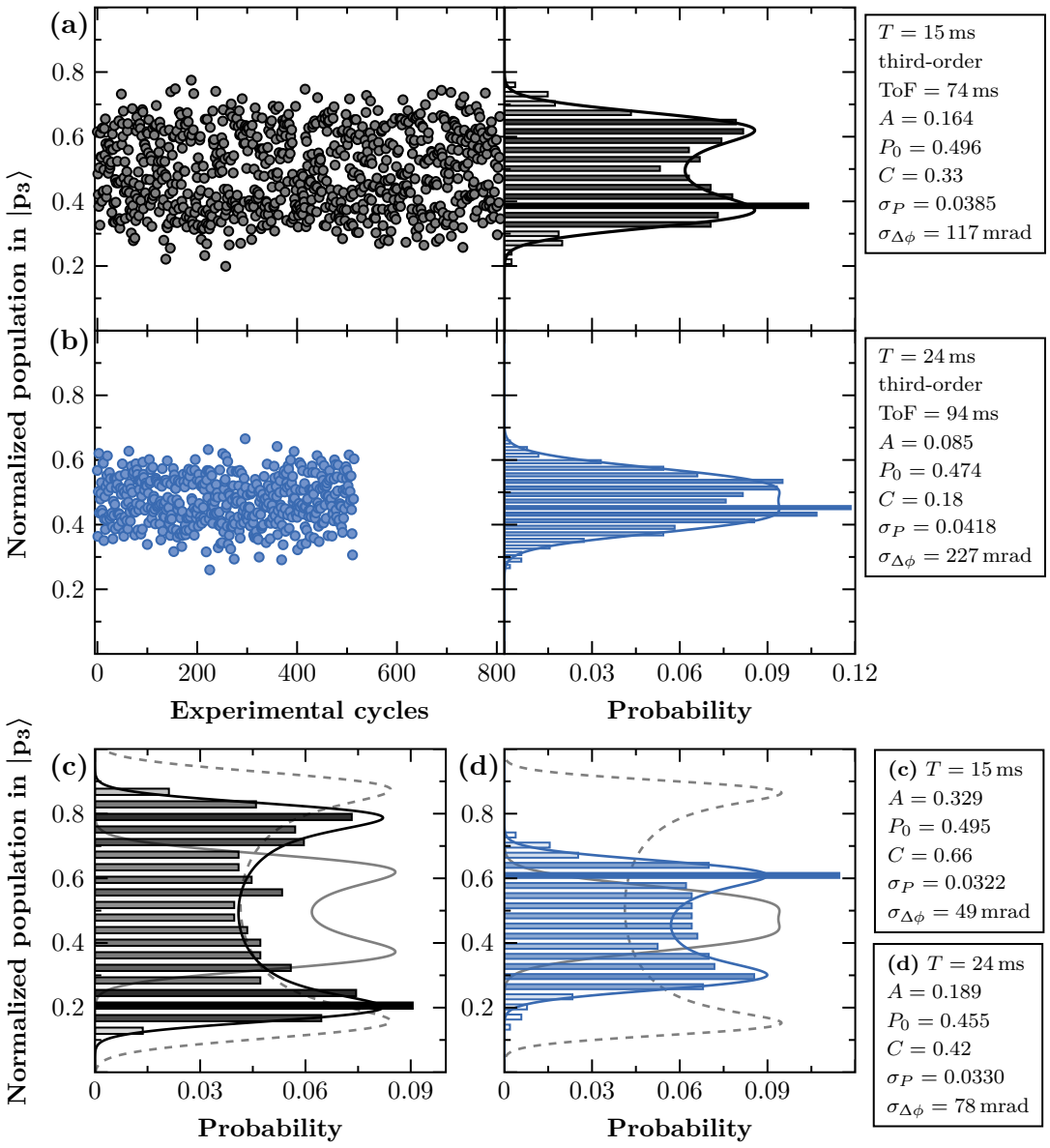

Figure 6.15: Output signal of the fountain gravimeter with third-order Bragg beam splitters for $T = 15\,\mathrm{ms}$ **(a** —**)** and $T = 24\,\mathrm{ms}$ **(b** —**)**. Using an aperture the contrast can be regained from $C = 0.33$ (—) to $C = 0.66$ (—) for $T = 15\,\mathrm{ms}$ **(c)** and from $C = 0.18$ (—) to $C = 0.42$ (—) in the case of $T = 24\,\mathrm{ms}$ **(d)**, in both cases still lower than for first-order beam splitters (- - -).

Results with delta-kick collimation and first-order Bragg diffraction

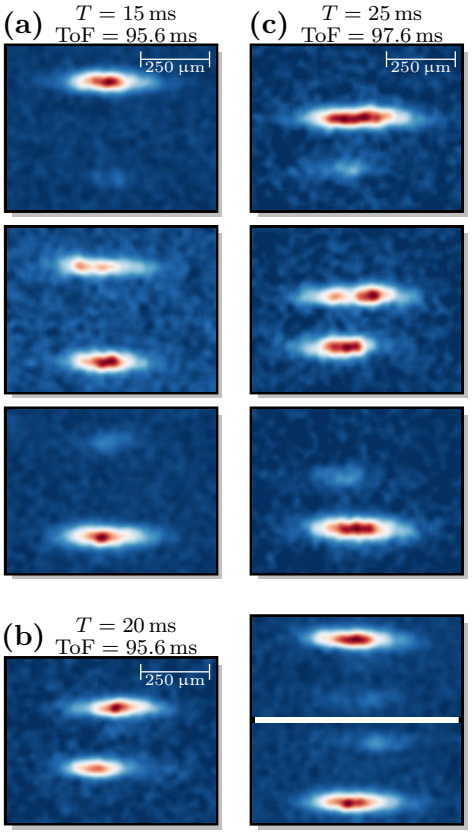

Fig. 6.16: Density plots of output ports in the fountain geometry for different populations using delta-kick collimated ensembles and interferometers with pulse separation times $T = 15\,\mathrm{ms}$ **(a)**, $T = 20\,\mathrm{ms}$ **(b)** and $T = 25\,\mathrm{ms}$ **(c)**.

A great advantage of the fountain geometry is, that delta-kick collimated condensates with slower expansion can be used, which remain smaller after the relaunch and during the free fall in the fountain. Already the exemplary density plots of output ports with different population in fig. 6.16 are cleaner than for the previous measurements. Additionally, the Stern-Gerlach-type deflection purifies the magnetic sub-states and the expected gain in contrast is between 5% and 10%. With this configuration the pulse separation time can even be extended to $T = 25\,\mathrm{ms}$. At this time, the output ports are still separated due to the smaller final size of clouds. The measurements and evaluation depicted in fig. 6.17 are again performed for Mach-Zehnder interferometers formed by first-order Bragg diffraction. To achieve better statistics, around thousand measurements are taken each for $T = 15$, 20 and $25\,\mathrm{ms}$. The histogram analysis now reveals contrasts of $C = 0.91$ for $15\,\mathrm{ms}$, $C = 0.86$ for $20\,\mathrm{ms}$ and still $C = 0.86$ for $25\,\mathrm{ms}$. This gain in contrast compared to the use of condensates without delta-kick collimation, but also compared to the experiments with dropped atoms, is remarkable. It is possible due to the interplay of the high-fidelity Bragg diffraction and the improved state preparation. The slight drop in contrast with increasing T can be explained by the decreasing port separation giving rise to a slight cross-talk between the output ports.

The technical noise level $\sigma_{\Delta\phi}$ is again extracted from the widths of the outer peaks in the fit to the density distribution. Already in the raw data sets it is visible, that the noise level is significantly lower compared to the previous interferometers using condensates without delta-kick collimation and it is now again close to the calculated shot noise of $\sigma_{\mathrm{qpn}} = 11\,\mathrm{mrad}$ for $N = 8\,000$ atoms. The technical noise compares well to the drop mode and the sensitivity improves directly with the larger pulse separation time to the square as well as with a larger contrast. The key feature to reach this low noise level at free-fall times close to 100 ms is using delta-kick collimated ensembles in the fountain geometry. These ultra-slow expansion rates would allow for even longer flight times and also give rise to a boost in sensitivity. The largest intrinsic sensitivity achieved in the measurements of $\Delta g/g = 1.4 \cdot 10^{-7}$ was observed for $T = 25\,\mathrm{ms}$ after a ToF $= 97.6\,\mathrm{ms}$ at a noise of $\sigma_{\Delta\phi} = 14\,\mathrm{mrad}$. This represents a more than 22-fold increase in sensitivity compared to the mode using dropped Bose-Einstein condensates and is an important step towards compact but precise sensors. An only slightly lower intrinsic sensitivity of $\Delta g/g = 1.7 \cdot 10^{-7}$ is obtained for $T = 20\,\mathrm{ms}$ and a sensitivity of $\Delta g/g = 3.4 \cdot 10^{-7}$ for $T = 15\,\mathrm{ms}$. The limit in T on the baseline of 7 mm is reached with $T = 25\,\mathrm{ms}$ and every further extension of the pulse separation time would result in a reduced contrast due to insufficient port separation.

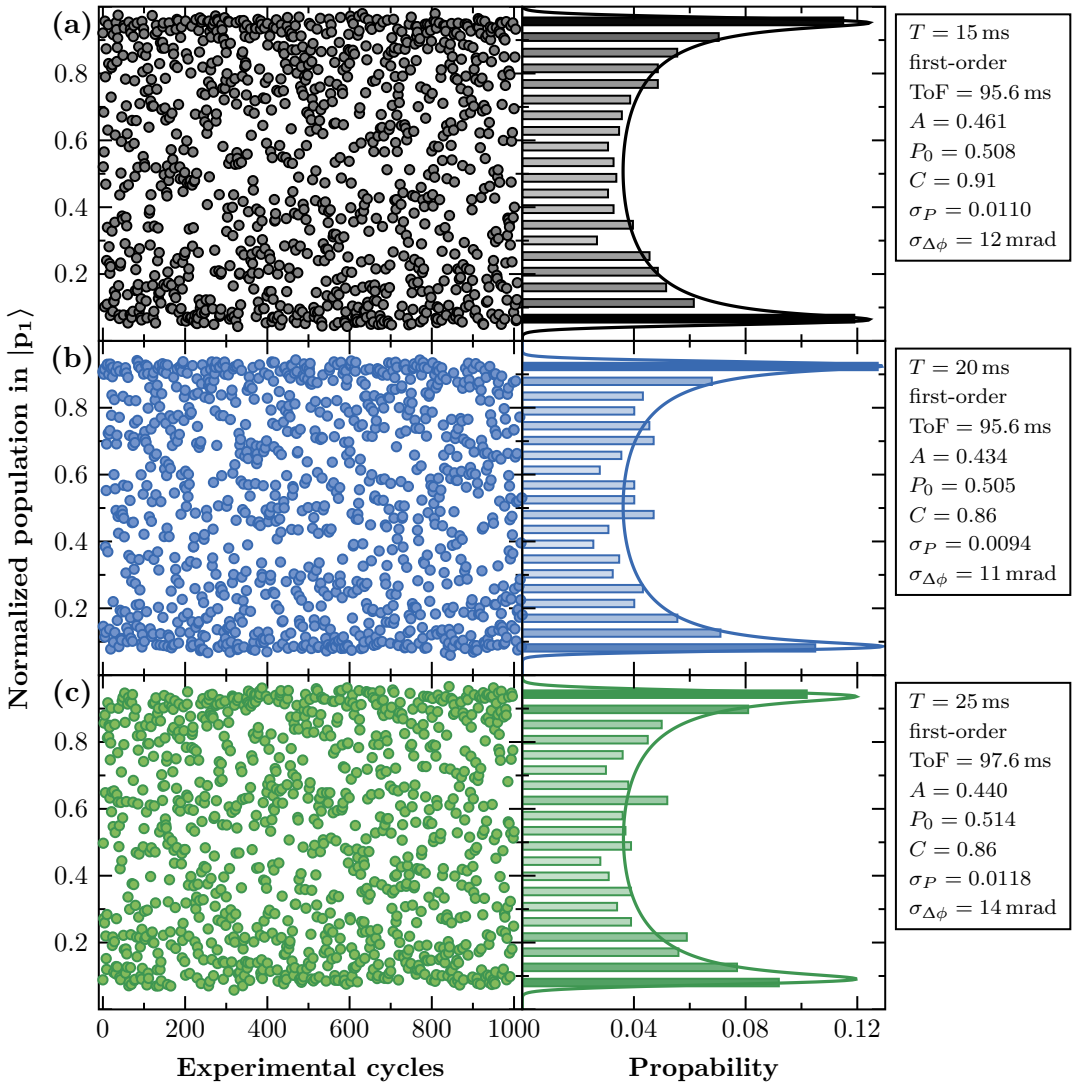

Figure 6.17: Output signal of the fountain geometry using delta-kick collimated ensembles for pulse separation times of $T = 15\,\text{ms}$ **(a ——)**, $T = 20\,\text{ms}$ **(b ——)** and $T = 25\,\text{ms}$ **(c ——)**. The Mach-Zehnder interferometers are performed with first-order Bragg diffraction and roughly 1 000 measurements are taken. Contrasts of $C = 0.90$ for the interferometer with $T = 15\,\text{ms}$, of $C = 0.87$ for $T = 20\,\text{ms}$ and $C = 0.86$ for $T = 25\,\text{ms}$ are obtained. The technical noise $\sigma_{\Delta\Phi}$ is close to shot noise.

Results with delta-kick collimation and third-order Bragg diffraction

The loss of contrast for the measurements with third-order Bragg diffraction is even larger compared to the outcome for condensates without delta-kick collimation. The output signals and histogram analysis for the interferometer with third-order Bragg diffraction and $T = 24\,\text{ms}$ are depicted in fig. 6.18(a). The contrast even vanishes completely, since the distribution appears fully Gaussian. It turns out, that in this case the much smaller output port size in vertical direction is not of noticeable relevance for the contrast. The cloud sizes in horizontal direction, which are susceptible to the defect, are of similar size. The more important contribution to the loss of contrast is, that the cut for the aperture runs now in the center of the output ports. In the steeper

trap prior to the kick the condensate has a smaller distance of the defect during the launch and the interferometer (see sec. 5.1.1), therefore the disturbance is larger. Figure 6.18(b,c,d) show the regions where contrast can be regained by an aperture, but due to a larger noise $\sigma_{\Delta\phi} = 63\,\text{mrad}$ the intrinsic sensitivity of $\Delta g/g = 2.3 \cdot 10^{-7}$ is slightly worse with respect to the measurement with first-order diffraction. Finally, the intrinsic sensitivities for all measurements with the fountain geometry are summed up in tab. 6.5.

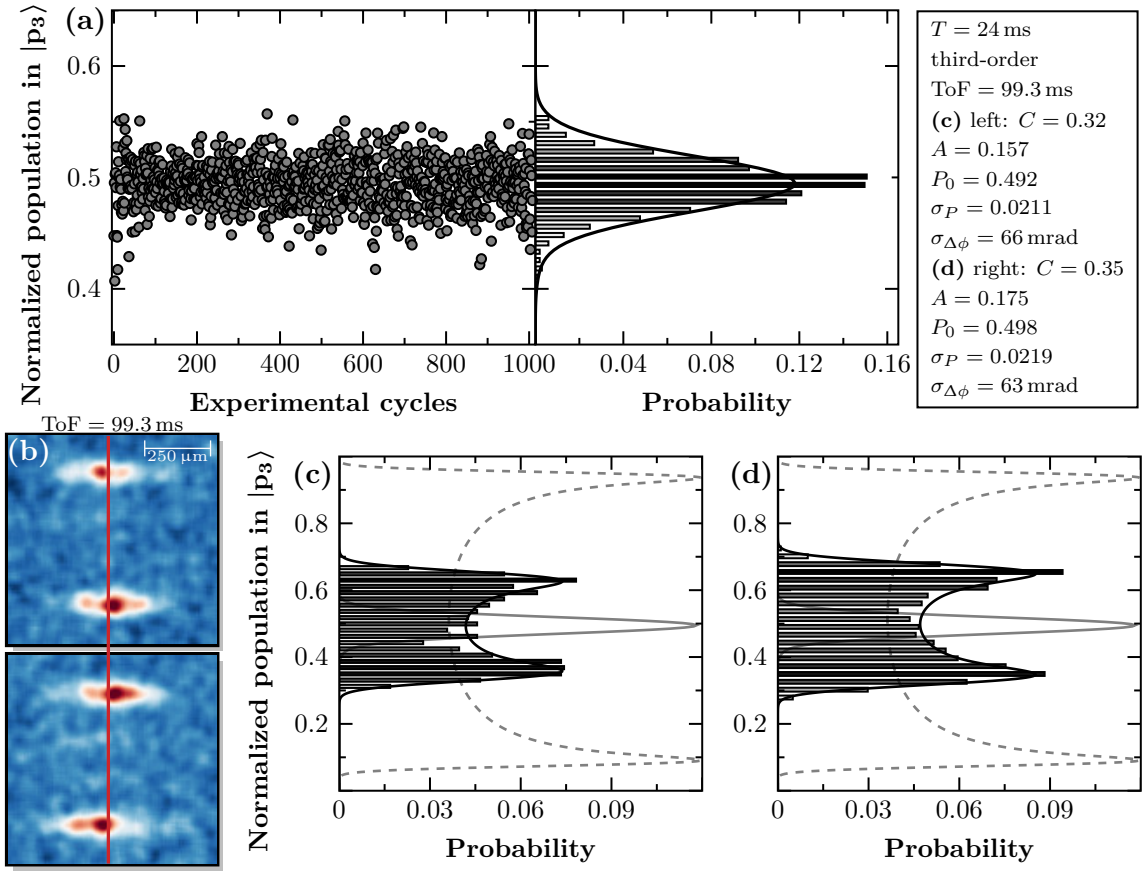

Figure 6.18: Output signal of the fountain geometry with third-order Bragg diffraction and $T = 24\,\text{ms}$ **(a)**. Without a central cut (—) the contrast vanishes completely **(b)**. A regain of $C = 0.32$ **(c)** for the left half of the cloud and $C = 0.35$ **(d)** for the right one are observed.

Table 6.5: Summary of the obtained intrinsic sensitivities for the fountain geometry. (* Due to the re-evaluation this intrinsic sensitivity is slightly better than the published value in ref. [156])

without delta-kick collimation, $n = 1$

T	C	$\sigma_{\Delta\phi}$	$\Delta g/g$
15 ms	0.75	49 mrad	$13.8 \cdot 10^{-7}$
20 ms	0.72	37 mrad	$5.9 \cdot 10^{-7}$

without delta-kick collimation, $n = 3$

T	C	$\sigma_{\Delta\phi}$	$\Delta g/g$
15 ms	0.66	49 mrad	$4.6 \cdot 10^{-7}$
24 ms	0.42	79 mrad	$2.9 \cdot 10^{-7}$

with delta-kick collimation, $n = 1$

T	C	$\sigma_{\Delta\phi}$	$\Delta g/g$
15 ms	0.89	12 mrad	$3.4 \cdot 10^{-7}$
20 ms	0.84	11 mrad	$1.7 \cdot 10^{-7}$
25 ms	0.82	14 mrad	$1.4 \cdot 10^{-7}$*

with delta-kick collimation, $n = 3$

T	C	$\sigma_{\Delta\phi}$	$\Delta g/g$
24 ms	0.35	63 mrad	$2.3 \cdot 10^{-7}$

6.3.2 Principal component analysis of the outputs

For the drop mode the output ports of the Mach-Zehnder interferometer are in all measurements perfectly "flat", e.g. there are no spatial features visible across the output ports and the atom number estimation is reliable. In the fountain mode a phase gradient across the wave front due to defects on the atom chip leads to a loss of contrast for third-order Bragg diffraction, if the evaluation integrates over the whole cloud. To accommodate that this integration is not the best way to analyze the output ports in the presence of a phase gradient, an image based evaluation is employed. The principal component analysis (PCA) is employed to spatially analyze oscillating modes in the outputs of the atom interferometer. Using a PCA-based evaluation the contrast for the measurement with $T = 24\,\mathrm{ms}$ and third-order Bragg diffraction is regained from $C = 0.35$ to 0.72 and thus increasing the intrinsic sensitivity to a new record of $\Delta g/g = 1.1 \cdot 10^{-7}$.

An idealized atom interferometer in principal component analysis

Principal component analysis (PCA) is a text book example of an application of linear algebra [290] and has been employed in cold atom experiments before [291, 292]. PCA performs statistics on a series of images, where each image is treated as a vector $\mathbf{I}$ of pixel values. If a series of images contains a number of N images $\mathbf{I}_i$ the mean value of peach pixel $\mathbf{M}$ is computed by

$$\mathbf{M} = \frac{1}{N} \sum_{n=0}^{N} \mathbf{I}_n. \tag{6.12}$$

In general each image $\mathbf{I}_i$ of the series is represented in a matrix $B = [\mathbf{I}_1 - \mathbf{M}\ \mathbf{I}_2 - \mathbf{M}\ \ldots\ \mathbf{I_N} - \mathbf{M}]$, which contains each pixel of each image and thus can be used to reconstruct each image in the basis of the pixels represented by orthogonal vectors with only a single entry

$$\mathbf{I}_i - \mathbf{M} = B_{1,i} \begin{bmatrix} 1 \\ 0 \\ \vdots \\ 0 \end{bmatrix} + B_{2,i} \begin{bmatrix} 0 \\ 1 \\ \vdots \\ 0 \end{bmatrix} + \ldots + B_{N,i} \begin{bmatrix} 0 \\ 0 \\ \vdots \\ 1 \end{bmatrix}. \tag{6.13}$$

The matrix B is as representation of the series of images not useful, because in fact it contains the same information as the original pixel values and the basis contains no information about modes or structures in the images. The PCA algorithm searches for a different basis $P = [\mathbf{u}_1\ \mathbf{u}_2\ \ldots\ \mathbf{u}_N]$ of orthogonal vectors $\mathbf{u}_n$ with minimal variance to the series of images and sorted by the significance, e.g. the standard deviation of the corresponding coefficient PC_n is larger than the one of PC_{n+1}

$$\mathbf{I}_i = PC_{0,i} \cdot \mathbf{M} + \sum_{n=0}^{N} PC_{n,i}\mathbf{u}_n \approx PC_{0,i} \cdot \mathbf{M} + \sum_{n=0}^{m} PC_{n,i}\mathbf{u}_n. \tag{6.14}$$

The basis P can be reduced from the total number of images N to a smaller quantity $m \ll N$, because the variance of the first PC-components is the smallest and still leads to an appropriate reconstruction of each image $\mathbf{I}$. The PC_0-coefficient corrects for total density fluctuations.

The PCA algorithm itself is a completely model and assumption free treatment of the series of images, but the computed basis vector - or PC-components - can represent physical quantities observed in an atom interferometer. Figure 6.19 illustrates a highly idealized representation of the two output ports $|p_0\rangle$ and $|p_n\rangle$ of an atom interferometer in the representation of the PCA. The coordinate system in the figure is chosen according to the atom-chip gravimeter.

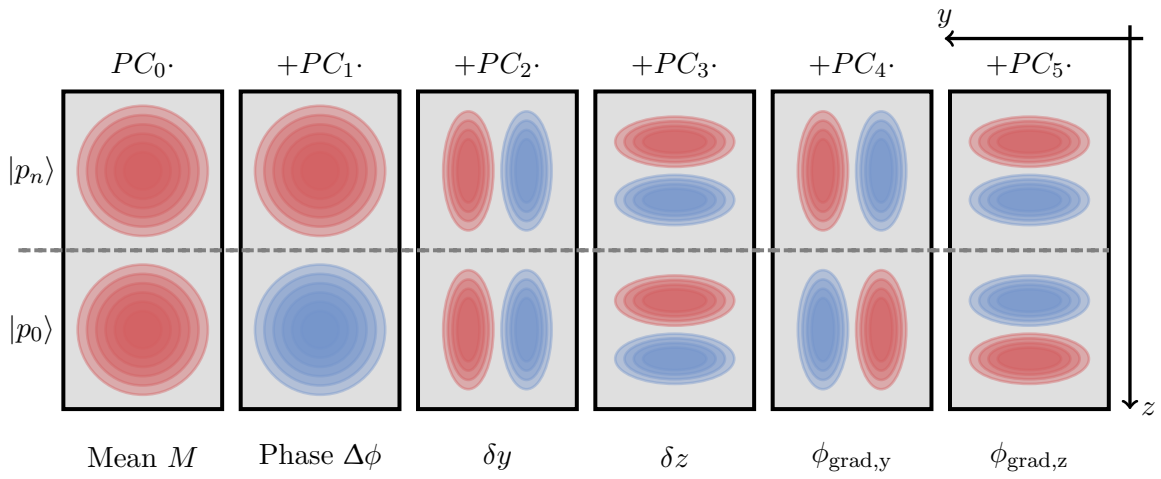

Figure 6.19: Idealized basis vectors in principle component analysis. The mean results in equally distributed atom number. Regions with different colors (■ and ■) indicate areas, where the atomic density oscillates against each other between subsequent pictures, e.g. experimental cycles.

The PC-components act on the density level of an image, regions with red color have larger density, while regions with blue color have a smaller density than the mean **M**. Darker colors indicate in general a stronger effect on the density, but the total strength of the effect depends on the coefficients. The distribution of red and blue regions across the PC-component gives rise to different features. The physical meanings of observable features in the PC-components are:

- The mean **M** corresponds to the **atom number** $N/2$ for equally distributed ports. For this mean a coefficient PC_0 can be computed to correct for atom number fluctuations.
- The **oscillating population** of the two interferometer output ports with the relative phase $\Delta\phi$ is the measured signal as it is normally extracted from the fit routine.
- Every movement of the output ports δy or δz due to **motion or position jitter** of the condensate is represented by a component where at the same part of both ports the density decreases while at the opposite part the density increases independently of $\Delta\phi$.
- An anti-symmetric decrease and increase in density is caused by **phase gradients** $\phi_{\mathrm{grad,y}}$ or $\phi_{\mathrm{grad,z}}$ across the ports. An oscillation with the interferometer's phase $\Delta\phi$ rather than causing a change in population, only redistributes the atoms inside the ports.
- The last influence is **background noise** which is not represented in the illustration. The PCA also suppresses noise as in refs. [70, 100], because the basis vectors average smaller features which statistically fluctuate and only appear in less significant components.

In a simple picture, the atom interferometer in PC-components starts from the mean **M** with equally distributed output ports which contain each $N/2$ of the total atoms. The coefficient of the first PC-component $\mathbf{u}_1$ acts as the relative phase $PC_1 \sim \Delta\phi$ by lowering the density of atoms in one port, respectively the atom number in this port, and increasing the other. In principle, all other PC-components are distortions to the atom interferometer, but only occurring phase gradients ϕ_{grad} distort the oscillation and lead to a loss of contrast by the density modulation.

Computation of the basis vectors and coefficients for the fountain geometry

For the implementation of principal component analysis in the experiment no additional data sets need to be taken, but rather the original images already used for the results in sec. 6.3.1 are reevaluated with the PCA formalism without making any additional assumptions. Hereby, the formalism is not applied to all previous data sets but only to those with the largest and smallest scaling factors. The four measurements examined are the ones without delta-kick collimation for $T = 15\,\mathrm{ms}$ and with delta-kick collimation for $T = 24/25\,\mathrm{ms}$, each with first- and third-order Bragg diffraction. Before the images are inserted into the algorithm a Gaussian filter with a width of two pixels is applied to diminish electronic noise of the camera.

Figure 6.20 shows the mean and the seven PC-components for each of these measurements encoded in the same colors as the idealized basis vectors in fig. 6.19. The background level in the mean is adjusted in such a way, that regions, where no atoms are expected, appear homogeneously in gray and no blue regions appear which represent a negative density. All other components are adjusted to this background level giving rise to the same red-blue areas as in the idealized representation. Areas in the components with the darkest respective color exhibit the highest atomic density. This adjustment only visually highlights the observable features and does not affect operations on the images which are done on the density level.

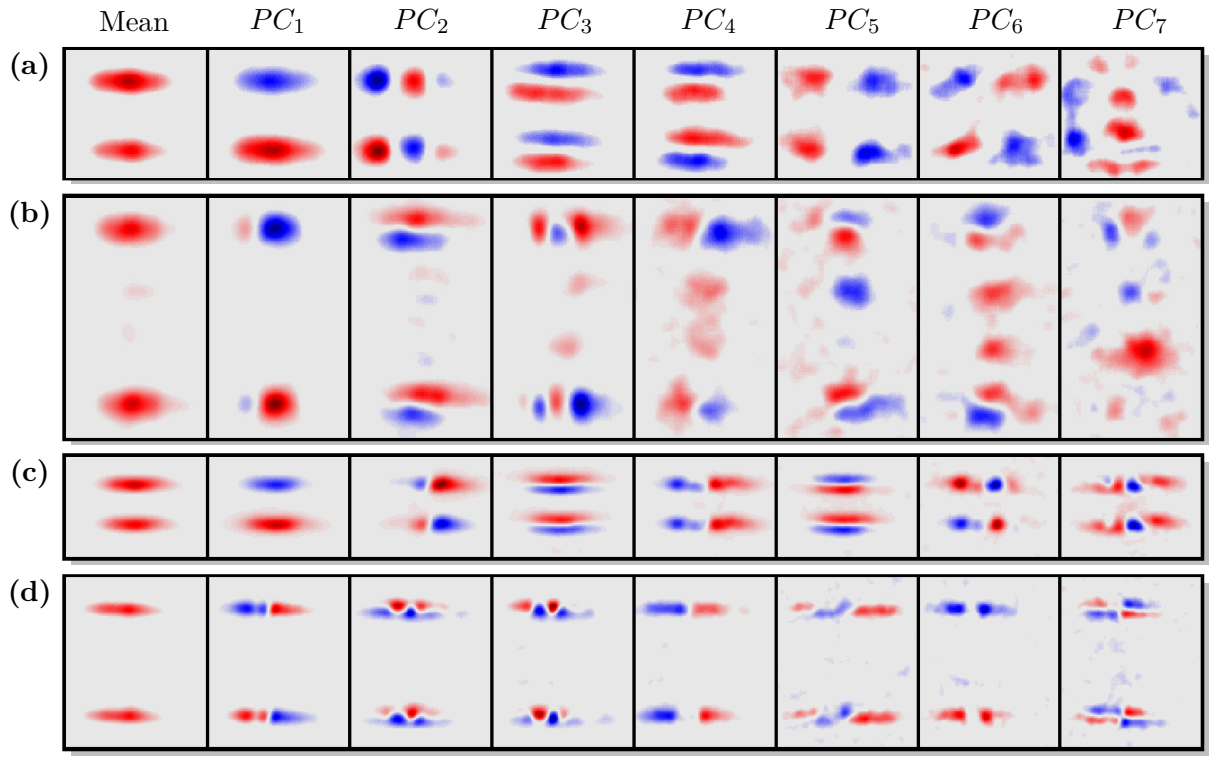

(a) $T = 15\,\mathrm{ms}$, $n = 1$ **(b)** $T = 15\,\mathrm{ms}$, $n = 3$ **(c)** $T = 25\,\mathrm{ms}$, $n = 1$ **(d)** $T = 24\,\mathrm{ms}$, $n = 3$

Figure 6.20: The first eight basis components found in the principal component analysis ordered by significance for Mach-Zehnder interferometers in the fountain geometry with $T = 15\,\mathrm{ms}$ **(a,b)** and $T = 24/25\,\mathrm{ms}$ **(c,d)**, each with first- and third-order Bragg diffraction. The first two components represent the mean density, proportional to the total atom number N and the dominant oscillating component with relative phase $\Delta\phi$. The six other displayed components represent higher-order moments, which are either center-of-mass motion or phase gradient related.

In the PC-components in fig. 6.19 the distortions introduced in the schematic can be recovered for each of the measurements, but of different significance. For the measurements with first-order Bragg diffraction (a,c), the PC_1-component directly gives rise to the oscillation in population due to the statistical output phase $\Delta\phi$ of the interferometer. The higher PC-components are in these cases suppressed by at least an order of magnitude compared to PC_1. Nevertheless, also in this case PC-components are found by the algorithm reflecting phase gradients and motion jitter, but these are too small to have an influence on the interferometric contrast.

The occurrence of the phase gradients across the output ports is clearly visible for the measurements with third-order Bragg diffraction (b,d). The PC_1-component in theses case has regions in both output ports which are of different color and modulate the density with changing $\Delta\phi$. From the appearance of these PC_1-components is also apparent, why the regain of contrast using an aperture has a large benefit for $T = 15\,\mathrm{ms}$, since in that case the regions which cause density modulation are comparably small and at the edge of the atomic cloud. The PC_1-component matches well with the chosen aperture in fig. 6.14 and the respective regain in contrast by this method is already maximized. For $T = 24\,\mathrm{ms}$ the regain is smaller because the component in fig. 6.19(d) cuts the cloud in two almost equally large halves and large distortion in the center due to the defects on the chip are clearly visible in different PC-components.

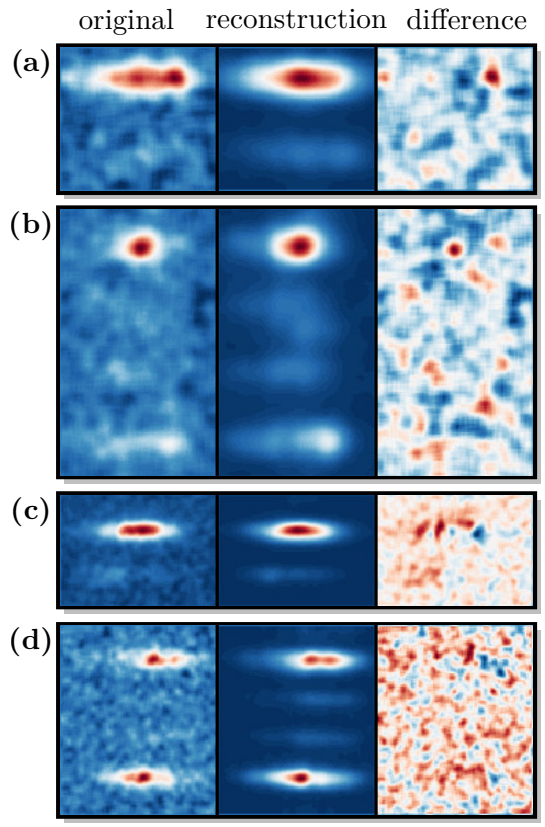

Fig. 6.21: Reconstruction of the original images of the fountain gravimeter by the mean and the most significant principal component for Mach-Zehnder interferometers with $T = 15\,\mathrm{ms}$ **(a,b)** and $T = 24/25\,\mathrm{ms}$ **(c,d)** with first- and third-order Bragg diffraction. The difference shows the subtracted background noise.

Figure 6.21 shows for each of the measurement a reconstruction of an exemplary density plot from the mean $\mathbf{M}$ and the most significant component $\mathbf{u}_1$ compared to the original picture. This visualizes the reconstruction on the density level, because each image $\mathbf{I}$ is a composition of individual coefficients PC_0 and PC_1 for the mean $\mathbf{M}$ and the most significant basis vector $\mathbf{u}_1$. The difference between reconstructed and original image reveals an almost homogeneous background level with some structure which is background noise. The background looks finer structured in the case of the delta-kick collimated condensates, because of the even lower residual fluctuations in the density. The background in each reconstructed image is noticeably enhanced by the reconstruction, while the shape of the output ports is mostly preserved. The difference between both images also gives rise to the error which is made if only a single component is used for the evaluation. A suppression at the peak density with respect to the residual background density of almost an order of magnitude is observed for delta-kick collimated condensates and, respectively, a factor of five without delta-kick collimation. The level of this suppression could even be enhanced as in refs. [70, 100] by centering the output ports in the image with a Gaussian fit prior to the PCA. This would reflect, compared to the conventional image evaluation, that the centers of the Gaussian peaks are also not fixed but rather a free parameter.

Performance evaluation using a PCA-based evaluation

A different performance evaluation is possible using the PCA formalism, which properly reflects the observed phase gradients and gives a realistic estimate on the intrinsic sensitivity. The basis vectors $\mathbf{u}$ only communicates a visualization of spatial features and does not give rise to the contrast of the measurement. To extract a measured value the individual coefficient PC_1 of each image $\mathbf{I}$ is used. Hereby, the evaluation is restricted to the use of only the coefficient PC_1 of the most significant basis vector $\mathbf{u}_1$ and all other coefficients are neglected. A complete depiction of the coefficients for up to seven PC-components and the cross-correlations between these coefficients can be found in ref. [293]. The PC_1-coefficients are not normalized and also take negative values to change the sign between increasing and decreasing density. To obtain an expression similar to the common normalized population P a normalization is chosen as

$$P_{\mathrm{PCA}} \equiv \frac{1}{2} + \frac{PC_1 + \bar{PC_1}}{PC_0} \text{ with } \bar{PC_1} = \frac{1}{N}\sum_{n=0}^{N} PC_{1,n}. \tag{6.15}$$

This population P_{PCA} is normalized by the coefficient PC_0 of the mean to correct for atom number fluctuations and offset free, leading to a contrast of two times the amplitude $C = 2A$. Due to this normalization the same fit routine as for the fluctuation dependent performance evaluation can be applied and the results directly be compared.

Figure 6.22 shows the obtained normalized populations P_{PCA} and the corresponding fits to the distributions for the data sets. The extracted intrinsic sensitivities from the fits to the distributions of the data sets are summarized in tab. 6.6 together with the previously obtained result. The main observation is, that the contrast for all measurements is of a similar value between $C = 0.72$ and 0.76, which is for the measurement with $T = 25\,\mathrm{ms}$ even slightly smaller than before, but does not lead to a reduced intrinsic sensitivity. The fit to the distribution for $T = 25\,\mathrm{ms}$ and first-order Bragg diffraction yields exactly the same technical noise $\sigma_{\Delta\phi}$ and intrinsic sensitivity of $\Delta g/g = 1.4 \cdot 10^{-7}$ as in the previous evaluation. Since in the previous evaluation, the noise was already close to the shot noise, this is a strong indicator, that the normalization in eq. 6.15 does not influence the performance evaluation.

Table 6.6: Summary of obtained parameters for the coefficients and estimated intrinsic sensitivities.

Data set		Fit-based evaluation			PCA-based evaluation		
T	n	C	$\sigma_{\Delta\phi}$	$\Delta g/g$	$2A$	$\sigma_{\Delta\phi}$	$\Delta g/g$
15 ms	1	0.75	49 mrad	$13.8 \cdot 10^{-7}$	0.76	33 mrad	$9.3 \cdot 10^{-7}$
15 ms	3	0.666	49 mrad	$5.9 \cdot 10^{-7}$	0.74	41 mrad	$3.8 \cdot 10^{-7}$
25 ms	1	0.82	14 mrad	$1.4 \cdot 10^{-7}$	0.74	14 mrad	$1.4 \cdot 10^{-7}$
24 ms	3	0.35	63 mrad	$2.3 \cdot 10^{-7}$	0.72	20 mrad	$1.1 \cdot 10^{-7}$

In the case of all other measurements the intrinsic sensitivities can be enhanced because the distributions provide enlarged contrasts and, respectively, reduced technical noise. In both cases with $T = 15\,\mathrm{ms}$ a gain of 1.5 in intrinsic sensitivity is observed due to the noise reduction. The largest gain in contrast from $C = 0.35$ to 0.72 for $T = 24\,\mathrm{ms}$ and third-order Bragg diffraction even leads to a new record in intrinsic sensitivity of $\Delta g/g = 1.1 \cdot 10^{-7}$. In the future, PCA is a promising way to not only investigate the contrast, but also the influence of wave front distortions on the accuracy of the interferometric phase, because these are one of the dominant systematic uncertainty in the current generation of atom interferometers [88, 294, 295].

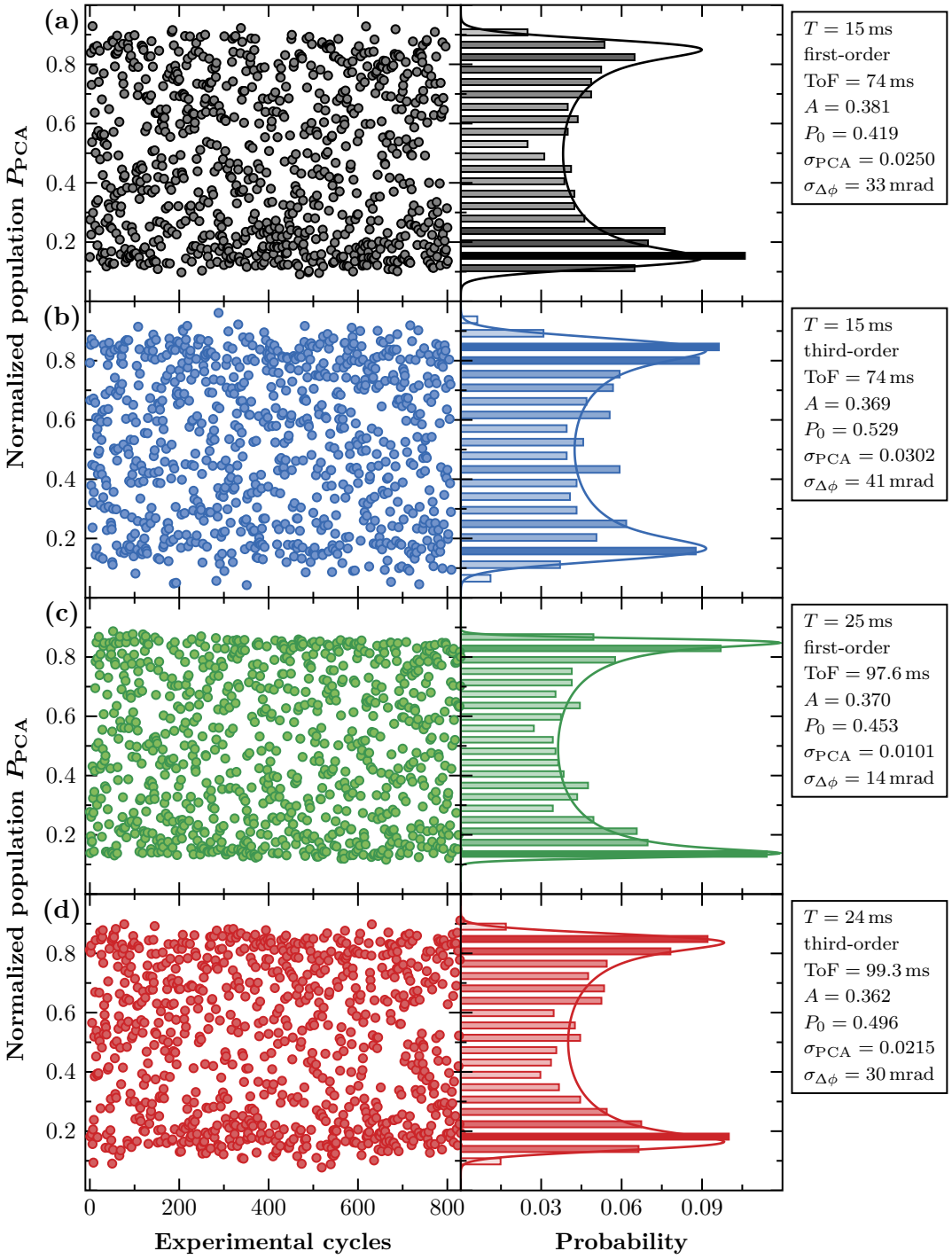

Figure 6.22: Output signals and histogram analysis using the normalized population P_{PCA} extracted from the PC_1-coefficient to obtain enhanced intrinsic sensitivities. The evaluated data sets are for a pulse separation of $T = 15\,\mathrm{ms}$ with first- (**a** ——) and third-order Bragg diffraction (**b** ——) as well as for $T = 24/25\,\mathrm{ms}$ also with first- (**c** ——) and third-order Bragg diffraction (**d** ——).

6.4 Systematic uncertainties and future perspective

A main drive behind the use of Bose-Einstein condensates for quantum sensors lies in the gain in accuracy, due to their unique properties which turn out to be the most beneficial for the suppression of inertial phase shift terms and wave front distortions. To estimate the performance of an atom interferometer one needs to distinguish between statistical noise and systematic uncertainty [296]. The first determines how stable a measured signal is, while the later determines the bias to the expected - or true - value. The prototype gravimeter realized in QUANTUS-1 is fully limited by statistical noise even after eight hours of integration. Thus a meaningful discussion of a systematic uncertainty budget for the current apparatus is not possible at the moment. Nevertheless, an estimation of already known systematic uncertainties allows to identify, which systematic uncertainties are the most critical and to set bounds on experimental parameters necessary for future experiments to venture into the μGal regime.

6.4.1 Estimation of systematic uncertainties

The following calculations of systematic uncertainties make use of previous work for the proposals for the STE-QUEST M3 mission proposal [280, 281] and VLBAI [282] as well as for the experiments ATLAS [262] and CASI [83–85] at the IQ. Primarily, these calculations use the parameters of the gravity estimation performed in sec. 6.2.3 which are summarized in tab. 6.7, because for this measurement a full set of experimental parameters is available. But, this discussion also grants valuable insight into error sources in the fountain geometry, even though at the current state of the experiment no phase can be read out, and it shows which of the assumed parameters need to be improved in the future.

MZI parameter	Value
Atom number N	10^4
Effective Temp. T_{eff}	4 nK
Expansion rate σ_v	600 μm/s
Pulse separation T	5 ms
Cycle time T_{cyc}	15 s
Wave vector k_{eff}	$\frac{4\pi}{780\,\text{nm}}$
Pulse width σ_τ	12.5 μs
Rabi frequency Ω_{eff}	$2\pi \cdot 4$ kHz
Initial radius σ_r	13 μm
Beam diameter ⌀	7 mm
Sensitivity $\Delta g/g$	$3.2 \cdot 10^{-6}$

Table 6.7: Summary of experimental parameters for the gravimeter operated with dropped BECs.

Magnetic stray fields and magnetic shield

The non-magnetic state $m_{\text{F}} = 0$ causes a vanishing linear Zeeman effect. Nevertheless, the atom interferometer is not immune to the quadratic or second order Zeeman effect, due to the hyperfine splitting of the ground states of ^{87}Rb and residual magnetic stray fields are a cause of systematic uncertainties. To reduce the magnetic background environment a magnetic shield is surrounding the vacuum chamber, which has a shielding factor of roughly one order of magnitude. In the case of Bragg diffraction there is no "clock-shift" [297] in the traditional sense, since both interferometer paths travel in the same internal ground state of ^{87}Rb. In a simple picture the second order Zeeman effect causes an acceleration by an magnetic field gradient

$$\Delta b_{2\text{nd}} = \frac{h}{m_{87}} K_{87} B_0 \delta B, \tag{6.16}$$

with the Zeeman shift $K_{87} = \Delta\omega_{\text{clock}}/(2\pi B^2)$ in the energies of the hyperfine levels of ^{87}Rb, the magnetic field gradient δB and the quantization field B_0. A non-vanishing magnetic field gradient δB results in a phase offset ϕ_{bf} between the different interferometer paths depending on their height difference due to the recoil of the beam splitter, which cannot be distinguished from the gravitational acceleration g. For the parameters of the current Mach-Zehnder interferometer

in tab. 6.7 with dropped atoms this phase shift calculates to

$$\phi_{\mathrm{bf}} = k_{\mathrm{eff}} \Delta b_{2\mathrm{nd}} T^2 = 4\pi v_{\mathrm{rec}} K_{87} B_0 \delta B T^2 = 1.06\,\mathrm{mrad}. \tag{6.17}$$

The resulting uncertainty of $\Delta g/g = 2.7 \cdot 10^{-7}$ is compared to other shifts the largest systematic uncertainty in the current device due to the limited shielding factor of the magnetic shield. Shielding factors of 10^5 with a three layer shield should be achievable [298], which would be sufficient for future experiments to reach the µGal regime, independent from Bragg or Raman diffraction. Alternatively, the Mach-Zehnder interferometer can be driven in alternating hyperfine states $F = 1$ and $F = 2$ to subtract a static or slowly changing magnetic field gradient [280] or the gradient can be measured directly with the atom interferometer [124].

Wavefront curvature and aberrations

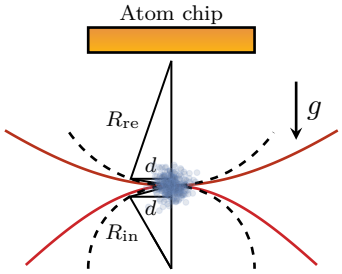

Fig. 6.23: Wavefront curvature of incoming and reflected beam [262].

The beam splitting light field cannot be treated as an ideal plane wave. Two different scales of distortions are of importance. The curvature of the whole Gaussian wave front due to its finite radius and possible misalignments, and the roughness of the phase front due to small aberrations. The bias phase shift due to these wave front distortions is a major contribution to the systematic uncertainties in most inertial sensors working with molasses cooled atoms [88, 294, 295]. The contribution due to the surface roughness and the defects of the atom chip is not easily calculated, since the exact surface is not known and not accessible in the vacuum chamber for a characterization [294, 295]. Such a characterization is not done in this thesis. A better surface quality using another technique producing atom chips seems a necessary step to reach optical qualities comparable to mirrors. As an approximate value surface qualities of $\lambda/10$ is aimed for in future experiments to not suffer from aberrations.

Using condensates is of major advantage for the suppression of wave front related uncertainties, because their sizes are much smaller, compared to molasses cooled atomic clouds. Especially the influence of the wave front curvature [88], which couples in due to the expansion of the clouds, can be greatly reduced by the use of delta-kick collimated condensates. How the phase shift due to this effect arises is schematically depicted in fig. 6.23 and it can be calculated to

$$\begin{aligned}\phi_{\mathrm{wf,c}} = k_{\mathrm{eff}} \Bigg[&(\sigma_r + \sigma_v t_0)^2 \left(\frac{1}{R_{\mathrm{in,c}}} - \frac{1}{R_{\mathrm{re,c}}} \right) - \Bigg((\sigma_r + \sigma_v (t_0 + T))^2 \left(\frac{1}{R_{\mathrm{in,t}}} - \frac{1}{R_{\mathrm{re,c}}} \right) \\ &+ (\sigma_r + \sigma_v (t_0 + T))^2 \left(\frac{1}{R_{\mathrm{in,m}}} - \frac{1}{R_{\mathrm{re,m}}} \right) \Bigg) + (\sigma_r + \sigma_v (t_0 + 2T))^2 \left(\frac{1}{R_{\mathrm{in,c}}} - \frac{1}{R_{\mathrm{re,c}}} \right) \Bigg] .\end{aligned} \tag{6.18}$$

In this equation the initial radius σ_r and the expansion rate σ_v of the cloud enters as well as the beam curvature R at each pulse and the pulse separation time T. Already the current beam diameter of 7 mm allows to suppress the bias arising from the wave front curvature below 1 µGal. Additionally, with the point-source nature [98, 100] of Bose-Einstein condensates it is possible to characterize systematic errors arising from wave-front distortions. Especially the principal component analysis used in sec. 6.3.2 can be a valuable tool to analyze curvature and aberrations. A first approach to theoretically express wave front distortions with PCA is performed in ref. [293], but no systematic analysis has been performed so far.

Engineering the mean field shift with delta-kick collimation

Atom-atom interactions in the case of Bose-Einstein condensates are not negligible as for thermal ensembles due to their much higher atomic density. These interactions lead to the so called mean field energy, that converts to kinetic energy after a certain time of expansion. This is the reason for the typical aspect ratio change observed in the expansion of Bose-Einstein condensates. These interactions cause a bias on the interferometer's phase shift depending on imperfections of the first beam splitting pulse σ_{BS} in a Mach-Zehnder interferometer [97, 128, 129]. The mean field energy is proportional to the chemical potential μ, that changes over time t with the expansion

$$\mu(t) = n(t) \cdot U = \frac{N}{V(t)} \cdot \frac{h a_{\mathrm{sc}}}{\pi m}, \tag{6.19}$$

with an atomic density $n(t)$, depending on the atom number N distributed over the volume of the ensemble $V(t) = 4\pi(\sigma_r + \sigma_v t)^3/3$ after a given expansion time t, and a constant interaction parameter U, depending on Planck's constant h, the intra species scattering length a_{87} and the atomic mass m_{87}. If now the atomic density $n(t)$ is different between the two paths in the interferometer a bias phase shift ϕ_{mf} is observed. With a simple model [97] this phase is calculated by integrating the expansion dependent frequency difference ω_{mf} between the two paths over the complete time $2T$ spent in the interferometer

$$\phi_{\mathrm{mf}} = \int_0^{2T} \mathrm{d}t\, \omega_{\mathrm{mf}}(t) = 1.09\,\mathrm{mrad} \text{ with } \omega_{\mathrm{mf}}(t) = 2\pi \frac{\nu(t)}{h\sigma_{\mathrm{BS}}} > 2\pi \frac{\sqrt{N}U}{hV(t)}. \tag{6.20}$$

The noise of the beam splitter is hereby limited due to the shot noise $\sigma_{\mathrm{BS}} > 1/\sqrt{N} = 0.01$ for 10^4 atoms. The measured noise of a beam splitter in the experiment is at that level. So, if the noise can be kept at shot noise for increasing atom number the uncertainty due to this shifts scales with $\sqrt{N}$. With the initial parameters and the expansion rate from tab. 6.7, divided by the scaling factor of the interferometer $k_{\mathrm{eff}}T^2$, an uncertainty contribution to the gravity measurement of $\Delta g/g = 2.8 \cdot 10^{-7}$ is obtained. Ideally, if the waiting time τ_{prep} before starting the interferometer can be enlarged [124], the density can be lowered to the required extend suppressing this contribution, independently of the given scaling factor, which suppresses this shift as well. However, lowering the density by long expansion times leads to larger devices that conflicts the idea behind the atom-chip gravimeter, especially if extremely small temperatures, respectively slow expansion rates, are employed. The largest acceptable waiting time before interferometry is the duration τ_{prep} of the preparation itself, which in the case of the experiment is only $\tau_{\mathrm{prep}} = 10.5\,\mathrm{ms}$. For example, in order to decrease the bias below 1 µGal at 4 nK and $T = 50\,\mathrm{ms}$ more than 100 ms of expansion would be needed at the current atom number.

Alternatively, the initial size of the cloud σ_r can be expanded at a larger rate followed by a delta-kick collimation pulse [98, 133] to afterwards lower the expansion rate. In that way, the density is lowered without a long expansion time and the final expansion rate can even be smaller than for the pure condensate. With this technique cloud size and expansion can be engineered and optimized in a wider parameter range to save expansion time. In the current delta-kick collimation procedure an effective temperature of $T_{\mathrm{eff}} = 200\,\mathrm{nK}$ allows to expand a Bose-Einstein condensate to 100 µm in less than 20 ms. The distance to the chip after this time of free fall is 2 mm which is still close enough to perform the lensing pulse with the bigger structures of the atom chip used in the QUANTUS-2 experiment [299]. This procedure is compatible with the fountain mode and allows to relax the mean field shift even for 10^5 atoms below 1 µGal.

Determination of initial motion by dipole oscillations

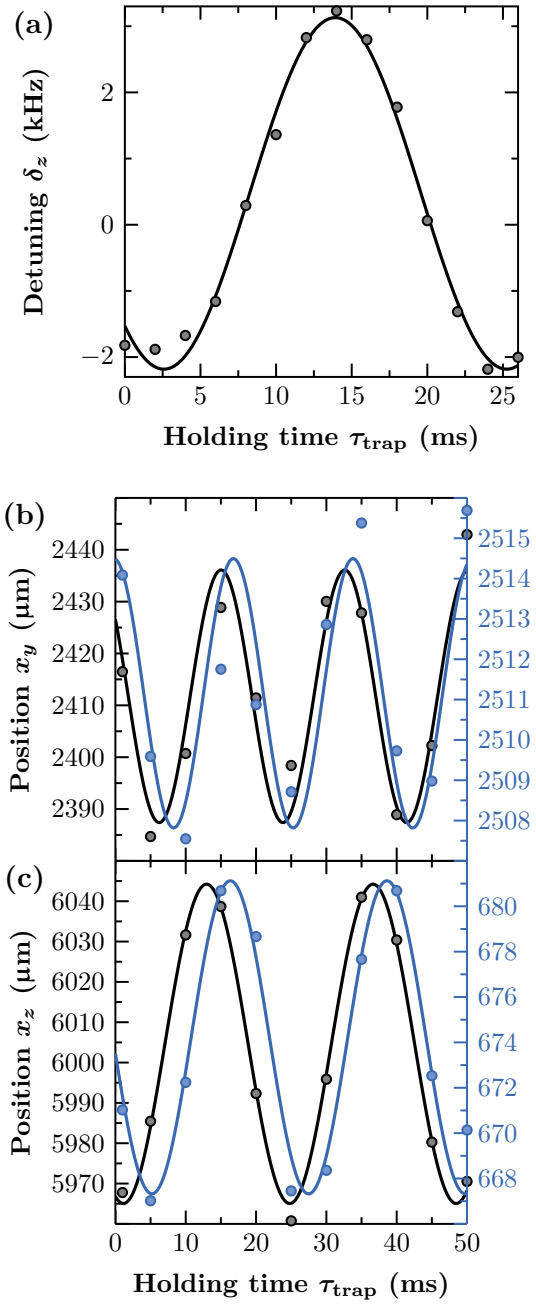

Fig. 6.24: Dipole oscillation in the shallow trap with $I_{\mathrm{bias}} = 0.36\,\mathrm{A}$ for an offset current of $I_{\mathrm{K2}} = -1\,\mathrm{A}$ depending on the holding time t_{trap} in the magnetic trap. Bragg spectroscopy in beam splitter direction determines the detuning to the atomic resonance as direct measure for the offset velocity **(a)**. In both directions time of flight measurements are performed for ToF = 0 ms (——) and ToF = 29 ms (——) **(b,c)**.

The condensate shows a residual horizontal and longitudinal motion due to the dipole oscillations in the final trap after decompression [164, 165]. The center of mass of the atomic ensemble oscillates around the potential minimum $x_{0,i}$ in position

$$x_i(\tau_{\mathrm{trap}}) = x_{0,i} + A_i \sin(\omega_i \tau_{\mathrm{trap}} + \phi_i) + \frac{1}{2} g_{\parallel} T^2, \quad (6.21)$$

and in velocity

$$v_i(\tau_{\mathrm{trap}}) = v_{0,i} + A_{v_i} \sin(\omega_{v_i} \tau_{\mathrm{trap}} + \phi_{v_i}). \quad (6.22)$$

These oscillations can be characterized depending on the holding time τ_{trap} in the final trap by either time of flight measurement or Bragg spectroscopy [232]. Hereby, Bragg spectroscopy has the advantage, that the atomic velocity can be directly measured and is not inferred between two different points in time. A complete mapping of the oscillation frequency and amplitudes for the shallowest trap with $I_{\mathrm{bias}} = 0.36\,\mathrm{A}$ depending on the initial shiftI_{K2} is found in fig. 5.4 and in ref. [171]. In fig. 6.24 an exemplary dipole oscillation for the release trap with $I_{\mathrm{bias}} = 0.36\,\mathrm{A}$ and an offset shift of $I_{\mathrm{K2}} = -1\,\mathrm{A}$ is shown. Hereby, fig. 6.24(a) shows the results for Bragg spectroscopy in beam splitter direction only, while fig. 6.24(b) shows time of flight measurements in y-direction and fig. 6.24(c) in beam splitter direction, each for ToF = 0 ms and for ToF = 29 ms. The third direction along the detection axis is not detectable at the moment.

The amplitude of the oscillation in horizontal y-direction is in the order of 5 kHz extracted from the Bragg spectroscopy or 50/70 µm in 29 ms time of flight which is definitely non-negligible for the systematic analysis. All interferometric measurements with the atom-chip gravimeter have been performed with an adjusted holding time τ_{trap}, such that both residual velocities are closest to their measured zero. The residual velocity in both directions which are measurable $v_{0,\mathrm{yz}}$ are thus estimated to be smaller than 0.5 mm/s. The residual horizontal motion in the non-detectable axis $v_{0,\mathrm{x}}$ also is expected to be smaller than 0.5 mm/s, because the trap frequency in this direction is much shallower than in the other two directions (see tab. 2.2).

Inertial phase shift terms and stability of the launch velocity

The residual initial velocities and jitters in the release positions are the second dominant systematic uncertainty where the use of a Bose-Einstein condensate promises to overcome the limitations of current sensors due to the ability to precisely measure the initial motion.

A Tailor expansion (see sec. 4.3.1) can be performed to obtain the analytical formulas for the higher-order phase shifts. The physical meaning of the next relevant contributions are given by the Coriolis effect, due to the rotation of the Earth and the gravity gradient along the trajectory of free-fall [138]. The phase shift contribution from the Coriolis effect due to the rotation of the Earth Ω_E is calculated depending on the horizontal release velocity $v_{0,\mathrm{xy}} < 500\mu\mathrm{m/s}$ using the Sagnac formula

$$\phi_{\Omega_\mathrm{E}} = 2\vec{\Omega}_\mathrm{E} \cdot (v_{0,\mathrm{xy}} \times \vec{k_\mathrm{eff}})T^2. \tag{6.23}$$

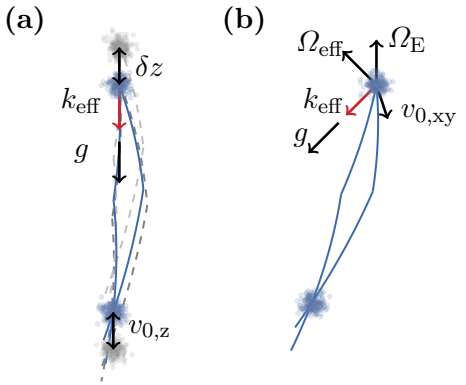

Fig. 6.25: The Coriolis force **(a)** and gravity gradients **(b)** cause a bias shift in the gravity measurement due to the uncertainty in initial velocity and position jitter of the atoms.

The corresponding uncertainty for the current parameters is $\Delta g/g = 1 \cdot 10^{-8}$ which already is a huge effect that needs to be mitigated. Gravity gradients couple in either via a jitter in initial position $\delta z < 5\,\mu\mathrm{m}$ or via a residual velocity $v_{0,\mathrm{z}} < 500\mu\mathrm{m/s}$ in the direction of gravity

$$\phi_{\mathrm{grad,z}} = k_\mathrm{eff} T_\mathrm{zz} \delta z T^2 \text{ and } \phi_{\mathrm{grad,v}} = k_\mathrm{eff} T_\mathrm{zz} v_{0,\mathrm{z}} T^3. \tag{6.24}$$

The arising uncertainties are due to the measured position jitter $\Delta g/g = 1.5 \cdot 10^{-9}$ and due to the residual velocity $\Delta g/g = 1.6 \cdot 10^{-10}$, so already comparably small with respect to the Coriolis effect. So far higher-order terms depending on the photon recoil [264] appear not be of relevant contribution. In all considered cases these contributions lie below $\Delta g/g < 1 \cdot 10^{-11}$. A special circumstance in the fountain geometry is, that the launch velocity $v_{0,\mathrm{z}}$ changes with the direction of the momentum kick $\pm k_\mathrm{eff}$ in the atom interferometer to not hit the chip. In a "k-flip" measurement a slight dependence on the initial velocity difference $v_\delta = 2n \cdot \hbar k/m$ remains.

These values represent thus no ultimate limit, because the initial motion of a condensate can be measured and the phase shift corrected to a much better degree than the assumed $500\mu\mathrm{m/s}$. This correction is the preferred option to the integration of an active Coriolis compensation by counter-rotating the reference plane with a tip-tilt stage and thereby compensating the Earth rotation [300, 301], because such a system is complicated to implement with the atom chip. To estimate the potential for a suppression or correction of the Coriolis effect, the stability of horizontal launch velocity $v_{0,\mathrm{y}}$ in the fountain geometry is analyzed. Because of its coherent nature, the launch does not influence the initial position jitter which therefore remains at $\delta z < 5\,\mu\mathrm{m}$. The stability of the launching velocity is measured from the jitter of the final position of the output ports via time-of-flight measurements. From the measurement with $T = 25\,\mathrm{ms}$ a jitter of $70\,\mu\mathrm{m/s}$ and a stability of $15\,\mu\mathrm{m/s}$ are extracted and displayed in fig. 6.26. These values are already sufficient to suppress the Coriolis effect below $1\,\mu\mathrm{Gal}$ even without further measures. To even advance this characterization, it is also possible to directly extract the position jitter as well as the motion of the condensate from each image and correct the phase shift terms per measurement. In that way only the resolution of the imaging system limits the correction.

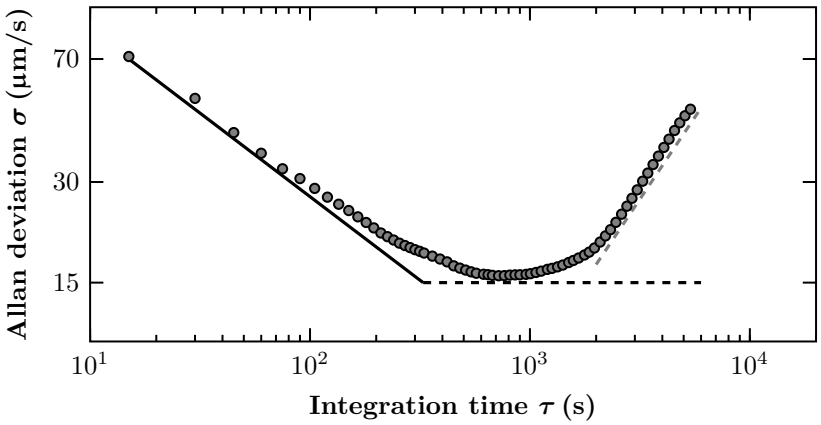

Figure 6.26: Stability of the horizontal launch velocity $v_{0,y}$ in the fountain extracted from the position of the output ports in the measurement with $T = 25\,\text{ms}$. The jitter of the launch velocity integrates down from 70 μm/s to 15 μm/s after roughly 10^3 s with a long term drift rate of 10 (nm/s)/s.

Self gravity effect due to the chip mount

Due to the relatively small distance between Bose-Einstein condensates and atom chip while performing interferometry the gravitational attraction of the atom chip itself becomes a relevant effect [302] as also observed in falling corner cube gravimeters [303]. Unlike free-space trapping and cooling in magnetic or dipole traps, the atom chip only has a distance of between 1 and 2 mm, when applying the first interferometry pulse in drop mode or even below 1 mm at the apex of the fountain. As depicted in fig. 6.27, not the chip substrate itself has the biggest mass contribution, but rather the copper mount where it is mounted on. To calculate the influence of self-gravity an estimation based on the CAD drawings depicted in fig. 6.27 is performed. The expected bias shift for the current mass distribution is at a level of $\Delta g/g = 1 \cdot 10^{-8}$ for the dropped Mach-Zehnder sequence but gets suppressed with larger T. The next generation chip mount has a factor of two less mass close to the atoms, which is beneficial to suppress this shift. Modeling the mass distribution to the 10% level [302] taking into account vacuum system, the ion getter pump and the supporting structure will allow to suppress the bias below 1 μGal.

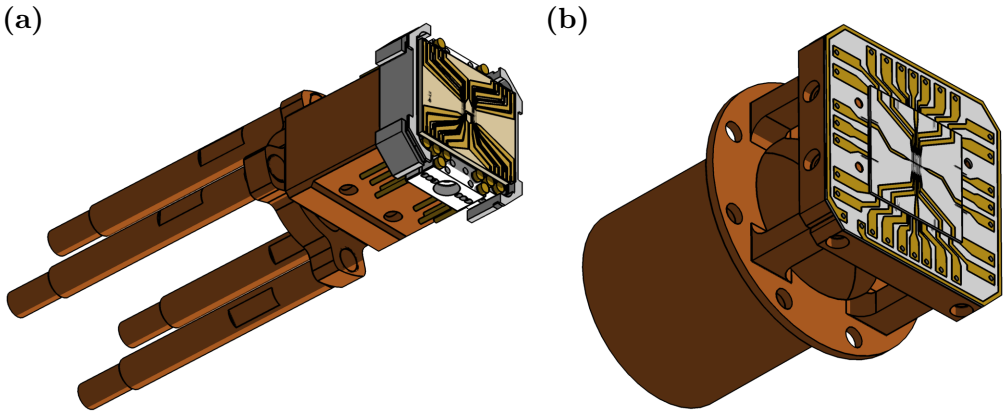

Figure 6.27: Drawing of the QUANTUS-1 atom-chip mount **(a)** compared to the mount used for the QG-1 experiment **(b)**, which has a factor of two less mass close to the atoms. The new design together with a modeling on the 10% level will be sufficient to reduce this shift below μGal

Light shift in atomic Bragg diffraction

In comparison to Raman diffraction the differential AC-Stark - or one-photon light shift - induced during Bragg diffraction is suppressed by at least three orders of magnitude due to the smaller relative laser frequencies $\omega_r + \omega_0 << \omega_{eg}$ defined in sec. 4.1.1. With the comparably large laser detuning of $\Delta = 100\,\mathrm{GHz}$ to the D_2 line the one-photon light shift gets negligible at all times. A second light shift results from two-photon coupling due to an off-resonant frequency pair in retro-reflective configuration, that was calculated numerically for Raman transitions before [304]. Recent work on the calculation of the two-photon light shift for Bragg diffraction performed in the group of W.P. Schleich in Ulm [152] came to the conclusion, that the two-photon light shift for Bragg diffraction for certain conditions can be even smaller compared to Raman diffraction.

For a Mach-Zehnder interferometer only the beam splitting and recombination pulses are affected by light shifts for first order calculations, the mirror pulse has no contribution due to its symmetry. Asymptotic treatment of the Bragg couplings taken from fig. 6.28 for large Doppler shift $\omega_0 \gg \omega_r$ and Gaussian-shaped pulses results in a bound for the light shift

$$\phi_{2\mathrm{ph}}^{(B)} \simeq \frac{\Omega_{\mathrm{eff}}}{4\omega_r}\left(\frac{\omega_r}{\omega_0}\right)^3 \approx 14\,\mu\mathrm{rad} < \phi_{2\mathrm{ph}}^{(R)} < \phi_{2\mathrm{ph,box}}^{(B)} \simeq \frac{\Omega_{\mathrm{eff}}}{4\omega_r}\frac{\omega_r}{\omega_0}, \tag{6.25}$$

which is smaller than the corresponding two-photon light shift for Raman beam splitters and Bragg beam splitters with box shaped pulses. For box shaped Bragg pulses the contribution $\phi_{2\mathrm{ph,box}}^{(B)} \simeq 2 \cdot \phi_{2\mathrm{ph}}^{(R)}$ would be two times larger than for Raman diffraction. As seen in eq. 6.25 the two-photon light shift is suppressed with larger Doppler shift ω_0. At the current status of the experiment, when the first beam splitter pulse is applied $\tau_{\mathrm{prep}} = 10.2\,\mathrm{ms}$ after release, this is corresponding to a Doppler detuning of $\omega_0 = 260\,\mathrm{kHz}$ and would result in an uncertainty of $\Delta g/g = 3.6 \cdot 10^{-9}$. But thanks to the favorable scaling behavior in third order for Gaussian-shaped pulses, already a Doppler detuning of $\omega_0 > 500\,\mathrm{kHz}$ - corresponding to a free-fall time before starting the interferometry of $\tau_{\mathrm{prep}} > 20\,\mathrm{ms}$ - leads to a suppression well below the µGal regime. One remark to be aware of is, that this asymptotic model only takes into account first-order contributions and for accuracies on the µGal level second order effects might not be negligible, which then would also affect the mirror pulse, not only splitting and recombination pulses [305].

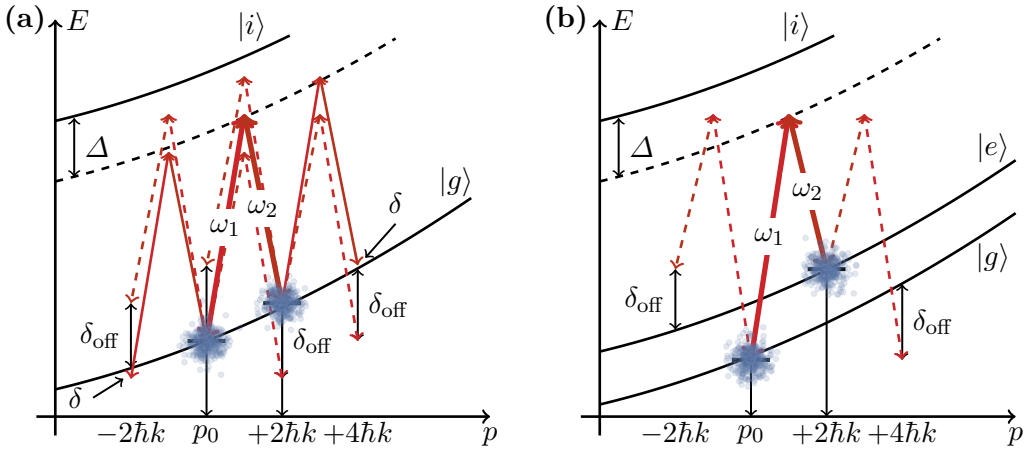

Figure 6.28: Schematic of the two parasitic couplings to other momentum states and the resulting three off-resonant couplings taken into account for the calculation of the two-photon light shift for first-order Bragg diffraction **(a)** compared to the simpler coupling scheme for Raman diffraction **(b)**.

Beam splitter alignment demands and miscellaneous effects

The knowledge of k_{eff} directly influences the accuracy of the measurement, since the value for gravity is deduced from the scaling factor, where k_{eff} enters. Three different contributions cause an insufficient knowledge or misalignment of the effective wave vector: the laser frequency, the horizontal alignment of the retro-reflector, and the precision of the retro-reflection. Additional noise contributions have been discussed in the literature, which are currently of minor relevance, are listed for completeness and need to be assessed in a future device. These effects are:

- The **laser frequency** of the beam splitter laser is determined by the detuning Δ relative to the Rubidium spectroscopy [172]. The D_2 line spectroscopy has previously been performed to a relative uncertainty of 10^{-11} [306] and a stability of a few hundred kHz is routinely achieved at the IQ [307]. In the experiment also the stability of locking electronics has to be considered, which is characterized to be typically on the same level. An uncertainty of only 100 kHz would be ideal to suppress the uncertainty well below µGal.
- In sec. 3.3 the procedure for the **horizontal alignment** of the atom chip has been introduced. For an accuracy below the precision of the measurement, the atom-chip surface needs to be aligned perpendicular to gravity to better than $\Theta = \arccos(1 - \Delta g/g)$. The precision of the alignment procedure depends on the path used to overlap incoming and reflected beam. For the current limited resolution a misalignment of below 6 mrad is sufficient, but in other experiments few percent of a mrad have been achieved [85, 262].
- The exact **retro-reflection** of the beam splitting light field can be adjusted by overlapping incoming and reflected beam and coupling the light back into the fiber to the distribution module. Using this procedure on a total laser traveling distance of $1 - 2$ m an adjustment of the parallelism of $k_1 \parallel k_2$ to better than 0.1 mrad is achieved [85, 262].
- The exact **phase shift calculation** for non-vanishing pulse durations [265–268] may lead to an uncertainty contribution. This can be eliminated using an appropriate measurement protocol by including alternating between the two mid-fringe positions with opposite slopes around the central fringe minimum and taking the difference between the signals.
- The larger **run-time delay** of the retro-reflected beam compared to the incident one can cause an enlarged laser phase noise due to the finite linewidth of the laser [308] which is also a problem in falling corner-cube gravimeters [309]. However, this effect is negligible due to the small distance of the atoms to the retro-reflector which is the chip in our set-up and the small linewidth of the fiber laser of < 1 kHz.
- Recently reported are influences on the interferometer due to laser frequency **chirping and symmetry limits** of the Mach-Zehnder interferometer [310, 311]. These effects are suppressed with the large laser detuning Δ compared to the given example by two orders of magnitude, but have to be re-calculated for a future device.
- The influence of **laser phase noise** is of major importance for Raman-type interferometers [10] and stable reference oscillators and wide bandwidth phase locks [312, 313] are mandatory. In the case of Bragg diffraction, the requirements are relaxed since a single RF source and AOM can be used for generating both laser frequencies. In the current setup, a robust and noise immune setup with a single AOM is chosen for generating the two laser frequencies which avoids uncommon noise due to effects on different paths.

6.4.2 Mitigation strategies for dominant uncertainties

To get a realistic estimate on the dominant uncertainties for a future experiment, the calculations are extrapolated using a source of the performance achieved in QUANTUS-2 - the direct successor of QUANTUS-1. This device reaches a state-of-the-art flux of 10^5 atoms per second [117] at a repetition rate of 1 Hz or higher fluxes at lower repetition rates. In the QUANTUS-1 experiment the fountain geometry already allows to extend the pulse separation time of the Mach-Zehnder interferometer to $T = 25\,\mathrm{ms}$ and the total time of flight to ToF = 97.6 ms on a baseline of only 7 mm. The technical noise of the Mach-Zehnder interferometer using delta-kick collimated ensembles and first-order Bragg beam splitters is still very close to the shot noise limit at a contrast of $C = 0.8$. With third-order Bragg diffraction still a contrast of $C = 0.72$ at slightly higher noise is obtained using the PCA-based evaluation. The total free-fall time for the extrapolated parameters is only slightly increased to ToF = 135 ms, given by the time of $\tau_{\mathrm{prep}} = 45\,\mathrm{ms}$ it takes the atoms to fall the distance of 1 cm. If the needed detection separation time stays at $\tau_{\mathrm{prep}} > 15\,\mathrm{ms}$, a maximum pulse separation time of $T = 35\,\mathrm{ms}$ remains, which combined with a fourth-order beam splitter leads to a shot-noise limited intrinsic sensitivity of $(\Delta g/g)/\sqrt{\mathrm{Hz}} = 5.3 \cdot 10^{-9}$ [156]. These parameters are summed up in tab. 6.8.

Param.	Current	Future
T	25 ms	35 ms
n	1 or 3	4
C	0.80	0.75
ToF	97.6 ms	135 ms
N	$8 \cdot 10^3$	10^5
T_{cyc}	15 s	1 s
$\Delta g/g$	$1.4 \cdot 10^{-7}$	$5.3 \cdot 10^{-9}$

Table 6.8: An extrapolated version pushes the fountain geometry to the limit on a 1 cm baseline using a future device which and is able to reach state-of-the-art performance.

The main drive for sensors to use Bose-Einstein condensate is reduced systematic uncertainties. From the estimations in sec. 6.4.1, the potential for reaching sub-μGal accuracies in a dedicated setup can be assessed and the most critical remaining contributions identified. Improvements on components have to be made in order to suppress bias shifts sufficiently. Table 6.9 summarizes the causes suspected to provide the largest contributions to the measurement uncertainty as well as mitigation strategies. If not stated otherwise the parameters from tab. 6.7 or tab. 6.8 apply.

- To reach the inferred sensitivity of $(\Delta g/g)/\sqrt{\mathrm{Hz}} = 5.3 \cdot 10^{-9}$ and a cycle time of roughly 1 s **improvements on the source and the detection system** have to be made. Hereby the flux of 10^5 atoms/s previously achieved in the QUANTUS-2 experiment is sufficient [117]. In addition the detection system needs to be able to detect the output ports **only limited by the shot noise** of 4.5 mrad at this atom number and $C = 0.7$, resulting from 90% beam splitter efficiency. The crucial part remains **suppressing the vibrational background noise**. A state-of-the-art vibration isolation would significantly improve the sensitivity, although maximum performance may only be reached at a more quiet site [314].
- The **mean field shift** can be relaxed by first lowering the atomic density via faster spreading of the wave packet during the 45 ms after release from the trap but before relaunch and then **stop them by delta-kick collimation** [98, 133]. For the final size of 300 μm at the first pulse, 10^5 atoms and 1% beam splitter stability phase shifts introduced by the mean field [97] can be sufficiently suppressed below μGal while expansion rates corresponding to nK temperatures are achievable which preserve the beam splitter fidelity.
- The fluctuations of the launch velocity, which cause a bias due to the **Coriolis effect or gravity gradients** [138], can be characterized to the required level and optimized by the tested release procedure. The scatter of 70 μm/s and the **stability of the launch velocity** of 15 μm/s extracted from the data in sec. 6.3.1 is sufficient to suppress this shift.

- The **surface quality of the atom chip** must be significantly improved for the next generation. This is crucial for higher-order Bragg diffraction and Bloch oscillations in order to preserve the **high efficiencies and contrasts** obtained for lower Bragg orders. A residual roughness of $\lambda/10$ would be on the order of a standard mirror and is assumed. For a beam of a diameter of $\oslash = 2\,\mathrm{cm}$ the phase shifts resulting from the **wave front curvature** are insignificant since Bose-Einstein condensates are smaller and expand slower compared to thermal clouds [88, 294]. Also the **point-source nature** [98, 100] of Bose-Einstein condensates may allow to characterize systematic errors arising from wave-front distortions.
- The **proximity of atoms close to the chip** leads to a bias phase shift due to its gravity [302]. A mass reduction of the chip mount by two combined with a **finite-element analysis** of the mass distribution of the chip mount which calculates the **self-gravity effect** with an accuracy at the ten-percent level is sufficient to reach the targeted level.
- Remarkably, compared to Raman diffraction, the influence of **light shifts** is reduced in Mach-Zehnder interferometers based on Bragg diffraction. Since the **two-photon light shift** effect scales [152] with the third power of the inverse of the atomic velocity, it is negligible for the parameters needed for the launch in the fountain geometry.
- As already discussed in sec. 6.4.1 the **magnetic shielding** factor can be greatly improved using a three instead of a one layer shield granting a residual gradient of below $10 \pm 3\,\mathrm{mG/m}$, which should be sufficient to suppress any residual bias [298].

Table 6.9: Estimates for the contributions to major systematic uncertainties in the atom-chip gravimeter using the fountain geometry. As a result the determination of local gravity with an in-accuracy below $\Delta g/g < 1 \cdot 10^{-9}$ in less than 100 s is compatible to the presented technique [156].

Contribution term	Mitigation strategy	Noise $(\Delta g/g)/\sqrt{\mathrm{Hz}}$	Bias $\Delta g/g$
Intrinsic sensitivity	Next generation source [117]	$5.3 \cdot 10^{-9}$	0
Mean field shift	Tailored expansion and DKC [98, 133]	$1.5 \cdot 10^{-10}$	$6.4 \cdot 10^{-11}$
Launch velocity	Scatter 70 µm/s, stability 15 µm/s [138]	$1.5 \cdot 10^{-12}$	$3.1 \cdot 10^{-13}$
Wave front quality	$\lambda/10$ chip-coating, $\oslash = 2$ cm beam [88]	$6.7 \cdot 10^{-10}$	$2.8 \cdot 10^{-10}$
Self gravity	Detailed modeling of chip mount [302]	$1.2 \cdot 10^{-12}$	$5 \cdot 10^{-10}$
Light-shifts	Suppressed in Bragg diffraction [152]	$1.4 \cdot 10^{-12}$	$1.4 \cdot 10^{-10}$
Magnetic fields	Three-layer magnetic shield [298]	$1 \cdot 10^{-10}$	$2.6 \cdot 10^{-10}$
Target estimation	Uncertainty after less than 100 s		$\approx 7.8 \cdot 10^{-10}$

CHAPTER 7

Novel interferometer geometries

Several novel atom interferometer geometries are developed in this chapter which additionally employ double Bragg diffraction in horizontal direction and take benefit of the narrow momentum widths of delta-kick collimated Bose-Einstein condensates.

Two geometries are implemented which each correlate two simultaneously operated Mach-Zehnder interferometers generated from a single Bose-Einstein condensate (sec. 7.1). Hereby, a Bragg or double Bragg diffraction pulse is applied to split the initial condensate into two sources with non-vanishing relative motion either in horizontal or vertical direction prior to the spanning of the Mach-Zehnder interferometer. The non-vanishing motions allows to individually address in the differential signal either rotations by spanning an enclosed area or to increase the dynamic range with different orders of the beam splitter. These dual interferometers show a large vibration noise immunity due to the rejection of common mode noise.

In addition, a novel method for symmetric scalable large momentum transfer is developed using the combination of double Bragg diffraction and Bloch oscillations in a dual-lattice (sec. 7.2). One holy grail of today's research in atom interferometry is the increase of wave packet separation by large momentum transfer to have an additional lever to improve the interferometer's scaling factor beside the pulse separation time T. For the detection of infrasound gravitational waves [315] the large momentum transfer is considered as one of the most relevant techniques, which leads to a maximum delocalization of the superposition of an atomic wave function [70]. The imprint of a larger momentum directly during the beam splitter with higher-order Bragg diffraction is limited by the available laser power. Further increase is either achieved by applying additional sequential pulses or Bloch oscillations in between the sequence of beam splitter pulses. Table 7.1 gives an overview of the previously performed experiments and the therein achieved momentum separation demonstrated in an atom interferometer. Hereby, an elegant method to surpass some systematic uncertainties is the use of symmetric beam splitting [77, 80]. With the novel method presented here, a momentum separation of $1008\,\hbar k$ in a single beam splitter and of $208\,\hbar k$ in a atom interferometer are shown.

Method	$\Delta n\,(\hbar k)$[Ref.]
Higher-order Bragg	$24\,\hbar k$ [67]
Sequential Bragg	$102\,\hbar k, 90\,\hbar k$ [68, 70]
Sequential Raman	$6\,\hbar k, 4\,\hbar k$ [16, 73]
Adiabatic Bragg	$10\,\hbar k$ [69]
Adiabatic Raman	$30\,\hbar k$ [74]
Double Bragg diff.	$8\,\hbar k$ [80]
Raman double-diff.	$8\,\hbar k$ [77], $4\,\hbar k$ [78]
Raman & Bloch osc.	$10\,\hbar k$ [75]
Bragg & Bloch osc.	$24\,\hbar k, 80\,\hbar k$ [71, 72]

Table 7.1: Comparison of different methods to realize large momentum transfer beam splitters.

7.1 Correlated atom interferometers

A differential measurement between two correlated atom interferometers is able to suppress inertial noise through common mode rejection [316]. This rejection is a key feature to operate atom interferometers beyond the noise level which exceeds its linear response [317] to be used in inertial sensing or in a dual atom interferometer [318, 319]. A major limitations connected to the previous approaches are the uncertainties of the two employed laser cooled sources [14, 16, 316].

Two different dual-interferometer geometries are presented here, which both exploit the correlation between two Mach-Zehnder interferometers. The sources for these interferometers are generated from a single Bose-Einstein condensate which is initial split by either Bragg or double Bragg diffraction causing a non-vanishing relative motion between the two sources. The initial pulse is either applied horizontally to perform a rotation measurement (sec. 7.1.1) or vertically to form two gravimeters with different scaling factors to enhance the dynamic range of the acceleration measurement (sec. 7.1.2). These geometries are of interest for future applications in particular for multi-axis sensing [320] or in extremely noisy environments [289].

7.1.1 Vibrational noise suppressed rotation measurement

With an foregoing double Bragg diffraction pulse it is possible to split the initial ensemble into two orthogonal halves that travel with $v_{\mathrm{split}} = 4\hbar k/m$ momentum apart from each other. Applying a Mach-Zehnder sequence with the original beam splitter oriented along gravity and $T = 5\,\mathrm{ms}$ now results in a sequence with two gravimeters depicted in fig. 7.1(a). The two atom

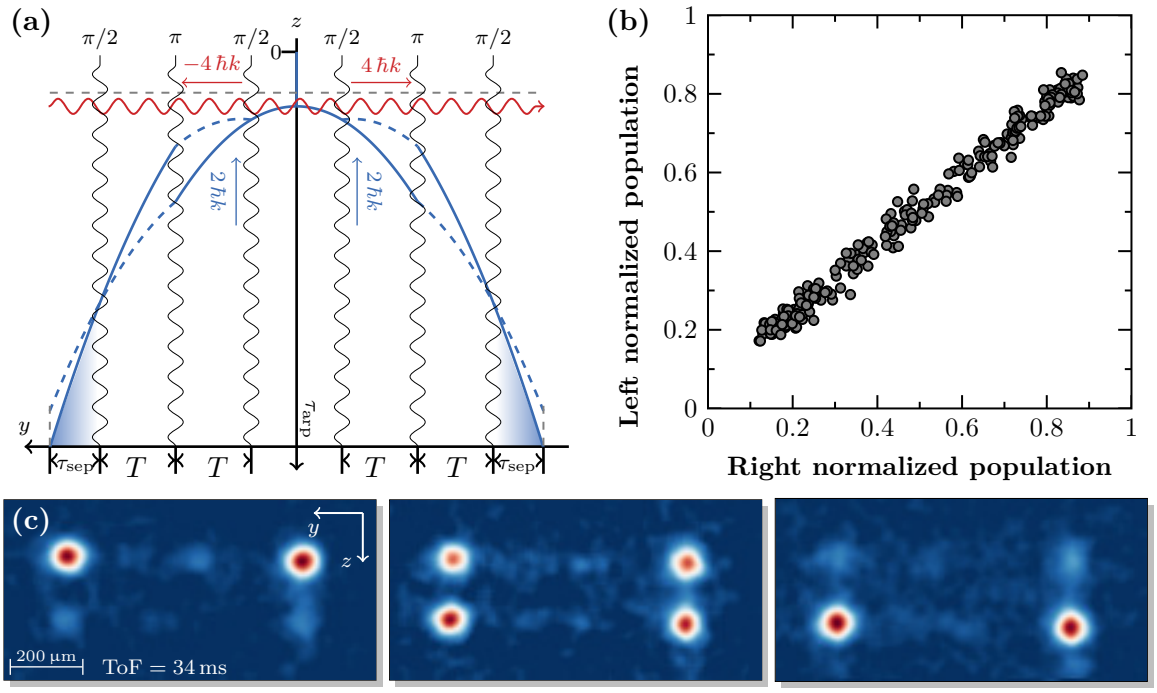

Figure 7.1: With an initial double Bragg diffraction pulse the ensemble is split into two parts with a relative motion of $v_{\mathrm{split}} = 4\hbar k/m$. A Mach-Zehnder pulse sequence with $T = 5\,\mathrm{ms}$ forms two correlated interferometers **(a)**. The signals of the two correlated interferometers plotted against each other form an ellipse plot **(b)**. Three exemplary density plots, with varying population in the output ports, demonstrate the high correlation between the interferometers **(c)**. A few data points are taken out because of failure shots. The residual noise is 25 mrad, given by the width of the ellipse.

interferometers in this scheme are highly correlated since they are falling along gravity altogether and are interrogated by a common light field.

The measurement of rotations with an atom interferometer relies on the spanned area A, which is enclosed inside the interferometer geometry. This area A is spanned in this case, since the atoms have now a non-vanishing velocity v_{split} perpendicular to the axis of the beam splitting light field. Therefore, after eq. 4.60 a differential Sagnac phase between both interferometers is induced by the Earth's rotation rate

$$\Delta\phi_{\Omega_{\mathrm{E}}} = 2k_{\mathrm{eff}}(\Omega_{\mathrm{E}}\cos\zeta v_{\mathrm{split}})T^2 = 0.83\,\mathrm{mrad}, \tag{7.1}$$

with $\zeta = 53.1°$ the latitude in Bremen and an opposite velocity of the two ensembles of v_{split} by the recoil of the double Bragg diffraction.

The density plots and an ellipse plot of the output ports of both interferometers plotted against each other is shown in fig. 7.1(b,c). To fill the complete ellipse independently from the amount of background noise the relative laser phase $\Delta\phi$ is scanned. This method allows a separation of these parts of the interferometer's phase shift, that are linear in gravity from other quantities of inertia, similar to [99]. The phase shift due to gravity drops out of the differential signal in the ellipse plot [321, 322]. A signal including gravity can still be measured by taking the sum of both upper and lower output ports and depicting the fringe pattern, but at the original vibrational noise level. The ellipse plot shows a differential noise between the two interferometers of about $\sigma_{\Delta\phi} = 25\,\mathrm{mrad}$, given by the width of the ellipse and resulting in a sensitivity of $3.4 \cdot 10^{-3}\,\mathrm{rad/s}$ to rotations. This noise is enlarged compared to the fringe scan because of a reduced atom number due to the distribution onto four output ports instead of two. Plotting the two output signals results in a line, indicating that the atom interferometers are in phase.

While the estimated sensitivity is too small to measure the rotation of the Earth in the current setup, anyhow this scheme is in general an interesting topology to measure rotations in a differential configuration utilizing only a single condensate. Until now most high precision atomic gyroscopes needed the simultaneous operation of two atomic source systems to suppress vibrational noise [14, 16, 316]. To reach a sensitivity able to resolve the Earth's rotation rate the scaling factor would have to be increased by a few orders of magnitude, by either enlarging the pulse separation time T, the momentum transfer k_{eff} or the initial splitting of v_{split}. The relative drift, however, has in general the disadvantage that the light field increase in size with drift time and velocity, similar to [14] and thus requires a large amount of laser power.

7.1.2 Increased dynamic range by multi-sensitivity

Synchronous generation of two Mach-Zehnder interferometers may also be employed to improve the overall dynamic range, which is for an atom interferometer limited by the need to stay on one fringe. This can be achieved with two Mach-Zehnder interferometers of different scaling factors and hence different sensitivities. While the first operates as highly sensitive probe for accelerations, the second is only needed for fringe identification. The different scaling factors are realized by interrogating both interferometers with individual beam splitter pulses of different Bragg order n, such that one interferometer is Δn more sensitive. The sequence is schematically depicted in fig. 7.2(a). The splitting of $v_{\mathrm{split}} = 10\hbar k$ is achieved by a sequence of a third-order Bragg $\frac{\pi}{2}$-pulse, followed by a second-order π-pulse. The resulting difference in Doppler shift of 150 kHz is sufficient to interrogate each ensemble independently by a sequence of beam splitter pulses. This is a slightly different scheme as in ref. [323] for example, where instead two noise conjugate Ramsey-Bordé interferometers are used to read out a differential signal.

For a demonstration of the correlation, both interferometers have a pulse separation time of $T = 5\,\mathrm{ms}$, but while the first interferometer is formed by a first-oder Bragg diffraction, the second interferometer operates with a second-order Bragg diffraction and is thereby a factor of $\Delta n = 2$ more sensitive to vibrational noise. As in the determination of gravity, the induced phase shift by vibrational noise in the first interferometer is still below π. In the example, which is depicted in fig. 7.2(b), the phase of the first interferometer is adjusted to mid-fringe position, so that it is always on the slope of a fringe. Only in this case, each measured phase is explicitly defined by the differential population at the output ports. To simulate a complete loss of phase information, the more sensitive interferometer is adjusted to top-fringe, where each phase leads to an ambiguity between the left and right slope. Due to the correlation of both interferometers, the phase of the second interferometer can be reconstructed by the known phase of the first one

$$\Delta\phi_{\mathrm{AI2}} = \Delta n \cdot \Delta\phi_{\mathrm{AI1}} + \phi_{\mathrm{AI2-AI1}} \tag{7.2}$$

with an offset phase $\phi_{\mathrm{AI2-AI1}}$ which is used as a free parameter to fit the correlation to the lowest residual. The residual noise after correlation is again on the order of $\sigma_{\Delta\phi} = 25\,\mathrm{mrad}$, which would reduce the sensitivities of both interferometers by roughly a factor of two compared to a single Mach-Zehnder interferometer without a second one. This correlation is presumingly limited because the pulses are not applied at the same time, but rather subsequently.

This technique would allow to extract the phase of atom interferometers in environments, where the acceleration signal dynamically changes. To enhance the difference in scaling factor between the two and therefore the overall sensitivity to accelerations the beam splitter order needs to be increased. A difference in T, that would also lead to a bigger difference in scaling, is in contrast unwanted, because the amount of correlation decreases, if both interferometers do not always measure simultaneously. Indeed, the pulse separation time T can be adjusted in a way, such that the less sensitive interferometer stays on a single fringe for any given noise level.

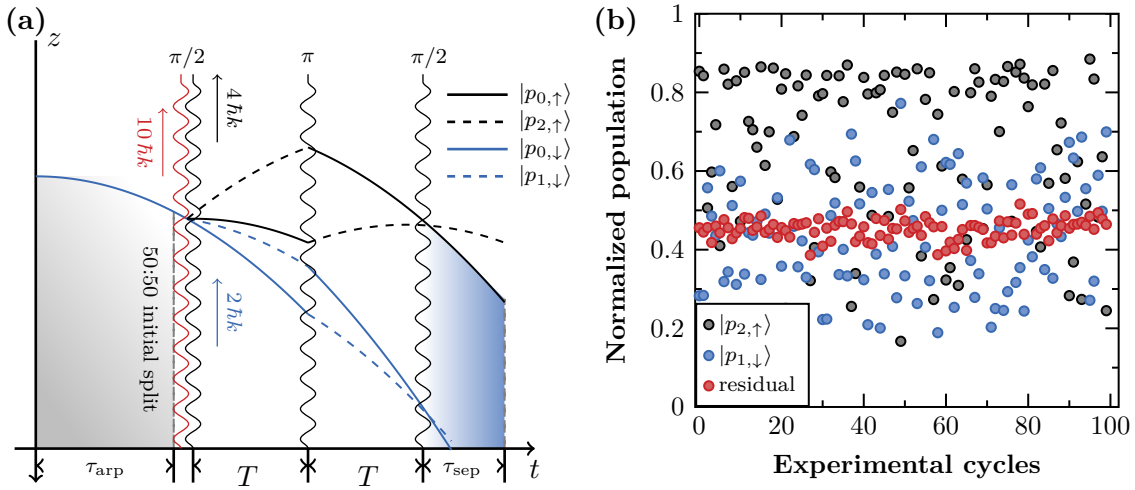

Figure 7.2: Correlation measurement between two atom interferometers with different scaling factors. After initial splitting to a relative velocity of $v_{\mathrm{split}} = 10\hbar k/m$ in vertical direction, two Mach-Zehnder interferometers are spanned by individual first- or second-order Bragg beam splitters and the same pulse separation time of $T = 5\,\mathrm{ms}$ **(a)**. The less sensitive interferometer (—) is adjusted to mid-fringe position and is used to correct the phase of the more sensitive atom interferometer (—). The residual noise (—) after correlation is in the order of 25 mrad **(b)**.

7.2 Symmetric scalable large momentum transfer

A new interferometer geometry using large momentum transfer beam splitters is introduced here, which combines double Bragg diffraction with adiabatic acceleration and deceleration by Bloch oscillations in a dual-lattice. The interferometer geometry schematically depicted in fig. 7.3 is an extension of the double Bragg interferometer published in ref. [80]. The interferometer comprises the following steps:

- **Generate a superposition** of two wave packets with sequential first-order double Bragg diffraction
- **Counter-accelerate** the wave packets with a retro-reflected optical lattice to large momentum separation
- **Study the coherence** of the process by obtaining oscillating populations at the output ports of an interferometer with a configuration similar to ref. [80].

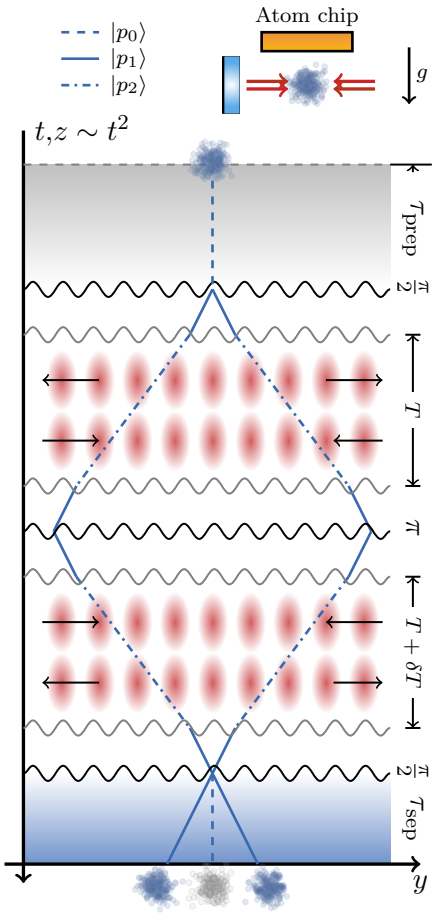

Fig. 7.3: Experimental sequence of the interferometer with large momentum transfer. Two accelerations and decelerations by Bloch oscillations (=) are integrated into a double Bragg interferometer (=) [80].

The advantage of this method is, that the symmetric nature of double Bragg diffraction is also exploited for the Bloch oscillations, which will intrinsically double the momentum transfer and keep the complete interferometer highly symmetric. While the efficiency to drive either higher-order or sequential double Bragg diffraction is limited and prohibits to increase the momentum transfer further and further, Bloch oscillations, in contrast, show so far the best scalability to increase the momentum transfer at high efficiency. Due to this advantageous scaling behavior a so far unprecedented momentum transfer can be achieved with this method.

In the following, experiments with this novel type of interferometer are presented which study the scaling behavior of the Bloch oscillations in the dual-lattice with respect to the theoretical predictions for Landau-Zener in sec. 4.2.3 and the coherence by the observation of oscillations at the output ports of an atom interferometer. In previous experiments where Bloch oscillations have been used to increase the momentum transfer [71, 72, 75], the Bloch oscillations have led to dephasing causing a loss of observable interference. Although the scaling behavior of the Bloch oscillations in the dual lattice is beneficial, this loss of coherence is also observed in the experiments and the limits on the momentum transfer are studied.

The efficiency to drive Bloch oscillations is limited by the available acceleration time τ_{acc}. The time for the horizontal beam splitter underlies the constrains set by the size of the beam splitting light field and the detection volume because the atoms are falling with gravity. Due to this fact the lattice acceleration will consume almost the complete pulse separation time T to maintain the largest possible efficiency. In this extreme case, this drastically changes the scaling behavior and sensitivity function of the atom interferometer depending on T and k_{eff} as in ref. [143].

7.2.1 Scaling behavior of the momentum transfer

The scaling behavior of the momentum transfer in the dual lattice with respect to the theory of a single lattice is investigated. Figure 7.4(a) summarizes the losses observed during double Bragg diffraction and shows that sequential transitions yield significantly lower losses compared to direct higher orders to increase the initial splitting. Even though the splitting of $4\,\hbar k$ due to first-order double Bragg diffraction is twice the separation as the $2\,\hbar k$ for first-order Raman diffraction as in refs. [229, 256], the influence of the non-resonant lattices cannot be ignored. Figure 7.4(b,c,d) show the Landau-Zener losses which occur due to the respective off-resonant lattice for a single Bloch oscillation which transfers $2\,\hbar k$ in each direction starting from splittings of $4\,\hbar k$, $8\,\hbar k$ and $12\,\hbar k$. The Bloch oscillation is performed in acceleration times in the range of $\tau_{\mathrm{acc}} = 52 - 800\,\mu\mathrm{s}$. Compared to the theoretical curves in fig. 4.14 the measured curves show the expected behavior but no sufficient quantitative agreement could be obtained with the simple model. The quantitative results need to be improved with the help of a better model as in ref. [275]. Anyway, these losses get suppressed fast with larger separations and no losses are observed for $12\,\hbar k$. For the beam splitter, a trade-off has to be made between the losses due additional double Bragg diffraction pulses and the ability to accelerate fast but nearly lossless.

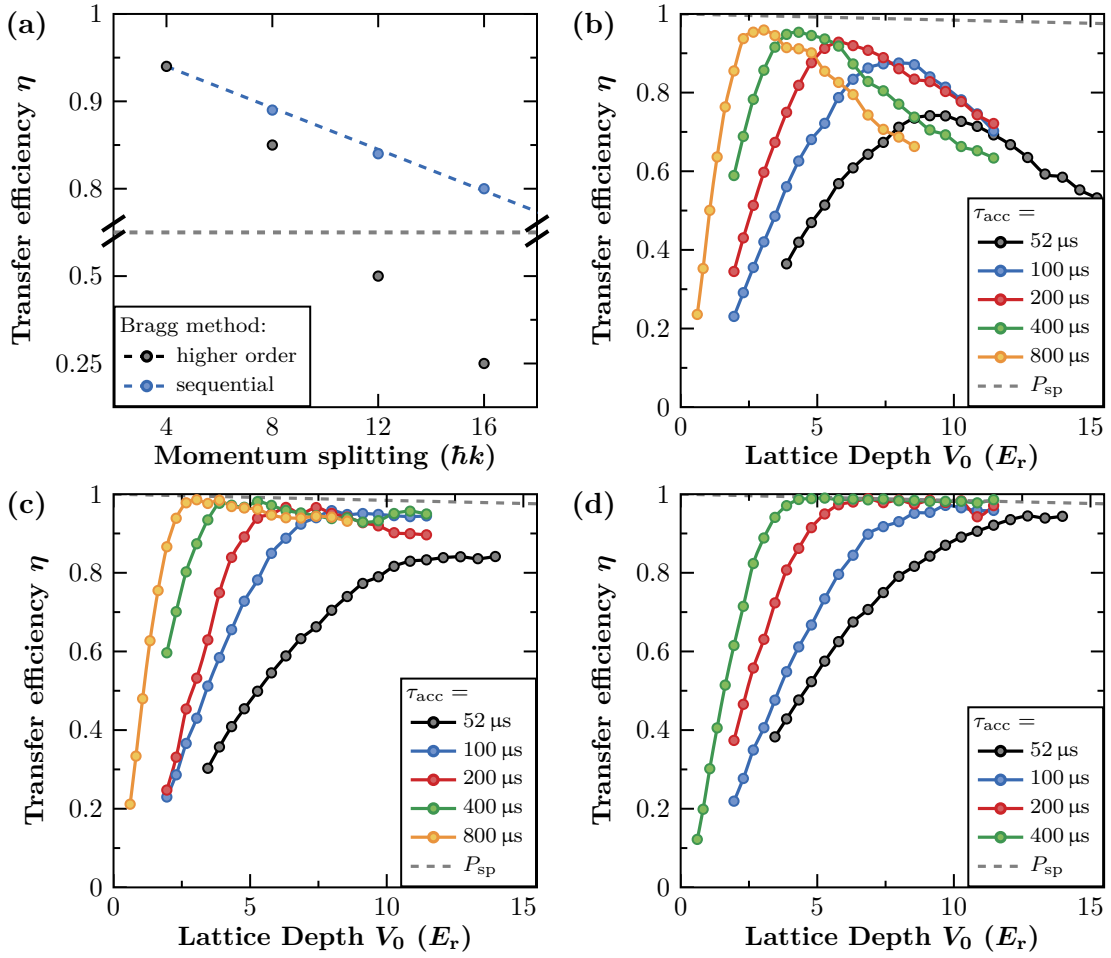

Figure 7.4: Losses during higher-order and sequential double Bragg diffraction **(a)**. Landau-Zener losses occurring during a single Bloch oscillation which transfers $2\,\hbar k$ in each direction measured for different lattice acceleration times τ_{acc} and splittings of $4\,\hbar k$ **(b)**, $8\,\hbar k$ **(c)** and $12\,\hbar k$ **(d)**.

To study the scalability, a first-order sequential transition is sufficient to accelerate reasonably fast while only 11% of the atoms are lost during initial splitting. The atoms are then loaded into the dual lattice at $\delta_{\mathrm{ini}} = 45\,\mathrm{kHz}$, each wave packet into the fundamental band of the respective lattice with less detuning. In $\tau_{\mathrm{acc}} = 1\,\mathrm{ms}$ the dual lattice is accelerated with a frequency ramp to $\delta_{\mathrm{end}} = 45 + n \cdot \omega_{\mathrm{r}}/2\pi$ and speeds up the wave packets with the momentum transferred from n photon pairs in opposite directions. Figure 7.5 shows density plots for increasing transfer of photon pairs during the acceleration in $\tau_{\mathrm{acc}} = 1\,\mathrm{ms}$ for up to $208\,\hbar k$ (always including the initial $8\,\hbar k$) as well as a transfer of $808\,\hbar k$ and $1008\,\hbar k$ in $\tau_{\mathrm{acc}} = 6\,\mathrm{ms}$. Starting from $128\,\hbar k$ the left half of the superposition has already left the detection region. The efficiencies of the momentum transfer for a smaller number of Bloch oscillations is close to unity $\eta \sim 1$. For an increasing number of Bloch oscillations the efficiency decreases slightly due to Landau-Zener losses in the off-resonant lattices. The total efficiency including initial losses for $208\,\hbar k$ is still above $\eta > 0.7$. The acceleration time of $\tau_{\mathrm{acc}} = 1\,\mathrm{ms}$ was chosen, because for a complete interferometer sequence enough time for four of these sequences has to be provided in addition to the pulses for the double Bragg interferometer and the separation time τ_{sep}. Therefore, it is not possible to close an interferometer with more than separation of $208\,\hbar k$ for the current experimental parameters.

Two beam splitters where Bloch oscillations are driven in a larger time of $\tau_{\mathrm{acc}} = 4\,\mathrm{ms}$ realize a separation of $808\,\hbar k$ and $1008\,\hbar k$ to demonstrate the scalability of the chosen method. For these beam splitters an efficiency of $\eta > 0.4$ for $808\,\hbar k$ and, respectively, an efficiency of $\eta > 0.25$ for $1008\,\hbar k$ is estimated. These efficiencies are not determined reliably, because the large velocity blurs out the condensates during the detection pulse. Increased Landau-Zener losses are observed due to the limited acceleration time and in particular for $1008\,\hbar k$ the diffracted part is close to the end of the detection region. Both parts of the superposition could only be observed, if they would be brought together first. The limit set on the momentum transfer is purely due to the available time τ_{acc} for the acceleration, there is no fundamental limit reached yet.

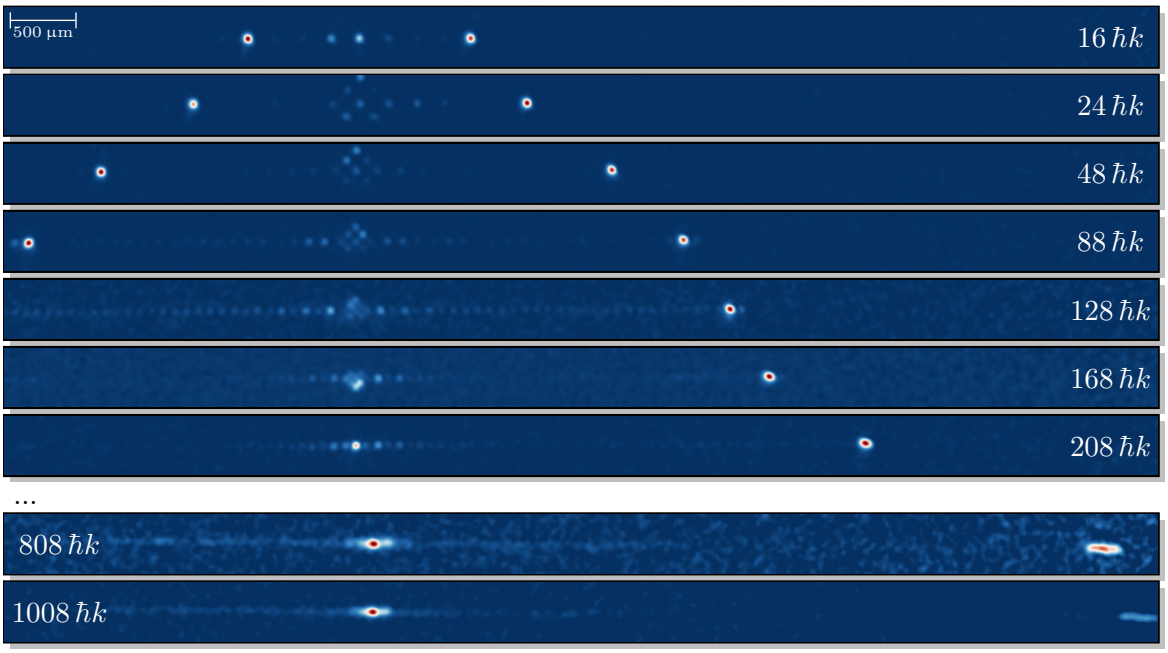

Figure 7.5: Density plots of large momentum transfer beam splitter with increasing differential separation. The initial splitting in all cases is $8\,\hbar k$ realized with sequential first-order double Bragg diffraction. Up to $208\,\hbar k$ the acceleration time is $\tau_{\mathrm{acc}} = 1\,\mathrm{ms}$, but 4 ms for the two largest separations.

7.2.2 Doppler selective removal of atoms

With double Bragg diffraction, all losses during the initial splitting pulse and the sequential transitions remain at the $0, \pm 2\hbar k$ states and are mixed into the output ports with the final recombination pulse. A limited beam splitter efficiency η does not only contribute to an increased shot noise due to a smaller atom number, but directly reduces the interferometric contrast and causes systematic uncertainties [281]. If these atoms are removed, the contrast can be directly enhanced and it allows to still observe interferometry at smaller atom numbers.

In the case of an interferometer using Raman double diffraction [77] or the SCI-scheme [16] the remaining atoms in the zero momentum state can be blown away with a simple resonant light field, due to the intrinsic internal state change during a $\frac{\pi}{2}$-pulse. This allows for independent addressing of only spurious atoms after the initial splitting and before the final recombination pulse. A similar individual addressing for a superposition in momentum states is only possible with the Doppler shift. The challenge is that the Doppler shift is only non-degenerate in the direction of the beam splitter while an additional shift along this direction is not helpful. So a diffraction under an angle is requested using the projection to the Doppler shift to individually address momentum states but also to have lateral deflection.

Instead of an additional beam pair in horizontal and vertical direction a single frequency component is used. The configuration is depicted in fig. 7.6(a) and a box-shaped pulse with $\Delta\nu_{\mathrm{hor}} = 11\,\mathrm{kHz}$ and $\Delta\nu_{\mathrm{ver}} = 225\,\mathrm{kHz}$ applied for $\tau = 300\,\mu\mathrm{s}$ yields an efficiency of $\eta > 0.9$ such that spurious orders are suppressed by at least an order of magnitude without disturbing the superposition. Density plots of the residuals after blow away compared to the losses during the initial double Bragg diffraction are depicted in fig. 7.6(b).

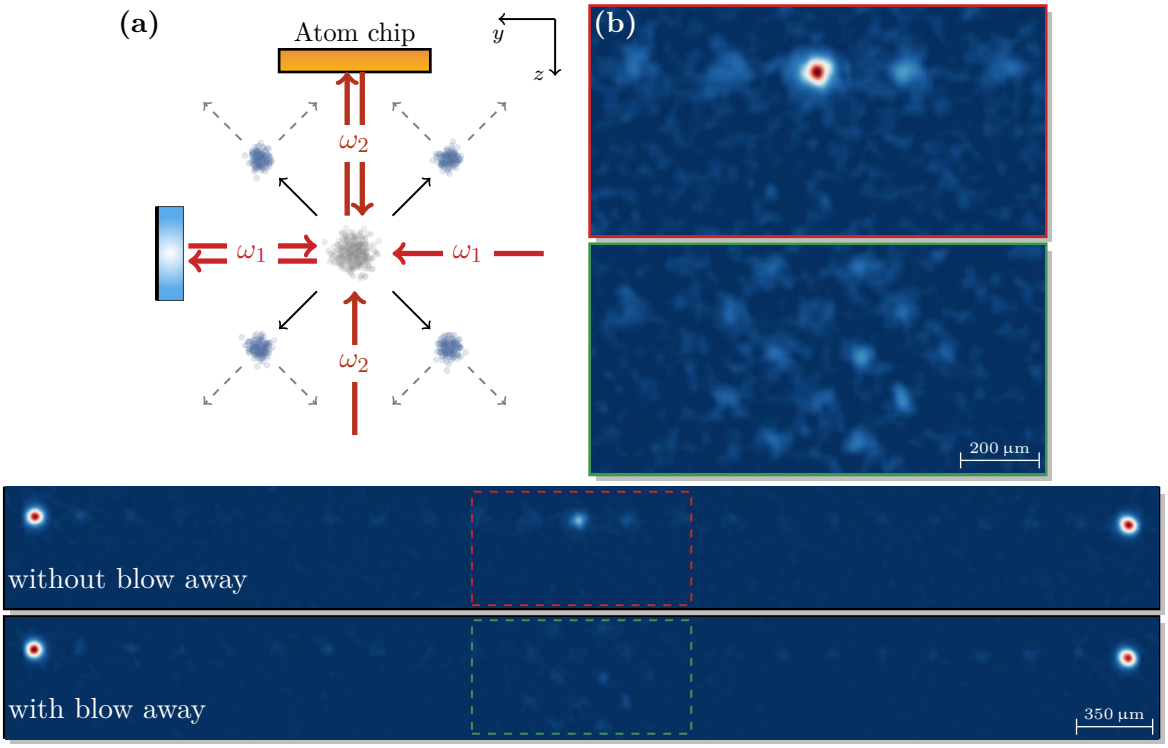

Figure 7.6: Coupling scheme for the Doppler selective blow away of spurious atoms **(a)**. The diagonal coupling provides individual addressing of momentum states and lateral deflection without disturbing the superposition. Spurious orders can be suppressed by at least an order of magnitude **(b)**.

7.2.3 Coherence study with contrast envelopes

To study the coherence of the developed beam splitter an interferometer geometry is spanned, which is essentially the double Bragg interferometer introduced in ref. [80], including each an acceleration and deceleration by Bloch oscillations two times. The resulting sequence in total consisting of seven double Bragg pulse and four lattice accelerations has been depicted already in fig. 7.3. However, the blow away, which is not depicted in fig. 7.3, is applied after the first acceleration. Due to the complexity of this sequence the atom number which is plotted in fig. 7.7(a) for an interferometer with $208\,\hbar k$ together with the efficiency of each step, is drastically reduced compared to only a single beam splitter. Especially, the double Bragg π-pulse on its own has only an efficiency of $\eta = 0.7$ such that in total less than 30% of the initial atoms are observed in the output ports. The remaining fraction of atoms is higher for smaller momentum separation because there are smaller losses during the acceleration and deceleration.

As in the case of the fountain gravimeter, due to the large sensitivity, specifically to any kind of vibrations, the population at the output ports is fluctuating statistically all the time. Instead of using a histogram analysis, a scan of the mismatch δT before the last deceleration sequence gives rise to a characteristic contrast envelope with a width $\sigma_{\delta T}$ which is schematically depicted in fig. 7.7(b). For this method, the evidence that there are actually coherent oscillations observed instead of technical noise is expressed by the difference in normalized fluctuations $2\sqrt{2}\sigma_{|p_1\rangle}$ between open and closed interferometers [70]. With this method even for a small amount of taken data points the coherence of the beam splitting process is proven.

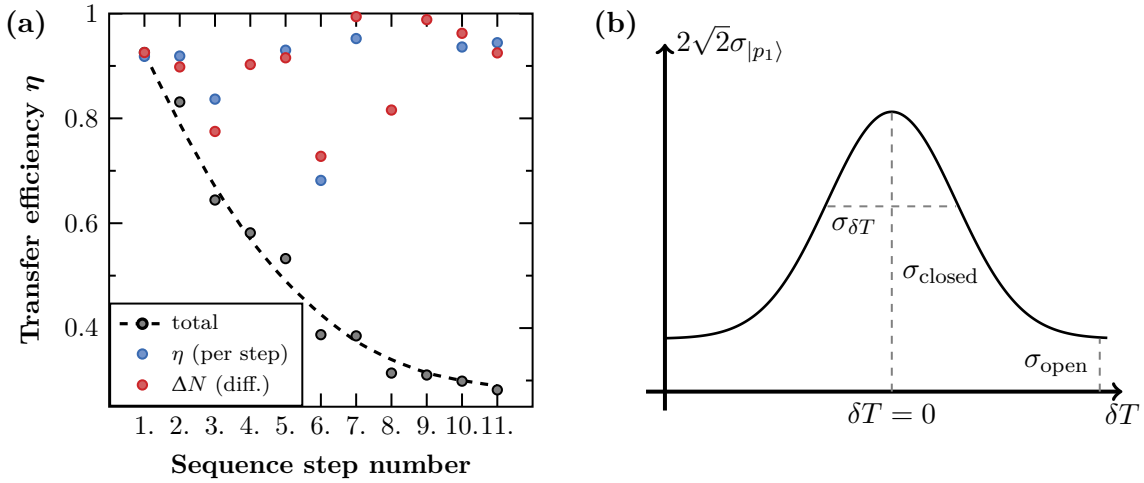

Figure 7.7: Efficiency per step and total atom number for the example of the interferometer with $208\,\hbar k$ **(a)**. For interferometer with smaller momentum transfer, the efficiency of the acceleration and deceleration is increased and the total atom number is accordingly higher. Coherence is proven with the contrast envelope of the fluctuations $2\sqrt{2}\sigma_{|p_1\rangle}$ in the output ports depending on the mismatch δT **(b)**.

The contrast envelopes are taken for separations between $16\,\hbar k$ and $208\,\hbar k$. Exemplary density plots of closed interferometers are depicted in fig. 7.8 showing in all cases almost equal losses from the double Bragg diffraction around the central output ports, but significantly increased losses during the lattice acceleration for separations of $88\,\hbar k$ or larger. Up to forty repetitions of the scans are taken requiring in total around 450 measurements for each contrast envelope, which consumes roughly two hours. During this time, the signal is required to be stable in amplitude and offset, otherwise the determination of the contrast envelope is overlaid with drifts. An accessible measure that indicates the stability of the system is the atom number stability in

the output ports. The atom number shows oscillating behavior on the 30%-50%-level, depending on the measurement. This drift in atom number results from a drift of the laser output power, which is drifting on the 10% level mostly influencing the double Bragg splitting ratio. To be less susceptible to these drifts δT is increased between each cycle, which are then repeated and not first taking a number of measurements with fixed δT and changing it afterwards.

Figure 7.8: Exemplary density plots of closed interferometer output ports. The losses due to the initial double Bragg diffraction are visible in all cases almost equally around the output ports, but significantly increased losses can be observed for the lattice acceleration with separations of $\geq 88\,\hbar k$.

The obtained contrast envelopes from the measurements are depicted in fig. 7.9(a). Because this plot with the large number of curves is complicated to read, the essential parameters extracted from the fitted Gaussian envelopes are plotted in two additional figures. In fig. 7.9(b) the values for the fluctuations $2\sqrt{2}\sigma_{|p_1\rangle}$ measured in open (extracted from the background plateau) and closed interferometers (extracted from the top of the curve) as well as their difference are depicted. The fluctuations for open interferometers are all between $2\sqrt{2}\sigma_{|p_1\rangle} = 0.05 - 0.1$ and only slightly increase by trend with larger separation due to the reduction in atom number. The fluctuations for closed interferometers, which are a measure of the oscillating signal, decrease rather rapidly and stay for separations $\geq 48\,\hbar k$ between $0.14 - 0.2$ such that the difference between both levels is by trend decreasing and reaches zero at a separation around $300\,\hbar k$ if the technical noise level is not reduced. However, transferring $300\,\hbar k$ is not possible in only 1 ms of acceleration time.

In ref. [70] the interferometric contrast C is defined purely as the fluctuations for the closed interferometer. Only for a stable offset the closed fluctuations would directly give rise to the contrast [324]. For the presented results a fair estimation is between the closed fluctuations and the difference of closed and open fluctuations. Thus, the difference represents a minimum bound for the contrast and even for $208\,\hbar k$ the peak is still significantly visible compared to the background noise. The second additional graph in fig. 7.9(c) shows the width $\sigma_{\delta T}$ and the center position of the contrast envelopes. The width of the curve $\sigma_{\delta T}$ is a measure of the "coherence length" in which the signal of the atom interferometer decays due to an insufficient wave packet overlap. As in ref. [70] this width decreases with larger separation as $\sigma_{\delta T} = 1/(nk\sigma_v)$ anti-proportional to the expansion rate σ_v and the resolution of 4 µs in δT limits the determination of the contrast envelope to separations below $500\,\hbar k$ at the current σ_v. The jitter in center position can by now only be explained by the drift in atom number at the output ports leading to asymmetries in the implementation of the geometry. The largest demonstrated separation

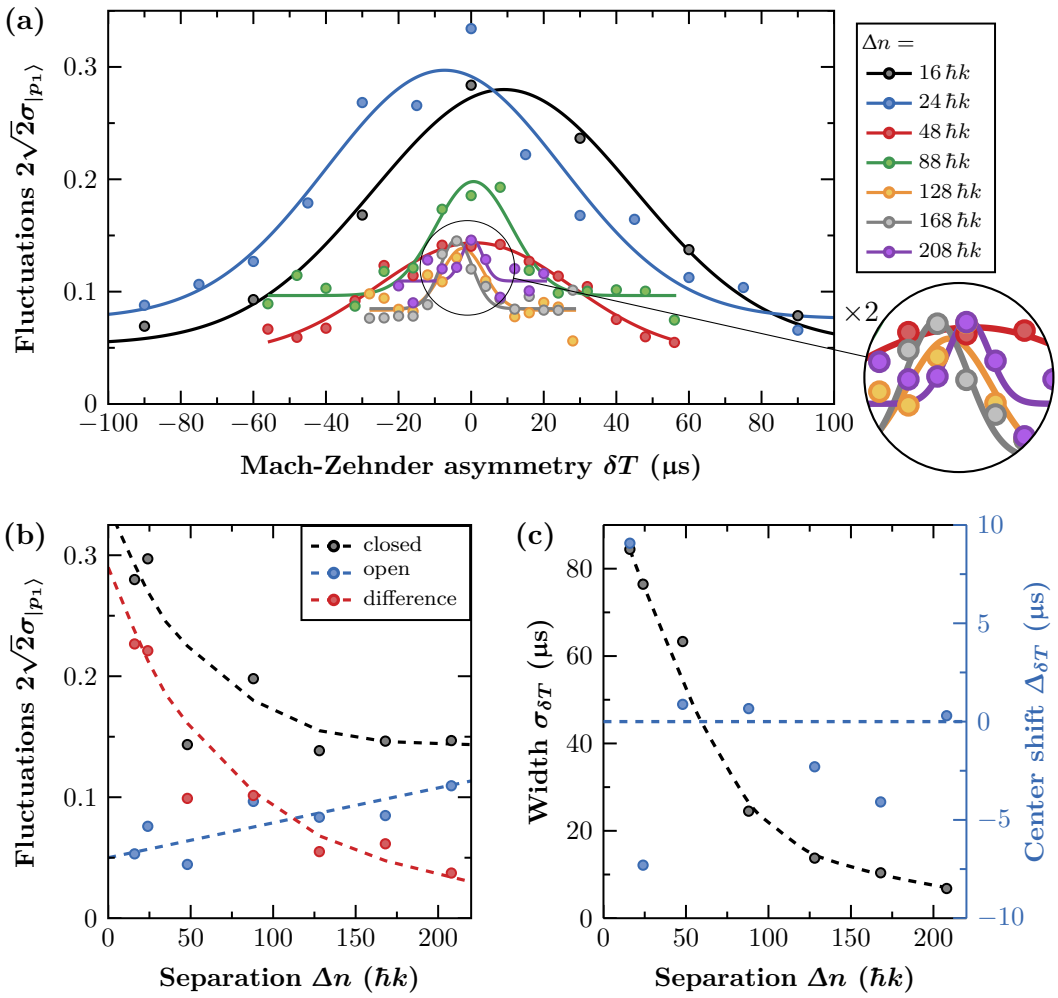

Figure 7.9: Contrast envelopes for interferometers using large momentum transfer **(a)**. Even for the largest separation of 208 $\hbar k$ coherent oscillations are still observed, which is twice the largest separation in an atom interferometer previously demonstrated. Comparison of the fluctuations $2\sqrt{2}\sigma_{|p_1\rangle}$ for closed and open interferometers extracted from the contrast envelopes and their difference **(b)**. A jitter in the center position of ±7µs and an exponential decay of the width σ is observed **(c)**.

of 208 $\hbar k$ during this demonstration represents more than twice the separation inside an atom interferometer compared to all that has been to the best knowledge reported previously.

The sensitivity of an interferometer with such large momentum transfer is too high to directly measure inertial quantities, besides in a very quite environment or in a dual atom interferometer with a differential measurement. Nevertheless, with the contrast envelopes the coherence of the beam splitter and the evolution of the contrast with increasing separation is studied. At the current status, the drop in contrast and the decreased atom number in the output ports set a limit to the achievable separation. The efficiency of the beam splitter itself is at the current status completely limited by technical means. The technical noise level may be reduced in the future with improvements in the passive laser power stability or by an active stabilization.

Different aspects need to be investigated in the future to better understand this new beam splitter and to find possible applications:

- The **Landau-Zener losses** observed for the beam splitter are not fully agreeing to the calculation taking into account just two Bloch bands. A proper simulation of losses using a 1D-reduced Gross-Pitaevskii model shows reasonable agreement for Bloch oscillations in a single lattice in ref. [275]. Improvements on the experimental calibration and the inclusion of the second lattice seems promising to obtain quantitative agreement to the experiment. With such a model predictions on the scalability of the method can be achieved.
- So far, every frequency ramp to accelerate the lattices was only a single linear chirp. From the Landau-Zener losses it is expected, that the largest losses occur, when the detuning of the off-resonant lattice is still small. With this knowledge and based on the simulations an **optimized acceleration sequence** may be found with slow acceleration first and then accelerating the frequency chirp to transfer the momentum in less time. It would be favorable to optimize not only the lattice acceleration, but also the efficiency of **double Bragg diffraction**, especially the π-pulse.
- Mechanisms leading to the **reduction of contrast** due to dephasing processes are not estimated by now. For example diffraction on the chip edge could cause similar spatial laser power inhomogeneities as observed in ref. [70] or density dependent effects along the lattice may cause heating [275] which is not visible in the short observation time, but leads to dephasing. Additionally, **systematic uncertainties**, as light shifts, connected to the large momentum transfer and the lattice need to be estimated.
- The shown interferometer geometry is **sensitive to a tilt** as the original example in ref. [80]. The combination of the relaunch together with the horizontal large momentum transfer beam splitter would allow for an order of magnitude longer acceleration times t_{acc} which could be used to further increase in momentum separation. A fountain would also allow to span a **four-pulse butterfly geometry**, which is sensitive to rotations [17].

CHAPTER 8

Future experiments, summary and conclusion

The atom-chip gravimeter realized in QUANTUS-1 and the in this thesis presented methods are a pathfinder for future experiments realizing precision measurements with Bose-Einstein condensates. In the framework of the collaborative research center geo-Q (SFB 1128) and the newly founded Hannover Institute for Technology (HITEC) [325], which is sketched in fig. 8.1, two experiments for novel atom interferometers are currently in progress. In this chapter a short overview on their directions of research is given and the relevance of the presented work for these experiments will be highlighted.

Fig. 8.1: Sketch of the Hannover Institute for Technology (HITEC) currently under construction. (image by CARPUS+PARTNER [325])

The first new experiment is the transportable Quantum Gravimeter QG-1 developed in collaboration with the Institut für Erdmessung (IFE) in Hannover (sec. 8.1). The QG-1 will employ a novel atom-chip source combined with Bragg interferometry to reach a state-of-the-art sensitivity, while exploiting ultracold ^{87}Rb atoms to improve on systematic uncertainties beyond the current state-of-the-art. It targets to measure gravity with an inaccuracy below 1 μGal and profits greatly from the work on gravimetry with BECs presented in this thesis to perform in field-measurements for geodetic application.

The second experiment will strive to increase the sensitivity of employed atom interferometers to gravity by extending the free-fall baseline to 10 m (sec. 8.2) which allows for interferometry times on the scale of seconds. Due to its large scale this device is called “Very Long Baseline Atom Interferometer” (VLBAI). Even with dropped atoms its sensitivity is impressive, but to push the scaling factor further large momentum transfer beam splitters and a fountain mode will be implemented, following the techniques developed in this thesis. The VLBAI device will be directly integrated as a research facility for atom interferometry on large scales into HITEC.

In the final section of this thesis a summary and a conclusion on the possible impact of the presented work for future developments is given (sec. 8.3). In addition to the two experiments, which are already under way today, ideas for a future miniaturized atom-chip gravimeter are gathered. The design of such an experiment further develops the combination of an atom chip with the fountain geometry and paths the way to miniaturized quantum sensors in the future.

8.1 Quantum gravimeter QG-I

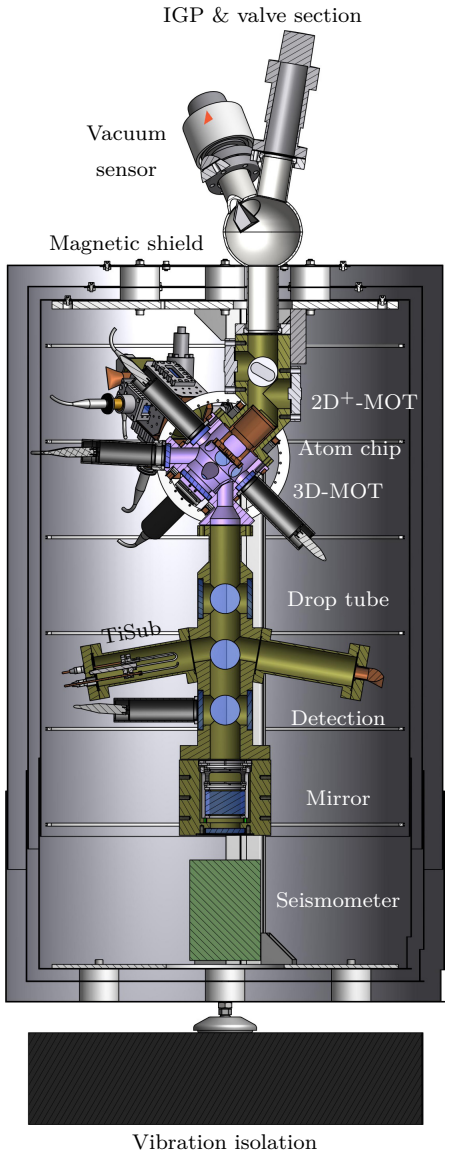

Fig. 8.2: A schematic depiction of the QG-1 sensor head. The vacuum system is mounted inside a three-layer magnetic shield and placed on a passive MINUS-K vibration isolation platform. For a high flux of ultracold atoms, a next generation atom chip in combination with a $2D^+$-MOT is used. A drop baseline of 30 cm length allows for high sensitivity using delta-kick collimated Bose-Einstein condensates in free fall with pulse separation times up to $T = 100$ ms and Bragg beam splitters. The device targets a systematic uncertainty in the gravity determination below 1 µGal in less than an hour of integration.

The QG-1 is a successor of the here presented atom-chip gravimeter prototype and is optimized for investigating the ultimate accuracy gain for gravimetry which is achievable due to the use of Bose-Einstein condensates. The apparatus, therefore, follows a more conservative design and uses the atom chip only for state preparation. Rather than implementing a relaunch and using a fountain geometry as introduced in sec. 6.3, the baseline is increased to approx. 30 cm enabling pulse separation times up to $T = 100$ ms using dropped Bose-Einstein condensates. From a technological point of view, QG-1 will be a step forward in every relevant aspect compared to the QUANTUS-1 prototype. With a sensor head which is specifically designed for gravimetry a measurement of gravity with an accuracy below 1 µGal is targeted. In a first step, the performance of the QG-1 will be studied in comparison to established instruments like a gPhone or an FG5X-220 [30, 326, 327]. The characterization of systematic uncertainties is pursued in HITEC to reach the anticipated accuracy and explore its limits. Future experiments comprise a gravity measurement campaign in Sweden leading to a more accurate observation of the so called Fennoscandian uplift by the IFE [135–137].

The complete apparatus consists of a sensor head, placed on a vibration isolation platform [314] and a separate temperature stabilized 19 inch rack containing the electronic control subsystem, the laser and optics distribution system, as well as the data acquisition hardware. This allows for an over all compact and transportable device capable of operation under non-laboratory conditions. The sensor head is depicted in fig. 8.2 and comprises the vacuum chamber which is mounted inside a three-layer magnetic shield with the ion getter pump at the top outside of the shield. The retro-reflection concept is different to the atom-chip gravimeter introduced in this thesis. Instead of using the atom chip itself as the retro-reflector, in the QG-1 a separate high-quality mirror is employed as retro-reflector. Herby, the laser beam is reflected from the atom chip at a 45° angle from the top of the apparatus and redirected onto the retro-reflecting mirror at the bottom of the vacuum system. Besides provid-

ing a superior optical quality, this allows for placing the inertial reference close to a seismometer and counter-acting the Earth's rotation via a piezo controlled tip-tilt mirror stage [300, 301].

The atomic source system for the QG-1 device emerged from the design developed and employed in the QUANTUS-2 experiment [117] which has several severe improvements over the source system of QUANTUS-1. The new source system combines a high-flux 2D$^+$-MOT with a next generation atom chip depicted on a photograph in fig. 8.3(a). Beside the "science" layer, which is still similar to the design used in QUANTUS-1 with a Z-type and a U-type wire, the next-generation chip has also a second "base" layer with bigger structures and mesoscopic wire structures underneath these layers. This design has the advantage, that magnetic traps with larger volumes can be generated and the coils for the magneto-optical trap can be substituted completely with the mesoscopic wire structures. The 3D-MOT coils are the biggest macroscopic coils in the QUANTUS-1 experiment which need to be water cooled and cause additional vibrations. The double stage source system with a 2D$^+$-MOT [328] provides a remarkable increase in loading rate compared to the loading from a background vapor as in QUANTUS-1. Previous experiments with a similar source achieved 10^5 condensed atoms per second [117] which makes delta-kick collimation to counteract mean field effects even more important. At a larger cycle time of 1.5 seconds even $5 \cdot 10^5$ condensed atoms are possible and the device can provide larger atom numbers in the hydrodynamic regime, between recoil limit and condensation threshold. The pulse separation time of $T = 100\,\mathrm{ms}$ combined with a flux of 10^5 atoms per second allows for sensitivities in the low 10^{-9} regime in $(\Delta g/g)/\sqrt{\mathrm{Hz}}$ already with first-order Bragg diffraction.

All necessary light fields for cooling, trapping, beam splitting and absorption detection of the final interferometer state are provided using a single frequency doubled telecom fiber laser system [329]. The anticipated output power obtained after frequency doubling is more than 2 W. Those powers are distributed and controlled via free-space optics on a honeycomb breadboard. The master laser at 1560 nm as well as the free-space light distribution at 780 nm are placed on a single $60 \times 40\,\mathrm{cm}$ breadboard as depicted in fig. 8.3(b) [202]. The frequency stabilization of the master laser is performed either by a beat measurement to an external cavity diode laser or a sideband modulation technique with an EOM [330]. The absolute frequency reference is in both cases a modulation transfer spectroscopy [307] mounted on a separate module.

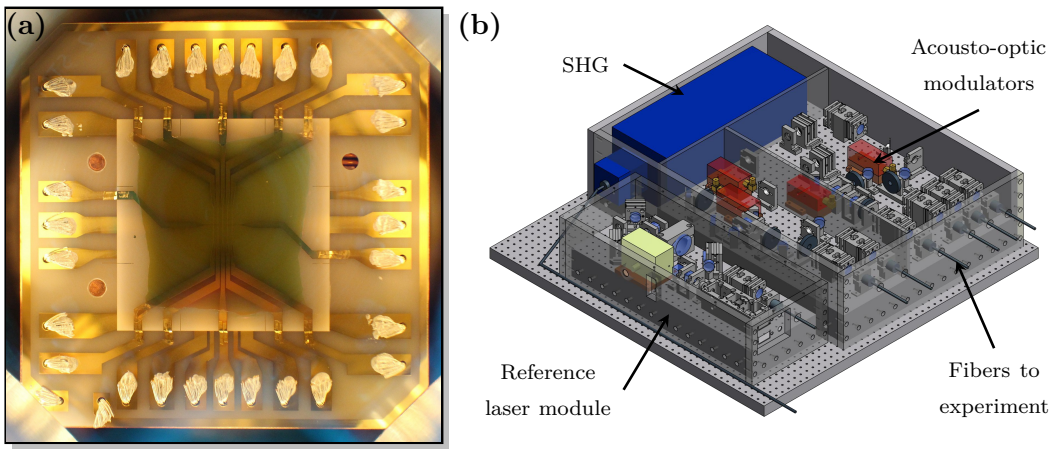

Figure 8.3: Details on the QG-1 atomic source. Next generation atom chip for high flux BEC generation which is only slightly modified from the QUANTUS-2 chip **(a)**. A single high-power laser provides the light for cooling and beam splitting **(b)**. A $60 \times 40\,\mathrm{cm}$ bread board contains the second harmonic generation, the free-space light distribution and a modulation transfer spectroscopy.

8.2 Very long baseline atom interferometry

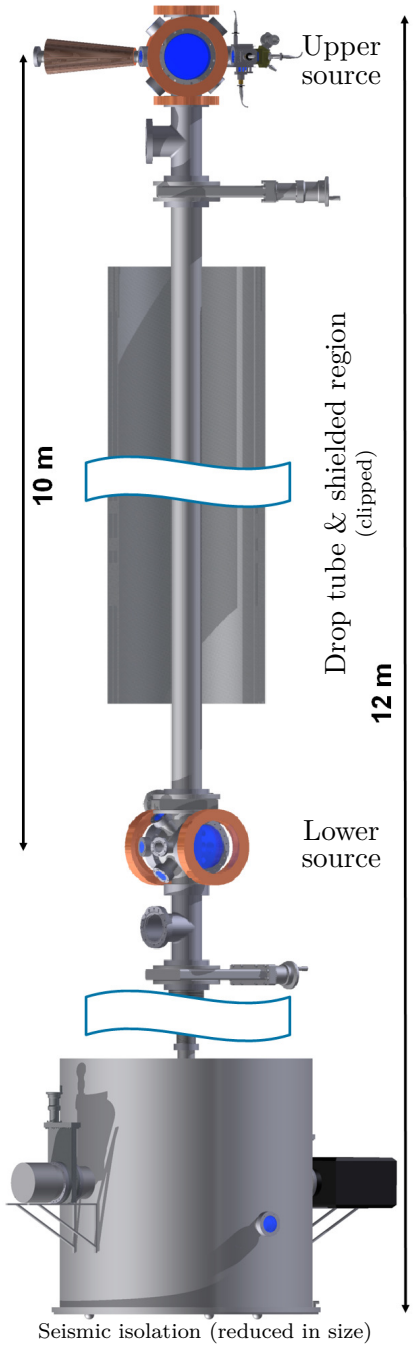

Fig. 8.4: The VLBAI vacuum assembly. The vacuum tank is downsized and the 10 m interferometry region cut in two parts with enlarged µmetal shield. Two atomic sources are placed on both ends of the drop tube.

A straight forward way to drastically increase the sensitivity of an atom interferometer is to extend the pulse separation time T further and further. The extension of pulse separation time to the scale of several seconds is only possible using delta-kick collimated Bose-Einstein condensates. On Earth this has the major consequence, that the free-fall baseline also increases quadratically with time. In consequence the whole experiment needs to grow as well and leads to a massive increase in investment into complex and large vacuum vessels. The construction of theses vacuum systems faces several challenges, as for example a magnetic shielding at 10 m length [331]. Very few experiments with free fall baselines as large as 10 m are operating right now [36, 100]. In Hannover the so called "Very long Baseline Atom Interferometer" (VLBAI) is in the progress of construction and will enable free evolution times in the order of a few seconds with a maximum flexibility in the choice of atomic species.

The VLBAI facility is one out of three major research instrumentations (DFG - Großgeräte) integrated into the HITEC building. It comprises an approximately 12 m long vacuum vessel of which almost 9 m are magnetically shielded for performing atom interferometry. Two sources on both sides of the free-all baseline will allow for the generation of ultracold Rb-Yb mixtures to be either dropped but also to be launched. A lattice launch of atoms from the lower source chamber will allow for a free-fall time of $2T = 2.6\,\mathrm{s}$ in total and combined with large momentum transfer beam splitters to reach the device's ultimate sensitivity. Therefore techniques investigated in sec. 5.3 and 7.2 are of high importance for this device in the future. A vacuum tank is placed at the lower end of the systems in which a vibration isolation will be placed, with a similar design to the ones used in the AEI 10 m prototype laser interferometer [332]. Since vibrational background noise is an important issue in all gravity measurements this will make VLBAI an ideal test bed to perform accurate measurements of gravity. Rather than using an atom chip for the atomic source, the VLBAI employs an optical dipole trap at a wavelength of 2 µm for trapping, condensation and to overlap two ensembles of different species. The condensation of ^{87}Rb in a dipole trap of this wavelength has been demonstrated before [333].

The major scientific goals of the VLBAI project in Hannover are outlined in the following. With its sensitivity a large scale device offers the possibility to perform a variety of measurements using atom interferometry, where in most

cases an even further increase in the scaling factor is preferable. In the near future VLBAI-type devices are expected to provide valuable insight into the understanding of fundamental physics. Each of these scientific goals itself is at the frontier of current research asking challenging, some controversially discussed, questions in the interest of modern physics:

- The accurate determination of gravity with quantum sensors is a primary goal in geo-Q. In this context VLBAI contributes an **accurate geodetic gravity reference**. With the stable vibration isolation and its high sensitivity to gravity it has ideal preconditions for accurate measurements. In addition, two gravimeters simultaneously operated with different atomic species lead to a test of the **universality of free fall** (UFF).
- With two source chambers separated by a large baseline VLBAI is able to perform differential measurements between two atomic ensembles at different positions and to measure gradients. **Quantum gradiometry** is not only of interest for Earth observation but moreover for testing prerequisites necessary for **gravitational wave detection** with atoms measuring the so-called space-time strain following the theoretical work in ref. [334, 335]

$$\Delta\phi_{\mathrm{GW}} = 8k_{\mathrm{eff}}hL\sin^4\left(\frac{\omega T}{2}\right)\left(\frac{7+8\cos\omega T}{2}\right)\sin\theta_{\mathrm{GW}}. \tag{8.1}$$

  After early suggestions how to measure gravitational waves in an atom interferometer [336, 337], a first concept for a space mission was proposed [338] which lead to discussions [339, 340]. New concepts were developed like using **single photons beam splitter** on the clock transition of alkaline atoms atoms [216], or new geometries and detection schemes [217].
- Interesting proposals have been made to test **general relativistic effects** all requiring the immense sensitivities VLBAI will be able to access. Examples are the occurrence of **higher order phase shift terms** in an atom interferometer [334, 341] or **interferometry with clock states** demonstrating time dilation with a superposition of clocks [342].
- Exploring the **bounds of quantum mechanics** with macroscopically delocalized superpositions [70] may reveal the mechanisms which fundamentally lead to a **decoherence of a superposition state** [343] at the transition between classical and quantum systems. Second-scale pulse separation with meters-per-second-scale beam splitters as demonstrated in this thesis are able to span superpositions **delocalized over several meters**.

Scenarios for testing the UFF with mixtures of Rubidium and Ytterbium

One driver behind the construction of large scale atom interferometers is to test special or general relativity, which is one of the major foundations of modern physics. Atom interferometric tests target to measure the UFF, one of the postulates underlying Einstein's principle of equivalence, by simultaneously comparing the free-fall rates of two different test masses as accurately as possible. Up to now mixed (comparing a quantum to a classical object) or pure (comparing two quantum objects) quantum tests as listed in tab. 8.1 can not compete with torsion balance experiments [38] or Lunar Laser Ranging [37]. Large scale devices offer the possibly to perform atom interferometry with second scale interrogation times on ground which allow to envision tests on these levels of accuracy and possibly go beyond. VLBAI will employ mixtures of ultracold Rubidium and Ytterbium targeting a test of the UFF compatible to todays' best classical tests at the parts in 10^{13} level. The combination of Rubidium and Ytterbium as test masses is a solid choice concerning the mass difference as well as their composition [282].

A test of the UFF is usually parametrized by the so called Eötvös ratio [344, 345]

$$\eta_{\mathrm{A,B}} \equiv 2\frac{g_{\mathrm{A}} - g_{\mathrm{B}}}{g_{\mathrm{A}} + g_{\mathrm{B}}} = 2\frac{\left(\frac{m_{\mathrm{gr}}}{m_{\mathrm{in}}}\right)_{\mathrm{A}} - \left(\frac{m_{\mathrm{gr}}}{m_{\mathrm{in}}}\right)_{\mathrm{B}}}{\left(\frac{m_{\mathrm{gr}}}{m_{\mathrm{in}}}\right)_{\mathrm{A}} + \left(\frac{m_{\mathrm{gr}}}{m_{\mathrm{in}}}\right)_{\mathrm{B}}} \tag{8.2}$$

with the gravitational acceleration g acting on the test bodies A and B and their respective ratios of gravitational mass m_{gr} and inertial mass m_{in}. The Eötvös ratio represents a parametrization of a possible violation coupling to the difference in these ratios between the two test masses. Theories predict, that violations could arise for example from spin-gravity coupling [31, 34, 346, 347] or metric fluctuations [348]. A strength of a quantum test is the variety of isotope pure and spin polarized test masses available, if the possibility to trap and laser-cool them exists. It is hence possible to access parameters, which are not well parametrized by mass and not available with classical test pairs. To reflect this fact, in the standard model extension possible violations of the UFF are parametrized dependent on the composition of the test masses [349–351].

Table 8.1: Overview of previously performed matter wave tests of the UFF. The first two semi-classical experiments compared the free fall of cold atoms to that of a falling corner cube by gravimetry.

Experiment	Reference	Mass A	Mass B	Eötvös ratio $\eta_{\mathrm{A,B}}$
Palo Alto	[9]	^{133}Cs	SiO_2	$(7.0 \pm 7.0) \times 10^{-9}$
Paris	[30]	^{87}Rb	SiO_2	$(4.4 \pm 6.5) \times 10^{-9}$
München	[31]	^{85}Rb	^{87}Rb	$(1.2 \pm 1.7) \times 10^{-7}$
Palaiseau	[32, 268]	^{85}Rb	^{87}Rb	$(1.2 \pm 3.2) \times 10^{-7}$
Firenze	[34]	^{87}Sr	^{88}Sr	$(0.2 \pm 1.6) \times 10^{-7}$
Hannover	[35]	^{39}K	^{87}Rb	$(0.3 \pm 5.4) \times 10^{-7}$
Wuhan	[36]	^{85}Rb	^{87}Rb	$(2.8 \pm 3.0) \times 10^{-8}$

Table 8.2: The three test scenarios for a test of the UFF in VLBAI taken from ref. [282].

Test case	Pulse separation T (Rb,Yb)	Beam splitter k_{eff} (Rb,Yb)	Comment	Target $\eta_{\mathrm{A,B}}$
Initial	500 ms, 505.7 ms	8π/(780nm), 4π/(399nm)	drop only	5.7×10^{-11}
Intermediate	500 ms, 500 ms	8π/(780nm), 4π/(399nm)	adv. source	6.7×10^{-12}
Advanced	1300 ms, 1300 ms	16π/(780nm), 8π/(399nm)	fountain	7.4×10^{-13}

The detailed error analysis published in ref. [282] allows to estimate the level on which a test of the UFF may be performed in this device and the parameters needed to reach these. The targeted test performance comprising three different anticipated test scenarios is listed in tab. 8.2 targeting tests ranging from the parts in 10^{11} to the parts in 10^{13} level which would catch up to classical tests. Hereby, the ultimate sensitivity utilizing a pulse separation time of $2T = 2.6\,\mathrm{s}$ which is needed for the most advanced test for VLBAI can only be reached in a fountain mode. The integration of a relaunch for the atoms is therefore mandatory and the technique presented in this thesis is a suitable way to realize this. A further increase in the scaling factor will only be possible integrating larger momentum transfer beam splitters, since only up to fourth-order has been considered in the current scenarios but already the largest possible pulse separation time.

8.3 Summary and conclusion

During the course of this thesis the first atom-chip gravimeter with Bose-Einstein condensates has been realized in the QUANTUS-1 experiment. In the implementation of the gravimeter the atom chip is used for the generation of Bose-Einstein condensates, state preparation, including magnetic sub-state transfer, delta-kick collimation and Stern-Gerlach-type deflection as well as a retro-reflector for the beam splitting light fields. In that way, Mach-Zehnder type interferometers using Bragg diffraction to measure gravity can be formed and their output ports detected in a cube below the atom chip with a side length of less than one centimeter. Starting with a simple experimental implementation with dropped Bose-Einstein condensates a determination of local gravity with an uncertainty of $\Delta g/g = 1.3 \cdot 10^{-5}$ in roughly eight hours has been demonstrated which is limited by background vibrations. The vibrational background noise acting on the non-isolated setup is in reasonable agreement to the level determined by two additional classical sensors. The intrinsic sensitivity, however, operating a Mach-Zehnder interferometer with first-order Bragg beam splitters, an interferometric contrast of $C = 0.75$ and the largest pulse separation time of $T = 5\,\mathrm{ms}$ is significantly better. The measured phase read out noise including all non-inertial noise contributions would allow to measure gravity to $\Delta g/g = 3.2 \cdot 10^{-6}$. Indeed, this limit is very close to the shot noise limit for $N = 10\,000$ atoms. Nonetheless, this successfully demonstrates already in this simple setup important techniques for the determination of gravity, which are of valuable contribution to the next generation Quantum Gravimeter QG-1. This device will by design achieve a much better performance as this demonstrator, but still has roughly the same size as other current generation devices.

A major limitation on the intrinsic sensitivity in this first mode of operation is the tightly constrained time of free fall ToF $= 34\,\mathrm{ms}$, given by the end of the detection region 7 mm below the atom chip. It permits to apply the state preparation as wanted and limits the pulse separation time to $T = 5\,\mathrm{ms}$. To overcome these constrains a novel mechanism was developed to relaunch Bose-Einstein condensates in a retro-reflected optical lattice. Bloch oscillations in an accelerated optical lattice are routinely used to transfer a large number of photon recoils with high fidelity. The challenge to implement this method in the atom-chip gravimeter is, to use the same retro-reflected light field for driving Bragg diffraction and Bloch oscillations, referenced to the atom chip. This causes large losses in the case of a single lattice acceleration due to an additional lattice with opposing Doppler shift and two standing waves, while crossing the zero momentum state, e.g. when atoms are at rest. With a combination of a deceleration stage by Bloch oscillations, a $16\,\hbar k$ double Bragg diffraction pulse, which inverts the momentum state and finally an acceleration sequence by Bloch oscillations these losses can be prevented. In total the efficiency of the relaunch process can be enhanced from 25% for a single lattice acceleration sequence to more than 75% for the optimized sequence at a total transfer of more than 100 photon recoils. The limits on the efficiency have been studied in detail. This new method provides a valuable tool, to be implemented into atomic inertial sensors, without changing the optical setup and therefore increasing the device's complexity. In QUANTUS-1, with application of the relaunch, the time of free fall can be elongated to ToF $= 97.6\,\mathrm{ms}$ without enlarging the baseline - so almost a factor of three larger compared to originally 34 ms.

With the implementation of the relaunch technique in the gravimeter sequence a fountain geometry has been realized, that almost closes the gap in scaling factor to the current state-of-the-art gravimeters, but keeping a smaller volume. The fountain geometry allowed to improve the intrinsic sensitivity of the atom-chip gravimeter to $\Delta g/g = 1.4 \cdot 10^{-7}$ by extending the total time of flight to ToF $= 97.6\,\mathrm{ms}$ and the pulse separation time to $T = 25\,\mathrm{ms}$ at a contrast of $C = 0.8$. Due

to the large vibrational background at high sensitivity a value for gravity can not be determined anymore. However, the technical noise of the Mach-Zehnder interferometer using delta-kick collimated ensembles and first-order beam splitters is still at or at least very close to the shot noise limit for the currently launched atom number. Additionally, the implementation of higher-order Bragg diffraction up to third-order is shown and the interferometer's signal is evaluated with the help of principal component analysis. The use of a PCA-based evaluation allows to overcome a loss of contrast which is caused by dephasing due to curved wave fronts. With a regain from $C = 0.35$ to 0.72 an even slightly improved intrinsic sensitivity of $\Delta g/g = 1.1 \cdot 10^{-7}$ can be reached. The current limits on these parameters in the QUANTUS-1 experiment are clearly set by the insufficient surface quality of the atom chip and the end of the detection region 7 mm below the chip and can be overcome in a dedicated setup. In combination with a source matching the performance of the QUANTUS-2 experiment [117] sensitivities of $(\Delta g/g)/\sqrt{\text{Hz}} = 5.3 \cdot 10^{-9}$ are in reach paving the way for miniaturized atomic devices in the future.

The additional effort to integrate a Bose-Einstein condensate in atomic sensors is mainly justified by the gain in accuracy due to its unique properties in size and expansion rate. The prototype gravimeter realized in QUANTUS-1 is fully limited by statistical noise even after eight hours of integration. Nevertheless, an estimation on the known effects, which cause systematic uncertainties, grants a valuable insight into the future perspective. The scheme and the atom-optics operations developed in this thesis already match the requirements to reach a high sensitivity in a dedicated setup with high atomic flux and improved sub-components. The improvements on the sub-components include the vibration isolation, magnetic shielding or specifically the surface quality of the atom chip, which are foremost limiting the device at the moment. But, especially delta-kick collimation to obtain high beam splitting fidelities after relaxing mean field interactions, the residual initial motion and the suppression of light shifts [152] pair favorably with the fountain geometry. Based on these techniques mitigation strategies have been discussed to reach accuracies below 1 µGal using delta-kick collimated condensates.

Several novel atom interferometer geometries have been developed in this thesis. Two geometries are implemented which each correlate two simultaneously operated Mach-Zehnder interferometers generated from a single condensate by a Bragg or double Bragg diffraction pulse which splits the condensate into two sources with non-vanishing relative motion. These dual interferometers allow to address either rotations or to increase the dynamic range, and show a large vibration noise immunity due to the rejection of common mode noise. Additionally, a novel method to realize a large momentum transfer mechanism has been investigated. The method combines the initial splitting with a double Bragg diffraction $\frac{\pi}{2}$-pulse with the differential acceleration of the wave packets by Bloch oscillations in a dual lattice. Performing the initial splitting with double Bragg diffraction of at least $4\,\hbar k$ momentum separation, or multiples with sequential transitions, shows a more advantageous scaling behavior than for only $2\,\hbar k$ of initial splitting by a single Bragg or Raman pulse. This scaling behavior together with the fact, that both retro-reflected lattices can be used to counter-accelerate atoms away from each other, allows to transfer more than $1000\,\hbar k$ of total differential splitting in a single acceleration sequence of only 4 ms duration and to still observe a fraction of approx. 25% remaining atoms. With this method an interferometer can be formed similar to [80] but with an acceleration and deceleration phase in-between each $\frac{\pi}{2}$-pulse and the π-pulse in the middle. Contrast in a closed atom interferometer has been observed up to $208\,\hbar k$ momentum separation, which equals a differential wave-packet velocity of approx. 1.1 m/s and a total of $832\,\hbar k$ transfered photon momenta during the interferometer. This result represents more than twice the separation inside an atom interferometer compared to all that to the best knowledge has been reported previously [68, 70, 72].

Concepts for future miniaturized quantum sensors

The atom-chip technology has proven to be versatile, reliable and very well suited for future development of compact quantum sensors. The unique element in the implementation of the atom-chip gravimeter developed in this thesis is the retro-reflection of the beam splitter laser from the chip surface and thus using it as inertial reference. The compactness of this arrangement is a strong argument in favor of this scheme having the perspective to be used for miniaturized sensors in the future. An artist illustration of such a miniaturized atom-chip fountain gravimeter is depicted in fig. 8.5 adapted from ref. [352, 353]. The surface quality of the current chip is thus the major limiting factor in the application of the relaunch or beam splitters, especially in higher order, as well as it is the source of phase gradients reducing the interferometric contrast. The feasibility to reach state-of-the-art performance strongly relies on the assumption which quality of the retro-reflector is reached by different ways of manufacturing. But also additional features may be added in the future to enhance the chip's capabilities [354] or to simplify the setup.

The technology currently used as a mirror is a transfer coating directly installed as top-layer on the chip as described in ref. [205]. By specification the height differences of the mirror surface equals 2 µm for 7 µm gold wires underneath. Alternatively a metal coating may be used as mirror [355, 356], but not directly over current carrying wires, so an isolation layer is needed. To further planarize the surface spin-on-glass or a polyimide can be used and installed on-top again a metal or dielectric coating. Planarizing three times a residual roughness of 300 nm with 5 µm wires was achieved in ref. [357]. Further chemical-mechanical polishing decreases the residual roughness [358] and roughnesses of 5 nm have been achieved in ref. [359]. This would be equal to a surface quality better than $\lambda/10$ which is the value assumed for the uncertainty budget.

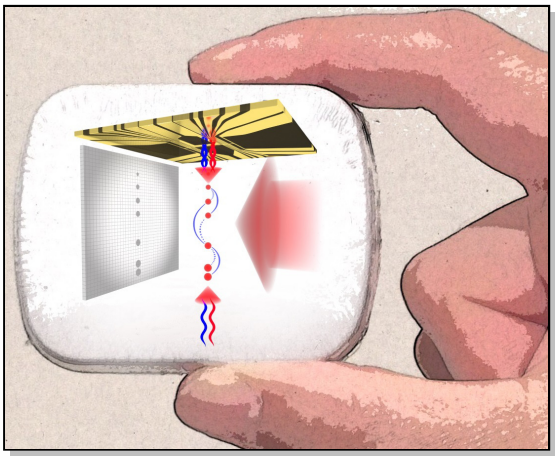

Fig. 8.5: Gravity in hand - vision of a miniaturized atom-chip fountain gravimeter [352, 353].

The fountain gravimeter scheme itself already represents an important step towards a miniaturized atomic sensor, since the drop baseline of the atoms can be significantly smaller and for the first time it has been demonstrated that the complete experimental sequence can be integrated in such a small volume. Of course a fully miniaturized sensor depends on all components needed to perform the experiment, like the laser system [161, 173] or electronics, but most importantly the vacuum systems itself as the QUANTUS-2 dual-chamber design depicted in fig. 8.6. Two different approaches can simplify chip-assisted state trapping and cooling using either a pyramidal-shaped retro-reflector [57, 58] or microfabricated grating chips [360]. Additionally, intra-cavity interferometry [361] may reduce the laser power required to drive Bragg diffraction or Bloch oscillations. Recently, the DLR started the project KACTUS to study several technological advancements over the currently used atom chip in the QUANTUS collaboration. One first improvement is to develop hermetically sealed chips to drastically decrease out-gas rates and eliminate conventional feedthroughs. This does not only help to increase the lifetime of produced condensates, but then the chip itself can be used to hermetically seal the vacuum, this drastically allows to shrink down the size of the vacuum system [116]. Eventually, the implementation of squeezing [101–109] combined with a low-noise detection [362, 363] would allow for smaller atom numbers while not

decreasing the intrinsic sensitivity, but reducing uncertainties due to mean field interactions. Miniaturization and robustness is not only important for gravity measurement in the field of terrestrial Earth observation but also offer a perspective for broadened applications, most prominently autonomous inertial navigation. Beside the accurate measurement of gravity in a single direction, these require the determination of all axis of inertia [320] at a comparably high data rate [364–366]. Joint measurements between more than one sample at the same time may reduce or even completely eliminate dead times between subsequent measurements [17, 367], which is an important ingredient to not lose track of an inertial signal at times the atom interferometer is not operated. So far most of these techniques have only been demonstrated for laser-cooled sources with larger flux of atoms, higher cycling rates and less susceptibility to atom loss due to stray light, but these aspects can be improved for interferometers using condensates in the future. An alternative applicable for Bose-Einstein condensates might be the use of a continuous atom laser [368, 369], where atoms are out-coupled from a larger reservoir. Similar schemes and techniques apply for additional valuable fields of application like airborne gravimetry or gradient measurements on satellites. In the end, these type of sensors are operated in a rougher environment where vibration isolation is no longer sufficiently doable but hybridizing with classical seismic sensors is needed [286].

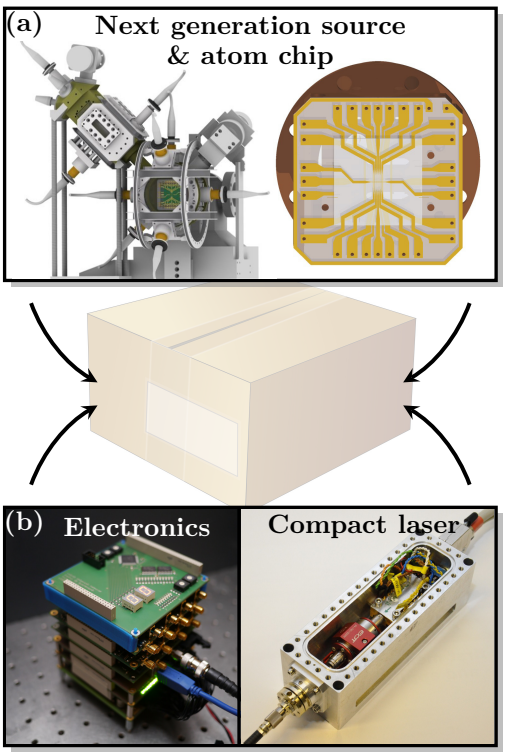

Fig. 8.6: Advanced technologies for a future miniaturized atom-chip fountain gravimeter. The next generation source from QUANTUS-2 provides a larger flux of cold atoms [117] **(a)**. Miniaturized electronics developed for the MAIUS rocket and a compact diode-laser system manufactured by the FBH [161, 173] **(b)**.

Further research with QUANTUS-1

The use of Bose-Einstein condensates for atom interferometry and to combine them with manipulation techniques relying on Bragg diffraction or Bloch oscillations is the central element of the experimental work presented in this thesis. For these experiments the QUANTUS-1 apparatus provides an ideal testbed. With the implementation of the atom-chip gravimeter this work has demonstrated novel opportunities to find schemes applicable for miniaturized quantum sensors and to mature atom interferometry with Bose-Einstein condensates. But beside from these compact devices, the presented experimental methods are also of relevance for large scale devices or space applications. The presented results show in a nutshell:

- **Bose-Einstein condensates** offer a promising route to reach improved accuracies for the next generation of quantum gravimeters and of interest for geodetic Earth observation.
- **Bragg and double Bragg diffraction** are valuable choices as beam splitters in atom interferometers and show even advantages compared to Raman diffraction.
- **Atom-chip technology** already allows to shrink atomic sensors down from laboratory sized experiments into robust, transportable devices and will lead to further miniaturization.

- **Bloch oscillations** in optical lattices are a mighty tool implemented in atom interferometry. Especially the combination with Bragg diffraction can solve problems in an elegant way, introducing new manipulation techniques to develop novel measurement schemes.

The research with QUANTUS-1 continuously offers exiting perspectives. The momentum broadening which is observed after the relaunch due to the disturbances on the chip surface needs to be eliminated prior to the next steps. It was already seen, that this effect can be minimized by shifting the Bose-Einstein condensate and the center of the laser beam to another region below the chip. At the same time reducing its diameter by an aperture to avoid hitting a defect immensely reduces diffraction patterns. For such a shift the optics used for double Bragg diffraction may not be used, because it is not possible to accelerate and later on stop the atoms. Instead, the optical setup needs to be changed and two additional counter-propagating but not retro-reflected beams driving Bloch oscillations can be shined in on the same axis aligned only slightly tilted to the double Bragg diffraction beam. In that way, the setup can be modified without removing the original optics used for double Bragg diffraction and keep this axis for the manipulation. The following list of topics summarizes the most interesting aspects:

- **Atom-chip gravimeter with unprecedented resolution in a $1\,\mathrm{cm}^3$ volume**. To further improve on the scaling factor and the intrinsic sensitivities, especially the application of higher-order Bragg diffraction with enhanced contrast seems feasible, when cloud size and beam curvature are reduced. Additionally, longer free-fall times can be accessed if the relaunch is performed below the detection region.
- **Pushing the record in momentum transfer towards thousand photon recoils**. Combining the relaunch with the horizontal beam splitter grants more time for Bloch oscillations and thus increasing the momentum transfer in an atom interferometer.
- **Novel interferometer geometries**. Moreover, with relaunch and beam splitter in two dimensions novel geometries can be spanned, which enable different inertial measurements. For example a butterfly geometry can be realized which is sensitive to rotations but not to gravity [320]. With geometries tailored to different phase shift terms, multi-axis sensing can be performed independently from the orientation of a device.
- **Improved estimations of systematic uncertainties**. With sensor fusion concepts the seismic noise can be decreased by correlation of the atom interferometer to a classical seismic sensor. Afterwards, the uncertainties due to wave front distortions can be studied using spatial imaging techniques and the influence of light shifts on higher orders.
- **Novel lattice based manipulation techniques**. In the current setup there are already two axes to perform lattice manipulation and explore lattice based physics in one or more dimensions. This includes effects connected to Landau-Zener tunneling [370, 371], but also the lattice may be used to perform guided atom interferometry to realize the proposal from ref. [148], where atoms are manipulated and at the same time guided by an optical lattice.
- **Study of surface related effects using an atom chip**. The presented atom-chip setup seems ideally suited to use the close proximity of atoms to the chip together with the precise control of the relaunch for measurements of surface related effects [372]. Observable physics include the measurement of short range forces like Casimir-Polder [373, 374] and the search of dark energy over Chameleon forces [39], or to study quantum reflections [375].

Bibliography

1. A. Einstein, 'Die Grundlage der allgemeinen Relativitätstheorie',
Ann. Phys. **49,** 769–822 (1916) (cit. on p. 1).
2. W. Heisenberg, 'Über quantentheoretische Umdeutung kinematischer und mechanischer Beziehungen.',
Z. Phys **33,** 879–893 (1925) (cit. on p. 1).
3. E. Schrödinger, 'Quantisierung als Eigenwertproblem',
Ann. Phys. **384,** 489–527 (1926) (cit. on p. 1).
4. A. Einstein, 'Über Gravitationswellen',
Sitzungsbericht Kgl. Preuss. Akad. Wiss. (1918) (cit. on p. 1).
5. B.P. Abbott *et al.*, 'Observation of Gravitational Waves from a Binary Black Hole Merger',
Phys. Rev. Lett. **116,** 061102 (2016) (cit. on p. 1).
6. N. Huntemann, C. Sanner, B. Lipphardt, C. Tamm, and E. Peik, 'Single-Ion Atomic Clock with 3×10^{-18} Systematic Uncertainty',
Phys. Rev. Lett. **116,** 063001 (2016) (cit. on pp. 1, 32).
7. M. Kasevich and S. Chu, 'Atomic interferometry using stimulated Raman transitions',
Phys. Rev. Lett. **67,** 181–184 (1991) (cit. on pp. 2–4, 29, 48).
8. M. Kasevich and S. Chu, 'Measurement of the gravitational acceleration of an atom with a light-pulse atom interferometer',
Appl. Phys. B **54,** 321–332 (1992) (cit. on pp. 2, 4, 29, 81).
9. A. Peters, K.-Y. Chung, and S. Chu, 'Measurement of gravitational acceleration by dropping atoms',
Nature **400,** 849–852 (1999) (cit. on pp. 2, 81, 136).
10. J. Le Gouët, T.E. Mehlstäubler, J. Kim, S. Merlet, A. Clairon, A. Landragin, and F. Pereira Dos Santos, 'Limits to the sensitivity of a low noise compact atomic gravimeter',
Appl. Phys. B **92,** 133–144 (2008) (cit. on pp. 2, 116).
11. P.A. Altin, M.T. Johnsson, V. Negnevitsky, G.R. Dennis, R.P. Anderson, J.E. Debs, S.S. Szigeti, K.S. Hardman, S. Bennetts, G.D. McDonald, L.D. Turner, J.D. Close, and N.P. Robins, 'Precision atomic gravimeter based on Bragg diffraction',
New J. Phys. **15,** 023009 (2013) (cit. on pp. 2–4, 67, 68, 79).
12. Z.-K. Hu, B.-L. Sun, X.-C. Duan, M.-K. Zhou, L.-L. Chen, S. Zhan, Q.-Z. Zhang, and J. Luo, 'Demonstration of an ultrahigh-sensitivity atom-interferometry absolute gravimeter',
Phys. Rev. A **88,** 043610 (2013) (cit. on pp. 2, 81, 85).
13. T.L. Gustavson, P. Bouyer, and M.A. Kasevich, 'Precision Rotation Measurements with an Atom Interferometer Gyroscope',
Phys. Rev. Lett. **78,** 2046–2049 (1997) (cit. on p. 2).
14. A. Gauguet, B. Canuel, T. Léveque, W. Chaibi, and A. Landragin, 'Characterization and limits of a cold-atom Sagnac interferometer',
Phys. Rev. A **80,** 063604 (2009) (cit. on pp. 2, 120, 121).

15. J.K. Stockton, K. Takase, and M.A. Kasevich, 'Absolute Geodetic Rotation Measurement Using Atom Interferometry',
Phys. Rev. Lett. **107,** 133001 (2011) (cit. on p. 2).

16. P. Berg, S. Abend, G. Tackmann, C. Schubert, E. Giese, W.P. Schleich, F.A. Narducci, W. Ertmer, and E.M. Rasel, 'Composite-Light-Pulse Technique for High-Precision Atom Interferometry',
Phys. Rev. Lett. **114,** 063002 (2015) (cit. on pp. 2–4, 119–121, 126).

17. I. Dutta, D. Savoie, B. Fang, B. Venon, C.L. Garrido Alzar, R. Geiger, and A. Landragin, 'Continuous Cold-Atom Inertial Sensor with 1 nrad/sec Rotation Stability',
Phys. Rev. Lett. **116,** 183003 (2016) (cit. on pp. 2, 4, 130, 140).

18. J.M. McGuirk, G.T. Foster, J.B. Fixler, M.J. Snadden, and M.A. Kasevich, 'Sensitive absolute-gravity gradiometry using atom interferometry',
Phys. Rev. A **65,** 033608 (2002) (cit. on pp. 2, 83).

19. G. Lamporesi, A. Bertoldi, L. Cacciapuoti, M. Prevedelli, and G.M. Tino, 'Determination of the Newtonian Gravitational Constant Using Atom Interferometry',
Phys. Rev. Lett. **100,** 050801 (2008) (cit. on p. 2).

20. M.J. Snadden, J.M. McGuirk, P. Bouyer, K.G. Haritos, and M.A. Kasevich, 'Measurement of the Earth's Gravity Gradient with an Atom Interferometer-Based Gravity Gradiometer',
Phys. Rev. Lett. **81,** 971–974 (1998) (cit. on p. 2).

21. J.B. Fixler, G.T. Foster, J.M. McGuirk, and M.A. Kasevich, 'Atom Interferometer Measurement of the Newtonian Constant of Gravity',
Science **315,** 74–77 (2007) (cit. on p. 2).

22. G. Rosi, F. Sorrentino, L. Cacciapuoti, M. Prevedelli, and G.M. Tino, 'Precision measurement of the Newtonian gravitational constant using cold atoms',
Nature **510,** 518–521 (2014) (cit. on p. 2).

23. G.W. Biedermann, X. Wu, L. Deslauriers, S. Roy, C. Mahadeswaraswamy, and M.A. Kasevich, 'Testing gravity with cold-atom interferometers',
Phys. Rev. A **91,** 033629 (2015) (cit. on p. 2).

24. P. Cladé, E. de Mirandes, M. Cadoret, S. Guellati-Khelifa, C. Schwob, F. Nez, L. Julien, and F. Biraben, 'Precise measurement of h/m_{Rb} using Bloch oscillations in a vertical optical lattice: Determination of the fine-structure constant',
Phys. Rev. A **74,** 052109 (2006) (cit. on p. 2).

25. H. Müller, S.-w. Chiow, Q. Long, C. Vo, and S. Chu, 'A new photon recoil experiment: towards a determination of the fine structure constant',
Appl. Phys. B **84,** 633–642 (2006) (cit. on p. 2).

26. R. Bouchendira, P. Cladé, S. Guellati-Khélifa, F. Nez, and F. Biraben, 'New Determination of the Fine Structure Constant and Test of the Quantum Electrodynamics',
Phys. Rev. Lett. **106,** 080801 (2011) (cit. on p. 2).

27. B. Estey, C. Yu, H. Müller, P.-C. Kuan, and S.-Y. Lan, 'High-Resolution Atom Interferometers with Suppressed Diffraction Phases',
Phys. Rev. Lett. **115,** 083002 (2015) (cit. on p. 2).

28. D. Hanneke, S. Fogwell, and G. Gabrielse, 'New Measurement of the Electron Magnetic Moment and the Fine Structure Constant',
Phys. Rev. Lett. **100,** 120801 (2008) (cit. on p. 2).

29. T. Damour, 'Testing the equivalence principle: why and how?',
Class. Quantum Grav. **13,** A33– (1996) (cit. on p. 2).

30. S. Merlet, Q. Bodart, N. Malossi, A. Landragin, F. Pereira Dos Santos, O. Gitlein, and L. Timmen, 'Comparison between two mobile absolute gravimeters: optical versus atomic interferometers',
Metrologia **47,** L9– (2010) (cit. on pp. 2, 81, 91, 132, 136).

31. S. Fray, C. A. Diez, T.W. Hänsch, and M. Weitz, 'Atomic Interferometer with Amplitude Gratings of Light and Its Applications to Atom Based Tests of the Equivalence Principle', *Phys. Rev. Lett.* **93,** 240404 (2004) (cit. on pp. 2, 136).

32. A. Bonnin, N. Zahzam, Y. Bidel, and A. Bresson, 'Simultaneous dual-species matter-wave accelerometer', *Phys. Rev. A* **88,** 043615 (2013) (cit. on pp. 2, 136).

33. C.C.N. Kuhn, G.D. McDonald, K.S. Hardman, S. Bennetts, P.J. Everitt, P.A. Altin, J.E. Debs, J.D. Close, and N.P. Robins, 'A Bose-condensed, simultaneous dual-species Mach–Zehnder atom interferometer', *New J. Phys.* **16,** 073035 (2014) (cit. on p. 2).

34. M.G. Tarallo, T. Mazzoni, N. Poli, D.V. Sutyrin, X. Zhang, and G.M. Tino, 'Test of Einstein Equivalence Principle for 0-Spin and Half-Integer-Spin Atoms: Search for Spin-Gravity Coupling Effects', *Phys. Rev. Lett.* **113,** 023005– (2014) (cit. on pp. 2, 136).

35. D. Schlippert, J. Hartwig, H. Albers, L.L. Richardson, C. Schubert, A. Roura, W.P. Schleich, W. Ertmer, and E.M. Rasel, 'Quantum Test of the Universality of Free Fall', *Phys. Rev. Lett.* **112,** 203002 (2014) (cit. on pp. 2, 4, 136).

36. L. Zhou *et al.*, 'Test of Equivalence Principle at 10^{-8} Level by a Dual-Species Double-Diffraction Raman Atom Interferometer', *Phys. Rev. Lett.* **115,** 013004 (2015) (cit. on pp. 2, 134, 136).

37. J.G. Williams, S.G. Turyshev, and D.H. Boggs, 'Lunar laser ranging tests of the equivalence principle', *Class. Quantum Grav.* **29,** 184004 (2012) (cit. on pp. 2, 135).

38. E.G. Adelberger, J.H. Gundlach, B.R. Heckel, S. Hoedl, and S. Schlamminger, 'Torsion balance experiments: A low-energy frontier of particle physics', *Prog. Part. Nucl. Phys.* **62,** 102–134 (2009) (cit. on pp. 2, 135).

39. P. Hamilton, M. Jaffe, P. Haslinger, Q. Simmons, H. Müller, and J. Khoury, 'Atom-interferometry constraints on dark energy', *Science* **349,** 849–851 (2015) (cit. on pp. 2, 141).

40. K. van Tilburg, N. Leefer, L. Bougas, and D. Budker, 'Search for Ultralight Scalar Dark Matter with Atomic Spectroscopy', *Phys. Rev. Lett.* **115,** 011802 (2015) (cit. on p. 2).

41. B. Elder, J. Khoury, P. Haslinger, M. Jaffe, H. Müller, and P. Hamilton, 'Chameleon dark energy and atom interferometry', *Phys. Rev. D* **94,** 044051 (2016) (cit. on p. 2).

42. A.G. Manning, R.I. Khakimov, R.G. Dall, and A.G. Truscott, 'Wheeler's delayed-choice gedanken experiment with a single atom', *Nat. Physics* **11,** 539–542 (2015) (cit. on p. 2).

43. J. Peise, I. Kruse, K. Lange, B. Lücke, L. Pezzè, J. Arlt, W. Ertmer, K. Hammerer, L. Santos, A. Smerzi, and C. Klempt, 'Satisfying the Einstein-Podolsky-Rosen criterion with massive particles', *Nat. Commun.* **6,** 8984 (2015) (cit. on p. 2).

44. N.J. Engelsen, R. Krishnakumar, O. Hosten, and M.A. Kasevich, 'Bell Correlations in Spin-Squeezed States of 500 000 Atoms', *Phys. Rev. Lett.* **118,** 140401 (14 2017) (cit. on p. 2).

45. R.P. Middlemiss, A. Samarelli, D.J. Paul, J. Hough, S. Rowan, and G.D. Hammond, 'Measurement of the Earth tides with a MEMS gravimeter', *Nature* **531,** 614–617 (2016) (cit. on p. 2).

46. L. Timmen, 'Absolute and relative gravimetry',
Sciences of Geodesy-I, Springer (2010), 1–48 (cit. on p. 2).

47. M.A. Zumberge, R.L. Rinker, and J.E. Faller, 'A Portable Apparatus for Absolute Measurements of the Earth's Gravity',
Metrologia **18,** 145 (1982) (cit. on p. 2).

48. T.M. Niebauer, G.S. Sasagawa, J.E. Faller, R. Hilt, and F. Klopping, 'A new generation of absolute gravimeters',
Metrologia **32,** 159 (1995) (cit. on pp. 2, 91).

49. W.A. Prothero Jr. and J.M. Goodkind, 'A superconducting gravimeter',
Rev. Sci. Instrum. **39,** 1257–1262 (1968) (cit. on p. 2).

50. S. Okubo, S. Yoshida, T. Sato, Y. Tamura, and Y. Imanishi, 'Verifying the precision of a new generation absolute gravimeter FG5—Comparison with superconducting gravimeters and detection of oceanic loading tide',
Geophys. Res. Lett. **24,** 489–492 (1997) (cit. on p. 2).

51. Y. Imanishi, T. Sato, T. Higashi, W. Sun, and S. Okubo, 'A Network of Superconducting Gravimeters Detects Submicrogal Coseismic Gravity Changes',
Science **306,** 476–478 (2004) (cit. on p. 2).

52. C. Salomon, J. Dalibard, W.D. Phillips, A. Clairon, and S. Guellati, 'Laser Cooling of Cesium Atoms Below 3 μK',
Eur. Phys. Lett. **12,** 683 (1990) (cit. on pp. 2, 32).

53. W.D. Phillips, P.D. Lett, S.L. Rolston, C.E. Tanner, R.N. Watts, C.I. Westbrook, C. Salomon, J. Dalibard, A. Clairon, and S. Guellati, 'Optical Molasses: The Coldest Atoms Ever',
Phys. Scripta **1991,** 20 (1991) (cit. on pp. 2, 32).

54. Y. Bidel, O. Carraz, R. Charrière, M. Cadoret, N. Zahzam, and A. Bresson, 'Compact cold atom gravimeter for field applications',
Appl. Phys. Lett. **102,** 144107 (2013) (cit. on pp. 2, 81).

55. C. Freier, M. Hauth, V. Schkolnik, B. Leykauf, M. Schilling, H. Wziontek, H.-G. Scherneck, J. Müller, and A. Peters, 'Mobile quantum gravity sensor with unprecedented stability',
J. Phys. Conf. Ser. **723,** 012050 (2016) (cit. on pp. 2, 81, 85).

56. B. Fang *et al.*, 'Metrology with atom interferometry: inertial sensors from laboratory to field applications',
J. Phys. Conf. Ser. **723,** 012049 (2016) (cit. on pp. 2, 81, 85).

57. Q. Bodart, S. Merlet, N. Malossi, F. Pereira Dos Santos, P. Bouyer, and A. Landragin, 'A cold atom pyramidal gravimeter with a single laser beam',
Appl. Phys. Lett. **96,** 134101 (2010) (cit. on pp. 2, 139).

58. URL: `http://www.muquans.com/` (cit. on pp. 2, 139).

59. URL: `http://www.aosense.com/` (cit. on p. 2).

60. A.D. Cronin, J. Schmiedmayer, and D.E. Pritchard, 'Optics and interferometry with atoms and molecules',
Rev. Mod. Phys. **81,** 1051–1129 (2009) (cit. on p. 3).

61. M. Kozuma, L. Deng, E.W. Hagley, J. Wen, R. Lutwak, K. Helmerson, S.L. Rolston, and W.D. Phillips, 'Coherent Splitting of Bose-Einstein Condensed Atoms with Optically Induced Bragg Diffraction',
Phys. Rev. Lett. **82,** 871–875 (1999) (cit. on pp. 3, 35).

62. Y. Torii, Y. Suzuki, M. Kozuma, T. Sugiura, T. Kuga, L. Deng, and E.W. Hagley, 'Mach-Zehnder Bragg interferometer for a Bose-Einstein condensate',
Phys. Rev. A **61,** 041602 (2000) (cit. on pp. 3, 35).

63. C. Antoine and C.J. Bordé, 'Quantum theory of atomic clocks and gravito-inertial sensors: an update',
Jour. Opt. B **5,** 199 (2003) (cit. on p. 3).

64. M. Kasevich, D.S. Weiss, E. Riis, K. Moler, S. Kasapi, and S. Chu, 'Atomic velocity selection using stimulated Raman transitions',
Phys. Rev. Lett. **66,** 2297–2300 (1991) (cit. on pp. 3, 4, 63, 79, 88).

65. C.J. Bordé, 'Atomic interferometry with internal state labelling',
Phys. Rev. A **140,** 10–12 (1989) (cit. on pp. 3, 34).

66. S.S. Szigeti, J.E. Debs, J.J. Hope, N.P. Robins, and J.D. Close, 'Why momentum width matters for atom interferometry with Bragg pulses',
New J. Phys. **14,** 023009 (2012) (cit. on pp. 3, 38, 54, 63, 84).

67. H. Müller, S.-w. Chiow, Q. Long, S. Herrmann, and S. Chu, 'Atom Interferometry with up to 24-Photon-Momentum-Transfer Beam Splitters',
Phys. Rev. Lett. **100,** 180405 (2008) (cit. on pp. 3, 37, 76, 98, 119).

68. S.-w. Chiow, T. Kovachy, H.-C. Chien, and M.A. Kasevich, '102$\hbar$k Large Area Atom Interferometers',
Phys. Rev. Lett. **107,** 130403 (2011) (cit. on pp. 3, 38, 119, 138).

69. T. Kovachy, S.-w. Chiow, and M.A. Kasevich, 'Adiabatic-rapid-passage multiphoton Bragg atom optics',
Phys. Rev. A **86,** 011606 (2012) (cit. on pp. 3, 40, 119).

70. T. Kovachy, P. Asenbaum, C. Overstreet, C.A. Donnelly, S.M. Dickerson, A. Sugarbaker, J.M. Hogan, and M.A. Kasevich, 'Quantum superposition at the half-metre scale',
Nature **528,** 530–533 (2015) (cit. on pp. 3, 38, 104, 106, 119, 127, 128, 130, 135, 138).

71. H. Müller, S.-w. Chiow, S. Herrmann, and S. Chu, 'Atom Interferometers with Scalable Enclosed Area',
Phys. Rev. Lett. **102,** 240403 (2009) (cit. on pp. 3, 119, 123).

72. G.D. McDonald, C.C.N. Kuhn, S. Bennetts, J.E. Debs, K.S. Hardman, M. Johnsson, J.D. Close, and N.P. Robins, '80 $\hbar$k momentum separation with Bloch oscillations in an optically guided atom interferometer',
Phys. Rev. A **88,** 053620 (2013) (cit. on pp. 3, 8, 95, 119, 123, 138).

73. J.M. McGuirk, M.J. Snadden, and M.A. Kasevich, 'Large area light-pulse atom interferometry',
Phys. Rev. Lett. **85,** 4498 (2000) (cit. on pp. 3, 119).

74. K. Kotru, D.L. Butts, J.M. Kinast, and R.E. Stoner, 'Large-Area Atom Interferometry with Frequency-Swept Raman Adiabatic Passage',
Phys. Rev. Lett. **115,** 103001 (2015) (cit. on pp. 3, 40, 119).

75. P. Cladé, S. Guellati-Khélifa, F. Nez, and F. Biraben, 'Large Momentum Beam Splitter Using Bloch Oscillations',
Phys. Rev. Lett. **102,** 240402– (2009) (cit. on pp. 3, 119, 123).

76. S. Abend, 'Grossflächige Atominterferometer für die Inertialsensorik',
Diplomarbeit, Leibniz Universität Hannover (2010) (cit. on p. 3).

77. T. Lévèque, A. Gauguet, F. Michaud, F. Pereira Dos Santos, and A. Landragin, 'Enhancing the Area of a Raman Atom Interferometer Using a Versatile Double-Diffraction Technique',
Phys. Rev. Lett. **103,** 080405 (2009) (cit. on pp. 3, 4, 36, 119, 126).

78. N. Malossi, Q. Bodart, S. Merlet, T. Lévèque, A. Landragin, and F. Pereira Dos Santos, 'Double diffraction in an atomic gravimeter',
Phys. Rev. A **81,** 013617 (2010) (cit. on pp. 3, 4, 119).

79. E. Giese, A. Roura, G. Tackmann, E.M. Rasel, and W.P. Schleich, 'Double Bragg diffraction: A tool for atom optics',
Phys. Rev. A **88,** 053608– (2013) (cit. on pp. 3, 30, 36).

80. H. Ahlers *et al.*, 'Double Bragg Interferometry',
Phys. Rev. Lett. **116,** 173601 (2016) (cit. on pp. 3, 6, 11, 30, 36, 119, 123, 127, 130, 138).

81. M.G. Sagnac, 'Sur la preuve de la réalité de l'éether lumineux par l'expérience de l'interférographe tournant',
Compt. Rend. des Sc. d. l'Acad d. Sc. **157,** 1410–1413 (1913) (cit. on p. 4).

82. M. Gilowski, 'Quantitative Analyse der Auflösungsbegrenzung eines atomaren Gyroskops',
Dissertation, Leibniz Universität Hannover (2010) (cit. on p. 4).

83. C. Schubert, 'Grossflächiges Sagnac Interferometer mit kalten Atomen',
Dissertation, Leibniz Universität Hannover (2012) (cit. on pp. 4, 109).

84. G. Tackmann, 'Raman interferometry with free-falling and trapped atoms',
Dissertation, Leibniz Universität Hannover (2013) (cit. on pp. 4, 109).

85. P. Berg, 'Ein rauscharmes Materiewellen-Gyroskop hoher Genauigkeit',
Dissertation, Leibniz Universität Hannover (2014) (cit. on pp. 4, 49, 90, 109, 116).

86. T. Müller, T. Wendrich, M. Gilowski, C. Jentsch, E.M. Rasel, and W. Ertmer, 'Versatile compact atomic source for high-resolution dual atom interferometry',
Phys. Rev. A **76,** 063611 (2007) (cit. on p. 4).

87. G. Tackmann, P. Berg, S. Abend, C. Schubert, W. Ertmer, and E.M. Rasel, 'Large-area Sagnac atom interferometer with robust phase read out',
C. R. Physique **15,** 884–897 (2014) (cit. on p. 4).

88. G. Tackmann, P. Berg, C. Schubert, S. Abend, M. Gilowski, W. Ertmer, and E. M. Rasel, 'Self-alignment of a compact large-area atomic Sagnac interferometer',
New J. Phys. **14,** 015002 (2012) (cit. on pp. 4, 7, 55, 88, 98, 107, 110, 118).

89. S.N. Bose, 'Plancks Gesetz und Lichtquantenhypothese',
Z. Phys. A **26,** (1924) (cit. on pp. 5, 19).

90. A. Einstein, 'Quantentheorie des einatomigen idealen Gases',
Sitzungsbericht Kgl. Preuss. Akad. Wiss. (1924) (cit. on pp. 5, 19).

91. M.H. Anderson, J.R. Ensher, M.R. Matthews, C.E. Wieman, and E.A. Cornell, 'Observation of Bose-Einstein Condensation in a Dilute Atomic Vapor',
Science **269,** 198–201 (1995) (cit. on pp. 5, 18, 19).

92. C.C. Bradley, C.A. Sackett, J.J. Tollett, and R.G. Hulet, 'Evidence of Bose-Einstein Condensation in an Atomic Gas with Attractive Interactions',
Phys. Rev. Lett. **75,** 1687–1690 (1995) (cit. on pp. 5, 19).

93. K.B. Davis, M.-O. Mewes, M.R. Andrews, N.J. van Druten, D.S. Durfee, D.M. Kurn, and W. Ketterle, 'Bose-Einstein Condensation in a Gas of Sodium Atoms',
Phys. Rev. Lett. **75,** 3969–3973 (1995) (cit. on pp. 5, 18, 19).

94. M.R. Andrews, C.G. Townsend, H.-J. Miesner, D.S. Durfee, D.M. Kurn, and W. Ketterle, 'Observation of Interference Between Two Bose Condensates',
Science **275,** 637–641 (1997) (cit. on p. 5).

95. Y. Shin, M. Saba, T.A. Pasquini, W. Ketterle, D.E. Pritchard, and A.E. Leanhardt, 'Atom Interferometry with Bose-Einstein Condensates in a Double-Well Potential',
Phys. Rev. Lett. **92,** 050405 (2004) (cit. on p. 5).

96. Y. Shin, C. Sanner, G.-B. Jo, T.A. Pasquini, M. Saba, W. Ketterle, D.E. Pritchard, M. Vengalattore, and M. Prentiss, 'Interference of Bose-Einstein condensates split with an atom chip',
Phys. Rev. A **72,** 021604 (2005) (cit. on p. 5).

97. J.E. Debs, P.A. Altin, T.H. Barter, D. Döring, G.R. Dennis, G. McDonald, R.P. Anderson, J.D. Close, and N.P. Robins, 'Cold-atom gravimetry with a Bose-Einstein condensate',
Phys. Rev. A **84,** 033610 (2011) (cit. on pp. 5, 6, 81, 111, 117).

98. H. Müntinga, H. Ahlers, A. Wenzlawski, M. Krutzik, *et al.*, 'Interferometry with Bose-Einstein Condensates in Microgravity',
Phys. Rev. Lett. **110,** 093602 (2013) (cit. on pp. 5–7, 11, 29, 58, 110, 111, 117, 118).

99. S.M. Dickerson, J.M. Hogan, A. Sugarbaker, D.M.S. Johnson, and M.A. Kasevich, 'Multiaxis Inertial Sensing with Long-Time Point Source Atom Interferometry',
Phys. Rev. Lett. **111,** 083001 (2013) (cit. on pp. 5, 6, 81, 121).

100. A. Sugarbaker, S.M. Dickerson, J.M. Hogan, D.M.S. Johnson, and M.A. Kasevich, 'Enhanced Atom Interferometer Readout through the Application of Phase Shear',
Phys. Rev. Lett. **111,** 113002 (2013) (cit. on pp. 5, 29, 81, 104, 106, 110, 118, 134).

101. O. Hosten, N.J. Engelsen, R. Krishnakumar, and M.A. Kasevich, 'Measurement noise 100 times lower than the quantum-projection limit using entangled atoms',
Nature (2016) (cit. on pp. 5, 139).

102. O. Hosten, R. Krishnakumar, N. J. Engelsen, and M.A. Kasevich, 'Quantum phase magnification',
Science **352,** 1552–1555 (2016) (cit. on pp. 5, 139).

103. C. Orzel, A. K. Tuchman, M. L. Fenselau, M. Yasuda, and M. A. Kasevich, 'Squeezed states in a Bose-Einstein condensate',
Science **291,** 2386–2389 (2001) (cit. on pp. 5, 139).

104. C. Klempt, O. Topic, G. Gebreyesus, M. Scherer, T. Henninger, P. Hyllus, W. Ertmer, L. Santos, and J.J. Arlt, 'Parametric Amplification of Vacuum Fluctuations in a Spinor Condensate',
Phys. Rev. Lett. **104,** 195303 (2010) (cit. on pp. 5, 139).

105. B. Lücke, J. Peise, G. Vitagliano, J.J. Arlt, L. Santos, G. Tóth, and C. Klempt, 'Detecting Multiparticle Entanglement of Dicke States',
Phys. Rev. Lett. **112,** 155304 (2014) (cit. on pp. 5, 139).

106. B. Lücke *et al.*, 'Twin Matter Waves for Interferometry Beyond the Classical Limit',
Science **334,** 773–776 (2011) (cit. on pp. 5, 139).

107. R. Bücker, J. Grond, S. Manz, T. Berrada, T. Betz, C. Koller, U. Hohenester, T. Schumm, A. Perrin, and J. Schmiedmayer, 'Twin-atom beams',
Nat. Phys. **7,** 608–611 (2011) (cit. on pp. 5, 139).

108. T. Berrada, S. van Frank, R. Bücker, T. Schumm, J.-F. Schaff, and J. Schmiedmayer, 'Integrated Mach-Zehnder interferometer for Bose-Einstein condensates',
Nat. Commun. **4,** 2077 (2013) (cit. on pp. 5, 8, 139).

109. I. Kruse, K. Lange, J. Peise, B. Lücke, L. Pezzè, J.J. Arlt, W. Ertmer, C. Lisdat, L. Santos, A. Smerzi, and C. Klempt, 'Improvement of an Atomic Clock using Squeezed Vacuum',
Phys. Rev. Lett. **117,** 143004 (2016) (cit. on pp. 5, 139).

110. T. van Zoest *et al.*, 'Bose-Einstein Condensation in Microgravity',
Science **328,** 1540–1543 (2010) (cit. on pp. 6, 11).

111. W. Hänsel, P. Hommelhoff, T.W. Hänsch, and J. Reichel, 'Bose–Einstein condensation on a microelectronic chip',
Nature **413,** 498–501 (2001) (cit. on p. 6).

112. R. Folman, P. Krüger, J. Schmiedmayer, J. Denschlag, and C. Henkel, 'Microscopic atom optics: from wires to an atom chip',
Adv. At. Mol. Opt. Phys. **48,** 263–356 (2002) (cit. on p. 6).

113. J. Fortágh and C. Zimmermann, 'Magnetic microtraps for ultracold atoms',
Rev. Mod. Phys. **79,** 235 (2007) (cit. on p. 6).

114. M. Horikoshi and K. Nakagawa, 'Atom chip based fast production of Bose–Einstein condensate',
Appl. Phys. B **82,** 363–366 (2006) (cit. on p. 6).

115. S. Aubin, S. Myrskog, M.H.T. Extavour, L.J. LeBlanc, D. McKay, A. Stummer, and J.H. Thywissen, 'Rapid sympathetic cooling to Fermi degeneracy on a chip',
Nat. Phys. **2,** 384–387 (2006) (cit. on p. 6).

116. D.M. Farkas, K.M. Hudek, E.A. Salim, S.R. Segal, M.B. Squires, and D.Z. Anderson, 'A compact, transportable, microchip-based system for high repetition rate production of Bose–Einstein condensates',
Appl. Phys. Lett. **96,** 093102 (2010) (cit. on pp. 6, 139).

117. J. Rudolph *et al.*, 'A high-flux BEC source for mobile atom interferometers',
New J. Phys. **17,** 065001 (2015) (cit. on pp. 6, 63, 117, 118, 133, 138, 140).

118. URL: `http://www.coldquanta.com/` (cit. on p. 6).

119. M.D. Barrett, J.A. Sauer, and M.S. Chapman, 'All-Optical Formation of an Atomic Bose-Einstein Condensate',
Phys. Rev. Lett. **87,** 010404 (2001) (cit. on p. 6).

120. G. Cennini, G. Ritt, C. Geckeler, and M. Weitz, 'All-Optical Realization of an Atom Laser',
Phys. Rev. Lett. **91,** 240408 (2003) (cit. on p. 6).

121. J.-F. Clément, J.-P. Brantut, M. Robert-de-Saint-Vincent, R. A. Nyman, A. Aspect, T. Bourdel, and P. Bouyer, 'All-optical runaway evaporation to Bose-Einstein condensation',
Phys. Rev. A **79,** 061406 (2009) (cit. on p. 6).

122. S. Stellmer, B. Pasquiou, R. Grimm, and F. Schreck, 'Laser Cooling to Quantum Degeneracy',
Phys. Rev. Lett. **110,** 263003 (2013) (cit. on p. 6).

123. E.W. Streed, A.P. Chikkatur, T.L. Gustavson, M. Boyd, Y. Torii, D. Schneble, G.K. Campbell, D.E. Pritchard, and W. Ketterle, 'Large atom number Bose-Einstein condensate machines',
Rev. Sci. Instrum. **77,** 023106 (2006) (cit. on p. 6).

124. K.S. Hardman *et al.*, 'Simultaneous Precision Gravimetry and Magnetic Gradiometry with a Bose-Einstein Condensate: A High Precision, Quantum Sensor',
Phys. Rev. Lett. **117,** 138501 (2016) (cit. on pp. 6, 110, 111).

125. S. Bernet, M.K. Oberthaler, R. Abfalterer, J. Schmiedmayer, and A. Zeilinger, 'Coherent Frequency Shift of Atomic Matter Waves',
Phys. Rev. Lett. **77,** 5160–5163 (1996) (cit. on p. 6).

126. Y. Castin and J. Dalibard, 'Relative phase of two Bose-Einstein condensates',
Phys. Rev. A **55,** 4330–4337 (1997) (cit. on p. 6).

127. J.E. Simsarian, J. Denschlag, M. Edwards, C.W. Clark, L. Deng, E.W. Hagley, K. Helmerson, S.L. Rolston, and W.D. Phillips, 'Imaging the Phase of an Evolving Bose-Einstein Condensate Wave Function',
Phys. Rev. Lett. **85,** 2040–2043 (2000) (cit. on p. 6).

128. A.O. Jamison, J.N. Kutz, and S. Gupta, 'Atomic interactions in precision interferometry using Bose-Einstein condensates',
Phys. Rev. A **84,** 043643 (2011) (cit. on pp. 6, 111).

129. R. Jannin, P. Cladé, and S. Guellati-Khélifa, 'Phase shift due to atom-atom interactions in a light-pulse atom interferometer',
Phys. Rev. A **92,** 013616 (2015) (cit. on pp. 6, 111).

130. S. Chu, J.E. Bjorkholm, A. Ashkin, J.P. Gordon, and L.W. Hollberg, 'Proposal for optically cooling atoms to temperatures of the order of 10- 6 K',
Opt. Lett. **11,** 73–75 (1986) (cit. on p. 6).

131. H. Ammann and N. Christensen, 'Delta Kick Cooling: A New Method for Cooling Atoms',
Phys. Rev. Lett. **78,** 2088–2091 (1997) (cit. on p. 6).

132. M. Morinaga, I. Bouchoule, J.-C. Karam, and C. Salomon, 'Manipulation of Motional Quantum States of Neutral Atoms',
Phys. Rev. Lett. **83,** 4037–4040 (1999) (cit. on p. 6).

133. T. Kovachy, J.M. Hogan, A. Sugarbaker, S.M. Dickerson, C.A. Donnelly, C. Overstreet, and M.A. Kasevich, 'Matter Wave Lensing to Picokelvin Temperatures',
Phys. Rev. Lett. **114,** 143004 (2015) (cit. on pp. 6, 58, 111, 117, 118).

134. O. Carnal and J. Mlynek, 'Young's double-slit experiment with atoms: A simple atom interferometer',
Phys. Rev. Lett. **66,** 2689–2692 (1991) (cit. on p. 6).

135. L. Timmen, O. Gitlein, J. Müller, G. Strykowski, and R. Forsberg, 'Absolute gravimetry with the Hannover meters JILAg-3 and FG5-220, and their deployment in a Danish-German cooperation',
Z. Geodäsie, Geoinformation und Landmanagement **133,** 149–163 (2008) (cit. on pp. 7, 132).

136. H. Steffen, O. Gitlein, H. Denker, J. Müller, and L. Timmen, 'Present rate of uplift in Fennoscandia from GRACE and absolute gravimetry',
Tectonophysics **474,** 69–77 (2009) (cit. on pp. 7, 132).

137. J. Müller, M. Naeimi, O. Gitlein, L. Timmen, and H. Denker, 'A land uplift model in Fennoscandia combining GRACE and absolute gravimetry data',
Phys. Chem. Earth **53,** 54–60 (2012) (cit. on pp. 7, 132).

138. A. Louchet-Chauvet, T. Farah, Q. Bodart, A. Clairon, A. Landragin, S. Merlet, and F. Pereira Dos Santos, 'The influence of transverse motion within an atomic gravimeter',
New J. Phys. **13,** 065025– (2011) (cit. on pp. 7, 8, 55, 83, 113, 117, 118).

139. G.-B. Jo, Y. Shin, S. Will, T.A. Pasquini, M. Saba, W. Ketterle, D.E. Pritchard, M. Vengalattore, and M. Prentiss, 'Long phase coherence time and number squeezing of two Bose-Einstein condensates on an atom chip',
Phys. Rev. Lett. **98,** 030407 (2007) (cit. on p. 8).

140. J.H.T. Burke, B. Deissler, K.J. Hughes, and C.A. Sackett, 'Confinement effects in a guided-wave atom interferometer with millimeter-scale arm separation',
Phys. Rev. A **78,** 023619 (2008) (cit. on p. 8).

141. Y.-J. Wang *et al.*, 'Atom Michelson Interferometer on a Chip Using a Bose-Einstein Condensate',
Phys. Rev. Lett. **94,** 090405 (2005) (cit. on p. 8).

142. G.D. McDonald *et al.*, 'Optically guided linear Mach-Zehnder atom interferometer',
Phys. Rev. A **87,** 013632 (2013) (cit. on p. 8).

143. G.D. McDonald, C.C.N. Kuhn, S. Bennetts, J.E. Debs, K.S. Hardman, J.D. Close, and N.P. Robins, 'A faster scaling in acceleration-sensitive atom interferometers',
Eur. Phys. Lett. **105,** 63001 (2014) (cit. on pp. 8, 123).

144. G. Tackmann, B. Pelle, A. Hilico, Q. Beaufils, and F. Pereira Dos Santos, 'Raman-laser spectroscopy of Wannier-Stark states',
Phys. Rev. A **84,** 063422 (2011) (cit. on pp. 8, 45).

145. A. Hilico, C. Solaro, M.-K. Zhou, M. Lopez, and F. Pereira Dos Santos, 'Contrast decay in a trapped-atom interferometer',
Phys. Rev. A **91,** 053616 (2015) (cit. on p. 8).

146. N. Poli, F.-Y. Wang, M.G. Tarallo, A. Alberti, M. Prevedelli, and G.M. Tino, 'Precision measurement of gravity with cold atoms in an optical lattice and comparison with a classical gravimeter',
Phys. Rev. Lett. **106,** 038501 (2011) (cit. on p. 8).

147. B. Pelle, A. Hilico, G. Tackmann, Q. Beaufils, and F. Pereira Dos Santos, 'State-labeling Wannier-Stark atomic interferometers',
Phys. Rev. A **87,** 023601 (2013) (cit. on p. 8).

148. T. Kovachy, J.M. Hogan, D.M.S. Johnson, and M.A. Kasevich, 'Optical lattices as waveguides and beam splitters for atom interferometry: An analytical treatment and proposal of applications', *Phys. Rev. A* **82,** 013638 (2010) (cit. on pp. 8, 141).

149. R. Charriere, M. Cadoret, N. Zahzam, Y. Bidel, and A. Bresson, 'Local gravity measurement with the combination of atom interferometry and Bloch oscillations', *Phys. Rev. A* **85,** 013639 (2012) (cit. on pp. 8, 68).

150. M. Andia, R. Jannin, F. Nez, F. Biraben, S. Guellati-Khélifa, and P. Cladé, 'Compact atomic gravimeter based on a pulsed and accelerated optical lattice', *Phys. Rev. A* **88,** 031605 (2013) (cit. on pp. 8, 68).

151. K.J. Hughes, J.H.T. Burke, and C.A. Sackett, 'Suspension of Atoms Using Optical Pulses, and Application to Gravimetry', *Phys. Rev. Lett.* **102,** 150403 (2009) (cit. on pp. 8, 68).

152. E. Giese, A. Friedrich, S. Abend, E.M. Rasel, and W.P. Schleich, 'Light shifts in atomic Bragg diffraction', *Phys. Rev. A* **94,** 063619 (6 2016) (cit. on pp. 8, 49, 115, 118, 138).

153. C. Henkel and S. Pötting, 'Coherent transport of matter waves', *Appl. Phys. B* **72,** 73–80 (2001) (cit. on p. 8).

154. J.H.T. Burke and C.A. Sackett, 'Scalable Bose-Einstein-condensate Sagnac interferometer in a linear trap', *Phys. Rev. A* **80,** 061603 (2009) (cit. on p. 8).

155. E.G. Marti, R. Olf, and D.M. Stamper-Kurn, 'Collective excitation interferometry with a toroidal Bose-Einstein condensate', *Phys. Rev. A* **91,** 013602 (2015) (cit. on p. 8).

156. S. Abend, M. Gebbe, M. Gersemann, H. Ahlers, H. Müntinga, E. Giese, N. Gaaloul, C. Schubert, C. Lämmerzahl, W. Ertmer, W. P. Schleich, and E. M. Rasel, 'Atom-Chip Fountain Gravimeter', *Phys. Rev. Lett.* **117,** 203003 (2016) (cit. on pp. 9, 81, 95, 102, 117, 118).

157. URL: `http://www.qurope.eu/manifesto/` (cit. on p. 10).

158. URL: `https://ec.europa.eu/digital-single-market/en/news/european-commission-will-launch-eu1-billion-quantum-technologies-flagship/` (cit. on p. 10).

159. J. Grosse, S.T. Seidel, D. Becker, M.D. Lachmann, M. Scharringhausen, C. Braxmaier, and E.M. Rasel, 'Design and qualification of an UHV system for operation on sounding rockets', *J. Vac. Sci. Technol. A* **34,** 031606 (2016) (cit. on p. 10).

160. A. Kubelka-Lange, S. Herrmann, J. Grosse, C. Lämmerzahl, E.M. Rasel, and C. Braxmaier, 'A three-layer magnetic shielding for the MAIUS-1 mission on a sounding rocket', *Rev. Sci. Instrum.* **87,** 063101 (2016) (cit. on p. 10).

161. V. Schkolnik *et al.*, 'A compact and robust diode laser system for atom interferometry on a sounding rocket', *Appl. Phys. B* **122,** 1–8 (2016) (cit. on pp. 10, 139, 140).

162. URL: `http://www.dlr.de/dlr/desktopdefault.aspx/tabid-10081/151_read-20337/#/gallery/25194/` (cit. on p. 10).

163. URL: `http://www.geoq.uni-hannover.de` (cit. on p. 10).

164. A. Wenzlawski, 'Matter-wave optics in microgravity: Laser technology and applications', Dissertation, Universität Hamburg (2013) (cit. on pp. 11, 12, 56, 59, 60, 62, 112).

165. M. Krutzik, 'Matter wave interferometry in microgravity', Dissertation, Humboldt-Universität zu Berlin (2014) (cit. on pp. 11, 12, 17, 19, 22, 59, 60, 62, 112).

166. T. van Zoest, 'Realisierung Erster Quantenentarteter Gase Unter Schwerelosigkeit', Dissertation, Leibniz Universität Hannover (2008) (cit. on pp. 11, 12, 14, 15, 17).

167. H.J. Metcalf and P. van der Straten, 'Laser Cooling and Trapping',
Springer (2002) (cit. on p. 11).

168. F. Dalfovo, S. Giorgini, L.P. Pitaevskii, and S. Stringari, 'Theory of Bose-Einstein condensation in trapped gases',
Rev. Mod. Phys. **71,** 463 (1999) (cit. on p. 11).

169. W. Ketterle, D.S. Durfee, and D.M. Stamper-Kurn, 'Making, probing and understanding Bose-Einstein condensates',
Proceedings of the International School of Physics 'Enrico Fermi' **Course 140,** 67–176 (1999) (cit. on pp. 11, 16, 18).

170. C.J. Pethick and H. Smith, 'Bose-Einstein condensation in dilute gases',
Cambridge University Press (2002) (cit. on pp. 11, 19, 20).

171. M. Gebbe, 'Determination of local gravity with an atom chip based matter wave interferometer',
Masterarbeit, Universität Bremen (2015) (cit. on pp. 14, 25, 54, 55, 85, 112).

172. J.H. Shirley, 'Modulation transfer processes in optical heterodyne saturation spectroscopy',
Opt. Lett. **7,** 537–539 (1982) (cit. on pp. 14, 116).

173. M. Schiemangk *et al.*, 'High-power, micro-integrated diode laser modules at 767 and 780 nm for portable quantum gas experiments',
Appl. Opt. **54,** 5332–5338 (2015) (cit. on pp. 14, 139, 140).

174. D.A. Steck, 'Rubidium 87 D Line Data available online at `http://steck.us/alkalidata`',
(revision 2.1.5, 13 January 2015) (cit. on pp. 16, 165, 166).

175. T.W. Hänsch and A.L. Schawlow, 'Cooling of gases by laser radiation',
Opt. Com. **13,** 68–69 (1975) (cit. on p. 17).

176. A. Ashkin, 'Trapping of atoms by resonance radiation pressure',
Phys. Rev. Lett. **40,** 729 (1978) (cit. on p. 17).

177. W.D. Phillips and H. Metcalf, 'Laser deceleration of an atomic beam',
Phys. Rev. Lett. **48,** 596 (1982) (cit. on p. 17).

178. S. Chu, L. Hollberg, J.E. Bjorkholm, A. Cable, and A. Ashkin, 'Three-dimensional viscous confinement and cooling of atoms by resonance radiation pressure',
Phys. Rev. Lett. **55,** 48 (1985) (cit. on p. 17).

179. E.L. Raab, M. Prentiss, A. Cable, S. Chu, and D.E. Pritchard, 'Trapping of Neutral Sodium Atoms with Radiation Pressure',
Phys. Rev. Lett. **59,** 2631–2634 (1987) (cit. on p. 17).

180. P.D. Lett, R.N. Watts, C.I. Westbrook, W.D. Phillips, P.L. Gould, and H.J. Metcalf, 'Observation of atoms laser cooled below the Doppler limit',
Phys. Rev. Lett. **61,** 169 (1988) (cit. on p. 17).

181. M. Kasevich and S. Chu, 'Laser cooling below a photon recoil with three-level atoms',
Phys. Rev. Lett. **69,** 1741–1744 (1992) (cit. on pp. 17, 40).

182. W.D. Phillips, 'Nobel Lecture: Laser cooling and trapping of neutral atoms',
Rev. Mod. Phys. **70,** 721–741 (1998) (cit. on p. 17).

183. S. Chu, 'Nobel Lecture: The manipulation of neutral particles',
Rev. Mod. Phys. **70,** 685–706 (1998) (cit. on p. 17).

184. K.B. Davis, M.-O. Mewes, M.A. Joffe, M.R. Andrews, and W. Ketterle, 'Evaporative Cooling of Sodium Atoms',
Phys. Rev. Lett. **74,** 5202–5205 (1995) (cit. on p. 17).

185. W. Petrich, M.H. Anderson, J.R. Ensher, and E.A. Cornell, 'Stable, Tightly Confining Magnetic Trap for Evaporative Cooling of Neutral Atoms',
Phys. Rev. Lett. **74,** 3352–3355 (1995) (cit. on p. 18).

186. Y.V. Gott, M.S. Ioffe, and V.G. Telkovskii, 'Some new results on confinement in magnetic traps', *Academy of Sciences, Moscow* (1962) (cit. on p. 18).

187. D.E. Pritchard, 'Cooling neutral atoms in a magnetic trap for precision spectroscopy', *Phys. Rev. Lett.* **51,** 1336 (1983) (cit. on p. 18).

188. V.S. Bagnato, G.P. Lafyatis, A.G. Martin, E.L. Raab, R.N. Ahmad-Bitar, and D.E. Pritchard, 'Continuous stopping and trapping of neutral atoms', *Phys. Rev. Lett.* **58,** 2194 (1987) (cit. on pp. 18, 20).

189. J. Reichel and V. Vuletic, 'Atom chips', John Wiley & Sons (2011) (cit. on p. 18).

190. M. Planck, 'Über das Gesetz der Energieverteilung im Normalspektrum', *Ann. Phys.* **4,** 553 (1901) (cit. on p. 19).

191. Y. Kagan, E.L. Surkov, and G.V. Shlyapnikov, 'Evolution of a Bose-condensed gas under variations of the confining potential', *Phys. Rev. A* **54,** R1753–R1756 (1996) (cit. on pp. 21, 22).

192. Y. Castin and R. Dum, 'Bose-Einstein Condensates in Time Dependent Traps', *Phys. Rev. Lett.* **77,** 5315–5319 (27 1996) (cit. on pp. 21, 22).

193. F. Lienhart, S. Boussen, O. Carraz, N. Zahzam, Y. Bidel, and A. Bresson, 'Compact and robust laser system for rubidium laser cooling based on the frequency doubling of a fiber bench at 1560 nm', *Appl. Phys. B* **89,** 177–180 (2007) (cit. on p. 23).

194. O. Carraz, F. Lienhart, R. Charrière, M. Cadoret, N. Zahzam, Y. Bidel, and A. Bresson, 'Compact and robust laser system for onboard atom interferometry', *Appl. Phys. B* **97,** 405 (2009) (cit. on p. 23).

195. URL: `http://www.nktphotonics.com/` (cit. on pp. 23, 24).

196. S.S. Sané, S. Bennetts, J.E. Debs, C.C.N. Kuhn, G.D. McDonald, P.A. Altin, J.D. Close, and N.P. Robins, '11 W narrow linewidth laser source at 780nm for laser cooling and manipulation of Rubidium', *Opt. Express* **20,** 8915–8919 (2012) (cit. on p. 24).

197. S.-w. Chiow, T. Kovachy, J.M. Hogan, and M.A. Kasevich, 'Generation of 43 W of quasi-continuous 780 nm laser light via high-efficiency, single-pass frequency doubling in periodically poled lithium niobate crystals', *Opt. Lett.* **37,** 3861–3863 (2012) (cit. on p. 24).

198. P. Kaebert, 'Frequenzkontrolle und Stabilisierung eines faserbasierten Lasers bei 780nm', Bachelorarbeit, Leibniz Universität Hannover (2013) (cit. on pp. 24, 25).

199. URL: `http://www.hcphotonics.com/` (cit. on p. 24).

200. E.D. Black, 'An introduction to Pound–Drever–Hall laser frequency stabilization', *Am. J. Phys.* **69,** 79–87 (2001) (cit. on p. 24).

201. D.L. Hecht, 'Multifrequency acoustooptic diffraction', *IEEE Trans. Sonics. Ultrason.* **24,** 7–18 (1977) (cit. on p. 24).

202. N. Grove, 'A fiber-based laser system for a transportable quantum gravimeter', Masterarbeit, Leibniz Universität Hannover (2017) (cit. on pp. 24, 133).

203. M. Gersemann, 'Kohärente Beschleunigung von atomaren Ensembles in optischen Gittern zur Anwendung in der Quantensensorik', Masterarbeit, Leibniz Universität Hannover (2016) (cit. on p. 26).

204. P. Brozynski, 'Demonstration eines Chip-Gravimeters in QUANTUS-I', Bachelorarbeit, Leibniz Universität Hannover (2014) (cit. on p. 27).

205. J. Reichel, W. Hänsel, P. Hommelhoff, and T.W. Hänsch, 'Applications of integrated magnetic microtraps',
Appl. Phys. B **72,** 81–89 (2001) (cit. on pp. 28, 139).

206. L. de Broglie, 'Recherches sur la théorie des Quantas',
PhD thesis, Sorbonne Paris (1924) (cit. on p. 29).

207. C. Davisson and L. H. Germer, 'The Scattering of Electrons by a Single Crystal of Nickel',
Nature **119,** 558–560 (1927) (cit. on p. 29).

208. R. Colella, A. W. Overhauser, and S. A. Werner, 'Observation of Gravitationally Induced Quantum Interference',
Phys. Rev. Lett. **34,** 1472–1474 (1975) (cit. on p. 29).

209. D.W. Keith, C.R. Ekstrom, Q.A. Turchette, and D.E. Pritchard, 'An Interferometer for Atoms',
Phys. Rev. Lett. **66,** 2693–2696 (1991) (cit. on p. 29).

210. M. Arndt, O. Nairz, J. Voss-Andreae, C. Keller, G.v.d. Zouw, and A. Zeilinger, 'Wave-particle duality of C60 molecules',
Nature **401,** 680 (1999) (cit. on p. 29).

211. S. Gerlich *et al.*, 'A Kapitza–Dirac–Talbot–Lau interferometer for highly polarizable molecules',
Nat. Phys. **3,** 711–715 (2007) (cit. on p. 29).

212. S. Gerlich, S. Eibenberger, M. Tomandl, S. Nimmrichter, K. Hornberger, P.J. Fagan, J. Tüxen, M. Mayor, and M. Arndt, 'Quantum interference of large organic molecules',
Nat. Commun. **2,** 263 (2011) (cit. on p. 29).

213. S. Nimmrichter, K. Hornberger, P. Haslinger, and M. Arndt, 'Testing spontaneous localization theories with matter-wave interferometry',
Phys. Rev. A **83,** 043621 (2011) (cit. on p. 29).

214. S. Nimmrichter and K. Hornberger, 'Macroscopicity of mechanical quantum superposition states',
Phys. Rev. Lett. **110,** 160403 (2013) (cit. on p. 29).

215. E.M. Rasel, M.K. Oberthaler, H. Batelaan, J. Schmiedmayer, and A. Zeilinger, 'Atom Wave Interferometry with Diffraction Gratings of Light',
Phys. Rev. Lett. **75,** 2633–2637 (1995) (cit. on p. 29).

216. P.W. Graham, J.M. Hogan, M.A. Kasevich, and S. Rajendran, 'New method for gravitational wave detection with atomic sensors',
Phys. Rev. Lett. **110,** 171102 (2013) (cit. on pp. 32, 135).

217. J.M. Hogan and M.A. Kasevich, 'Atom-interferometric gravitational-wave detection using heterodyne laser links',
Phys. Rev. A **94,** 033632 (3 2016) (cit. on pp. 32, 135).

218. N. Nemitz, T. Ohkubo, M. Takamoto, I. Ushijima, M. Das, N. Ohmae, and H. Katori, 'Frequency ratio of Yb and Sr clocks with 5× 10- 17 uncertainty at 150 seconds averaging time',
Nat. Photon. **10,** 258–261 (2016) (cit. on p. 32).

219. C.J. Foot, 'Atomic Physics',
Oxford University Press (2005) (cit. on p. 33).

220. P.J. Martin, B.G. Oldaker, A.H. Miklich, and D.E. Pritchard, 'Bragg scattering of atoms from a standing light wave',
Phys. Rev. Lett. **60,** 515–518 (1988) (cit. on p. 35).

221. G. Birkl, M. Gatzke, I.H. Deutsch, S.L. Rolston, and W.D. Phillips, 'Bragg Scattering from Atoms in Optical Lattices',
Phys. Rev. Lett. **75,** 2823–2826 (1995) (cit. on p. 35).

222. W.L. Bragg, 'The Specular Reflection of X-rays.',
Nature **90,** 410 (1912) (cit. on p. 35).

223. W. Friedrich, P. Knipping, and M. Laue, 'Interferenzerscheinungen bei Röntgenstrahlen', *Ann. Phys.* **346,** 971–988 (1913) (cit. on p. 35).

224. A.O. Jamison, B. Plotkin-Swing, and S. Gupta, 'Advances in precision contrast interferometry with Yb Bose-Einstein condensates', *Phys. Rev. A* **90,** 063606 (2014) (cit. on p. 35).

225. T. Mazzoni, X. Zhang, R. Del Aguila, L. Salvi, N. Poli, and G.M. Tino, 'Large-momentum-transfer Bragg interferometer with strontium atoms', *Phys. Rev. A* **92,** 053619 (2015) (cit. on pp. 35, 68).

226. S. Wu, E. Su, and M.G. Prentiss, 'Demonstration of an Area-Enclosing Guided-Atom Interferometer for Rotation Sensing', *Phys. Rev. Lett.* **99,** 173201 (2007) (cit. on pp. 35, 98).

227. E. Su, S. Wu, and M.G. Prentiss, 'Atom interferometry using wave packets with constant spatial displacements', *Phys. Rev. A* **81,** 043631 (2010) (cit. on p. 35).

228. H. Müntinga, 'In Preparation', Dissertation, Universität Bremen (2017) (cit. on p. 36).

229. P. Cladé, T. Plisson, S. Guellati-Khélifa, F. Nez, and F. Biraben, 'Theoretical analysis of a large momentum beamsplitter using Bloch oscillations', *Eur. Phys. J. D* **59,** 349–360 (2010) (cit. on pp. 36, 47, 124).

230. H. Müller, S.-w. Chiow, and S. Chu, 'Atom-wave diffraction between the Raman-Nath and the Bragg regime: Effective Rabi frequency, losses, and phase shifts', *Phys. Rev. A* **77,** 23609 (2008) (cit. on p. 37).

231. F.J. Harris, 'On the use of windows for harmonic analysis with the discrete Fourier transform', *Proc. IEEE* **66,** 51–83 (1978) (cit. on p. 40).

232. J. Stenger, S. Inouye, A.P. Chikkatur, D.M. Stamper-Kurn, D.E. Pritchard, and W. Ketterle, 'Bragg Spectroscopy of a Bose-Einstein Condensate', *Phys. Rev. Lett.* **82,** 4569–4573 (1999) (cit. on pp. 40, 112).

233. S. Pötting, M. Cramer, C.H. Schwalb, H. Pu, and P. Meystre, 'Coherent acceleration of Bose-Einstein condensates', *Phys. Rev. A* **64,** 023604 (2001) (cit. on p. 41).

234. J. Hecker Denschlag, J.E. Simsarian, H. Häffner, C. McKenzie, A. Browaeys, D. Cho, K. Helmerson, S.L. Rolston, and W.D. Phillips, 'A Bose-Einstein condensate in an optical lattice', *J. Phys. B At. Mol. Opt. Phys.* **35,** 3095 (2002) (cit. on pp. 41, 43, 70).

235. M. Gustavsson, E. Haller, M.J. Mark, J.G. Danzl, G. Rojas-Kopeinig, and H.-C. Nägerl, 'Control of interaction-induced dephasing of Bloch oscillations', *Phys. Rev. Lett.* **100,** 080404 (2008) (cit. on pp. 41, 80).

236. M. Takamoto, F.-L. Hong, R. Higashi, and H. Katori, 'An optical lattice clock', *Nature* **435,** 321–324 (2005) (cit. on p. 41).

237. R. Jördens, N. Strohmaier, K. Günter, H. Moritz, and T. Esslinger, 'A Mott insulator of fermionic atoms in an optical lattice', *Nature* **455,** 204–207 (2008) (cit. on p. 41).

238. W.S. Bakr, J.I. Gillen, A. Peng, S. Fölling, and M. Greiner, 'A quantum gas microscope for detecting single atoms in a Hubbard-regime optical lattice', *Nature* **462,** 74–77 (2009) (cit. on p. 41).

239. J.F. Sherson, C. Weitenberg, M. Endres, M. Cheneau, I. Bloch, and S. Kuhr, 'Single-atom-resolved fluorescence imaging of an atomic Mott insulator', *Nature* **467,** 68–72 (2010) (cit. on p. 41).

240. J. Simon, W.S. Bakr, R. Ma, M.E. Tai, P.M. Preiss, and M. Greiner, 'Quantum simulation of antiferromagnetic spin chains in an optical lattice',
Nature **472,** 307–312 (2011) (cit. on p. 41).

241. F. Bloch, 'Über die Quantenmechanik der Elektronen in Kristallgittern',
Z. Phys. **52,** 555 (1929) (cit. on p. 41).

242. M. Ben Dahan, E. Peik, J. Reichel, Y. Castin, and C. Salomon, 'Bloch Oscillations of Atoms in an Optical Potential',
Phys. Rev. Lett. **76,** 4508–4511 (1996) (cit. on pp. 41, 43, 44).

243. E. Peik, M. Ben Dahan, I. Bouchoule, Y. Castin, and C. Salomon, 'Bloch oscillations of atoms, adiabatic rapid passage, and monokinetic atomic beams',
Phys. Rev. A **55,** 2989–3001 (1997) (cit. on pp. 41, 43, 45).

244. S.R. Wilkinson, C.F. Bharucha, K.W. Madison, Q. Niu, and M.G. Raizen, 'Observation of Atomic Wannier-Stark Ladders in an Accelerating Optical Potential',
Phys. Rev. Lett. **76,** 4512–4515 (1996) (cit. on p. 41).

245. M. Raizen, C. Salomon, and Q. Niu, 'New light on quantum transport',
Phys. Today **50,** 30–35 (1997) (cit. on p. 41).

246. C. Zener, 'Non-adiabatic crossing of energy levels',
Proc. Roy. Soc. A **137,** 696–702 (1932) (cit. on pp. 41, 46).

247. R. Grimm, M. Weidemüller, and Y.B. Ovchinnikov, 'Optical dipole traps for neutral atoms',
Adv. At. Mol. Opt. Phys. **42,** 95–170 (2000) (cit. on pp. 41, 42).

248. C. Kittel, 'Einführung in die Festkörperphysik',
Oldenbourg (2005) (cit. on p. 43).

249. M. Glück, A.R. Kolovsky, and H.-J. Korsch, 'Wannier-Stark resonances in optical and semiconductor superlattices',
Phys. Rep. **366,** 103–182 (2002) (cit. on pp. 45, 72).

250. Q. Beaufils, G. Tackmann, X. Wang, B. Pelle, S. Pelisson, P. Wolf, and F. Pereira Dos Santos, 'Laser controlled tunneling in a vertical optical lattice',
Phys. Rev. Lett. **106,** 213002 (2011) (cit. on p. 45).

251. G.H. Wannier, 'Wave functions and effective Hamiltonian for Bloch electrons in an electric field',
Phys. Rev. **117,** 432 (1960) (cit. on p. 45).

252. J. Callaway, 'Optical absorption in an electric field',
Phys. Rev. **130,** 549 (1963) (cit. on p. 45).

253. M. Glück, A.R. Kolovsky, H.-J. Korsch, and N. Moiseyev, 'Calculation of wannier-bloch and wannier-stark states',
Eur. Phys. J. D **4,** 239–246 (1998) (cit. on p. 45).

254. P. Lemonde and P. Wolf, 'Optical lattice clock with atoms confined in a shallow trap',
Phys. Rev. A **72,** 033409 (2005) (cit. on p. 45).

255. R. Messina, S. Pelisson, M.-C. Angonin, and P. Wolf, 'Atomic states in optical traps near a planar surface',
Phys. Rev. A **83,** 052111 (2011) (cit. on pp. 45, 46).

256. P. Cladé, 'Bloch oscillations in atom interferometry',
Proceedings of the International School of Physics 'Enrico Fermi' **Course 188,** 419–455 (2014) (cit. on pp. 47, 124).

257. N.F. Ramsey, 'A Molecular Beam Resonance Method with Separated Oscillating Fields',
Phys. Rev. **78,** 695–699 (1950) (cit. on p. 48).

258. C.J. Bordé, 'Theoretical tools for atom optics and interferometry',
Compt. Rend. des Sc. d. l'Acad d. Sc. **2,** 509–530 (2001) (cit. on p. 49).

259. C.J. Bordé, 'Atomic clocks and inertial sensors',
Metrologia **39,** 435 (2002) (cit. on p. 49).

260. C. Antoine and C.J. Bordé, 'Exact phase shifts for atom interferometry',
Phys. Lett. A **306,** 277–284 (2003) (cit. on p. 49).

261. A. Peters, K.-Y. Chung, and S. Chu, 'High-precision gravity measurements using atom interferometry',
Metrologia **38,** 25– (2001) (cit. on p. 49).

262. D. Schlippert, 'Quantum test of the Universality of Free Fall',
Dissertation, Leibniz Universität Hannover (2014) (cit. on pp. 49, 52, 109, 110, 116).

263. J.M. Hogan, D.M.S. Johnson, and M.A. Kasevich, 'Light-pulse atom interferometry',
Proceedings of the International School of Physics 'Enrico Fermi' **Course 168,** 411–447 (2009) (cit. on p. 49).

264. P. Asenbaum, C. Overstreet, T. Kovachy, D.D. Brown, J.M. Hogan, and M.A. Kasevich, 'Phase Shift in an Atom Interferometer due to Spacetime Curvature across its Wave Function',
Phys. Rev. Lett. **118,** 183602 (18 2017) (cit. on pp. 49, 113).

265. P. Cheinet, B. Canuel, F. Pereira Dos Santos, A. Gauguet, F. Yver-Leduc, and A. Landragin, 'Measurement of the Sensitivity Function in a Time-Domain Atomic Interferometer',
IEEE Trans. Instrum. Meas. **57,** 1141–1148 (2008) (cit. on pp. 50, 51, 116).

266. C. Antoine, 'Rotating matter-wave beam splitters and consequences for atom gyrometers',
Phys. Rev. A **76,** 033609 (2007) (cit. on pp. 51, 116).

267. R. Stoner, D. Butts, J. Kinast, and B. Timmons, 'Analytical framework for dynamic light pulse atom interferometry at short interrogation times',
J. Opt. Soc. Am. B **28,** 2418–2429 (2011) (cit. on pp. 51, 116).

268. A. Bonnin, N. Zahzam, Y. Bidel, and A. Bresson, 'Characterization of a simultaneous dual-species atom interferometer for a quantum test of the weak equivalence principle',
Phys. Rev. A **92,** 023626 (2015) (cit. on pp. 51, 116, 136).

269. D.A. Smith, A.S. Arnold, M.J. Pritchard, and I.G. Hughes, 'Experimental single-impulse magnetic focusing of launched cold atoms',
J. Phys. B At. Mol. Opt. Phys. **41,** 125302 (2008) (cit. on p. 58).

270. A.E. Leanhardt, T.A. Pasquini, M. Saba, A. Schirotzek, Y. Shin, D. Kielpinski, D.E. Pritchard, and W. Ketterle, 'Cooling Bose-Einstein condensates below 500 picokelvin',
Science **301,** 1513–1515 (2003) (cit. on p. 58).

271. A. Sugarbaker, 'Atom Interferometry in a 10 m Fountain',
PhD thesis, Stanford University (2014) (cit. on pp. 68, 73).

272. F. Impens, P. Bouyer, and C.J. Bordé, 'Matter-wave cavity gravimeter',
Appl. Phys. B **84,** 603–615 (2006) (cit. on p. 68).

273. Y.B. Ovchinnikov, J.H. Müller, M.R. Doery, E.J.D. Vredenbregt, K. Helmerson, S.L. Rolston, and W.D. Phillips, 'Diffraction of a released Bose-Einstein condensate by a pulsed standing light wave',
Phys. Rev. Lett. **83,** 284 (1999) (cit. on p. 70).

274. C. Sias, A. Zenesini, H. Lignier, S. Wimberger, D. Ciampini, O. Morsch, and E. Arimondo, 'Resonantly enhanced tunneling of Bose-Einstein condensates in periodic potentials',
Phys. Rev. Lett. **98,** 120403 (2007) (cit. on p. 72).

275. J.-N. Siemss, 'Simulations of Bose-Einstein Condensate Dynamics in Optical Lattices for Large Momentum Transfer Experiments',
Masterarbeit, Leibniz Universität Hannover (2016) (cit. on pp. 72, 124, 130).

276. L. Zhou *et al.*, 'Development of an atom gravimeter and status of the 10-meter atom interferometer for precision gravity measurement',
Gen. Rel. Gravit. **43,** 1931–1942 (2011) (cit. on p. 79).

277. D. Witthaut, M. Werder, S. Mossmann, and H.J. Korsch, 'Bloch oscillations of Bose-Einstein condensates: Breakdown and revival',
Phys. Rev. E **71,** 036625 (2005) (cit. on p. 80).

278. H. Pichler, A.J. Daley, and P. Zoller, 'Nonequilibrium dynamics of bosonic atoms in optical lattices: Decoherence of many-body states due to spontaneous emission',
Phys. Rev. A **82,** 063605 (2010) (cit. on p. 80).

279. F. Gerbier and Y. Castin, 'Heating rates for an atom in a far-detuned optical lattice',
Phys. Rev. A **82,** 013615 (2010) (cit. on p. 80).

280. D. Aguilera *et al.*, 'STE-QUEST - Test of the Universality of Free Fall Using Cold Atom Interferometry',
Class. Quantum Grav. **31,** 115010 (2014) (cit. on pp. 81, 109, 110).

281. C. Schubert *et al.*, 'Differential atom interferometry with ^{87}Rb and ^{85}Rb for testing the UFF in STE-QUEST',
arXiv preprint arXiv:1312.5963 (2013) (cit. on pp. 81, 109, 126).

282. J. Hartwig, S. Abend, C. Schubert, D. Schlippert, H. Ahlers, K. Posso-Trujillo, N. Gaaloul, W. Ertmer, and E.M. Rasel, 'Testing the universality of free fall with rubidium and ytterbium in a very large baseline atom interferometer',
New J. Phys. **17,** 035011 (2015) (cit. on pp. 81, 109, 135, 136).

283. D.W. Allan, 'The Statistics of Atomic Frequency Standards',
Proc. IEEE **54,** 221 (1966) (cit. on p. 87).

284. URL: `http://www.bkg.bund.de/` (cit. on pp. 89, 165).

285. URL: `https://www.guralp.com/` (cit. on p. 90).

286. J. Lautier, L. Volodimer, T. Hardin, S. Merlet, M. Lours, F. Pereira Dos Santos, and A. Landragin, 'Hybridizing matter-wave and classical accelerometers',
Appl. Phys. Lett. **105,** 144102 (2014) (cit. on pp. 90, 93, 140).

287. P. Gillot, O. Francis, A. Landragin, F. Pereira Dos Santos, and S. Merlet, 'Stability comparison of two absolute gravimeters: optical versus atomic interferometers',
Metrologia **51,** L15 (2014) (cit. on p. 91).

288. URL: `http://www.alamath.com/` (cit. on p. 94).

289. R. Geiger *et al.*, 'Detecting inertial effects with airborne matter-wave interferometry',
Nat. Commun. **2,** 474 (2011) (cit. on pp. 95, 120).

290. D.C. Lay, 'Linear algebra and its applications',
Addison-Wesley (2003), 124 (cit. on p. 103).

291. S.R. Segal, Q. Diot, E.A. Cornell, A.A. Zozulya, and D.Z. Anderson, 'Revealing buried information: Statistical processing techniques for ultracold-gas image analysis',
Phys. Rev. A **81,** 053601 (2010) (cit. on p. 103).

292. R. Dubessy, C. De Rossi, T. Badr, L. Longchambon, and H. Perrin, 'Imaging the collective excitations of an ultracold gas using statistical correlations',
New J. Phys. **16,** 122001 (2014) (cit. on p. 103).

293. S.J. Seckmeyer, 'Statistical Methods for Image Analysis in Atom Interferometry',
Bachelorarbeit, Leibniz Universität Hannover (2017) (cit. on pp. 107, 110).

294. V. Schkolnik, B. Leykauf, M. Hauth, C. Freier, and A. Peters, 'The effect of wavefront aberrations in atom interferometry',
Appl. Phys. B **120,** 311–316 (2015) (cit. on pp. 107, 110, 118).

295. M. Zhou, Q. Luo, L. Chen, X. Duan, and Z. Hu, 'Observing the effect of wave-front aberrations in an atom interferometer by modulating the diameter of Raman beams',
Phys. Rev. A **93,** 043610 (2016) (cit. on pp. 107, 110).

296. F. Riehle, 'Frequency Standards',
Wiley-VCH Verlag GmbH (2004) (cit. on p. 109).

297. G. Breit and I. I. Rabi, 'Measurement of Nuclear Spin',
Phys. Rev. **38,** 2082–2083 (1931) (cit. on p. 109).

298. A. Milke, A. Kubelka-Lange, N. Gürlebeck, B. Rievers, S. Herrmann, T. Schuldt, and C. Braxmaier, 'Atom interferometry in space: Thermal management and magnetic shielding',
Rev. Sci. Instrum. **85,** 083105 (2014) (cit. on pp. 110, 118).

299. J. Rudolph, 'Matter-Wave Optics with Bose-Einstein Condensates in Microgravity',
Dissertation, Leibniz Universität Hannover (2016) (cit. on p. 111).

300. J.M. Hogan, J. Hammer, S.-w. Chiow, S. Dickerson, D.M.S. Johnson, T. Kovachy, A. Sugarbaker, and M.A. Kasevich, 'Precision angle sensor using an optical lever inside a Sagnac interferometer',
Opt. Lett. **36,** 1698–1700 (2011) (cit. on pp. 113, 133).

301. S.-Y. Lan, P.-C. Kuan, B. Estey, P. Haslinger, and H. Müller, 'Influence of the Coriolis Force in Atom Interferometry',
Phys. Rev. Lett. **108,** 090402 (2012) (cit. on pp. 113, 133).

302. G. D'Agostino, S. Merlet, A. Landragin, and F. Pereira Dos Santos, 'Perturbations of the local gravity field due to mass distribution on precise measuring instruments: a numerical method applied to a cold atom gravimeter',
Metrologia **48,** 299 (2011) (cit. on pp. 114, 118).

303. Z. Li, H. Hu, K. Wu, G. Li, G. Wang, and L.J. Wang, 'Self-attraction effect and correction on the T-1 absolute gravimeter',
Metrologia **52,** 793 (2015) (cit. on p. 114).

304. A. Gauguet, T. E. Mehlstäubler, T. Lévèque, J. Le Gouët, W. Chaibi, B. Canuel, A. Clairon, F. Pereira Dos Santos, and A. Landragin, 'Off-resonant Raman transition impact in an atom interferometer',
Phys. Rev. A **78,** 043615 (2008) (cit. on p. 115).

305. A. Friedrich *et al.*, 'Higher-order light shifts in Bragg diffraction',
unpublished (2017) (cit. on p. 115).

306. J. Ye, S. Swartz, P. Jungner, and J. L. Hall, 'Hyperfine structure and absolute frequency of the ^{87}Rb $5P_{3/2}$ state',
Opt. Lett. **21,** 1280–1282 (1996) (cit. on p. 116).

307. C. Schubert, 'Realisierung eines schmalbandigen Diodenlasersystems hoher Ausgangsleistung für Präzisionsmessungen an ^{87}Rb Atomen',
Diplomarbeit, Leibniz Universität Hannover (2007) (cit. on pp. 116, 133).

308. J. Le Gouët, P. Cheinet, J. Kim, D. Holleville, A. Clairon, A. Landragin, and F. Pereira Dos Santos, 'Influence of lasers propagation delay on the sensitivity of atom interferometers',
Eur. Phys. J. D **44,** 419–425 (2007) (cit. on p. 116).

309. K. Kuroda and N. Mio, 'Correction to interferometric measurements of absolute gravity arising from the finite speed of light',
Metrologia **28,** 75 (1991) (cit. on p. 116).

310. B. Cheng, P. Gillot, S. Merlet, and F. Pereira Dos Santos, 'Influence of chirping the Raman lasers in an atom gravimeter: Phase shifts due to the Raman light shift and to the finite speed of light',
Phys. Rev. A **92,** 063617 (2015) (cit. on p. 116).

311. P. Gillot, B. Cheng, S. Merlet, and F. Pereira Dos Santos, 'Limits to the symmetry of a Mach-Zehnder-type atom interferometer',
Phys. Rev. A **93,** 013609 (2016) (cit. on p. 116).

312. P. Cheinet, F. Pereira Dos Santos, T. Petelski, J. Le Gouët, J. Kim, K.T. Therkildsen, A. Clairon, and A. Landragin, 'Compact laser system for atom interferometry',
Appl. Phys. B **84,** 643–646 (2006) (cit. on p. 116).

313. J. Le Gouët, J. Kim, C. Bourassin-Bouchet, M. Lours, A. Landragin, and F. Pereira Dos Santos, 'Wide bandwidth phase-locked diode laser with an intra-cavity electro-optic modulator',
Opt. Com. **282,** 977 –980 (2009) (cit. on p. 116).

314. B. Tang, L. Zhou, Z. Xiong, J. Wang, and M. Zhan, 'A programmable broadband low frequency active vibration isolation system for atom interferometry',
Rev. Sci. Instrum. **85,** 093109 (2014) (cit. on pp. 117, 132).

315. W. Chaibi, R. Geiger, B. Canuel, A. Bertoldi, A. Landragin, and P. Bouyer, 'Low frequency gravitational wave detection with ground-based atom interferometer arrays',
Phys. Rev. D **93,** 021101 (2 2016) (cit. on p. 119).

316. D.S. Durfee, Y.K. Shaham, and M.A. Kasevich, 'Long-Term Stability of an Area-Reversible Atom-Interferometer Sagnac Gyroscope',
Phys. Rev. Lett. **97,** 240801 (2006) (cit. on pp. 120, 121).

317. S. Merlet, J. Le Gouët, Q. Bodart, A. Clairon, A. Landragin, F. Pereira Dos Santos, and P. Rouchon, 'Operating an atom interferometer beyond its linear range',
Metrologia **46,** 87 (2009) (cit. on p. 120).

318. B. Barrett, L. Antoni-Micollier, L. Chichet, B. Battelier, P.A. Gominet, A. Bertoldi, P. Bouyer, and A. Landragin, 'Correlative methods for dual-species quantum tests of the weak equivalence principle',
New J. Phys. **17,** 085010 (2015) (cit. on p. 120).

319. S.-w. Chiow, J. Williams, and N. Yu, 'Noise reduction in differential phase extraction of dual atom interferometers using an active servo loop',
Phys. Rev. A **93,** 013602 (2016) (cit. on p. 120).

320. B. Canuel, F. Leduc, D. Holleville, A. Gauguet, J. Fils, A. Virdis, A. Clairon, N. Dimarcq, C.J. Bordé, A. Landragin, and P. Bouyer, 'Six-Axis Inertial Sensor Using Cold-Atom Interferometry',
Phys. Rev. Lett. **97,** 010402 (2006) (cit. on pp. 120, 140, 141).

321. G.T. Foster, J.B. Fixler, J.M. McGuirk, and M.A. Kasevich, 'Method of phase extraction between coupled atom interferometers using ellipse-specific fitting',
Opt. Lett. **27,** 951–953 (2002) (cit. on p. 121).

322. J.K. Stockton, X. Wu, and M.A. Kasevich, 'Bayesian estimation of differential interferometer phase',
Phys. Rev. A **76,** 033613 (2007) (cit. on p. 121).

323. S.-w. Chiow, S. Herrmann, S. Chu, and H. Müller, 'Noise-Immune Conjugate Large-Area Atom Interferometers',
Phys. Rev. Lett. **103,** 050402 (2009) (cit. on p. 121).

324. H. Müller, S.-w. Chiow, S. Herrmann, S. Chu, and K.-Y. Chung, 'Atom-Interferometry Tests of the Isotropy of Post-Newtonian Gravity',
Phys. Rev. Lett. **100,** 031101 (2008) (cit. on p. 128).

325. URL: `http://www.hitec.uni-hannover.de/` (cit. on p. 131).

326. Z. Jiang *et al.*, 'The 8th International Comparison of Absolute Gravimeters 2009: the first Key Comparison (CCM. G-K1) in the field of absolute gravimetry',
Metrologia **49,** 666 (2012) (cit. on p. 132).

327. M. Schilling, J. Müller, and L. Timmen, 'Einsatz der Atominterferometrie in der Geodäsie', *Zeitschrift für Vermessungswesen*, 185–194 (2012) (cit. on p. 132).

328. K. Dieckmann, R. J. C. Spreeuw, M. Weidemüller, and J.T.M. Walraven, 'Two-dimensional magneto-optical trap as a source of slow atoms', *Phys. Rev. A* **58,** 3891–3895 (1998) (cit. on p. 133).

329. V. Ménoret, R. Geiger, G. Stern, N. Zahzam, B. Battelier, A. Bresson, A. Landragin, and P. Bouyer, 'Dual-wavelength laser source for onboard atom interferometry', *Opt. Lett.* **36,** 4128–4130 (2011) (cit. on p. 133).

330. F. Theron, O. Carraz, G. Renon, N. Zahzam, Y. Bidel, M. Cadoret, and A. Bresson, 'Narrow linewidth single laser source system for onboard atom interferometry', *Appl. Phys. B* **118,** 1–5 (2015) (cit. on p. 133).

331. S.M. Dickerson, J.M. Hogan, D.M.S. Johnson, T. Kovachy, A. Sugarbaker, S.-w. Chiow, and M.A. Kasevich, 'A high-performance magnetic shield with large length-to-diameter ratio', *Rev. Sci. Instrum.* **83,** 065108 (2012) (cit. on p. 134).

332. A. Wanner, 'Seismic attenuation system (AEI-SAS) for the AEI 10 m prototype', Dissertation, Leibniz Universität Hannover (2013) (cit. on p. 134).

333. M. Zaiser, J. Hartwig, D. Schlippert, U. Velte, N. Winter, V. Lebedev, W. Ertmer, and E. M. Rasel, 'Simple method for generating Bose-Einstein condensates in a weak hybrid trap', *Phys. Rev. A* **83,** 035601 (2011) (cit. on p. 134).

334. S. Dimopoulos, P.W. Graham, J.M. Hogan, and M.A. Kasevich, 'General relativistic effects in atom interferometry', *Phys. Rev. D* **78,** 042003– (2008) (cit. on p. 135).

335. S. Dimopoulos, P.W. Graham, J.M. Hogan, M.A. Kasevich, and S. Rajendran, 'Gravitational wave detection with atom interferometry', *Phys. Lett. B* **678,** 37–40 (2009) (cit. on p. 135).

336. G.M. Tino and F. Vetrano, 'Is it possible to detect gravitational waves with atom interferometers?', *Class. Quantum Grav.* **24,** 2167 (2007) (cit. on p. 135).

337. P. Delva and E.M. Rasel, 'Matter wave interferometry and gravitational waves', *J. Mod. Opt.* **56,** 1999–2004 (2009) (cit. on p. 135).

338. J.M. Hogan *et al.*, 'An atomic gravitational wave interferometric sensor in low earth orbit (AGIS-LEO)', *Gen. Rel. Gravit.* **43,** 1953–2009 (2011) (cit. on p. 135).

339. P.L. Bender, 'Comment on "Atomic gravitational wave interferometric sensor"', *Phys. Rev. D* **84,** 028101 (2011) (cit. on p. 135).

340. P.L. Bender, 'Comparison of atom interferometry with laser interferometry for gravitational wave observations in space', *Phys. Rev. D* **89,** 062004 (2014) (cit. on p. 135).

341. S. Dimopoulos, P.W. Graham, J.M. Hogan, and M.A. Kasevich, 'Testing General Relativity with Atom Interferometry', *Phys. Rev. Lett.* **98,** 111102– (2007) (cit. on p. 135).

342. M. Zych, F. Costa, I. Pikovski, and Č. Brukner, 'Quantum interferometric visibility as a witness of general relativistic proper time', *Nat. Commun.* **2,** 505 (2011) (cit. on p. 135).

343. L. Hackermüller, K. Hornberger, B. Brezger, A. Zeilinger, and M. Arndt, 'Decoherence of matter waves by thermal emission of radiation', *Nature* **427,** 711–714 (2004) (cit. on p. 135).

344. L. Eötvös, 'Über die Anziehung der Erde auf verschiedene Substanzen',
Mathematische und naturwissenschaftliche Berichte aus Ungarn **8,** 65– (1889) (cit. on p. 136).

345. L. Eötvös, D. Pekár, and E. Fekete, 'Beiträge zum Gesetze der Proportionalität von Trägheit und Gravität',
Ann. Phys. **373,** 11–66 (1922) (cit. on p. 136).

346. C. Lämmerzahl, 'Quantum tests of the foundations of general relativity',
Class. Quantum Grav. **15,** 13– (1998) (cit. on p. 136).

347. C. Lämmerzahl, 'The search for quantum gravity effects I',
Appl. Phys. B **84,** 551–562– (2006) (cit. on p. 136).

348. E. Göklü and C. Lämmerzahl, 'Metric fluctuations and the weak equivalence principle',
Class. Quantum Grav. **25,** 105012– (2008) (cit. on p. 136).

349. D. Colladay and V.A. Kostelecký, 'CPT violation and the standard model',
Phys. Rev. D **55,** 6760–6774 (1997) (cit. on p. 136).

350. V.A. Kostelecký and C.D. Lane, 'Constraints on Lorentz violation from clock-comparison experiments',
Phys. Rev. D **60,** 116010 (1999) (cit. on p. 136).

351. V.A. Kostelecký and J.D. Tasson, 'Matter-gravity couplings and Lorentz violation',
Phys. Rev. D **83,** 016013– (2011) (cit. on p. 136).

352. URL: `http://physics.aps.org/articles/v9/131/` (cit. on p. 139).

353. S. Abend and E.M. Rasel, 'Kompaktes Fontänen-Gravimeter auf einem Atomchip',
Physik in unserer Zeit **48,** 61–62 (2017) (cit. on p. 139).

354. C.J.E. Straatsma, M.K. Ivory, J. Duggan, J. Ramirez-Serrano, D.Z. Anderson, and E.A. Salim, 'On-chip optical lattice for cold atom experiments',
Opt. Lett. **40,** 3368–3371 (2015) (cit. on p. 139).

355. P. Böhi, M.F. Riedel, J. Hoffrogge, J. Reichel, T.W. Hänsch, and P. Treutlein, 'Coherent manipulation of Bose–Einstein condensates with state-dependent microwave potentials on an atom chip',
Nat. Phys. **5,** 592–597 (2009) (cit. on p. 139).

356. B. Lev, 'Fabrication of micro-magnetic traps for cold neutral atoms',
arXiv preprint quant-ph/0305067 (2003) (cit. on p. 139).

357. P. Treutlein, 'Coherent manipulation of ultracold atoms on atom chips',
Dissertation, Ludwig Maximilian Universität München (2008) (cit. on p. 139).

358. P.B. Zantye, A. Kumar, and A.K. Sikder, 'Chemical mechanical planarization for microelectronics applications',
Mater. Sci. Eng: R. **45,** 89–220 (2004) (cit. on p. 139).

359. C.-W. Chuang H.-C.and Weng and H.-F. Li, 'Design, microfabrication and characterization of planarized multilayer atom chips with enhanced heat dissipation',
J. Micromech. Microeng. **21,** 125009 (2011) (cit. on p. 139).

360. C.C. Nshii, M. Vangeleyn, J.P. Cotter, P.F. Griffin, E.A. Hinds, C.N. Ironside, P. See, A.G. Sinclair, E. Riis, and A.S. Arnold, 'A surface-patterned chip as a strong source of ultracold atoms for quantum technologies',
Nat. Nanotechnol. **8,** 321–324 (2013) (cit. on p. 139).

361. P. Hamilton, M. Jaffe, J.M. Brown, L. Maisenbacher, B. Estey, and H. Müller, 'Atom Interferometry in an Optical Cavity',
Phys. Rev. Lett. **114,** 100405 (2015) (cit. on p. 139).

362. D. B. Hume, I. Stroescu, M. Joos, W. Muessel, H. Strobel, and M. K. Oberthaler, 'Accurate Atom Counting in Mesoscopic Ensembles',
Phys. Rev. Lett. **111,** 253001 (2013) (cit. on p. 139).

363. I. Stroescu, D.B. Hume, and M.K. Oberthaler, 'Double-well atom trap for fluorescence detection at the Heisenberg limit',
Phys. Rev. A **91,** 013412 (2015) (cit. on p. 139).

364. H.J. McGuinness, A.V. Rakholia, and G.W. Biedermann, 'High data-rate atom interferometer for measuring acceleration',
Appl. Phys. Lett. **100,** 011106–4 (2012) (cit. on p. 140).

365. A.V. Rakholia, H.J. McGuinness, and G.W. Biedermann, 'Dual-Axis High-Data-Rate Atom Interferometer via Cold Ensemble Exchange',
Phys. Rev. A. **2,** 054012 (2014) (cit. on p. 140).

366. G. Biedermann, A.V. Rakholia, and H. McGuinness, 'High data-rate atom interferometers through high recapture efficiency',
US Patent 8,941,053 (, 2015) (cit. on p. 140).

367. M. Meunier, I. Dutta, R. Geiger, C. Guerlin, C.L. Garrido Alzar, and A. Landragin, 'Stability enhancement by joint phase measurements in a single cold atomic fountain',
Phys. Rev. A **90,** 063633 (2014) (cit. on p. 140).

368. N.P. Robins, C. Figl, M. Jeppesen, G.R. Dennis, and J.D. Close, 'A pumped atom laser',
Nat. Phys. **4,** 731–736 (2008) (cit. on p. 140).

369. N.P. Robins, P.A. Altin, J.E. Debs, and J.D. Close, 'Atom lasers: Production, properties and prospects for precision inertial measurement',
Phys. Rep. **529,** 265–296 (2013) (cit. on p. 140).

370. V.M. Akulin and W.P. Schleich, 'Landau-Zener transition to a decaying level',
Phys. Rev. A **46,** 4110–4113 (1992) (cit. on p. 141).

371. M.V. Fedorov, M.A. Efremov, V.P. Yakovlev, and W.P. Schleich, 'Dynamics of spontaneous radiation of atoms scattered by a resonance standing light wave',
J. Exp. Theor. Phys. **97,** 522–538 (2003) (cit. on p. 141).

372. H.-C. Chuang, E.A. Salim, V. Vuletic, D.Z. Anderson, and V.M. Bright, 'Multi-layer atom chips for atom tunneling experiments near the chip surface',
Sensor. Actuat. A: Phys. **165,** Transducers 2009, 101 –106 (2011) (cit. on p. 141).

373. P. Wolf, P. Lemonde, A. Lambrecht, S. Bize, A. Landragin, and A. Clairon, 'From optical lattice clocks to the measurement of forces in the Casimir regime',
Phys. Rev. A **75,** 063608 (2007) (cit. on p. 141).

374. M. Fattori, C. D'Errico, G. Roati, M. Zaccanti, M. Jona-Lasinio, M. Modugno, M. Inguscio, and G. Modugno, 'Atom Interferometry with a Weakly Interacting Bose-Einstein Condensate',
Phys. Rev. Lett. **100,** 080405 (2008) (cit. on p. 141).

375. T.A. Pasquini, M. Saba, G.-B. Jo, Y. Shin, W. Ketterle, D.E. Pritchard, T.A. Savas, and N. Mulders, 'Low Velocity Quantum Reflection of Bose-Einstein Condensates',
Phys. Rev. Lett. **97,** 093201 (2006) (cit. on p. 141).

List of Constants

Fundamental constants and properties of the D2-line of Rubidium-87 in ref. [174].

Fundamental constant	Symbol	CODATA 2006 recommended value
Speed of light	c	$2.997\,924\,58 \cdot 10^{8}\,\mathrm{m/s}$ (exact)
Permeability of vacuum	μ_0	$4\pi \cdot 10^{-7}\,\mathrm{N/A^2}$ (exact)
Permittivity of vacuum	ε_0	$8.854\,187\,817\,... \cdot 10^{-12}\,\mathrm{F/m}$
Plancks quantum	$h = 2\pi\hbar$	$2\pi \cdot 1.054\,571\,628(53) \cdot 10^{-34}\,\mathrm{Js}$ $2\pi \cdot 6.582\,118\,99(16) \cdot 10^{-16}\,\mathrm{eV{\cdot}s}$
Bohr magneton	μ_B	$9.274\,009\,15(23) \cdot 10^{-24}\,\mathrm{J/T}$ $h \cdot 1.399\,624\,604(35)\,\mathrm{MHz/G}$
Elementary charge	e	$1.602\,176\,487(40) \cdot 10^{-19}\,\mathrm{C}$
Bohr radius	a_0	$0.529\,177\,208\,59(36) \cdot 10^{-10}\,\mathrm{m}$
Boltzmanns constant	k_B	$1.380\,6504(24) \cdot 10^{-23}\,\mathrm{J/K}$
Atomic mass unit	u	$1.660\,538\,782(83) \cdot 10^{-27}\,\mathrm{kg}$

D2-line properties	Symbol	Value
Mass of Rubidium-87	m_{87}	$1.443\,160\,60(11) \cdot 10^{-25}\,\mathrm{kg}$
Clock shift	$\Delta\omega_\mathrm{clock}/B^2$	$2\pi \cdot 575.15\,\mathrm{Hz/G^2}$
Wavelength	λ	$780.241\,209\,683(13)\,\mathrm{nm}$
Frequency	ω	$2\pi \cdot 384.230\,484\,468\,5(62)\,\mathrm{THz}$
Wavenumber	k	$2\pi \cdot 12\,816.549\,389\,93(21)\ \mathrm{cm^{-1}}$
Natural linewidth	Γ	$2\pi \cdot 6.065(9)\,\mathrm{MHz}$
Saturation intensity	I_{sat}	$1.666\,\mathrm{mW/cm^2}$
Lifetime	τ	$26.2348(77)\ \mathrm{ns}$
Hyperfine splitting	ω_{eg}	$2\pi \cdot 6.834\,682\,610\,904\,29(9)\,\mathrm{GHz}$
Recoil frequency	ω_r	$2\pi \cdot 3.7710\,\mathrm{kHz}$
Recoil velocity	v_r	$5.8845\,\mathrm{mm/s}$
Doppler shift	ω_0	$2\pi \cdot 7.5419\,\mathrm{kHz}$

Gravity at ZARM [284]	g_ref	$(9.81327 \pm 0.00002)\ \frac{\mathrm{m}}{\mathrm{s^2}}$

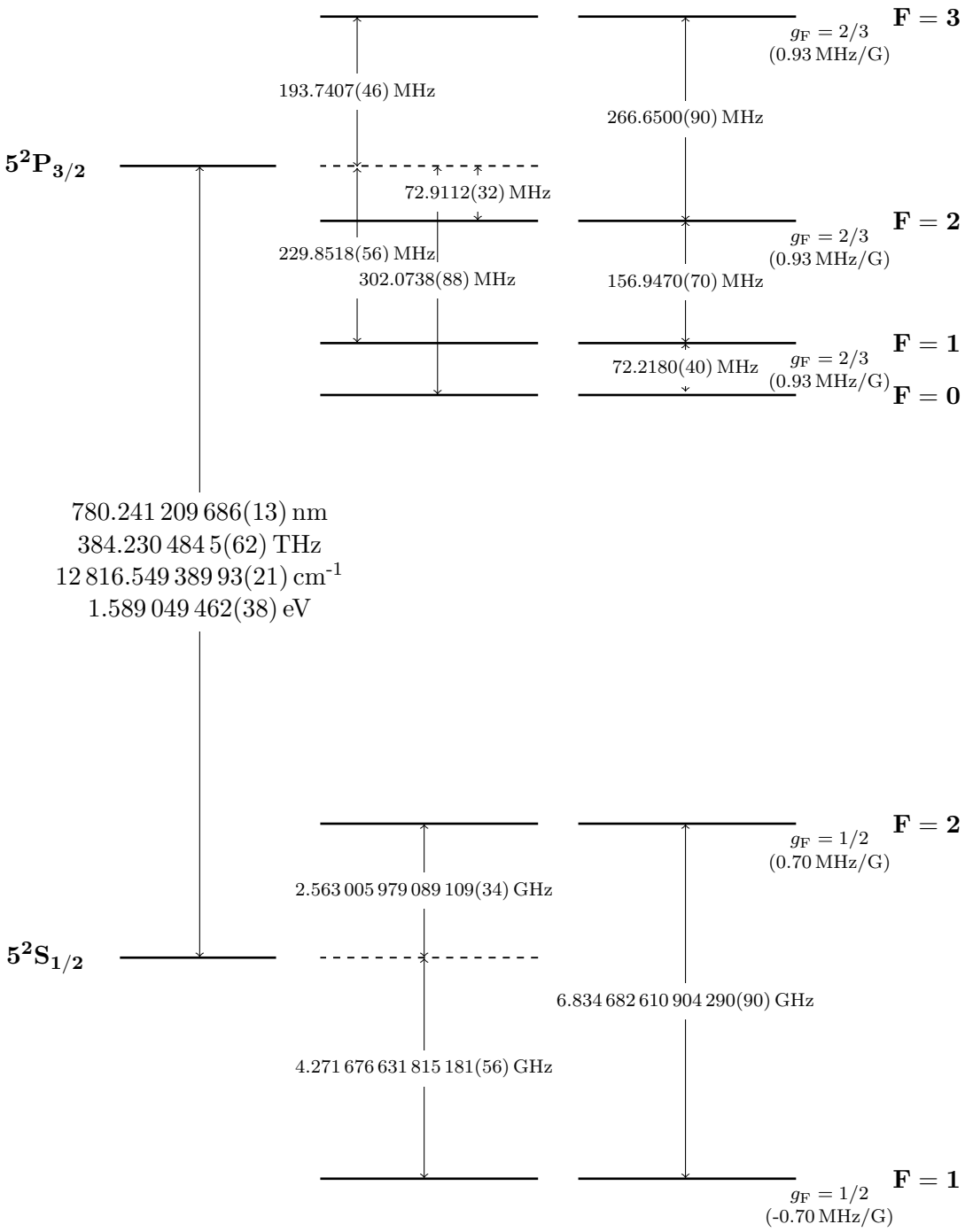

Level scheme of the Rubidium-87 D2-line adapted from ref. [174].

List of Figures

List of Tables

List of Publications

Publications in peer-reviewed journals:

1. J. T. Schultz, **S. Abend**, D. Döring, J. E. Debs, P. A. Altin, J. D. White, N. P. Robins, and J. D. Close,
   "Coherent 455 nm beam production in a cesium vapor",
   Opt. Lett. **34**, 2321-2323 (2009)
2. G. Tackmann, P. Berg, C. Schubert, **S. Abend**, M. Gilowski, W. Ertmer, and E. M. Rasel,
   "Self-alignment of a compact large-area atomic Sagnac interferometer",
   New J. Phys. **14**, 015002 (2012)
3. G. Tackmann, P. Berg, **S. Abend**, C. Schubert, W. Ertmer, and E. M. Rasel,
   "Large-area Sagnac atom interferometer with robust phase read out",
   C. R. Physique **15**, 884-897 (2014)
4. P. Berg, **S. Abend**, G. Tackmann, C. Schubert, E. Giese, W. P. Schleich, F. A. Narducci, W. Ertmer, and E. M. Rasel,
   "Composite-Light-Pulse Technique for High-Precision Atom Interferometry",
   Phys. Rev. Lett. **114**, 063002 (2015)
5. J. Hartwig, **S. Abend**, C. Schubert, D. Schlippert, H. Ahlers, K. Posso-Trujillo, N. Gaaloul, W. Ertmer, and E. M. Rasel,
   "Testing the universality of free fall with rubidium and ytterbium in a very large baseline atom interferometer",
   New J. Phys. **17**, 035011 (2015)
6. H. Ahlers, H. Müntiga, A. Wenzlawski, M. Krutzik, G. Tackmann, **S. Abend**, N. Gaaloul, E. Giese, A. Roura, R. Kuhl, C. Lämmerzahl, A. Peters, P. Windpassinger, K. Sengstock, W. P. Schleich, W. Ertmer, and E. M. Rasel,
   "Double Bragg Interferometry",
   Phys. Rev. Lett. **116**, 173601 (2016)
7. **S. Abend**, M. Gebbe, M. Gersemann, H. Ahlers, H. Müntiga E. Giese, N. Gaaloul, C. Schubert, C. Lämmerzahl, W. Ertmer, W. P. Schleich, and E. M. Rasel,
   "Atom-Chip Fountain Gravimeter",
   Phys. Rev. Lett. **117**, 203003 (2016)
8. E. Giese, A. Friedrich, **S. Abend**, E. M. Rasel, and W. P. Schleich,
   "Light shifts in atomic Bragg diffraction",
   Phys. Rev. A. **94**, 063619 (2016)

Others:

1. **S. Abend** *et al.*
   "Atom-chip based quantum gravimetry with Bose-Einstein condensates",
   Poster prize at the *International School of Physics 'Enrico Fermi'*, **Course 197** (2016)
2. **S. Abend** and E. M. Rasel
   "Kompaktes Fontänen-Gravimeter auf einem Atomchip",
   Physik in unserer Zeit **40**, 61-62 (2017)

Curriculum Vitae

Personalien

Sven Abend
geboren am 07.06.1986 in Lehrte (Niedersachsen)
verheiratet, deutsch

Promotion

10/2010 - heute	Wissenschaftlicher Mitarbeiter in der Arbeitsgruppe Prof. Ernst M. Rasel am Institut für Quantenoptik, Leibniz Universität Hannover

Studium

10/05 - 10/2010	Leibniz Universität Hannover, Studium der Physik
Oktober 2010	Abschluss: Diplom-Physiker
	Thema der Diplomarbeit: 'Großflächige Atominterferometer für die Inertialsensorik', durchgeführt in der Arbeitsgruppe Prof. Ernst M. Rasel am Institut für Quantenoptik, Leibniz Universität Hannover

Schulbildung

07/99 - 04/2005	Gymnasium Burgdorf
April 2005	Abschluss: Abitur, allgmeine Hochschulreife